5-7-2015

Production of Ultracold Molecules with Chirped Nanosecond-Timescale Pulses

Jennifer Carini
University of Connecticut - Storrs, carini@phys.uconn.edu

Production of Ultracold Molecules with Chirped Nanosecond-Timescale Pulses

Jennifer Larke Carini, Ph.D.

University of Connecticut, 2015

We present results on the effects of nanosecond-timescale frequency-chirped laser light on the formation of $^{87}Rb_2$ ultracold ground-state molecules. We investigate these effects through photoassociation (PA) experiments and quantum mechanical simulations. The PA experiments show that at higher intensities, the positive chirps have a higher formation rate than the unchirped or negative linear chirps. The quantum mechanical simulations reveal the mechanism responsible for this enhancement. Contributions from stimulated emission cause the positive chirp to be the most efficient for molecule formation.

Production of Ultracold Molecules with Chirped Nanosecond-Timescale Pulses

Jennifer Larke Carini

Bachelor of Arts, Colby College, Waterville, ME, 2004,

Master of Science, University of Connecticut, Storrs, CT, 2014

A Dissertation

Submitted in Partial Fulfillment

of the Requirements for the Degree of

Doctor of Philosophy

at the

University of Connecticut

2015

2015

APPROVAL PAGE

Doctor of Philosophy Dissertation

Production of Ultracold Molecules with Chirped Nanosecond-Timescale Pulses

Presented by

Jennifer Larke Carini

Major advisor _____
Phillip Gould

Associate advisor _____
Winthrop Smith

Associate advisor _____
Susanne Yelin

University of Connecticut

2015

Contents

List of Tables

List of Figures

Chapter 1
Introduction

Ultracold systems have been investigated for over 25 years, leading to many interesting discoveries and several Nobel Prizes in atom cooling and trapping [1–3], atomic Bose-Einstein condensation (BEC) [4, 5], and trapped ions [6, 7]. Investigations of ultracold (< 1 mK) systems have led to a variety of applications including quantum degenerate gases (bosons, fermions, and mixtures), precision measurements, atomic and optical clocks, quantum information, quantum computing, quantum optics and cavity QED, ultracold chemistry, and ultracold collisions.

Ultracold molecules [8–12] with their vibrational and rotational degrees of freedom, as well as electronic degrees of freedom, are of particular interest. Cold molecules (temperatures > 1 mK) can be produced directly from hot molecules through means such as buffer gas cooling and Stark deceleration. Some groups have had success directly creating ultracold molecules with laser cooling of specific molecules. Ultracold molecules can also be produced indirectly through magnetoassociation or photoassociation. Creating large samples of ultracold molecules in their electronic and rovibrational ground state is an ongoing research field.

Coherent control [13–19] is also of particular interest. This quantum mechanical technique uses laser light to control dynamical processes. Often the phase of the field is shaped to control quantum interferences. Coherent control often requires optimization techniques to find the optimal phase for the system.

This thesis combines coherent control techniques with ultracold atoms and molecules. We start with ultracold atoms and use nanosecond-timescale frequency-chirped photoassociation pulses to form ultracold ground-state molecules. We find that the details of the chirp affect the molecule formation rate.

1.1 Ultracold Molecules

Although the vibrational and rotational degrees of freedom of molecules are useful in various applications, this additional structure makes cooling difficult. There are a variety of popular methods for forming ultracold molecules which can be broadly classified as either direct or indirect methods. For the direct methods, hot molecules are cooled to produce ultracold molecules. The indirect methods involve production of ultracold molecules from ultracold atoms.

1.1.1 Direct Methods of Ultracold Molecule Production

There are several popular methods of directly taking hot molecules and cooling them to produce ultracold molecules. Two such direct methods are buffer gas cooling and Stark deceleration, but the molecules produced in this manner are generally at relatively high temperatures, > 1 mK. Recent laser cooling of molecules has proven to be a potentially useful direct method of producing ultracold molecules.

1.1.1.1 Buffer Gas Cooling

The buffer gas cooling method has been pioneered at Harvard [20]. Molecules are thermalized with a cold helium or neon buffer gas, producing cold, slow-moving molecules. The main advantages to this method are that it is applicable to almost any molecule and that it cools the molecule translationally, vibrationally, and rotationally. The main disadvantages to this method are the temperature limit and the increase of apparatus complexity as lower temperatures are sought.

1.1.1.2 Stark Deceleration

Another popular method of directly producing ultracold molecules is Stark deceleration, first realized at the University of Nijmegen [21]. This method takes advantage of the Stark shift induced by an applied electric field. Stark deceleration slows molecules by controlling their motion using an inhomogeneous electric field. In such an apparatus, there are a series of variable high-voltage electrodes that each remove a small amount of kinetic energy as the molecules are slowed. Although again this method can be applied to a variety of molecules, the main disadvantage is the temperature limit and low resulting density.

1.1.1.3 Laser Cooling of Molecules

The most direct method of producing ultracold molecules is laser cooling of molecules. Several groups are actively engaged in research on direct laser cooling of molecules including SrF at Yale [22], YO at JILA [23], and CaF at Imperial College [24]. Although some specific molecules have been successfully laser cooled, a general laser cooling method to produce a high density of a given cold molecule has yet to be realized.

1.1.2 Indirect Methods of Ultracold Molecule Production

Ultracold molecules can also be formed through indirect methods such as photoassociation (PA) or magnetoassociation, but the resulting molecules are generally in states of high vibrational excitation. Some methods such as optical pumping with broadband light and STIRAP transfer have successfully made molecules at ultracold temperatures in states of low vibrational excitation.

1.1.2.1 Magnetoassociation

Magnetoassociation is a method in which the magnetic field is swept through a Feshbach resonance adiabatically to form a molecular state out of two ground-state atoms. Feshbach resonances were first predicted in 1976 [25]. The main advantage to this method is that it is possible to efficiently produce ultracold molecules at very low temperatures (nK). The main disadvantages of magnetoassociation are that the molecules are produced in high vibrational levels, the atomic species must have available Feshbach resonances, and the production is not continuous. Recently, this method has been used in studying the BEC-BCS crossover [26], and in conjunction with stimulated Raman adiabatic passage (STIRAP) to transfer the Feshbach-formed molecules to the absolute ground state (in KRb [27] and Rb_2 [28]).

1.1.2.2 Photoassociation

Photoassociation (PA) is a popular technique for the production of ultracold molecules, and the one utilized in this thesis. Two laser-cooled colliding atoms absorb a resonant photon to form a molecule in a bound vibrational level of the excited electronic state. The molecule can then decay through spontaneous emission or stimulated emission to a bound vibrational level in the electronic ground state. For each transition, the transfer efficiency is determined by the transition probabilities between the two electronic states, including the Franck-Condon factors. The resulting molecules have temperatures on the order of the ultracold atoms (μK range). A major advantage of PA is that it can be done continuously. For continuous PA, a disadvantage is that spontaneous emission can populate a variety of states, including the continuum. PA spectroscopy has been demonstrated for both homonuclear (for example [29–31]) and heteronuclear (for example [32–34]) alkali dimers. A more detailed description of PA is given in section 2.2.

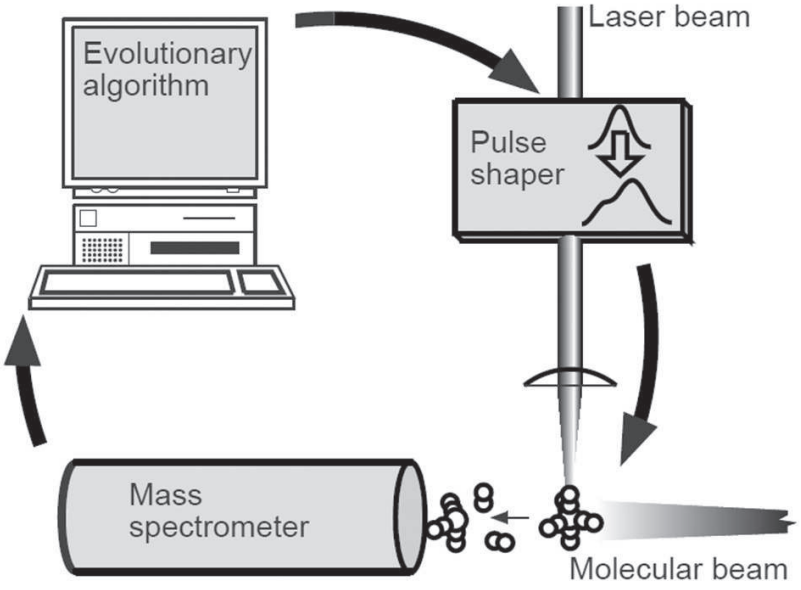

Figure 1.1. Coherent Control

Schematic of experimental setup described in reference [13]. Femtosecond laser pulses are modified in a computer-controlled pulse shaper. Ionic fragments from molecular photodissociation are recorded and then this signal is input into the controlling evolutionary computer algorithm to optimize the branching ratios of this photochemical reaction.

1.2 Coherent Control

Coherent control [13–19] is another field of great interest. Here the optical waveform is manipulated to control the quantum system. Coherent control has applications in physics, chemistry, and biology. Traditionally, coherent control has been employed with a series of ultrafast laser pulses that are shaped with an evolutionary algorithm to optimize a desired outcome.

As an example, researchers at Universität Würzburg conducted an experiment [13] using coherent control techniques to control a dissociation process. In this experiment, femtosecond (fs) laser light was modified in a computer-controlled pulse shaper and used to control a photochemical reaction, as shown in figure 1.1. By employing feedback to the computer algorithm, they were able to optimize the time-

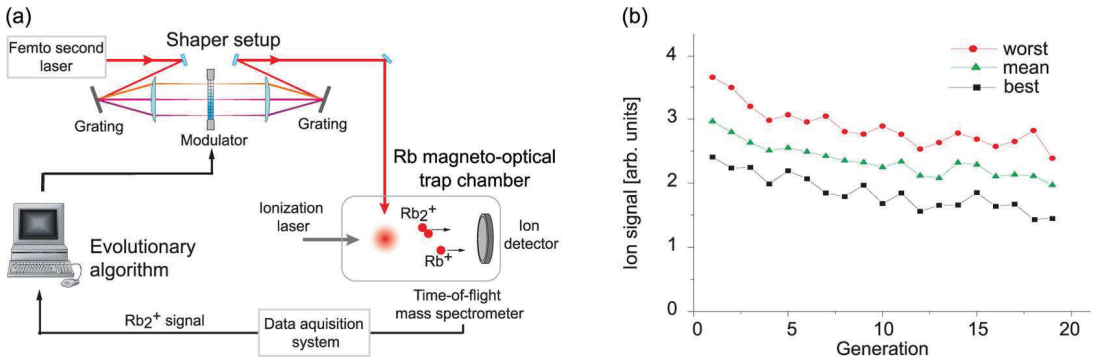

Figure 1.2. Femtosecond Coherent Control Photodestruction Experiment

(a) Experimental setup for iterative closed-loop maximization of ultracold Rb_2 excitation from the electronic ground state by shaped femtosecond pulses. Ultracold molecules are formed by the trapping lasers used for magneto-optically trapping a gas of Rb atoms. Excited molecules are ionized and detected with an ion detector. Each femtosecond laser pulse shape represents an individual of a learning algorithm. (b) Rb_2^+ molecular ion signal evolving during optimization. Worst, mean, and best individuals of the population for each generation are depicted. Fitness of each individual is evaluated by the reduction of the ion signal resulting from more effective excitation of ground-state population to higher lying molecular states. Adapted from reference [36]. Figure and citation taken from reference [38].

dependent phase of the fs pulse and thus the branching ratios of the photodissociation. The authors were able to tailor their pulse to optimize the production of $FeCl^+$ and $CpFeCOCl^+$ from $CpFe(CO)_2Cl$.

Recently, efforts have been made to combine the fields of coherent control and ultracold physics to control ultracold chemical reactions. Many schemes for coherently-controlled ultracold molecule formation have been proposed [8, 17, 18, 35].

Initial femtosecond-timescale experiments showed coherent control of only the photo-destruction of ultracold molecules [36, 37]. Researchers at the Universität Freiburg [36] employed evolution strategies in a feedback loop in an attempt to optimize the photoexcitation of Rb_2, followed by ionization or fragmentation. Through fs pulse shaping, the authors were able to optimize the destruction, as shown in figure 1.2. Researchers at the University of Oxford [37] varied the amount of the chirp, showing that frequency-chirped femtosecond pulses destroyed ultracold ground-state

molecules more efficiently than unchirped pulses. They showed that pulse shaping affects the destruction rate, providing evidence that this quenching is a coherent process.

Recent experiments and simulations have shown photoassociation of excited-state ultracold molecules with femtosecond laser techniques [39–43]. Researchers at the Universität Freiburg [39] employed a pump-probe scheme to photoassociate ultracold ^{85}Rb atoms into Rb_2^* with a cut in the Fourier plane of their femtosecond pulse shaper to eliminate frequencies near the atomic resonance for their "pump" laser. A second "probe" pulse at a variable delay was used to ionize the molecules, as shown in figure 1.3. They observed coherent transient oscillations in the excited-state population as a function of the cutoff frequency of the probe pulse. The delay-dependent modulations in the molecular count rate were too fast to correspond to wavepacket motion of the excited molecules. Their simulations revealed that this oscillatory motion comes from the interaction of the time-dependent laser field and the molecular electronic dipole. The authors also reported a decrease in the ion signal with frequency-chirped pulses compared to unchirped pulses. Similarly, researchers at University of Oxford [40] also employed a pump-probe scheme. They reported similar findings, but saw smaller coherent transient oscillations due to their less sharp spectral cut.

1.3 Outline of This Dissertation

The main focus of this thesis is utilizing coherent control techniques with nanosecond-timescale pulses and ultracold molecules to produce ^{87}Rb molecules in the lowest triplet ground state, $a\ ^3\Sigma_u^+$. These molecules are produced via nanosecond frequency-chirped photoassociation pulses primarily via excitation through $1\ ^3\Pi_g\ (2\ 0_g^-)$. As shown in figure 1.4, we use nanosecond-timescale frequency-chirped photoassociation (PA) light followed by stimulated emission (STE) to enhance the molecular forma-

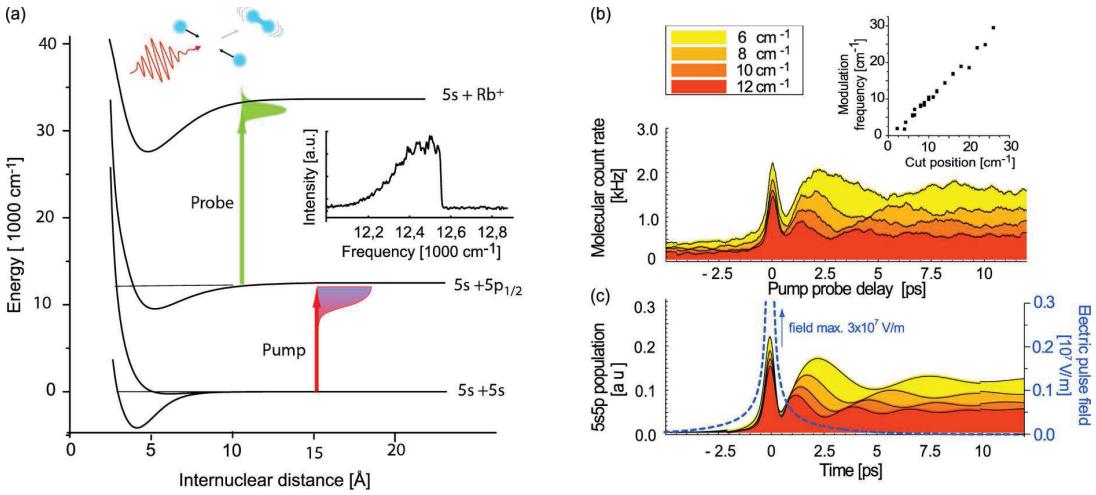

Figure 1.3. Femtosecond Coherent Control Photoassociation Experiment

Transient dynamics in an ultrafast pump-probe experiment. (a) Pump-probe scheme for photoassociation and detection of ultracold Rb_2 molecules using ultrashort laser pulses. First the pump pulse excites the colliding atoms, initiating the wave packet propagation in the higher lying molecular potential. Second, the probe pulse with a variable delay of a few picoseconds probes the dynamics by exciting the molecular pairs to levels close to the ionization threshold. (Inset) Shaped spectrum of the pump pulse, with a sharp frequency cut in order to restrict it below the $5S + 5P_{1/2}$ molecular potential asymptote. (b) Experimental pump-probe molecular ion signal for different cut positions below the $5S + 5P_{1/2}$ asymptote. (Inset) Modulation frequency dependence on the cut position. Note that the modulation frequency perfectly matches the cutoff detuning. (c) $5S + 5P_{1/2}$ state population as calculated from quantum dynamical simulation of excitation of the ground-state excitation with a shaped femtosecond pulse. Dashed blue line shows the temporal envelope of the pump pulse electric field for values below $3*10^6$ V/m. Adapted from reference [36]. Figure and citation taken from reference [38].

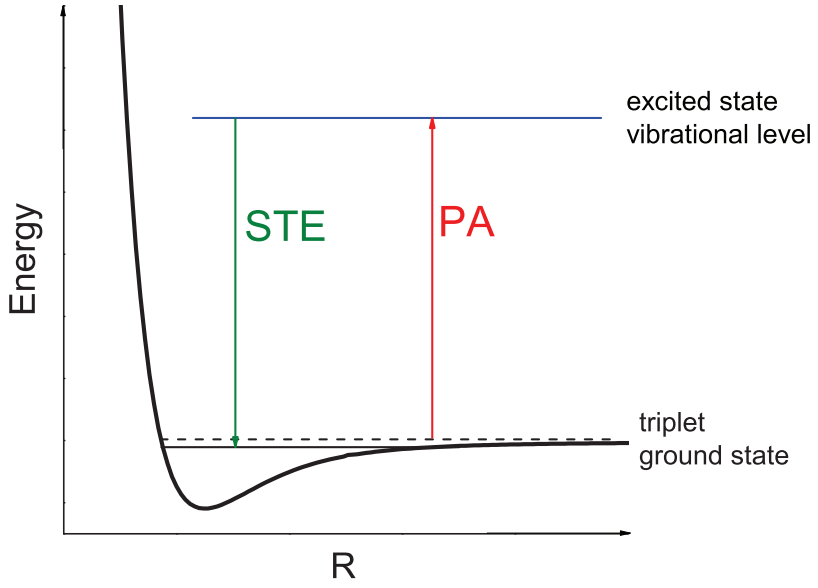

Figure 1.4. Photoassociation Followed by Stimulated Emission

We use photoassociation (PA) from the continuum to a vibrational level in the excited state. Then we use stimulated emission (STE) to a vibrational level in the ground state.

tion rate in a bound target state. Adjusting the details of the frequency-chirped photoassociation pulse can lead to enhancement of the photoassociation rate.

This dissertation is organized as follows:

Chapter 2: Ultracold Atoms and Molecules

This chapter discusses laser cooling and trapping, including magneto-optical traps (MOTs), and the method of photoassociation to form ground-state molecules.

Chapter 3: Experimental Apparatus and Procedure

This chapter discusses the experimental set-up: ^{87}Rb magneto-optical trap (MOT), molecular detection scheme, frequency-chirped photoassociation pulse generation, and data acquisition.

Chapter 4: Quantum Mechanical Simulations

This chapter describes the quantum mechanical simulations we perform in collaboration with Shimshon Kallush and Ronnie Kosloff. We solve the time-dependent Schrödinger equation and follow the wavepacket evolution. We present ^{85}Rb trap-loss collision simulations, which was published as reference [44]. We also present $^{87}Rb_2$ molecular formation rate simulations: for 100 ns chirps, which was published in reference [45]; involving local control, which was published in reference [46]; and further simulations involving faster chirps.

Chapter 5: Experimental Results

This chapter describes measurements of MOT-formed molecules and photoassociation rates from frequency-chirped pulses. These experiments demonstrate that positive chirps can have a higher formation rate than negative chirps and unchirped pulses.

Chapter 6: Conclusions/Outlook

This chapter summarizes the results presented in this thesis and some possible future directions of this research. Along with proposed experiments, further experimental and theoretical results are presented. Incorporating new lasers to take advantage of the D_1 line in Rb allows us to avoid the hyperfine "spaghetti" of the D_2 line. Employing faster electronics, amplification, optimization, and incorporating intensity as well as phase modulation will open the door to many more atomic, molecular, and optical experiments.

Chapter 2
Ultracold Atoms and Molecules

For the experiments presented in this thesis, we use laser cooling and trapping as a source of ultracold atoms. Rubidium atoms are sub-Doppler cooled and trapped in a phase-stable ^{87}Rb magneto-optical trap (MOT). Then we use the method of photoassociation to form ground-state molecules.

2.1 Laser Cooling and Trapping

Laser cooling refers to the various methods of using one or more laser fields to cool atomic and molecular samples to near absolute zero. Methods of laser cooling include Doppler cooling, Sisyphus cooling, resolved sideband cooling, anti-Stokes inelastic light scattering, sympathetic cooling, and a Zeeman slower. In this thesis, we utilize Doppler and sub-Doppler cooling with a magneto-optic trapping force to cool rubidium 87 atoms (^{87}Rb) and form a magneto-optical trap (MOT), as discussed in section 2.1.1. Laser cooling and trapping is discussed in detail in reference [47].

Doppler cooling was first proposed in 1975 [48, 49]. Briefly, laser light is tuned slightly below an electronic transition in an atom. Then, if an atom moves towards the light source, it will absorb more photons, due to the Doppler effect. With counter-propagating laser beams, the atoms will always absorb more photons from the laser beam pointing opposite to their direction of motion. With each absorption, the photon's momentum is transferred to the atom. The excited-state atom can then undergo

spontaneous emission, resulting in a recoil from the emitted photon momentum. Since the photon is emitted in a random direction, these recoils average to zero after many cycles. The momentum kick of a single photon is quite small, but by exciting a strong cycling atomic transition, more than ten million photons per second can be scattered, producing a large total velocity change. The dependence of absorption rate on velocity, via the Doppler shift, results in a damping force which reduces the kinetic energy of the atom, thereby cooling it.

2.1.1 Magneto-Optical Trap (MOT)

Let's consider a two-level atomic model in the presence of laser light, w_L, and a magnetic field gradient provided by a pair of anti-Helmholtz coils. The anti-Helmholtz coils are a pair of coils with current in opposite directions that create a zero field at the center. The corresponding level diagram is shown in figure 2.1. The ground state is J=0 and the excited state is J=1. The z direction is along the symmetry axis through the center of the coils, therefore the magnetic fields cancel at the center, z = 0. The laser beam in the +z/-z direction is σ^+/σ^- polarized. The linear magnetic field gradient, generated by anti-Helmholtz coils, Zeeman splits the m_J levels in the J=1 state into three Zeeman components, m_J = +1,0, and -1. For an atom at rest, there are three possible cases:

1. Atom is at z=0: The magnetic field is zero, so the absorption rates are equal for both σ^+ and σ^-.

2. Atom is at z>0: The atom preferentially absorbs from the σ^- beam, resulting in a net force in the -z direction.

3. Atom is at the z<0: The atom preferentially absorbs photons from the σ^+ beam, resulting in a net force in the +z direction.

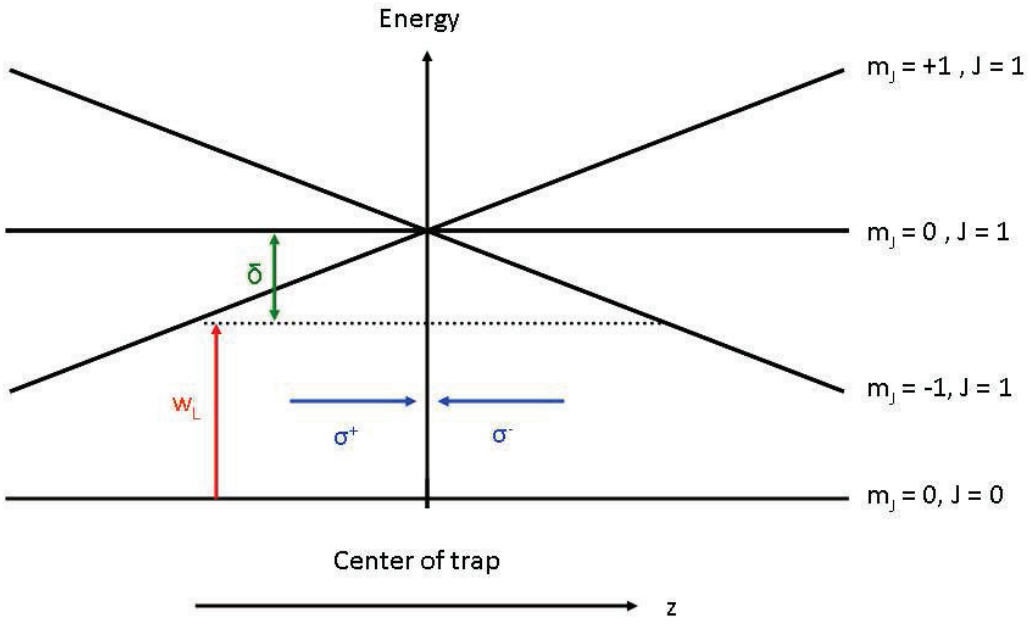

Figure 2.1. Two-level Atomic Model for MOT Operation

Two-level atomic model where J = 0 is the ground state and J = 1 is the excited state. A linear magnetic field gradient, generated by anti-Helmholtz coils, Zeeman shifts the m_J levels in the excited state, giving rise to the three Zeeman components: m_J = +1,0, and -1. The σ^+ and σ^- circularly polarized laser beams are of frequency w_L detuned by δ from the J=1 state. These drive $\Delta m = +1$ and Δm = -1 transitions, respectively. The laser and magnetic fields create the necessary damping and restoring forces to cool and trap an atomic sample.

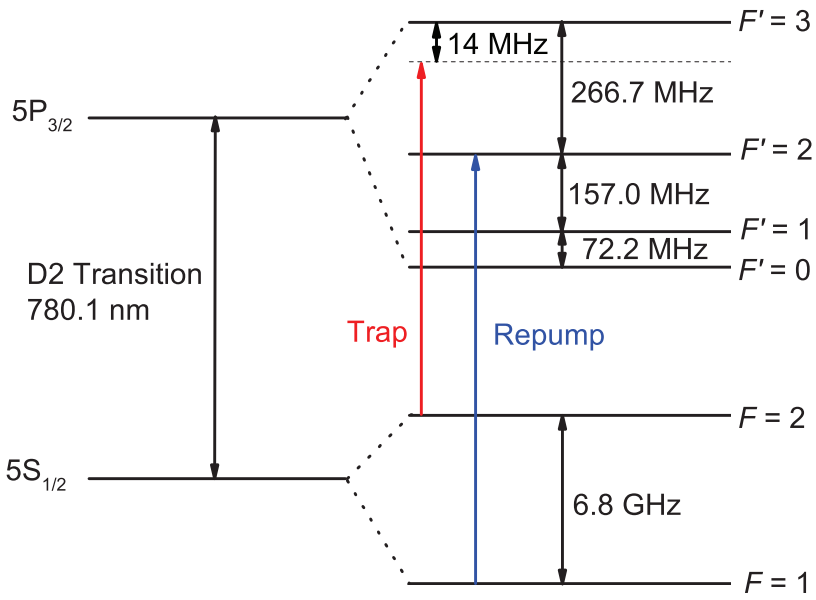

Figure 2.2. ^{87}Rb MOT Transitions

Energy level diagram for ^{87}Rb atoms showing hyperfine levels F of the ground electronic state ($5S_{1/2}$) and F' of the electronic excited state ($5P_{3/2}$). The trap laser is detuned -14 MHz from the $F = 2 \rightarrow F' = 3$ cycling transition. The repump laser used to optically pump atoms back into the cycling transition is also shown. The various energy splittings are for the purpose of illustration and are not drawn to scale.

This results in the atoms experiencing a restoring force directed towards the center of the trap, at z=0. Doppler cooling is still effective, so the atoms are also being cooled towards zero kinetic energy.

For actual atomic systems, this two-level representation is inadequate. An energy level diagram for ^{87}Rb D_2 line is shown in figure 2.2. The trap laser is red-detuned by -14 MHz from the $F = 2 \rightarrow F' = 3$ cycling transition. Although excited atoms mostly decay back to the F=2 state, occasionally they end up in the F=1 state where they are no longer able to be re-excited by the trap light. Therefore we add a repump laser tuned to the F=1 $\rightarrow$ F'=2 transition to optically pump the atoms back into the F=2 state.

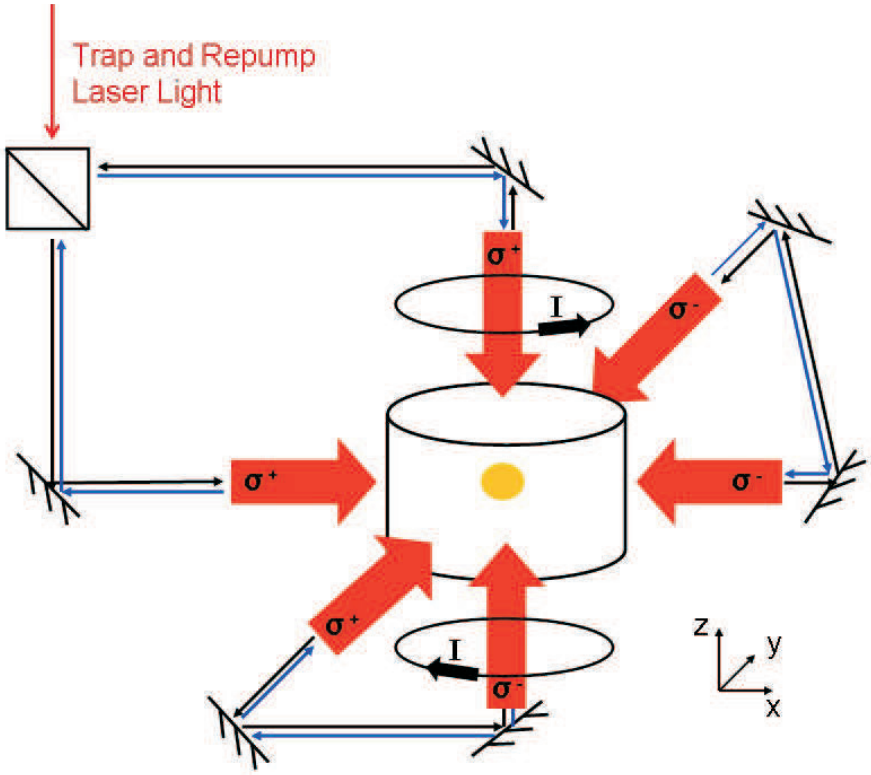

Figure 2.3. Magneto-optical Trap (MOT)

The MOT is operated in a phase-stable configuration. For this example configuration, the first beam (black line) travels along the +x axis, -y axis, and then the +z axis. The second beam (blue line) travels along -z, +y, and then -x.

Extending now from 1D to 3D, we have counter-propagating beams in all three directions and a radial as well as axial magnetic field gradient, resulting in a dense cloud of cold atoms in the center of the trap. Typically the lasers are split into three beams, one for each axis. Each beam travels through the chamber, and is then retro-reflected. In our experiments, we operate the MOT in a phase-stable configuration [50]. A diagram of the phase-stable MOT configuration is shown in figure 2.3. Our chamber has the same anti-Helmholtz magnetic coils as the traditional MOT configuration. However, instead of three beams that are retro-reflected, we start

by splitting our beams in two. As depicted in the example configuration shown in figure 2.3, the first beam travels along the +x axis, -y axis, and then the +z axis. The second beam counterpropagates, traveling along -z, +y, and then -x. The MOT in this phase-stable configuration, as its name denotes, is more stable then a traditional configuration. The phase-stable MOT keeps the spatial phase of the combined electric field of the trapping beams constant, regardless of small fluctuations in the mirror positions. Verifications of this phase stability are given in references [51, 52].

2.2 Photoassociation

Photoassociation (PA) is a method of using laser light to transfer two free atoms to a bound molecular state [53]. A diagram of the PA method is shown in figure 2.4. In this figure, two free atoms in the continuum are illuminated with PA laser light. The atoms form a molecule in a bound vibrational level v' of the excited state. The molecule then undergoes stimulated or spontaneous emission to a bound vibrational level v" of the ground state. Although shown for homonuclear PA (forming Rb_2 for this thesis), heteronuclear PA is also possible. The PA process can be represented by:

$$Rb + Rb + h\nu_{PA} \rightarrow Rb_2^*(v'). \tag{2.1}$$

Once the molecule is formed, it can decay by spontaneous emission (SE) to a bound state or back into two free atoms. The process of decaying to a ground-state molecule can be represented by:

$$Rb_2^*(v') \rightarrow Rb_2(v'') + h\nu, \tag{2.2}$$

and the excited molecule decaying back into two free atoms is represented by:

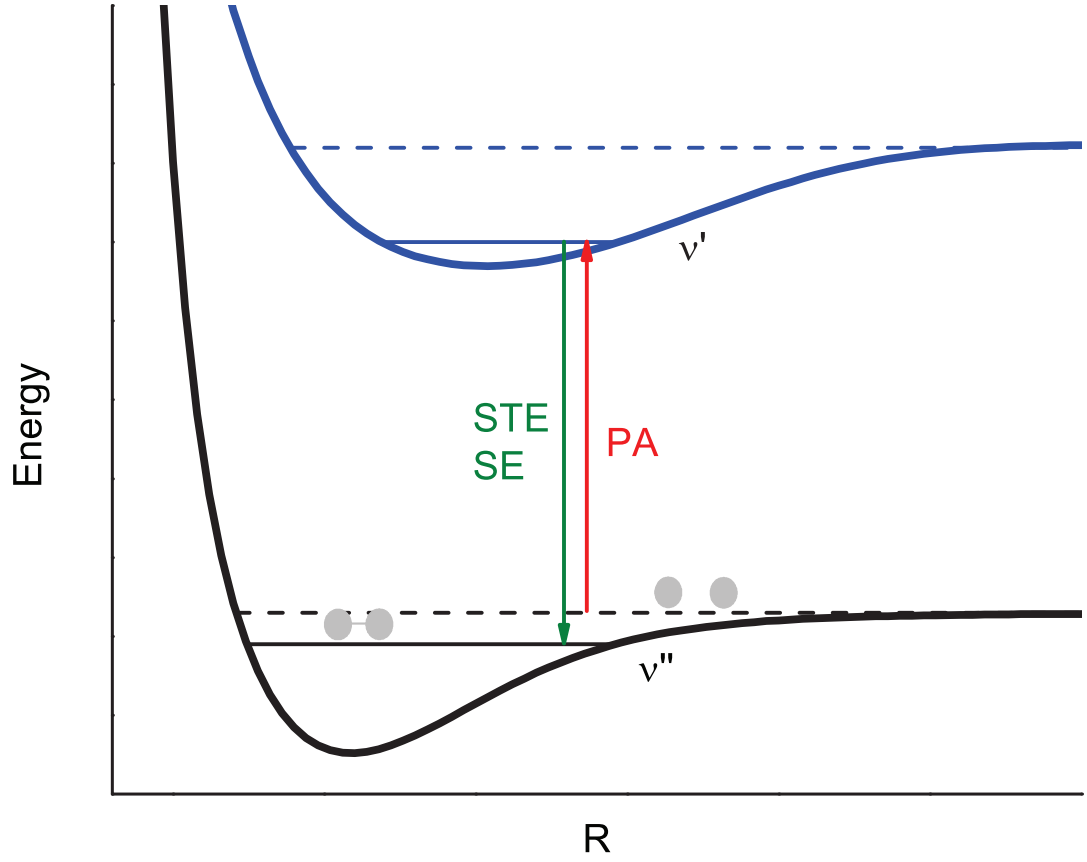

Figure 2.4. Diagram of Photoassociation (PA) Method

The black potential is the ground state with the low-energy continuum as a black dashed line. The blue potential is the excited state with the atomic asymptote marked as the dashed line. Two free atoms in the continuum of the ground state undergo photoassociation (PA) to form a molecule in a vibrational level v' of the excited state. This molecule undergoes stimulated emission (STE) or spontaneous emission (SE) to a bound vibrational level v" of the ground state.

$$Rb_2^*(v') \rightarrow Rb + Rb + h\nu. \tag{2.3}$$

Under the correct conditions, for example if the PA laser frequency shifts in time, the PA laser can also dump the molecule down into a bound vibrational level of the ground state. This stimulated emission can be represented by:

$$Rb_2^*(v') + h\nu_{PA} \rightarrow Rb_2(v'') + 2h\nu_{PA}^{'}. \tag{2.4}$$

At each step, the yield is governed by the transition probabilities between the two electronic states, including the Franck-Condon Factors (FCFs). Since diatomic molecules spend most of their time at the inner and outer turning points, electronic transitions are more likely to occur at these turning points. It is also assumed that these transitions are very fast compared to the timescales of the nuclear motion (Born-Oppenheimer approximation). The probabilities of these transition are proportional to the FCFs, the square of the overlap integral between vibrational wavefunctions:

$$FCF_{mn} = \left| \int (\psi_{gm}^*(x)\psi_{en}(x)dx \right|^2, \tag{2.5}$$

where x is the coordinate of motion along the potential surface, ψ_{gm} is the mth vibrational wavefunction of the ground state, and ψ_{en} is the nth vibrational wavefunction of the excited state. The FCF is between zero and one. The strength of a transition is characterized by not only the FCF, but also the transition dipole moment. As calculated in reference [53], using a perturbative quantum mechanical approach, the PA rate Γ is given by

$$\Gamma \propto n\lambda^3\omega^2\Delta^{-1/2}, \tag{2.6}$$

where n is the MOT density, λ is the thermal de Broglie wavelength, ω is the Rabi frequency, and Δ is the PA detuning with respect to the asymptote. Therefore, the PA rate will also increase with a higher MOT density, higher PA laser intensity, and lower atom temperature.

Some molecules are formed without actively photoassociating with a PA laser. These MOT-formed molecules are presumably the result of PA by the MOT laser beams. Since the MOT trap laser is detuned by only -14 MHz, the atom pairs are excited at large internuclear distances. Therefore, they experience minimal acceleration and are likely to decay before reaching short range. Additionally, the MOT laser intensity is much less than the typical PA laser intensity. These factors result in significantly less spontaneously formed molecules than with a PA laser. Nevertheless, they do constitute a background signal which must be accounted for.

It is important to note that, unfortunately, the bound molecules can also undergo photodestruction (PD) by the very light that creates them or cools and traps them. During this process, the laser light excites the molecule to an excited-state vibrational level. From there, it can decay back into two free atoms. In particular, subsequent pulses from our PA laser can cause PD of already existing molecules. This process can be represented by:

$$Rb_2(v'') + h\nu_{PA} \rightarrow Rb_2^*(v') \rightarrow Rb + Rb + h\nu. \tag{2.7}$$

Since there are many electronically excited states in Rb, and their vibrational levels are closely spaced near the asymptote, the excited-state vibrational level responsible for PD need not be the same one used for PA. When inferring molecule production rates from the number of detected molecules, we must account for this PD loss process.

Chapter 3
Experimental Apparatus and Procedure

For the experiments presented in this thesis, we use a phase-stable ^{87}Rb magneto-optical trap (MOT) to provide ultracold atoms. We utilize a dual-chamber setup where the magneto-optical trap (MOT) in the ultra-high vacuum (UHV) "science" chamber is loaded by a MOT in the low-velocity intense source (LVIS) chamber. An electro-optical phase modulator is used to frequency-chirp our photoassociation (or "probe") laser. Resonantly-enhanced multiphoton ionization (REMPI), in conjunction with time-of-flight (TOF) mass spectroscopy, is employed to selectively detect the Rb_2^+ resulting from chirped photoassociation. We then integrate and average the ion signals and record them with the data acquisition software.

3.1 ^{87}Rb magneto-optical trap (MOT)

The source of ultracold atoms for the experiments in this thesis is a phase-stable [50] ^{87}Rb magneto-optical trap (MOT) [54]. We use four diode lasers to cool and trap the atoms in our dual MOT set-up. We load a $\sim$150 μK ^{87}Rb MOT in an ultra-high vacuum (UHV) chamber from a low-velocity intense source (LVIS) MOT in a separate chamber [55]. This dual-chamber setup allows us to conduct experiments in the UHV chamber with a lower background-gas pressure. The LVIS is in a semi-phase-stable configuration, allowing for a push beam to load the UHV MOT through a small aperture (0.035" diameter) at one end of a stainless steel tube 4" long by 1/2"

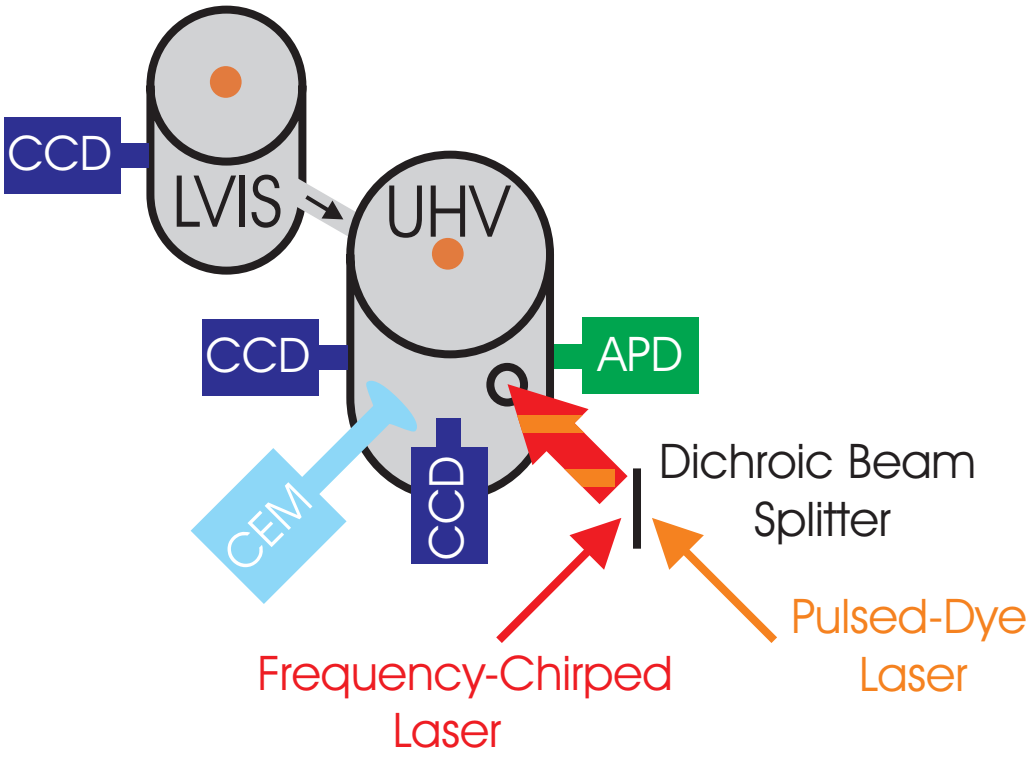

Figure 3.1. Experimental Set-up

A diagram of the experimental apparatus (not to scale). A ^{87}Rb MOT in the ultra-high vacuum (UHV) chamber is loaded from the low-velocity intense source (LVIS) chamber and operated in a phase-stable configuration. For diagnostics, we have charge-coupled device (CCD) cameras to image the MOTs and an avalanche photodiode (APD) to measure the UHV MOT fluorescence. A pulsed-dye laser used for resonance-enhanced multiphoton ionization (REMPI) is combined with the frequency-chirped probe laser on a dichroic beam splitter. There is a channel electron multiplier (CEM) to directly detect the Rb_2^+. Not shown are the MOT lasers.

in diameter connecting the two chambers. This hole allows the cold beam of atoms through while being small enough to maintain the pressure difference between the two chambers. The UHV chamber is pumped by a 20 l/s ion pump, easily achieving at least 10^{-10} torr. The LVIS chamber is pumped by a 3 l/s ion pump, often operated with a background vapor pressure of 10^{-8} torr. The source of the Rb background vapor is typically a set of seven Rb getters. Passing a small current ($\sim$ 4 A) through a single getter supplies this steady Rb background vapor. During the course of the work presented in this thesis, a coating of Rb formed over the ceramic insulators in the LVIS ion pump creating an electrical leakage current between the anode and cathode of the ion pump element. Therefore, for some of the experimental data presented in this thesis, part of the LVIS chamber near the getters was employed as a cold finger (kept at $\sim 8^\circ$ C) to maintain low pressure with the LVIS ion pump off. Under these conditions, the LVIS ion pump was turned on briefly ($\sim$ 3 minutes per week) to act as a source of Rb by the heating of the ion pump as a result of the leakage current.

The UHV anti-Helmholtz coils are approximately 20 turns of water-cooled 1/8" outer diameter copper tubing driven with 50 A, providing an axial field gradient of $\sim$ 12 G/cm. The LVIS anti-Helmholtz coils were originally approximately 20 turns of ribbon cable driven with 1 A. Due to undesirable heating effects, these were replaced with 6 turns of water-cooled 1/8" outer diameter copper tubing driven with 20 A. To compensate for stray magnetic fields (such as the earth's magnetic field) and the fields from the other chamber, we have small shim coils on both sides of each axis of both chambers. Each opposing pair of coils has the current flowing in the same direction, producing a dc offset of the magnetic field in that direction. These $\sim$ 100 turns of 18 AWG copper wire are driven with up to 3 A each. The shim coils can also be used to slightly move the UHV MOT to optimize position, peak density, and

shape, whereas with the LVIS chamber these slight adjustments are used primarily to optimize the loading of the UHV MOT.

The UHV MOT is operated with up to N = 2.5*10^7 trapped atoms and a peak atomic density of n = 1*10^{11} cm^{-3}. For diagnostics, we have an avalanche photodiode (APD, Hamamatsu C5460-01) to monitor the UHV MOT fluorescence and charge-coupled device (CCD) cameras to take images of the MOTs. A schematic diagram of the experimental apparatus is shown in figure 3.1. The APD has a high signal-to-noise ratio and has been calibrated to have ~ 0.158 μV per excited atom. The frequency-chirped photoassociation (or "probe") laser (see section 3.3) is combined on a dichroic beam splitter with a pulsed dye-laser beam used for resonance-enhanced multiphoton ionization (REMPI) of the molecules (see section 3.2.1). A channel electron multiplier (CEM) directly detects the resulting Rb_2^+ (see section 3.2.2).

We use homemade external-cavity diode lasers (ECDL) and free-running diode lasers (FRDLs) for the cooling and trapping of ^{87}Rb. The laser design is based on [56] and the schematics can be found in [51, 52, 57]. Two ECDLs are locked to the appropriate saturated absorption peaks corresponding to the trap and repump transitions, as shown in figure 2.2. The trap laser is typically operated at a detuning of -14 MHz from the $F = 2 \rightarrow F' = 3$ cycling transition. The electronics for locking are described in [51, 52, 57]. The trap laser (50 mW Hitachi HL7852G) is used as a master laser to injection lock two FRDL slave lasers. For injection locking, a small amount of master light (typically ~ 250 μW) is aligned through the rejection port on the optical isolator and injected into the slave. Then, at particular diode currents, the slave will match the master injection frequency or lock to the master laser. Injection locking slaves reduces the number of lasers that need to be locked to saturated absorption peaks and allows us to have higher intensity trapping light since the external cavity configuration significantly reduces the output power. The first

slave laser (90 mW Thorlabs L785P090) provides the trap light for the UHV MOT. It is coupled through an optical fiber for optical alignment stability. The light from the repump ECDL (90 mW Thorlabs L785P090) is sent directly to the UHV chamber since low repump intensity is sufficient due to the very slow rate of optical pumping of atoms into the lower hyperfine state. The second slave laser (80 mW Sanyo DL-7140-201W) is for the LVIS chamber. It also provides the repump light for the LVIS through a ~ 6.6 GHz blue sideband. We generate this sideband by a voltage-controlled oscillator (VCO) (Emhiser EVCO-04 668/000-00Vt) and an amplifier (Mini-Circuits ZX60-183-S+) which is coupled into the diode injection current using a bias tee (Mini-Circuits ZX86-12G-S+). This sideband frequency is optimized to the repump transition by adjusting the tuning voltage of the VCO while the amplitude (typically $> 2\%$) is adjusted through the use of in-line RF attenuators. The current is coupled into the diode using a short length of RG-174 coaxial cable soldered directly to the diode pins. Two-frequency generation with a frequency-modulated injection-locked diode was first investigated in [58]. For certain experiments, being able to change the number of trapped atoms, N, or maintain a particular N is important. With the current setup, we can attenuate the intensity of the LVIS MOT beams, reducing the loading rate of the UHV, and thereby reducing N while maintaining the same n. An image of a UHV MOT taken with a CCD camera is shown in figure 3.2. The CCD camera records 640 by 480 pixels along the x and z axes respectively. The image in figure 3.2 is cropped to 350 by 350 pixels for clarity. The CCD camera is calibrated to 0.0011 cm per pixel. An iris is used to attenuate the UHV MOT intensity to avoid saturation. Due to radial symmetry, the y-axis is assumed to have an identical profile to the x-axis. A LabVIEW program finds the peak amplitude in each direction and fits Gaussians at those locations, determining the $1/e^2$ radii. For the image in figure 3.2, the $1/e^2$ radii are determined to be $r_x = r_y = 172$ μm and $r_z = 179$ μm, yielding

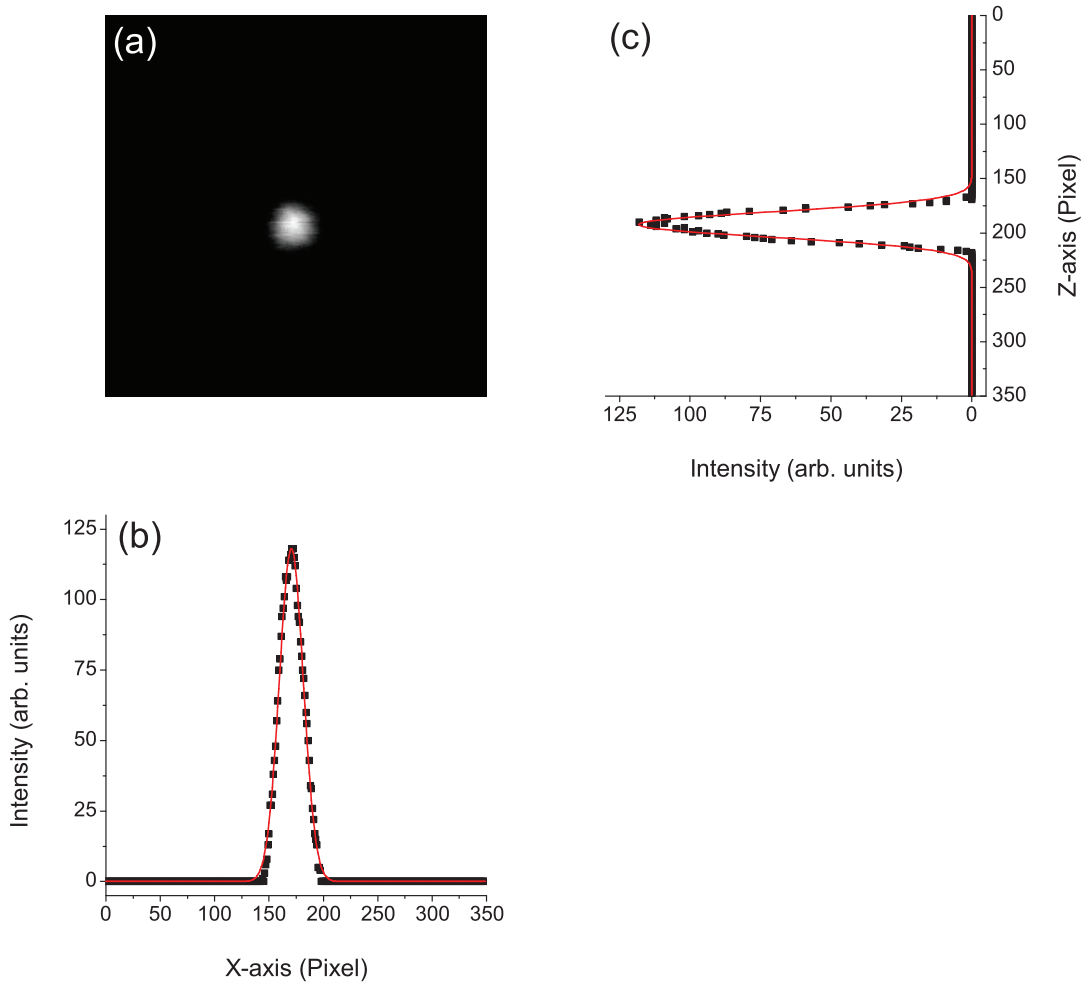

Figure 3.2. MOT Image

An image of the UHV MOT taken with a CCD camera is shown in (a). The density profiles (black points) and corresponding Gaussian fits (red lines) are shown for the x-axis (b) and z-axis (c). Due to radial symmetry, we assume that the y-axis has an identical profile to the x-axis. Converting the fits to μm, the $1/e^2$ radii are then $r_x = r_y = 172$ μm and $r_z = 179$ μm or an average $1/e^2$ radius of 174 μm. The number of trapped atoms, N, is $\sim 3*10^6$ and the peak density, n, is $\sim 1*10^{11}$ cm^{-3}.

an average $1/e^2$ radius of 174 μm. Based on the image analysis and APD reading, the number of trapped atoms is $\sim 3*10^6$ and the peak density is $\sim 1*10^{11}$ cm^{-3}.

3.2 Molecular Detection Scheme

We are able to directly detect our molecules via resonantly-enhanced multiphoton ionization (REMPI). We use a 10 Hz Nd:YAG-pumped tunable pulsed dye laser for REMPI detection of the $^{87}Rb_2$ molecules. The time-of-flight (TOF) of the ions to the channel electron multiplier (CEM) detector allows us to distinguish Rb_2^+ from Rb^+ using a digital boxcar averager.

3.2.1 Resonance-enhanced multiphoton ionization (REMPI)

Our ionization scheme utilizes the potentially state-selective resonantly-enhanced multiphoton ionization (REMPI) technique [59]. Typically, a resonant single or multiple photon absorption to an electronically excited intermediate state is followed by another photon which ionizes the atom or molecule. Generally, the optical intensity required to drive a multiphoton transition is significantly larger than for a single-photon transition. The REMPI process typically produces a single positive ion and a free electron. The REMPI technique employed for the data in this thesis is shown in figure 3.3. Molecules from the triplet ground state, $a\ ^3\Sigma_u^+$, are excited to an intermediate electronically excited state, $^3\Pi_g$, with a single photon. Then a second photon of the same wavelength ionizes the Rb_2^* to form Rb_2^+. The intermediate state, $^3\Pi_g$, assignment is based on [60]. The $^3\Sigma_g^+$ and $^1\Sigma_g^+$ states are also nearby [59–61]. Since the pulsed laser can also ionize ground-state atoms, we distinguish between Rb_2^+ from Rb^+ using time-of-flight (TOF), as described in Section 3.2.2.

The REMPI detection laser is a tunable pulsed dye laser (Continuum ND6000) operating at ~ 602 nm. It is pumped by a frequency-doubled (532 nm) 10 Hz Nd:YAG

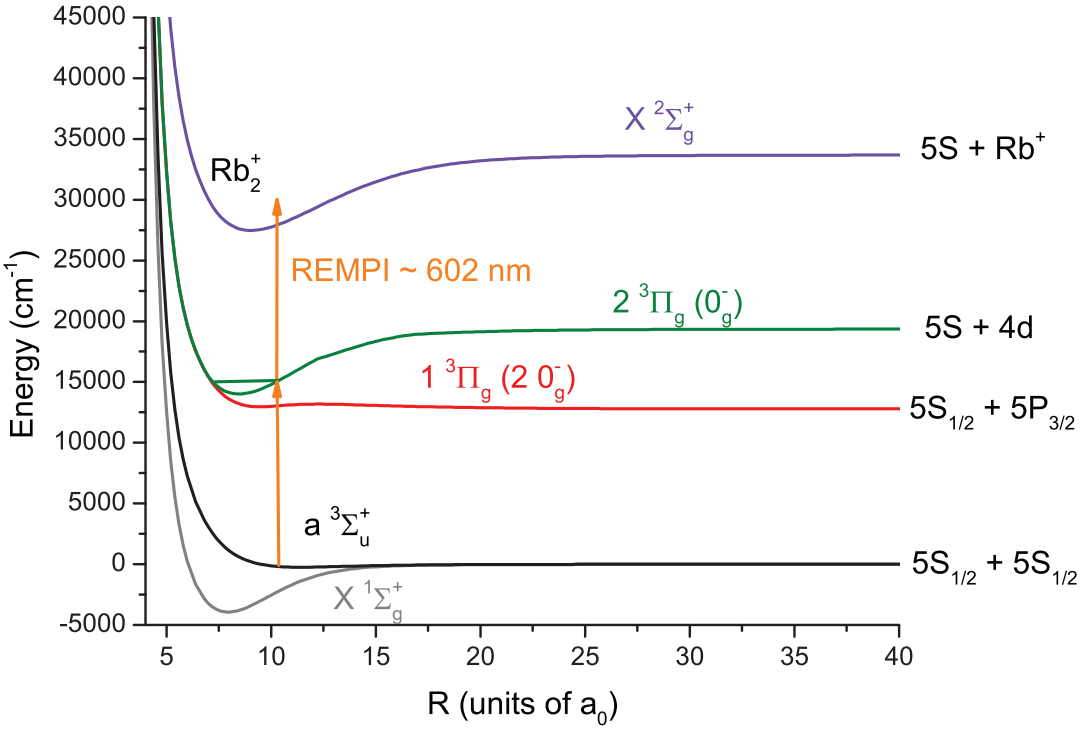

Figure 3.3. REMPI Detection Pathways

Resonantly-enhanced multiphoton ionization (REMPI) detection scheme. Molecules from the triplet ground state, $a\ ^3\Sigma_u^+$, are excited to an intermediate electronically excited state, $^3\Pi_g$, with a single photon. Then a second photon of the same wavelength ionizes the Rb_2^* to form Rb_2^+.

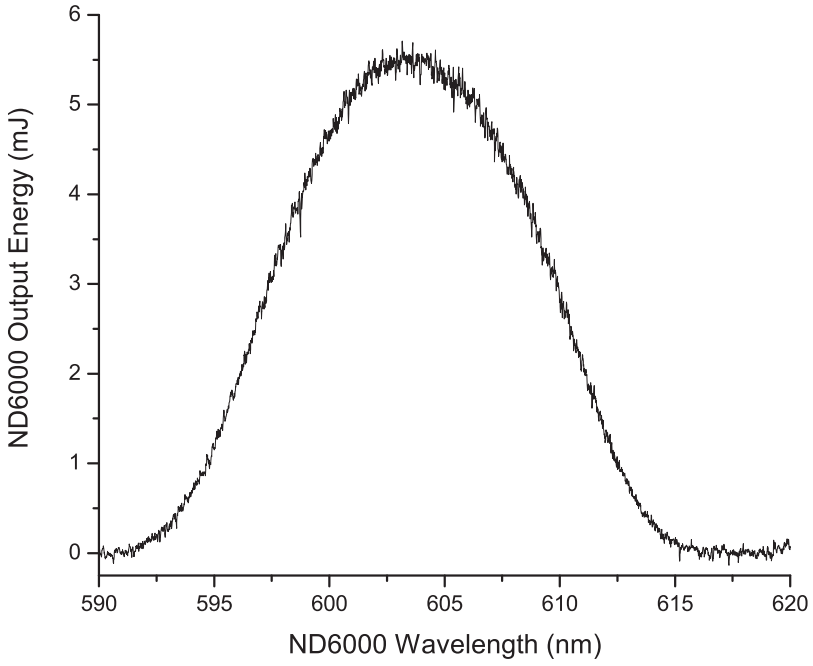

Figure 3.4. ND6000 Pulse Energy vs. Wavelength

ND6000 Pulse Energy vs. Wavelength. The mixture of Rhodamine 610 and Rhodamine 640 allows us to operate between $\sim$ 595 nm and $\sim$ 612 nm, with our typical operating wavelength of $\sim$ 602 nm near the peak of the energy curve. The pump power is 52.3 mJ.

laser (Continuum Surelite II). For the work in this thesis, we use a mixture of Rhodamine 610 and Rhodamine 640 dyes dissolved in methanol. A typical energy vs. wavelength plot for this mixture is shown in figure 3.4. The pulse energy of the dye beam is measured directly with a Thorlabs PM100D power meter with a S350C head, or using a pick-off, with a Gentec S121C power meter. This mixture allows us to operate between $\sim$ 595 nm and $\sim$ 612 nm, with our typical operating wavelength of $\sim$ 602 nm near the peak of the energy curve. The beam is slightly focused to produce a $\sim$5 ns, $\sim$4.5 mJ, $\sim$3 mm diameter beam at the MOT position. The detection beam is significantly larger than the MOT diameter allowing us to detect the ballistically expanding cloud of untrapped molecules. The typical shot-to-shot fluctuations in the

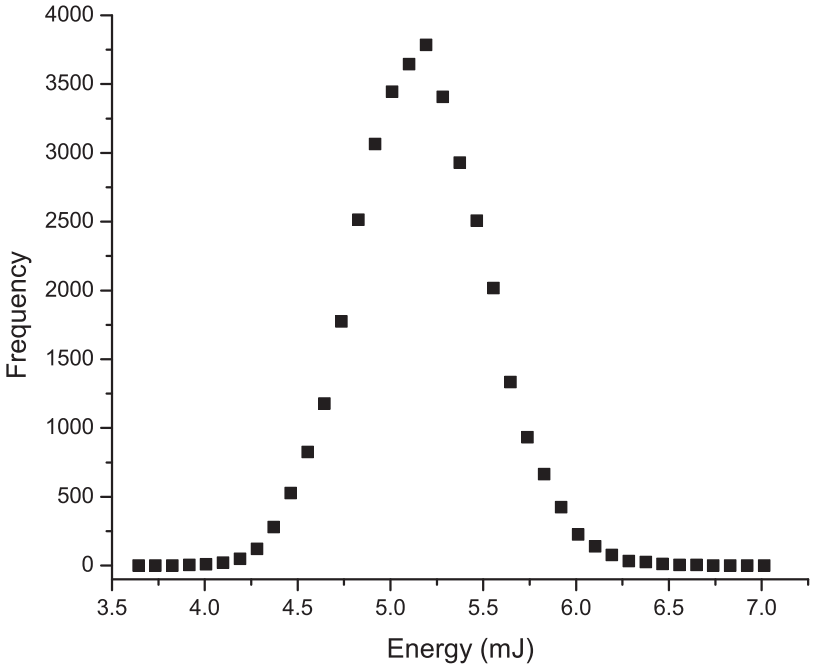

Figure 3.5. ND6000 Shot-to-shot Noise

ND6000 shot-to-shot noise. One hour of 10 Hz individual shot energies were recorded and placed in ∼0.1 mJ bins. The average pulse energy is 5.13 mJ with a standard deviation of 0.35 mJ or just under 7%.

ND6000 output are displayed in figure 3.5. The standard deviation is found to be under 7%. To determine the linewidth of the ND6000, we take a REMPI scan, as described in section 3.4.1, over an atomic resonance at low power ($\sim$ 1 mJ) and fit the resulting points to a Lorentzian function. A typical curve is shown in figure 3.6. This REMPI scan is taken across the two-photon 5s $\rightarrow$ 17d line and the full-width-at-half-maximum (FWHM) linewidth is found to be 0.135 cm^{-1}. This linewidth is much broader than the typical rotational spacings of ultracold Rb_2 in high v" levels, precluding the REMPI spectra from having rotational resolution. Although we have some vibrational resolution, we are not able to distinguish between the very high vi-

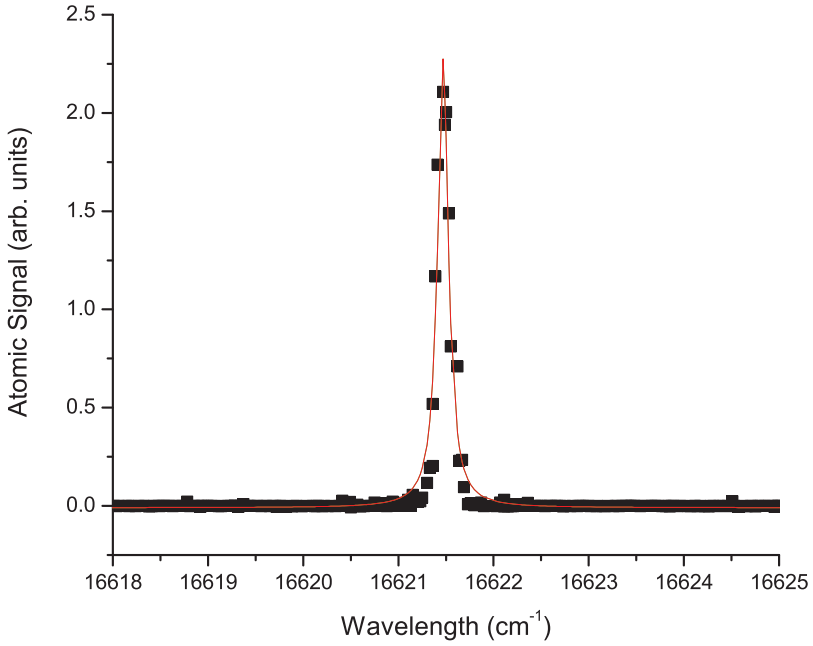

Figure 3.6. ND6000 Linewidth

ND6000 Linewidth. A Lorentzian fit of a REMPI scan across the 17d atomic resonance yields a linewidth of 0.135 cm^{-1}

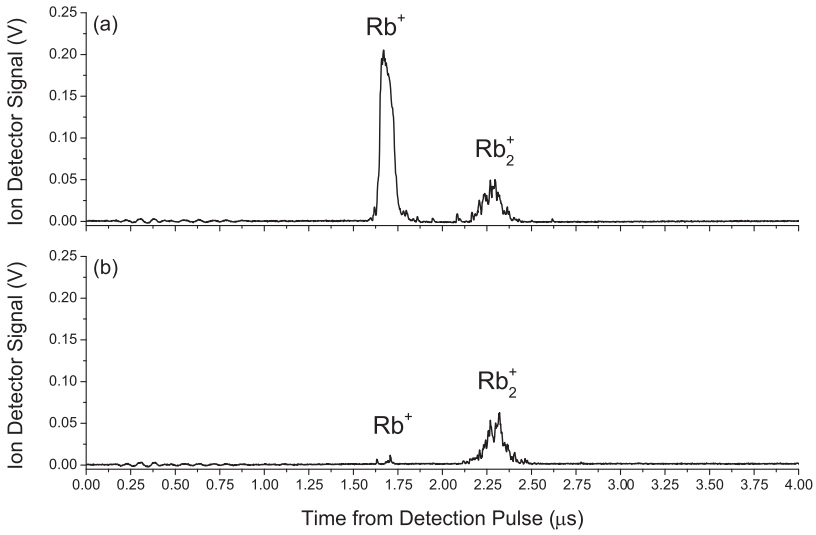

Figure 3.7. Time-of-Flight

Time-of-flight spectra with (a) MOT lasers left continuously on and (b) MOT lasers turned off for 50 μs centered on the arrival of the REMPI detection pulse. The spectra is of MOT-produced molecules only (the probe laser is off) and the REMPI laser is tuned to 16607.97 cm^{-1}.

brational levels $a\ ^3\Sigma_u^+$ (v"=37-39) due to their close spacing and our relatively large linewidth.

3.2.2 Ion Detection

The ions resulting from the pulsed photoionization are detected by a channel-electron multiplier (CEM) "Channeltron" (Photonics CEM 4860 C). Since the Rb^+ and Rb_2^+ differ in mass, they can be distinguished by their time-of-flight (TOF) to the detector. An example of a TOF spectrum is shown in figure 3.7. The molecules arrive a factor of $\sqrt{2}$ later in time due to the difference in mass. A TOF spectrum with the MOT on all the time is shown in figure 3.7 (a). Typically, we turn off the MOT for 50 μs centered on the detection pulse to reduce ionization of excited atoms by the pulsed detection light, as shown in figure 3.7 (b). The CEM is located 1.02" away from the MOT [62] and operated at negative high voltage. There is a circular

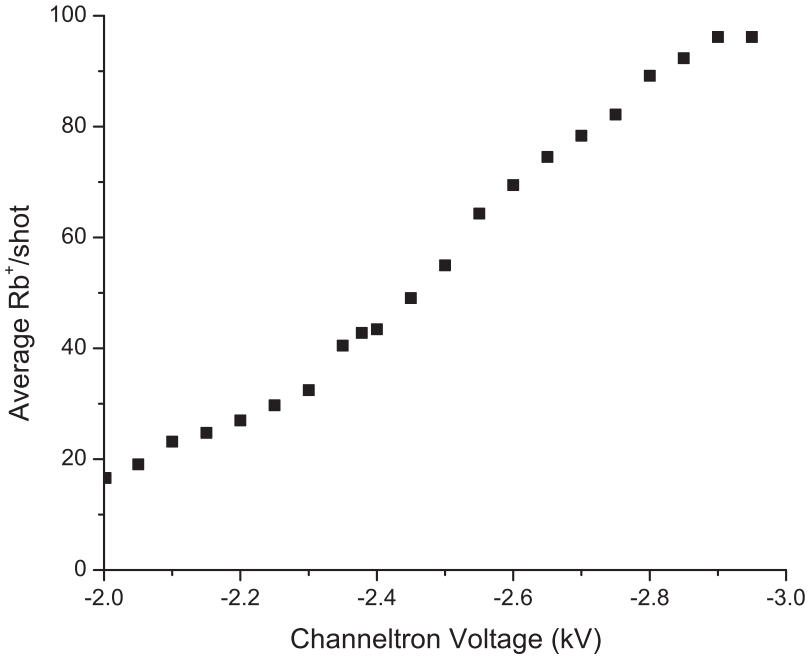

Figure 3.8. Channeltron Voltage

We monitor the average Rb^+ signal while varying the channeltron voltage to find the optimal operating voltage.

oxygen-free high-conductivity copper field plate that is currently grounded located symmetrically in the chamber on the other side of the MOT. In future experiments, this field plate could be set to another electrical potential to optimize the TOF signal. Implementing a wire-mesh grid in future experiments could also optimize the TOF signal [63–66]. To optimize the operating voltage, we tune the REMPI laser to a known atomic resonance and look at how the 1000-shot-averaged signal changes using a digital boxcar averager (discussed in section 3.2.3). We adjust the window we look at as we adjust the operating voltage since the ion arrival times move with the changing voltage. In this manner, the optimal operating voltage for the conditions in this thesis is found to be -2.85 kV. A plot of the average Rb^+ signal versus operating voltage is shown in figure 3.8. We note that this optimization is complicated by the fact that

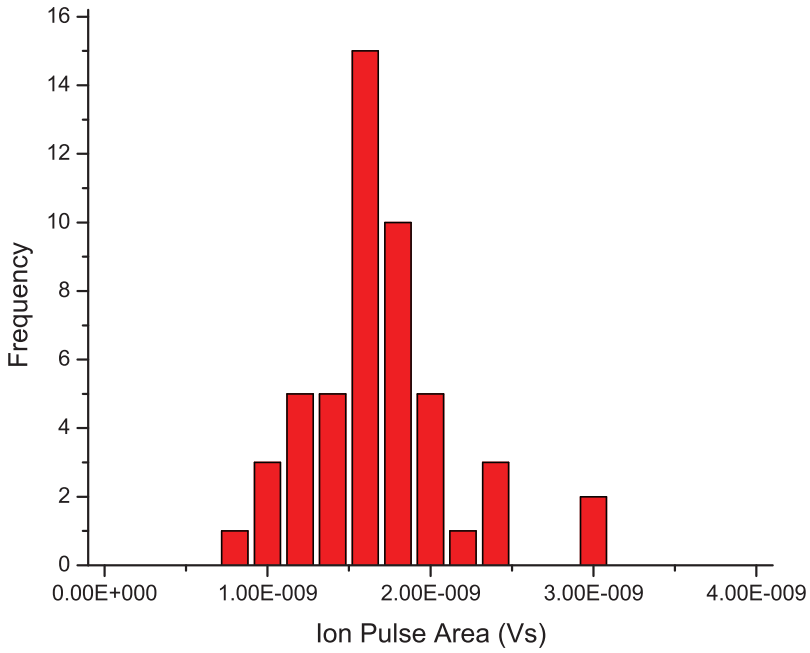

Figure 3.9. Ion Calibration

Calibrating the channeltron to find the pulse area (Vs) per ion. 50 single-ion events were recorded and placed in 2E-10 Vs bins. The average ion produces $1.57*10^{-9}$ Vs.

both the ion optics and the gain depend on the voltage. The output of the channeltron is sent through a 5x gain amplifier (Stanford Research Systems SR445 DC-300 MHz amplifier). To convert the amplified voltage to an ion count, we measured 50 single ion MOT molecule events and found the average pulse area per ion to be $1.57*10^{-9}$ Vs, as shown in figure 3.9.

3.2.3 Digital Boxcar

A LabVIEW digital boxcar (using the National Instruments NI PCI-5112 acquisition card) averages the signal from the CEM. The original program was written by C. E. Rogers III and has been extensively updated and modified by the author. Presently, one gate is centered on the atomic ions and another gate is centered on

the molecular ions ($\sqrt{2}$ later in time). A third gate to measure the background is located 40 μs after the end of the molecular gate. This background is automatically subtracted for each shot. Each gate is currently set to be 500 ns wide. Both the atomic and molecular gated-windows are integrated and then averaged over the desired number of shots. The integration includes the voltage-to-ion-count calibration (figure 3.9). The resulting averaged ion counts, as well as their standard deviations, are recorded and sent to the main computer for data acquisition, as discussed in section 3.4.

3.3 Probe Laser

We use an electro-optical phase modulator to frequency-chirp our probe laser; an overview of the set-up is shown in figure 3.10. The center frequency of the probe laser is set by a master external-cavity diode laser (ECDL) which is stabilized (see section 3.3.4) to the trap master ECDL. A pulse from this master laser is used to injection lock a slave free-running diode laser (FRDL). The output of the slave is coupled into a delay fiber and then into the phase modulator, which provides the time-dependent phase, or frequency chirp. The output of the fiber is then self-injection locked into the slave. Once the light has gone around the phase modulation loop enough times to build up a sufficient frequency change, the light is switched out of the loop and sent to the main table where it injection locks another slave FRDL. The output of this second slave laser follows the frequency chirp. The desired portion of the chirp is selected out and the overall intensity is adjusted using a 200 MHz AOM (Brimrose TEM-00-50-780). The generation of arbitrary chirps in this manner was initially investigated in [67].

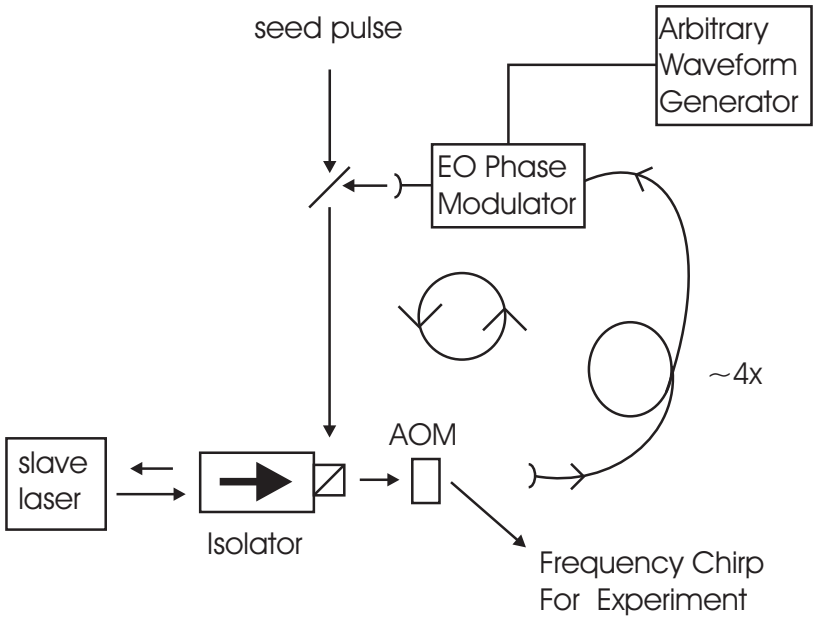

Figure 3.10. Probe Frequency Chirp Generation Overview

Frequency chirp generation overview: A pulse from a seed laser is used to injection lock a slave laser. The output of the slave laser is sent into a fiber containing an EO phase modulator. A voltage is applied from an arbitrary waveform generator to create a phase change. The resulting phase-modified pulse re-injection locks the slave laser. This self-injection locked loop is repeated several times to build up the appropriate frequency change which is then sent out of the fiber loop by switching the AOM.

3.3.1 Phase Modulator

The phase modulator (PM) is a fiber-coupled lithium niobate waveguide device (EOSpace PM-0K1-00-PFA-PFA-790-S S/N: 73732) capable of modulation rates up to 40 Gbit/s. For the data in this thesis, the PM is terminated with a 1 W internal terminator and is driven by a 240 MHz arbitrary waveform generator (AWG) (Tektronix AFG 3252). The electric field created from the AWG voltage changes the index of refraction of the lithium niobate crystal, thereby changing the speed at which light travels through it. The phase of the light leaving the crystal is directly proportional to the length of time it takes that light to pass through it. Therefore, the AWG voltage can control the phase of the light. The voltage V_π required for a π phase change is $\sim$1.8 V at 1 GHz for this modulator.

3.3.2 Phase Modulator Loop Set-up

The phase modulator (PM) loop set-up is shown in more detail in figure 3.11. An 80 MHz acoustic-optical modulator (AOM) selects out an 80 ns pulse from the master ECDL, "PM Master" (50 mW Hitachi HL7852G). This pulse is injected into the slave FRDL, "PM Slave" (80 mW Sanyo DL-7140-201W), selecting the center frequency of the chirp. The output of the "PM Slave" is directed into a 7 m polarization-maintaining optical fiber delay line containing the fiber-coupled electro-optic PM. The time-dependent phase is created by the amplified (Minicircuits ZHL-1-2W) voltage, V, from the 240 MHz AWG. The frequency of the phase modulated light, f(t) is related to the modulated phase, ϕ(t), by:

$$f(t) = f_0 + \frac{1}{2\pi}\frac{d\phi}{dt}, \tag{3.1}$$

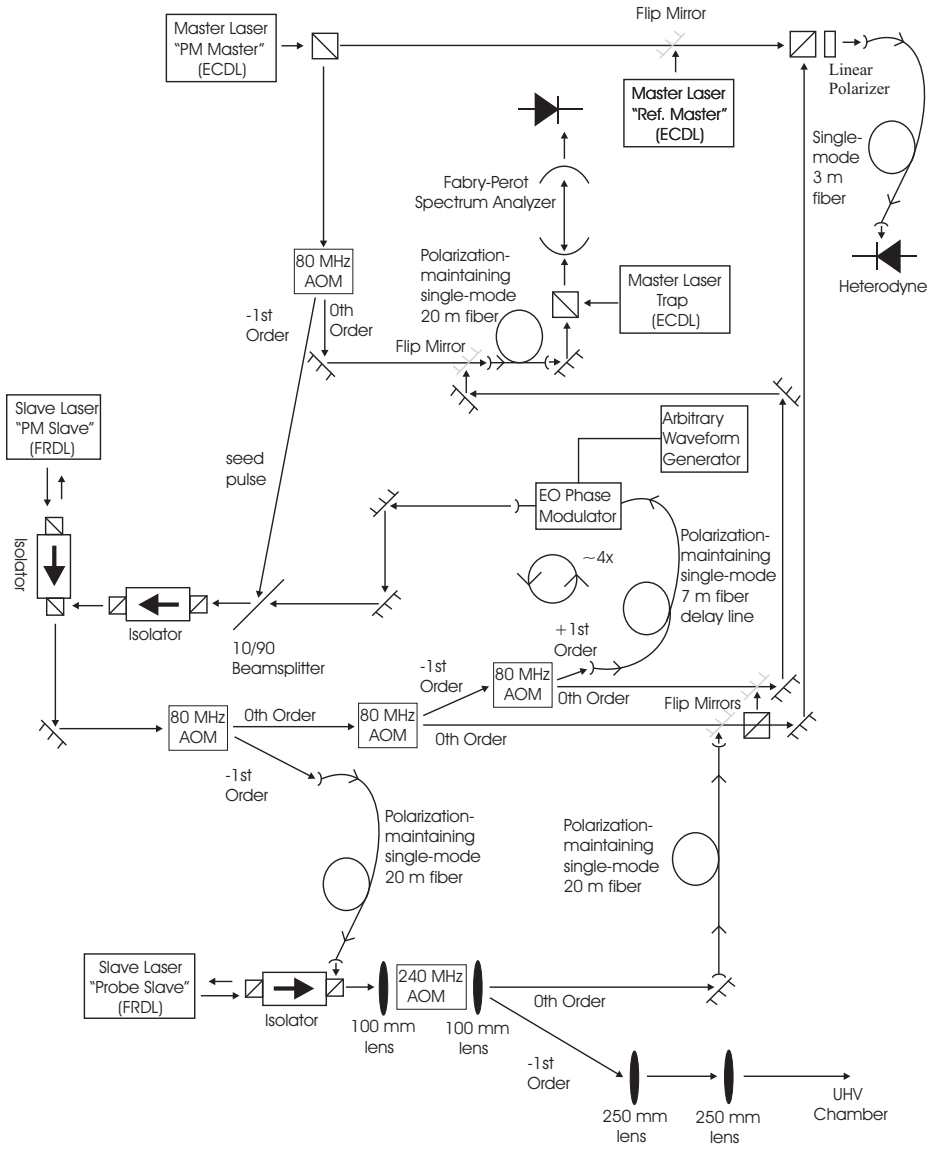

Figure 3.11. Probe Frequency Chirp Generation

Frequency chirp generation: A pulse from a seed laser ("PM Master") injection locks a slave laser ("PM Slave"). The output of "PM Slave" is coupled into a fiber loop containing an electro-optic phase modulator (PM). A voltage is applied from an arbitrary waveform generator to create a phase change. The resulting phase change is re-injected into "PM Slave". This self-injection lock loop is repeated several times to build up the appropriate frequency change which is then sent out of the fiber loop. The output of the loop with the frequency chirp is used to injection lock another slave laser ("Probe Slave"). The desired pulse and amplitude are selected with a 200 MHz AOM, and then the light goes to the UHV chamber.

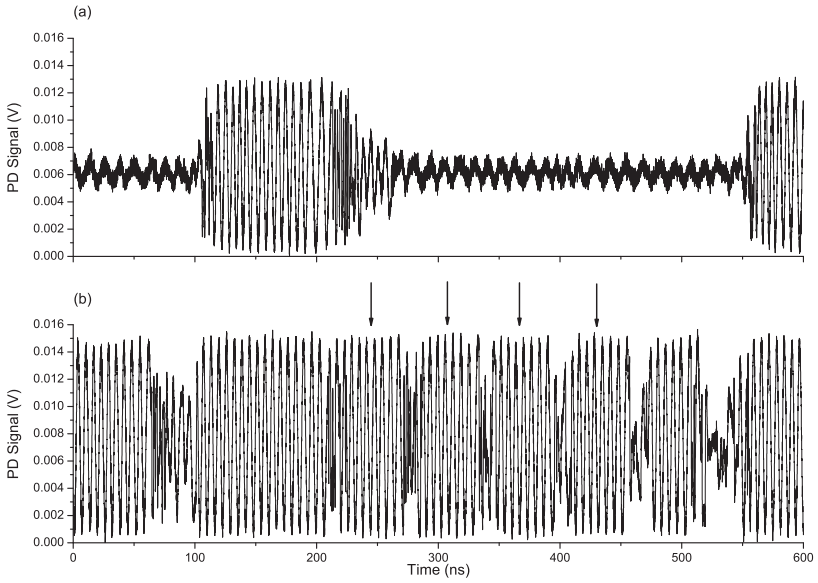

Figure 3.12. Probe Loop Timing

Phase Modulator (PM) Loop Set-up: Loop Timing. Shown is the heterodyne signal between the "PM Master" and "Probe Slave" lasers. The ∼80 ns "PM Master" pulses are shown in (a). The four "PM Slave" ∼60 ns self-injection pulses (arrows) and the ∼60 ns output pulse are shown in (b). The repetition time for the sequence is 450 ns. The 160 MHz heterodyne frequency is from the accumulation of AOM frequencies. Note: there is no phase modulation here and the "Probe Slave" is injection-locked for the whole sequence.

where f_0 is the original carrier (center) frequency set by the master ECDL, "PM Master". This frequency chirped pulse then re-injection locks the "PM Slave"*. This self-injection lock loop takes $\sim$ 60 ns for each pass and is repeated 4 times. It is

*Note on self-injection lock alignment: For injection lock alignments we typically tune the slave laser current close to threshold, inject ≤ 250 μW of seed light, and monitor the slave output power while optimizing the alignment for at least a factor of 10 gain with the injected seed light. For seed light coming from a polarization-maintaining single-mode fiber, it is often helpful to align the light rejected from the isolator backwards through this fiber as an initial alignment. For the current probe setup at least 11 μW needs to be aligned backwards through the PM and 7 m delay fiber. With the self-injection locking, monitoring the output power, would, of course, block the self-injection light. Therefore, to optimize the self-injection lock, the author has found it useful to extend the repetition time to several μs (typically 4.45 μs) and adjust the alignment of the self-injection light and the electronics to optimize the number of loops followed in the heterodyne (typically ~ 2 μs worth or $>$ 20 loops). The electronics is then configured back to the desired repetition time (typically 450 ns for the current setup).

critical that the repeat time of the voltage waveform is synchronized with the loop time. The phase change, $\Delta\phi$, produced by N passes through the PM is then given by:

$$\Delta\phi = N\pi\frac{V}{V_\pi}. \tag{3.2}$$

The AOMs to produce the pulses are controlled by two AWGs (20 MHz Agilent 33220A and 80 MHz Agilent 33250A). These loops can be seen in a heterodyne (see section 3.3.3) between the "PM Master" laser and the "PM Slave" laser or the "Probe Slave" laser (discussed later in this section), as shown in figure 3.12 (no phase modulation applied). The ∼80 ns seed pulses from the "PM Master" with a repetition time of 450 ns are shown in figure 3.12(a) and the four subsequent ∼60 ns "PM Slave" self-injection loops are shown in figure 3.12(b). Also shown in figure 3.12(b) is a fifth ∼60 ns loop which is the typical output of the loop set-up. This final pulse injection locks a second slave FRDL, "Probe Slave". The "Probe Slave" is a 150 mW diode (Axcel Photonics M9-785-0150-S5P), in order to provide sufficient intensity for our experiments. Although the "Probe Slave" is injection-locked for the entire sequence in figure 3.12, one could pulse the AOM to just select out the last output pulse and injection-lock only this final pulse. Having the "Probe Slave" only injection-locked for the final pulse reduces the background since it is then far off-resonance for >85% of the time. The output of the "Probe Slave" is directed to a 200 MHz AOM, where the desired pulse and intensity level are selected. The second channel of the 240 MHz AWG (Tektronix AFG 3252) is used to control the 200 MHz AOM. The Gaussian intensity pulse is centered on the chirp which is centered in the ∼60 ns window. The -1st order from the AOM goes through a 250 mm lens pair used to focus the probe beam down to approximately the size of the UHV MOT cloud.

3.3.3 Chirp Characterization

In order to characterize the chirp, we look at both the optical spectrum and an optical heterodyne signal, as shown in the layout in figure 3.11. The spectrum analyzer (SA) (Coherent 33-6131-000) has a 1.5 GHz free spectral range which aids in verifying the chirp range and detuning relative to the frequency-locked cw trap laser (see section 3.3.4). For the optical heterodyne signal, we beat the frequency-chirped probe laser light with either the PM Master or a cw reference laser, "Ref. Master". The center frequency of the "Ref. Master" laser is chosen to optimize the resolution of the heterodyne, typically $\sim$ 1 GHz away from the center frequency of the "PM Master". This prevents the heterodyne frequency from passing through zero. The two lasers are combined on a polarizing beam cube followed by a linear polarizer oriented at 45 degrees to the axes of the beam cube and coupled into a single-mode optical fiber whose output goes into a fiber-coupled 2 GHz photodiode (Thorlabs SV2-FC). The polarizer effectively matches the polarizations of the two lasers, but means that we are only able to couple about half of the intensity of each beam into the fiber. However, we are able to get sufficient intensity through the fiber to measure the heterodyne signal on an 8 GHz, 40 GSa/s oscilloscope (Agilent DSO80804A). Shown in figure 3.13(b) is the heterodyne signal resulting from application of the AWG output shown in figure 3.13(a) to the PM. The instantaneous frequencies are extracted from the heterodyne signal by taking the inverse of the local period between adjacent maximums and minimums. The resulting frequency versus time plot is shown in figure 3.13(c). Note that the frequency shift in (c) should be proportional to the derivative of the voltage in (a). Here, the quadratic voltage vs. time yields a linear chirp. Since the reference laser was detuned by $\sim$ 2 GHz, the amplitude of the heterodyne signal for the highest frequencies of the chirp is reduced. In this example, the desired positive chirp is approximately 1.2 GHz in 46 ns. Typical AWG outputs

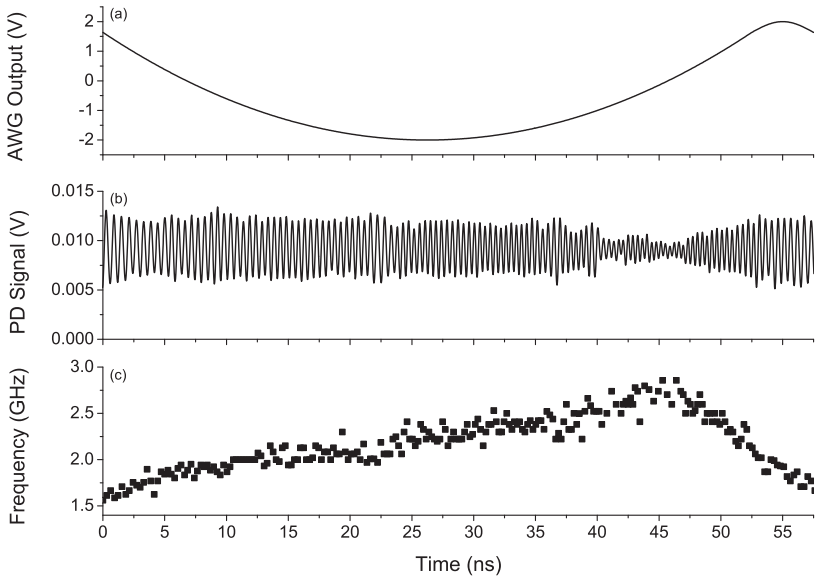

Figure 3.13. Frequency Chirp Characterization

(a) AWG Output. (b) Heterodyne signal from the frequency chirp heterodyned with a cw reference laser detuned by $\Delta/2\pi = 2.147$ GHz. (b) Derived instantaneous frequency versus time. The slight time shift between (a) and (b+c) is due to an accumulated electronic delay.

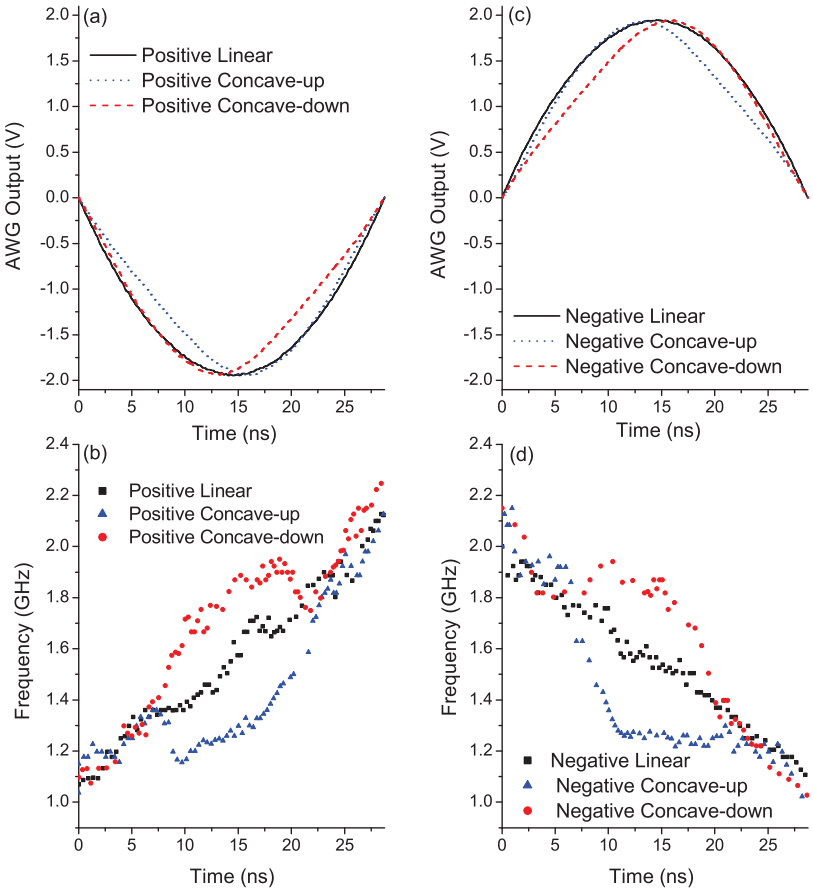

Figure 3.14. Example AWG Outputs and Frequency Chirps

AWG outputs (a+c) and derived instantaneous frequencies (b+d) from positive (a+b) and negative (c+d) chirps. Linear, concave-down and concave-up example chirps are shown.

and their corresponding frequencies for several faster linear and concave shapes are shown in figure 3.14. The concave shapes are programmed by adding a Gaussian to a linear chirp. These chirps are approximately 1 GHz in 28.75 ns.

3.3.4 Probe Stabilization Program

The probe laser stabilization program helps counteract drifts in the probe laser frequency through feedback to its PZT. Pick-offs of both the "PM Master" laser (or

the "Probe Slave") and the trap lasers are sent into the spectrum analyzer (SA). The stabilization program uses two peaks from the reference (trap) laser, separated by the 1.5 GHz free spectral range, and a peak from the target laser to find the detuning of the probe laser relative to the trap laser. The program then determines the error from the target detuning and feeds back to the "PM Master" PZT driver to adjust the probe detuning. The gain and timescale for this feedback has to be slightly adjusted for each diode. Unfortunately, since the SA is not temperature stabilized, the entire peak pattern drifts slowly and manual re-centering (using the offset on the SA controller) is required every few hours. This method of stabilization of the probe laser has a stability of < 3 MHz over several hours. This could be further improved by temperature stabilizing the SA, using orthogonally polarized beams, and after the cavity, directing the beams to two separate photodiodes (such as the stabilization setup described in [68]).

3.4 Data Acquisition

There are currently four computers involved in data acquisition for the data presented in this thesis: one for MOT images; one to control the ND6000 REMPI laser (section 3.2.1); one to run the boxcar program (section 3.2.3); and a main computer. Various LabVIEW programs have been developed by the author to automate data acquisition and some analysis. The MOT image computer is currently set up for manual image acquisition and transfer to the main computer where a LabVIEW program determines the $1/e^2$ radii, atom number, and density. The ND6000 computer is connected to the main computer through a serial cable. The boxcar computer is connected to the main computer via Ethernet. The main computer also has a data acquisition card (National Instruments NI PCI-MIO-16E-4) with various analog inputs (including UHV MOT florescence from the APD; Gentec energy meter output;

SA photodiode and trigger signals) and outputs (including probe stabilization PZT feedback voltage, section 3.3.4). The heterodyne signal from the 8 GHz oscilloscope (section 3.3.3) as well as other traces can be transferred or monitored in real time via Ethernet to the main computer. The output of the wavemeter (Coherent WaveMaster Wavelength Meter) is also an input into the main computer (via a serial to USB connection). The output of the Thorlabs energy or power meter can also be input into the main computer via a USB connection. The 240 MHz AWG essential for the probe set-up (section 3.3) is also connected to the main computer via Ethernet. The three main types of data acquisition discussed in this section are REMPI scans, probe scans, and determining molecular formation rates.

3.4.1 REMPI Scans

REMPI scans are important for tuning the detection laser (section 3.2.1) to the desired frequency. REMPI spectra are obtained by scanning the pulsed laser while the PA laser is either off or fixed on a known resonance. During REMPI scans, the LabVIEW program steps the ND6000, waits for the stepper motor to finish moving, waits for the boxcar (section 3.2.3) to acquire the desired number of shots, records various signals, and then repeats this until the end of the scan. Typical REMPI scans cover 1.5 nm (41.4 cm^{-1}) with 0.001 nm (0.03 cm^{-1}) steps and are averaged over 10 shots. REMPI scans are typically performed either with the probe frequency stabilized (section 3.3.4) or with the MOT only. During the scan, the average number of atomic ions and its standard deviation, the average number of molecular ions and its standard deviation, the REMPI wavelength (both the wavelength programmed into the ND6000 and actual wavelength as read by the wavemeter), the UHV MOT APD signal, and the probe detuning (if applicable) are recorded. An example of a REMPI scan is shown in figure 3.15. For this REMPI scan, the probe laser was off

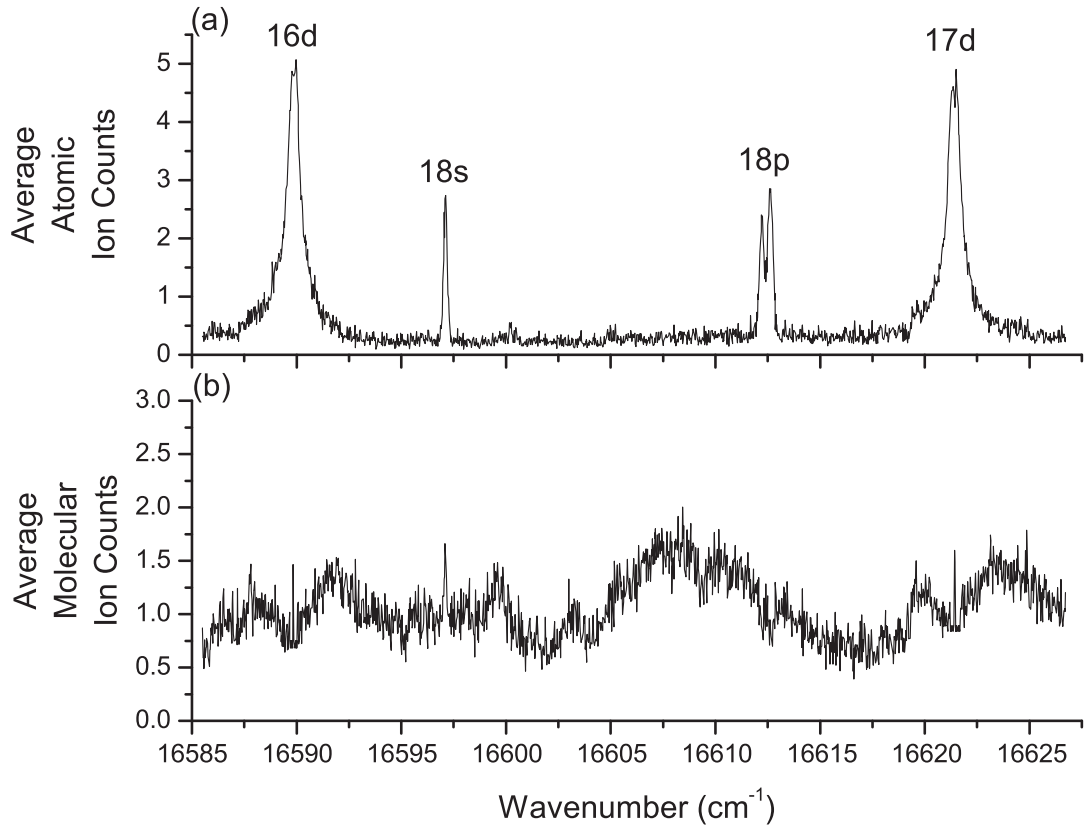

Figure 3.15. REMPI Scan

REMPI Scan of spontaneously formed MOT molecules. The 10-shot-averaged atomic (a) and molecular (b) signals are shown. The REMPI laser was stepped by 0.001 nm.

(the scan is of MOT-produced molecules only), the ND6000 was stepped by 0.001 nm and the ion signals were averaged over 10 shots. The atomic lines are assigned by a simple calculation based on [69]. Due to a combination of atomic signal strength as well as detector and electronics bandwidth, there is some small leakage of the atomic signal in the molecular gate on the boxcar. Note that as discussed in section 3.2.1, our REMPI linewidth is broad enough that we are not able to distinguish between $a\ ^3\Sigma_u^+$ (v"=37-39). For probe scans (section 3.4.2) and for determining molecular formation rates (section 3.4.3), we fix the REMPI laser at a particular wavelength between the atomic lines, typically $\sim$ 16608 cm^{-1}, where this leakage is negligible.

3.4.2 Probe Scans

Finding the optimal probe detuning is important for optimizing the molecular signal. PA spectra are obtained by scanning the probe laser while keeping the pulsed REMPI laser fixed on a known resonance. Before we take the PA spectra, we must align the probe laser to the MOT. First, we tune the PA laser near the $5S_{1/2}$ (F=2) $\rightarrow$ $5P_{3/2}$ (F'=3) asymptote and optimize the probe alignment, making the MOT disappear by resonant "pushing". Then, watching the 1.5 GHz FSR SA signal, we carefully tune the probe detuning to the red. For the data in this thesis, we typically tune to 7.79 GHz below the $5S_{1/2}$ (F=2) $\rightarrow$ $5P_{3/2}$ (F'=3) asymptote. For much larger detunings, we would still align the probe near resonance, but then one would use the wavemeter instead of the SA to measure the detuning. Once the probe laser is close to the desired detuning, we scan it. With the REMPI laser wavelength fixed, the LabVIEW program slowly steps the PA detuning, waits for the boxcar to average the desired number of shots, and then repeats. During the scan, the average number of atomic ions and its standard deviation, the average number of molecular ions and its standard deviation, the REMPI wavelength, the UHV MOT APD signal, and the

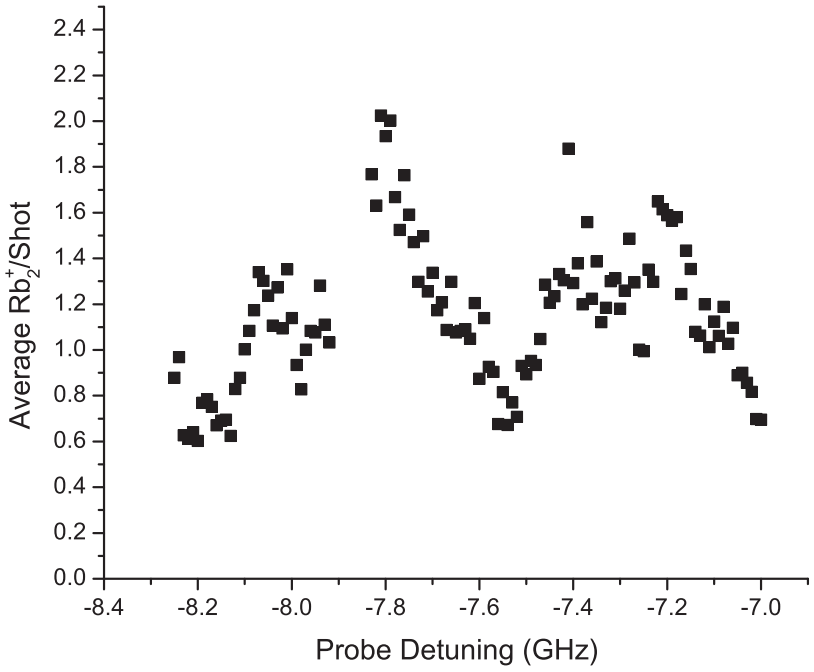

Figure 3.16. Probe Scan

Probe Scan. With the REMPI laser fixed, the probe laser is slowly stepped to various detunings below the $5S_{1/2}$ (F=2) $\rightarrow$ $5P_{3/2}$ (F'=3) asymptote. The main PA resonance used in this thesis is the peak at -7.79 GHz.

probe detuning are recorded. Using the probe stabilization program, we can scan hundreds of MHz or even a few GHz if one is careful about changing parameters near the overlaps between the probe and the trap laser peaks in the SA. Again, with another method of stabilization (see section 3.3.4), the probe laser could be scanned even farther. A typical probe scan is shown in figure 3.16. For this scan, the probe laser was stepped by 10 MHz, the ion signals were averaged over 1000 shots, the REMPI laser was tuned to 16607.96 cm^{-1}, and the $\sim$ 30 W/cm^2 probe was on for a 20 ns FWHM Gaussian pulse every 450 ns for the 10 ms before the detection pulse. The photoassociation of atoms into molecules can also be detected by monitoring the fluorescence of the MOT with the APD signal. This detection method, "trap loss",

works well for strong PA transitions, which are usually at small PA laser detunings. Dips in the fluorescence signal originate from loss of atoms from the MOT, indicating that the photoassociation laser is on resonance with an electronic excited state.

3.4.3 Molecular Formation Rates

In order to determine the molecular formation rate, we must account for the losses during the 10 ms window when the probe beam is on. Therefore, we measure the average ion counts vs. peak intensity with the probe on for 1 to 10 ms, as well as the rate at which the molecules escape the detection volume. Once we have made these various measurements, we can determine the molecular formation rate.

First we perform REMPI scans (section 3.4.1) to find the optimal REMPI wavelength, typically $\sim$ 602 nm for the data in this thesis. Then we perform probe scans (section 3.4.2) to find the optimal probe detuning, typically $\Delta/(2\pi)$ = -7.79 GHz below the $5S_{1/2}$ (F=2) $\rightarrow$ $5P_{3/2}$ (F'=3) asymptote for the data in this thesis.

3.4.3.1 Timing

The overall timing of the experiment is controlled by a SRS DG535 Pulse Generator. The DG535 triggers the Nd:YAG to fire at 10 Hz and triggers two BNC 555 Pulse Generators. The BNC pulse generators control the probe on time and the MOT off time. A diagram of the timing is shown in figure 3.17. The REMPI detection laser fires at 10 Hz. All of the MOT beams (UHV trap and repump, LVIS beam) are turned off for 50 μs centered on the REMPI pulse in order to minimize atomic photoionization. The probe pulses are on for up to 10 ms before the REMPI pulse. During this window, the probe pulses repeat every 450 ns (as shown in the insert of figure 3.17), meaning we could have up 22,222 chirped pulses per detection shot. The main computer controls the AWG (the chirp shape/timing as well as the

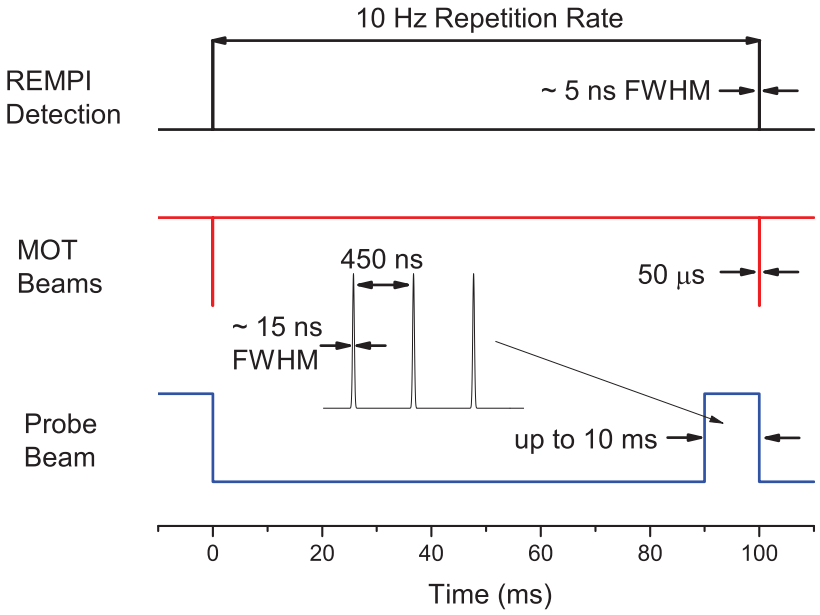

Figure 3.17. Experimental Timing

Experiment Timing. The REMPI detection laser fires at 10 Hz. The MOT beams are turned off for 50 μs centered on the REMPI pulse. The probe pulses are on for up to 10 ms before the REMPI pulse.

peak intensity and Gaussian FWHM) and automatically records the boxcar signals and other relevant information for the various chirp shapes and peak intensities.

3.4.3.2 Determining Formation Rates

The number of detectable molecules, N, is described by a competition between production and loss:

$$\dot{N}(t) = R - (\Gamma_{esc} + \Gamma_{PD})N, \tag{3.3}$$

where R is the formation rate, Γ_{PD} is the photodestruction rate, and Γ_{esc} is the escape rate [45, 62]. The solution is:

$$N(t) = N(\infty)(1 - e^{-(\Gamma_{esc}+\Gamma_{PD})t}), \tag{3.4}$$

where the quantity

$$N(\infty) = \frac{R}{\Gamma_{esc} + \Gamma_{PD}} \tag{3.5}$$

is the steady-state number of detected molecules.

First, we must determine the escape rate, Γ_{esc}, the rate at which formed molecules leave the detection region. This is done using MOT-formed molecules. We turn off the probe beam for this entire sequence. The MOT beams are turned off for at least 7 ms and we vary the amount of off time before the detection pulse. We measure the $^{87}Rb_2^+$ signal for each delay time. The resulting normalized decay curve for the number of molecules, N(t) is fit to a simple exponential:

$$N(t) = e^{-\Gamma_{esc}(t)}. \tag{3.6}$$

Typically, Γ_{esc} is ~ 0.1 ms^{-1}, as shown in figure 3.18. If we assume that the molecular

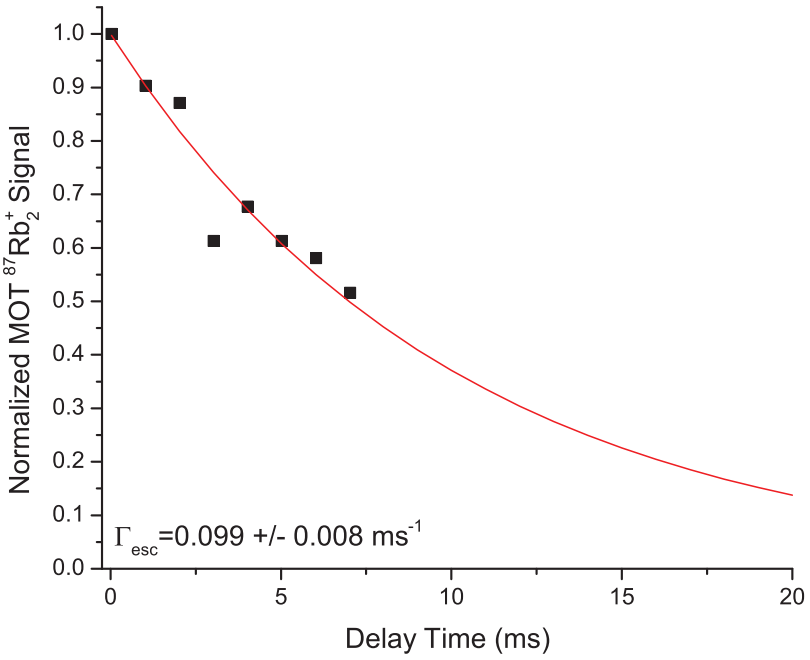

Figure 3.18. Escape Rate

We turn the MOT off for 7 ms and measure the $^{87}Rb_2^+$ signal for various amounts of off time before the detection pulse. A fit to the normalized data, using eq. 3.6, yields the escape rate $\Gamma_{esc} = 0.099 \pm 0.008$ ms^{-1}

temperature is equal to the atomic temperature of $\sim 150\ \mu$K, we calculate the typical time it takes for a molecule to go from the center of the detection area (center of the MOT) to the edge of the 3 mm diameter detection area to be approximately 10 ms. Although we are characterizing the curve by a single rate when the actual time dependence due to the thermal velocity distribution and gravity are undoubtedly quite complicated, this decay rate is consistent with the 10 ms time.

For a given chirp shape and peak intensity (determined by the 200 MHz AOM), we vary the probe on time from 1 to 10 ms. We subtract out the background MOT-formed Rb_2^+ signal which is measured separately. For each peak intensity, we plot the signal as a function of the probe on time. We then fit these curves to equation 3.4, extracting the steady-state number of detected molecules, equation 3.5, and the total loss rate, Γ:

$$\Gamma = \Gamma_{esc} + \Gamma_{PD}. \tag{3.7}$$

Since we already found Γ_{esc}, using equation 3.7, we can then determine the photodestruction rate, Γ_{PD}. Finally putting all of these factors together, using equation 3.4, we can finally determine the molecular formation rate, R, for each chirp shape. This is the primary quantity of interest since it indicates the yield and can be directly compared to the results of the simulations.

Chapter 4
Quantum Mechanical Simulations

4.1 Introduction

We perform quantum mechanical simulations in collaboration with Shimshon Kallush from ORT-Braude in Israel and Ronnie Kosloff from the Hebrew University, also in Israel. These simulations are written in Fortran 90 and are computationally expensive. Briefly, we use the Chebyshev polynomial expansion with a mapped Fourier grid to solve the time-dependent Schrödinger equation with the Hamiltonian in the dressed-state. As the chirp evolves in time, we are able to follow the wavepacket evolution. With some modifications we are able to use these simulations to model ^{85}Rb trap-loss collisions (section 4.2, reference [44]) as well as $^{87}Rb_2$ molecular formation rates (sections 4.3, 4.4, and 4.5; references [45, 46]).

4.1.1 Hardware

The current hardware for the simulations, constructed and maintained in our lab, consists of a main machine with a secondary server attached via a gigabit Ethernet connection. The main machine is an HP Z820 (with custom modifications) with two E5-2620 2.0 GHz Hex-core Intel Xeon processors with 16 GB of RAM. These E5-2620 have two logistical cores per physical core, allowing for 12 threads per processor. The secondary server gives an additional 32 cores from a Dell PowerEdge C6100 XS23 4 in 1 Cloud Server (also with custom modifications) with a total of 8 L5420 2.5 GHz Quad-core Intel Xeon Processors with 64 GB RAM total (16 GB RAM per

motherboard). Even with the combined package of 44 cores (56 threads), it takes weeks to get results from the simulations. Currently the code is set up to run one point per thread. The author utilizes Perl scripts to efficiently and automatically execute the multitude of runs.

4.1.2 Solving the Time-Dependent Schrödinger Equation

The time-dependent Schrödinger equation is solved with the Chebyshev polynomial expansion method [70] and with a mapped Fourier grid [71–73]. Equally spaced Fourier grids faithfully represent wavefunctions where the projection is in a rectangular phase space. Mapping the Fourier grid allows us to address the wide range of length scales in the system and reduce the necessary computation time. The mapped Fourier grid is an uneven grid with a higher population of points around the well of the potential with a decreasing density of points further out. Here the R-dependent basis set of plane waves is scaled by the inverse of the local de Broglie wavelength [73]. The minimal spacing is estimated from the kinetic energy, resulting in the lower density of points with increasing R.

The Hamiltonian, $\hat{H}$, is given by:

$$\hat{H} = \hat{T} + \hat{V}, \tag{4.1}$$

where $\hat{T}$ is the kinetic energy operator and $\hat{V}$ is the potential energy operator. For the collisional simulations, we use a two-channel Hamiltonian, whereas for the molecular formation simulations we use a three-channel Hamiltonian. The dressed-state Hamiltonians are shown in table 4.1. The internuclear potentials in $\hat{V}$ correspond to the electronic states included in the simulations (collision simulation states are given in table 4.2, molecular formation rate simulation states are given table 4.3). For the

Collision Simulations
$\hat{H} = \begin{pmatrix} \hat{T} + \hat{V}_g(R) & \hbar\Omega(t) \\ \hbar\Omega^*(t) & \hat{T} + \hat{V}_e(R) + \hbar\Delta \end{pmatrix}$
Molecular Formation Simulations
$\hat{H} = \begin{pmatrix} \hat{T} + \hat{V}_{gJ} & \hbar\Omega_{e_0}(t) & \hbar\Omega_{e_1}(t) \\ \hbar\Omega^*_{e_0}(t) & \hat{T} + \hat{V}_{e_0} + \hbar\Delta & 0 \\ \hbar\Omega^*_{e_1}(t) & 0 & \hat{T} + \hat{V}_{e_1} + \hbar\Delta \end{pmatrix}$

Table 4.1. Simulation Hamiltonians

Dressed-state Hamiltonians used in the simulations. $\hat{T}$ is the kinetic energy operator, Δ is the central detuning of the chirped light from the asymptote, $\hbar\Omega$ are the time-dependent couplings between the states, and $\hat{V}_{g/e}$ or $\hat{V}_{g/e_0,e_1}$ are the ground/excited-state potentials. For the molecular formation simulations, for partial waves beyond s we add a rotational barrier V_J=J(J+1)/2μR^2, as described in section 4.1.5.

State	**State Included**
Singlet Ground State	$X\ ^1\Sigma_g^+$
Triplet Ground State	$a\ ^3\Sigma_u^+$
Excited State	0_u^+

Table 4.2. States Included in Collision Simulations

State	**State Included**
Ground State	$a\ ^3\Sigma_u^+$
Ground Continuum	$a\ ^3\Sigma_u^+$ continuum
Excited State (e_0)	0_g^-
Excited State (e_1)	1_g

Table 4.3. States Included in Molecular Formation Simulations

State	State Included	Included Bandwidth	Included Vibrational Levels
Ground State	$a\ ^3\Sigma_u^+$	278 GHz	v" = 30 to 40
Ground Continuum	$a\ ^3\Sigma_u^+$ continuum	16 MHz	E/k_B = 0.77 mK
Excited State (e_0)	0_g^-	15 GHz	v' = 67 to 87
Excited State (e_1)	1_g	15 GHz	v' = 217 to 239

Table 4.4. Vibrational Levels Included in Molecular Formation Simulations

molecular formation simulations, we cover a very narrow bandwidth. Therefore, we move to a vibrational representation. In this new basis, the Hamiltonian is

$$\hat{H} = \hat{H}_0 + \hat{H}_\epsilon = \begin{pmatrix} \hat{H}_g & 0 & 0 \\ 0 & \hat{H}_{e_0} & 0 \\ 0 & 0 & \hat{H}_{e_1} \end{pmatrix} + \begin{pmatrix} 0 & \hbar\hat{\Omega}_0(t) & \hbar\hat{\Omega}_1(t) \\ \hbar\hat{\Omega}_0^*(t) & 0 & 0 \\ \hbar\hat{\Omega}_1^*(t) & 0 & 0 \end{pmatrix}, \tag{4.2}$$

where $\hat{H}_j$ is the field-free Hamiltonian for the electronic state j = g, 0 or 1 for the $a\ ^3\Sigma_u^+$, 0_g^-, and 1_g electronic states, respectively, and in the interaction Hamiltonian $\hat{H}_\epsilon$, the coupling between the states is given by the Rabi frequency $\hat{\Omega}_j$. The vibrational levels covered in this new basis are shown in table 4.4. For all of the simulations presented in this thesis, the time-dependent couplings due to the chirped pulse are given by:

$$\hbar\Omega_j = \mu_{gj}\epsilon_0 e^{[-\frac{(t-t_{center})^2}{2\sigma^2} + i\widetilde{\omega}(t)(t-t_{center})]}, \tag{4.3}$$

where μ_{gj} are the R-independent transition dipole moments, ϵ_0 is the peak electric field, σ corresponds to the intensity pulse FWHM, t_{center} is the center of the pulse, and $\widetilde{\omega}(t)$ are instantaneous frequency offsets from Δ. To incorporate the chirp into the simulations, first the experimental chirps are characterized by a heterodyne signal as described in section 3.3.3. These instantaneous frequencies are then interpolated

using a piecewise cubic Hermite interpolating polynomial (PCHIP) to yield a frequency value every 0.1 ns. The resulting values are smoothed using a 5 ns FWHM Gaussian function, ensuring that the slope is always < 0 for negative chirps or > 0 for positive chirps. The resulting smoothed interpolated instantaneous frequencies are then interpolated again using a PCHIP time step corresponding to the temporal propagation step of the simulations. The time step is adjusted for convergence and is ~ 0.45 ps for the collisional simulations, whereas for the molecular formation simulations we use a shorter time step of $\sim$0.075 ps. The resulting instantaneous frequencies are then input into the simulations.

We start with all of the population in a continuum state corresponding to the temperature of the atoms in the MOT. For each time step, we calculate the intensity profile, find the field from the combined intensity and instantaneous chirp frequency, and then propagate the wavefunction through Chebyshev recursion [74]. We monitor the field and the various state populations.

4.1.3 Potential Energy Curves and Scattering Lengths

The potential energy curves (PEC) used for the collisional simulations are shown in figure 4.1 and the PECs used for the molecular formation simulations are shown in figure 4.2. For the collisional simulations, we include both the singlet $X\ ^1\Sigma_g^+$ and the triplet $a\ ^3\Sigma_u^+$ ground states and the 0_u^+ excited state. The singlet and triplet simulations are performed separately and then a weighted average is taken. A summary of these states is given in table 4.2. For the molecular formation simulations, the triplet $a\ ^3\Sigma_u^+$ ground state as well as two excited states (0_g^- and 1_g) are included. A summary of these states is given in table 4.3. For all of the simulations presented in this thesis, the inner walls of the ground-state potentials were ever so slightly, carefully, and smoothly adjusted to obtain the proper scattering lengths [75, 76]. The scattering

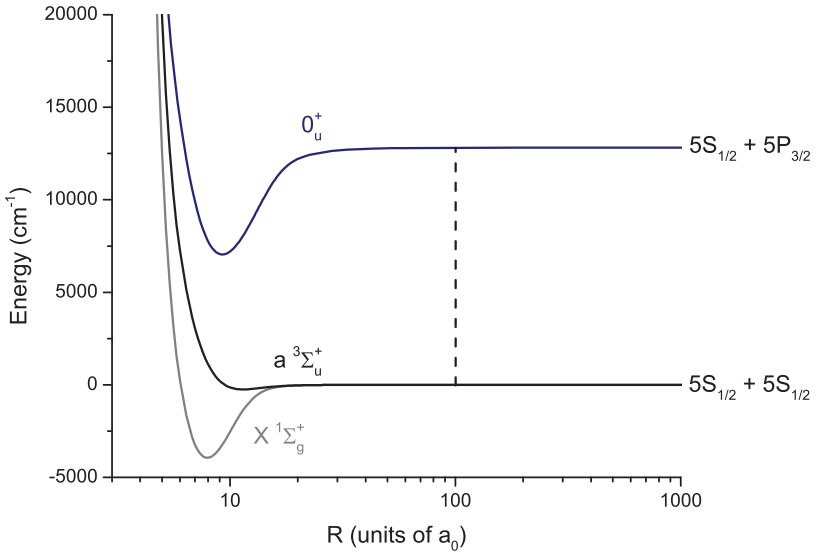

Figure 4.1. Collision Simulations Potential Energy Curves

Relevant energy levels included in the collisions simulations. To model the trap-loss mechanism, we place an absorbing boundary on the excited-state potential at $R = 100\ a_0$ to absorb incoming collisional flux. Note that the horizontal axis is logarithmic.

Ground State	^{85}**Rb**	^{87}**Rb**
Singlet $X\ ^1\Sigma_g^+$	2400	90
Triplet $a\ ^3\Sigma_u^+$	-369	106

Table 4.5. Scattering Lengths

Scattering lengths in units of a_0 taken from reference [75].

lengths, taken from reference [75], are shown in table 4.5. For the simulations the initial s-wave scattering state is computed by diagonalization of the time-independent Hamiltonian of the ground-state potential in the mapped Fourier grid basis. These initial scattering states are shown in figure 4.3. The potentials go out to $\sim$ 20,000 a_0, to ensure the correct representation of the scattering and bound states.

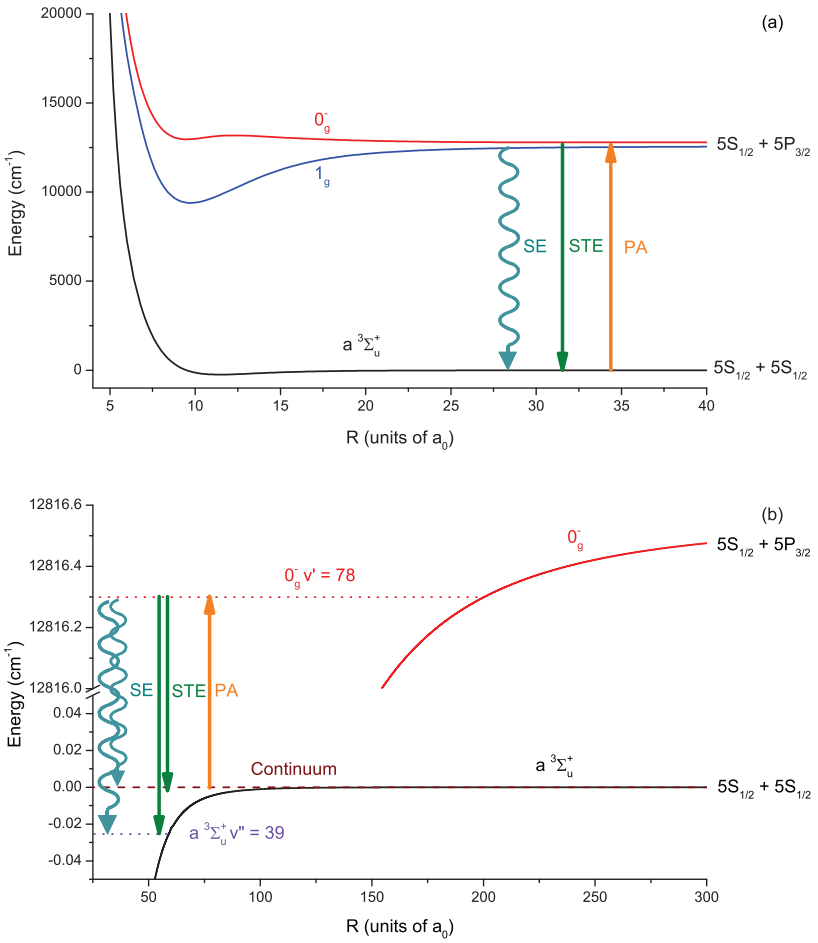

Figure 4.2. Molecular Formation Simulations Potential Energy Curves

Energy levels considered for the simulations of molecular formation rates. (a) Relevant energy levels included in the simulations. We use chirped light to photoassociate (PA) to various vibrational levels in the excited states. The formed molecules either decay through spontaneous emission (SE) to the continuum and various vibrational levels in the triplet ground state or the chirped light stimulates emission (STE) down to the triplet ground state. (b) An expanded view of the most important levels: the initial free-atom ground-state continuum, the $a\ ^3\Sigma_u^+$ v"=39 target state, and 0_g^- v'=78 intermediate excited state. Note the difference in energy scales for the ground and excited states.

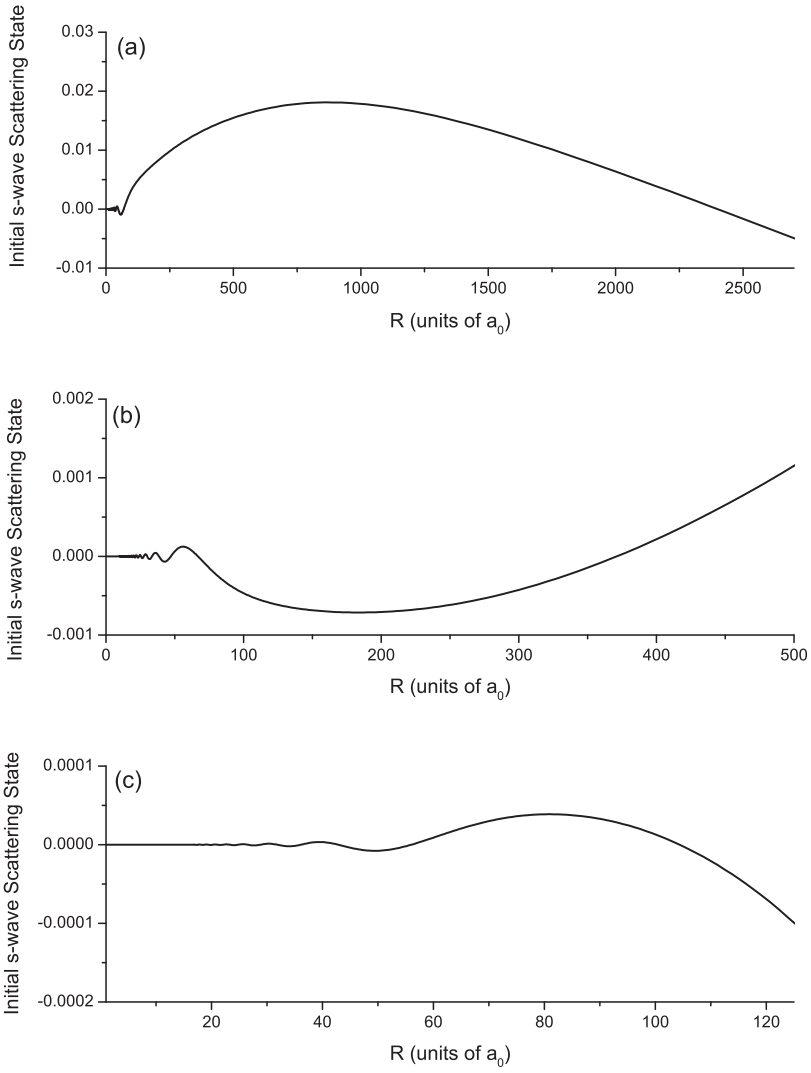

Figure 4.3. Initial S-wave Scattering

Initial s-wave scattering states for (a) ^{85}Rb Singlet, (b) ^{85}Rb Triplet, and (c) ^{87}Rb Triplet. The ^{87}Rb Singlet looks very similar to (c).

Excited State	Lifetime (ns)
0_u^+	22
0_g^-	26.2
1_g	22.8

Table 4.6. Excited-State Lifetimes

4.1.4 Spontaneous Emission

For the time scales presented in this thesis, spontaneous emission cannot be ignored. This decay process is modeled by coupling the excited state(s) to a sink channel. For the damping rates, we use $\Gamma = 1/(\text{the excited-state lifetime})$. These lifetimes [77, 78] are shown in table 4.6. This is a unidirectional decay, whose products are not allowed to further interact with the laser field, thereby precluding multiple incoherent interactions. For the molecular simulations we expand the spontaneous emission to include multiple sink channels, weighted by their Franck-Condon factors. These sink channels correspond to a decay from each of the excited-state (0_g^- and 1_g) vibrational levels into various vibrational levels or the continuum of $a\ ^3\Sigma_u^+$.

For the collisional simulations we have an additional loss mechanism to represent trap loss. Since atom pairs reaching short range in the excited state will likely gain enough kinetic energy to be ejected from the trap, we model this loss mechanism by placing an absorbing boundary on the excited-state potential at $R = 100\ a_0$ to absorb incoming collisional flux. Any population that reaches this boundary is considered to result in the loss of the two colliding atoms from the trap. It is important to note that this boundary is distinct from an absorbing wall of the calculational box and that the collision simulations (section 4.2, based on reference [44]) show that the calculated losses are insensitive to the exact location of this somewhat arbitrary boundary.

4.1.5 Thermal and Intensity Averaging

In order to compare to experiments, we need to do a thermal average. In order to avoid repeating the calculation for each of the levels within the ensemble and then performing an incoherent sum, we can use the analytic expressions of reference [79] and use only a single energy state. Using the collisional simulations, we explicitly thermally averaged eleven scattering states (0.13 μK to 102.9 μK) and found that the result was within $\sim$1% of the thermally-averaged result based on one state. Since our Hamiltonian is on a finite grid and the gas is dilute, we can divide the trap volume V into many small boxes of volume ν_{box}, where the number of these boxes is much larger than the total number of atoms in the trap, N. Then following reference [79], the number of excited-state molecules, N_{mol}, at a temperature T is given by

$$N_{mol} = \frac{1}{2} N^2 \frac{\nu_{box}}{V} \langle \hat{P}_e \rangle_{T,box}. \tag{4.4}$$

The thermally-averaged probability to make such a molecule, $\langle \hat{P}_e \rangle_{T,box}$, is given by:

$$\langle \hat{P}_e \rangle_{T,box} = \frac{2\pi^2 \hbar^3}{\mu^{3/2} \nu_{box}} \frac{P_{E_0}}{\Delta E_0 \sqrt{kT}}, \tag{4.5}$$

where E_0 is the single energy eigenstate, ΔE_0 is the energy width of this level (the inverse of the density of states in the box), μ is the reduced mass, and P_{E_0} is the excitation (leading to trap loss) probability. Combining equations 4.4 and 4.5, we find

$$N_{mol} = \frac{\pi^2 \hbar^3 N^2}{\mu^{3/2} V} \frac{P_{E_0}}{\Delta E_0 \sqrt{kT}}. \tag{4.6}$$

For the collisional simulations, we are interested in the collisional trap-loss rate, β. The time-averaged loss rate per atom is β x N/V, where N is twice the number of

molecules, N_{mol}:

$$\beta = NP_{cycle}\frac{V}{N^2}, \tag{4.7}$$

where P_{cycle} is the chirp repetition rate.

For the molecular formation simulations, we're interested in the formation rate, $R(I_0)$, for each peak intensity, I_0. The formation rate for each partial wave, J, for each peak intensity $R_J(I_0)$, is defined as:

$$R_J(I_0) = N_{mol}^{ave} * P_{cycle}, \tag{4.8}$$

where P_{cycle} is the chirp repetition rate as in the collisional simulations case, N_{mol}^{ave} is a spatial average (described below) of N_{mol} from equation 4.6. We run the simulations for a number of different intensities, with a finer grid at lower intensities. For the typical work presented in this thesis (up to 2000 W/cm^2 peak intensity), we use ∼100 intensity points. The resulting N_{mol} are then spatially averaged over the Gaussian density distribution in the MOT (section 3.1) and the Gaussian intensity profile of the photoassociation laser:

$$N_{mol}^{ave} = \int_{r=0}^{10*MOT_{Waist}} P(I) * \frac{2}{MOT_{Waist_X} * MOT_{Waist_Z}} * r * e^{\frac{-2*\pi*r^2}{PA_{Waist_X}{}^{*PA_{Waist_Y}{}^{*\pi}}}} dr, \tag{4.9}$$

where $MOT_{Waist_{X,Z}}$ are the $1/e^2$ radii of a fit of the experimental MOT cloud, $PA_{Waist_{X,Y}}$ are the $1/e^2$ radii of the photoassociation laser, and P(I) are the cubic interpolations of N_{mol} at various intensities, I:

$$I = I_0 * e^{\frac{-2*\pi*r^2}{PA_{Waist_X}{}^{*PA_{Waist_Y}{}^{*\pi}}}}. \tag{4.10}$$

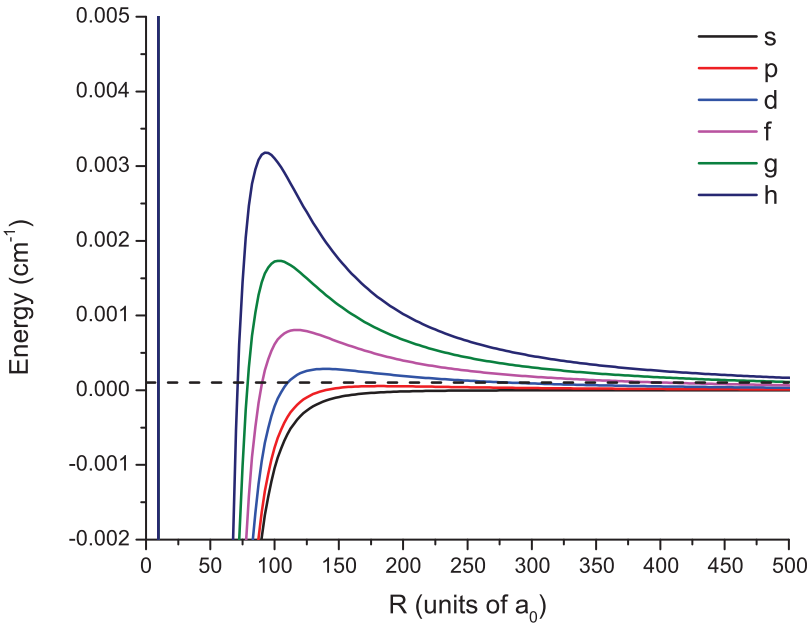

Figure 4.4. Partial Wave Potential Energy Curves

Barriers for J=0 to 5 corresponding to partial waves s,p,d,f,g,h are shown. The dashed horizontal black line corresponds to the atomic temperature, 150 μK, used in section 4.3 (reference [45]).

Now that we have the formation rate for each peak intensity, $R_J(I_0)$, we sum over partial waves. For the various partial waves beyond s (J=0), we add a rotational barrier $V_J = J(J+1)/2\mu R^2$ to the $a\ ^3\Sigma_u^+$ potential, where μ is the reduced mass. An expanded view of the $a\ ^3\Sigma_u^+$ potential with the barriers is shown in figure 4.4. For convergence, we found it necessary to use J = 0 to 5. This gives us coverage above the atomic temperature, taken to be 150 μK (section 4.3, reference [45]). The various barrier height energies are shown in table 4.7. After we've run the simulations for J = 0 to 5 and found all of the peak intensity formation rates, $R_J(I_0)$, we then sum over the partial waves:

$$R(I_0) = \sum_{J=0}^{5} (2J+1) R_J(I_0), \tag{4.11}$$

J	Partial Wave	Barrier Height Energy (μK)
0	s	0
1	p	79.2
2	d	410.8
3	f	1160.5
4	g	2493.9
5	h	4576.3

Table 4.7. Partial Wave Barrier Energies

to finally find the formation rates.

4.1.6 Contents of This Chapter

The collisional simulations are presented in section 4.2, which was published as reference [44]. The corresponding experiments were described in references [62, 80]. For these atomic trap-loss collisions, we examine the dependencies on chirp direction, chirp shape, and center detuning. The molecular formation simulations for 100 ns chirps are presented in section 4.3, which was published as reference [45]. The corresponding experiments were described in references [45, 62]. For these molecular formation rates, we examine unchirped pulses as well as $\sim$ 1 GHz in 100 ns positive and negative chirps. We reveal the mechanism responsible for an enhancement of the molecular formation rate by the positive chirp relative to the negative chirp. The molecular formation simulations involving local control, LC, are presented in section 4.4, which was published as reference [46]. LC is a simple unidirectional non-iterative time propagation scheme which adjusts the field at each instant of time in order to optimize a target at the next time step. By utilizing LC of the phase, we can further enhance molecular formation rates. Further simulations with faster chirps are presented in section 4.5 with some corresponding experiments described in Chapter 5. The incorporation of different chirp shapes (on faster timescales) leads to an enhancement of the molecular formation rate.

4.2 Quantum dynamical calculations of ultracold collisions induced by nonlinearly chirped light*

4.2.1 Introduction

Efforts to bring the techniques of coherent control to bear on ultracold molecule formation [81] have attracted significant attention in recent years. This has been motivated in large part by the interest in improving the production efficiency and manipulation of ultracold molecules [8, 9, 82, 83] for the myriad of applications in ultracold chemistry, many-body dipolar systems, quantum information, and precision spectroscopy. Direct laser cooling of atoms is now a standard technique [47]. Although progress is being made [22], extending this concept to molecules is, in general, not straightforward. The impediment is the multitude of internal levels [84]. Since coherent control techniques [14, 85] typically deal with internal degrees of freedom, while atom cooling schemes [47] manipulate the translational degrees of freedom, combining the two offers the prospect of complete control over molecular systems. The process of photoassociation [86–89], in which laser light converts colliding atoms into bound molecules, is one specific possibility. A number of such schemes [18, 79, 90–102], using coherent control with ultrafast pulses to form molecules, have been considered. Experimental progress, however, has been limited. Early experiments demonstrated that the photodestruction of ultracold molecules could be coherently controlled using shaped [36] and chirped [37] ultrafast pulses. More recently, coherent transients were observed in excited-state molecules photoassociated with femtosecond pulses [39–43]. In addition, some evidence for the production of molecules in the electronic ground state was reported [42]. Photoassociative ionization studies with short pulses have also been carried out [103, 104].

---

*Text and figures reprinted with permission from [44]. Copyright 2012 The American Institute of Physics.

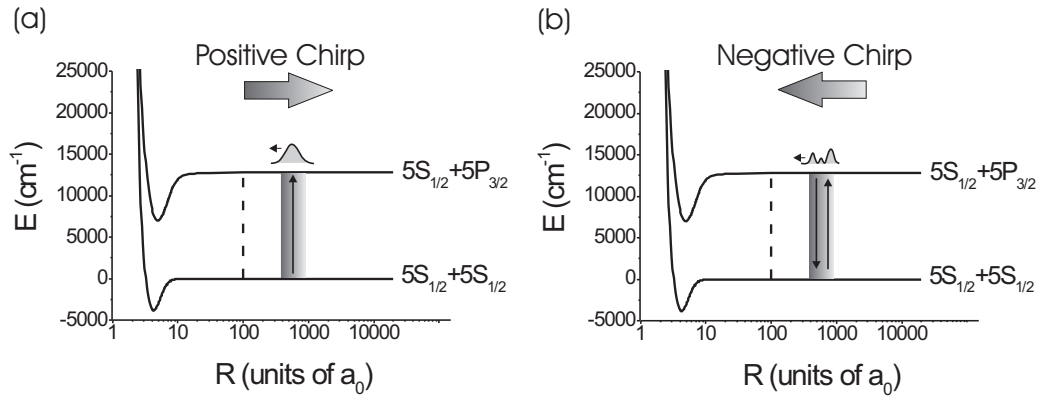

Figure 4.5. Ultracold collisions in Rb induced by frequency-chirped light

The ground- and excited-state potentials are shown as well as the excited-state wave packet, the region of R swept over by the chirp, and the absorbing boundary (dashed line). Note that the horizontal axis is logarithmic. For the positive chirp (a), the excitation radius (upward arrow) moves outward in time while the excited-state wave packet moves inward. However, for the negative chirp (b), the excitation radius moves inward in time, following the excited wave packet trajectory. This leads to multiple interactions, which can return a portion of the wave packet to the ground state (downward arrow).

We have recently performed a series of experiments with frequency-chirped light [51, 80, 105, 106] that are related to coherently-controlled molecule formation, but that differ in two important aspects. Instead of detecting molecules formed by photoassociation, we measure the rate of laser-induced trap-loss collisions between ultracold Rb atoms. Also, in contrast to the short pulse work, our experiments take place on a nanosecond time scale, which is better matched to the motion of atoms undergoing long-range collisions. We have demonstrated coherent control of these collisions by varying the direction of the frequency chirp [106]. Because the atom pair always accelerates inward on the attractive potential, and a negative chirp provides an excitation (or Condon) radius which can follow this motion, there can be multiple interactions between the atom pair and the light, as shown in Fig. 4.5 (b). This can lead to coherent de-excitation and thus the suppression of the short-range inelastic collision rate, a process we denote as "coherent collision blocking". This cannot happen for a positive chirp where the excitation radius moves outward with time (Fig. 4.5 (a)). In our most recent work [80], we demonstrate further coherent control by varying not only the direction, but also the shape of the frequency chirp. We find that under certain conditions, the details of the chirp nonlinearity significantly affect the rate of trap-loss collisions. This type of control of the collisional wave function as it evolves from long range to short range may benefit the process of photoassociative molecule formation. Dynamical studies of trap-loss collisions may also help to improve our understanding of the mechanisms of these important loss processes [107].

In the present work, we discuss the results of quantum dynamical calculations of these most recent experiments. The dynamics of the collisional wave functions, on both ground-state and excited-state potentials, are followed in the presence of various frequency chirps. Collisional loss, as measured in the experiment, is assumed to occur when the atom pair reaches short range in the excited state. In general, the

simulations reproduce the trends observed in the experimental data. A dependence of the collisional loss rate on the shape of the negative chirp is demonstrated for certain parameters, while the loss rate for positive chirps is found to be relatively insensitive to the details of the chirp shape. These variations with negative chirp shape occur in the regime of coherent collision blocking, indicating that details of the chirp are most important when the internuclear separation and the Condon radius vary on similar time scales. This concurrence allows multiple interactions between the collisional wavefunction and the chirped light, resulting in an increased sensitivity of the excited-state wavefunction evolution to the chirp shape. We also find that the dependence on negative chirp shape involves the efficiency of collisional loss for a given amount of excitation, and not simply the amount of excitation.

The paper is organized as follows. In Section 4.2.2, we present the theory used in the quantum dynamical calculations of the ultracold collisions. The specific non-linear frequency chirps used in the simulations are also described. In Section 4.2.3, we present results of the simulations, including not only the overall collisional loss rate constants, but also examples of population and wave function dynamics. The results are also compared to the experimental measurements. Section 4.2.4 comprises concluding remarks.

4.2.2 Theory

The time-dependent Schrödinger equation for two interacting ^{85}Rb atoms is solved with the Chebyshev polynomial expansion method [70] for the temporal operators, and with a mapped Fourier grid to address the wide range of length scales in the system [72]. In the dressed-state picture, the two-channel Hamiltonian has the form:

$$\hat{H} = \begin{pmatrix} \hat{T} + \hat{V}_g(R) & \hbar\Omega(t) \\ \hbar\Omega^*(t) & \hat{T} + \hat{V}_e(R) + \hbar\Delta_p \end{pmatrix}. \tag{4.12}$$

In Eq. (4.12), $\hat{T}$ is the kinetic energy operator, Δ_p is the center detuning of the linearly-chirped pulse with respect to the atomic asymptote (defined as $5S_{1/2}$ ($F = 3$) $\rightarrow$ $5P_{3/2}$ ($F' = 4$)), and $\hat{V}_{g/e}$ are the ground/excited-state potentials. We restrict the treatment to a single excited-state potential, 0_u^+ [92, 108], and ignore hyperfine structure. To account for the two possible initial scattering states the computation is performed separately for the singlet $X\ ^1\Sigma_g^+$ and the triplet $a\ ^3\Sigma_u^+$ states [92, 108], each adjusted for its proper scattering length [75], and then a weighted average is taken. At long range, hyperfine mixing relaxes the u-g selection rule, allowing both of these ground states to be excited. Within the rotating-wave approximation, the time-dependent coupling between the ground- and excited-states due to the chirped pulse is given by:

$$\hbar\Omega = \mu E_0 \exp\left[-\left(\frac{t - t_{center}}{2\sigma}\right)^2 + i\nu_{chirp}(t - t_{center})^2\right], \tag{4.13}$$

where μ is the transition dipole moment, E_0 is the peak electric field, σ is the pulse width, ν_{chirp} is the chirp rate, and t_{center} defines the center of the intensity pulse. Due to the nature of the nonlinear chirps, instead of using a chirp rate, we input instantaneous frequency offsets, $\tilde{\omega}(t)$, from the center frequency of the linearly-chirped pulse, Δ_p. Therefore,

$$\hbar\Omega = \mu E_0 \exp\left[-\left(\frac{t - t_{center}}{2\sigma}\right)^2 + i\tilde{\omega}(t)(t - t_{center})\right]. \tag{4.14}$$

The chirps (concave-down, concave-up, and linear for both positive and negative directions, chirping $\sim$ 1 GHz in 100 ns) are characterized by a heterodyne signal [80]. A reference beam is combined with the modulated beam on a photodiode. The resulting beat frequency yields the instantaneous offset frequency as a function of time, $\tilde{\omega}(t)$, through analysis of the maxima and minima. These data points are then

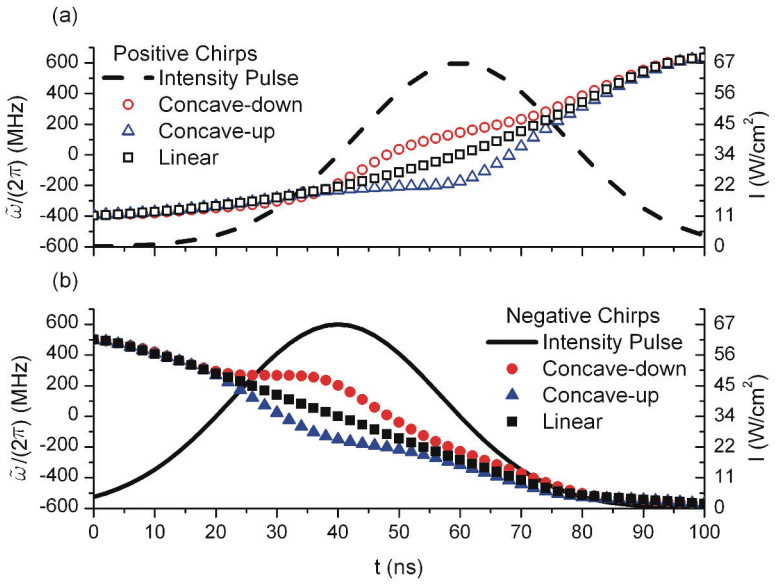

Figure 4.6. Frequency Chirps

Shaped positive (a) and negative (b) frequency chirps. The curves shown are smoothed interpolations of the actual heterodyne signals. Indicated frequencies $\tilde{\omega}(t)$ are relative to the centers of the linear chirps. Also shown are the corresponding 40 ns FWHM Gaussian intensity pulses I(t).

interpolated using a piecewise cubic Hermite interpolating polynomial (PCHIP) to yield a frequency value every 0.1 ns. The resulting values are smoothed using a 5 ns full-width-at-half-maximum (FWHM) Gaussian function, ensuring that the slope is always < 0 for negative chirps or > 0 for positive chirps. The smoothed frequencies are then interpolated again using a PCHIP time step of ~ 0.45 ps, corresponding to the temporal propagation step of the simulations. The resulting instantaneous frequencies, in 2 ns steps, are shown in Fig. 4.6. The corresponding 40 ns FWHM intensity profiles of the pulses with peak intensity $I = 67$ W/cm^2 are also displayed. We run the simulations for 200 ns to ensure full convergence, keeping the frequencies constant at the value they reached at 100 ns for the duration of the run. In Section 4.2.3 we present results for the first 100 ns since this more closely matches the timescale of the experiment [80] and convergence is already met to within a few percent at 100 ns. Based on the range of the frequency chirps, any positive (negative) chirp with Δ_p closer to the atomic resonance than $\sim$ -635 (-500) MHz would go through resonance during the 100 ns chirp. The atomic resonance is problematic because it corresponds to an infinite excitation radius. Also, we have not included a repulsive excited-state potential that would be relevant for positive detunings. For our set of Δ_p values, passage through the atomic resonance only happens for the positive chirp with $\Delta_p/2\pi$ = -550 MHz. Even here, this occurs near the end of the 100 ns period, where the pulse intensity is greatly reduced.

The initial s-wave scattering state is computed by diagonalization of the time-independent Hamiltonian of the ground-state potential in the mapped Fourier grid basis. Observables are computed by taking a single initial state that corresponds to the 50 μK temperature of the sample and factorizing according to [79]. This thermal averaging is discussed in Section 4.2.3. Contributions to the loss from higher partial waves are found to be negligible.

We model the trap loss as follows. If the atom pair reaches short range in the excited state ($5S_{1/2} + 5P_{3/2}$), the atoms can gain sufficient kinetic energy to be ejected from the trap. This can occur either by radiative escape, where the excited atom pair spontaneously decays at short range, or by fine-structure predissociation, where a short-range curve crossing results in the atom pair emerging on the lower fine-structure asymptote ($5S_{1/2} + 5P_{1/2}$) [78]. Decay into a bound molecular state, which would occur primarily inside the absorbing boundary, also results in loss of the colliding atoms because molecules are not confined in the atom trap. We model these loss mechanisms by placing an absorbing boundary on the excited-state potential at $R = 100\ a_0$ to absorb incoming collisional flux. Any collisional flux reaching this internuclear separation is considered to result in the loss of the atoms from the trap. We have checked that the calculated losses are rather insensitive to the exact location of this boundary, as discussed in Section 4.2.3. We note that this short-range absorbing boundary is distinct from an absorbing wall of a calculational box used to prevent population from leaving the box.

In the collisions we are simulating, the atoms initially move very slowly and interact at long range. The relevant time scale can therefore be quite long and spontaneous emission cannot be ignored. We model this decay process by coupling the excited state to a sink channel with a damping rate of $\Gamma = (22\ \text{ns})^{-1}$ [78]. This sink channel represents loss of excited-state population occurring outside the absorbing boundary and thus not resulting in loss from the trap. We note that this treatment takes into account only a unidirectional decay from the excited state, and does not account for any incoherent interactions that result from decay of this population back to the ground state. Therefore, some incoherent effects that are relevant to our discussion, such as flux enhancement (see next section), are not included.

4.2.3 Results and Analysis

To understand the results of the quantum dynamical calculations, we first examine the population transfers and losses shown in Fig. 4.7. As discussed in Section 4.2.2, the trap loss is defined as the cumulative fraction of the initial ground-state population which encounters the excited-state absorbing boundary. As can be seen from these plots, most of the population remains in the ground state throughout the 100 ns chirp. At long times, the total population (ground-state plus excited-state) does not sum to unity because of the irreversible transfer to the trap-loss channel and to the spontaneous emission sink. The excited-state maxima for the positive chirps (Fig. 4.7 (a,b)) come slightly after the peak of the intensity pulse at 60 ns whereas the excited-state maxima for the negative chirps (Fig. 4.7 (c,d)) come slightly before the peak of the intensity pulse at 40 ns. This time ordering was also observed in simulations of chirped photoassociation on much faster time scales [90]. The population plots from the positive chirps (Fig. 4.7 (a,b)) are smooth with some slight variations for the various shapes whereas the negative chirps (Fig. 4.7 (c,d)) show rapid small-amplitude oscillations. These are out of phase for the ground and excited states and are likely residual Rabi oscillations resulting from extended interactions as the wave packet and excitation radius both move inward. Although we have only shown population plots for chirps with $\Delta_p/2\pi$ = -750 MHz, detunings of -550 MHz and -950 MHz yield similar results. The losses for the singlet potential (Fig. 4.7 (a,c)) considerably exceed those for the triplet potential (Fig. 4.7 (b,d)) because the larger singlet scattering length yields more wave function amplitude at the relevant values of R. The positive chirps all yield similar losses for each potential at a given detuning (Fig. 4.7 (a,b)), whereas the losses show more variation with shape for the negative chirps, especially at $\Delta_p/2\pi$ = -750 MHz (Fig. 4.7 (c,d)).

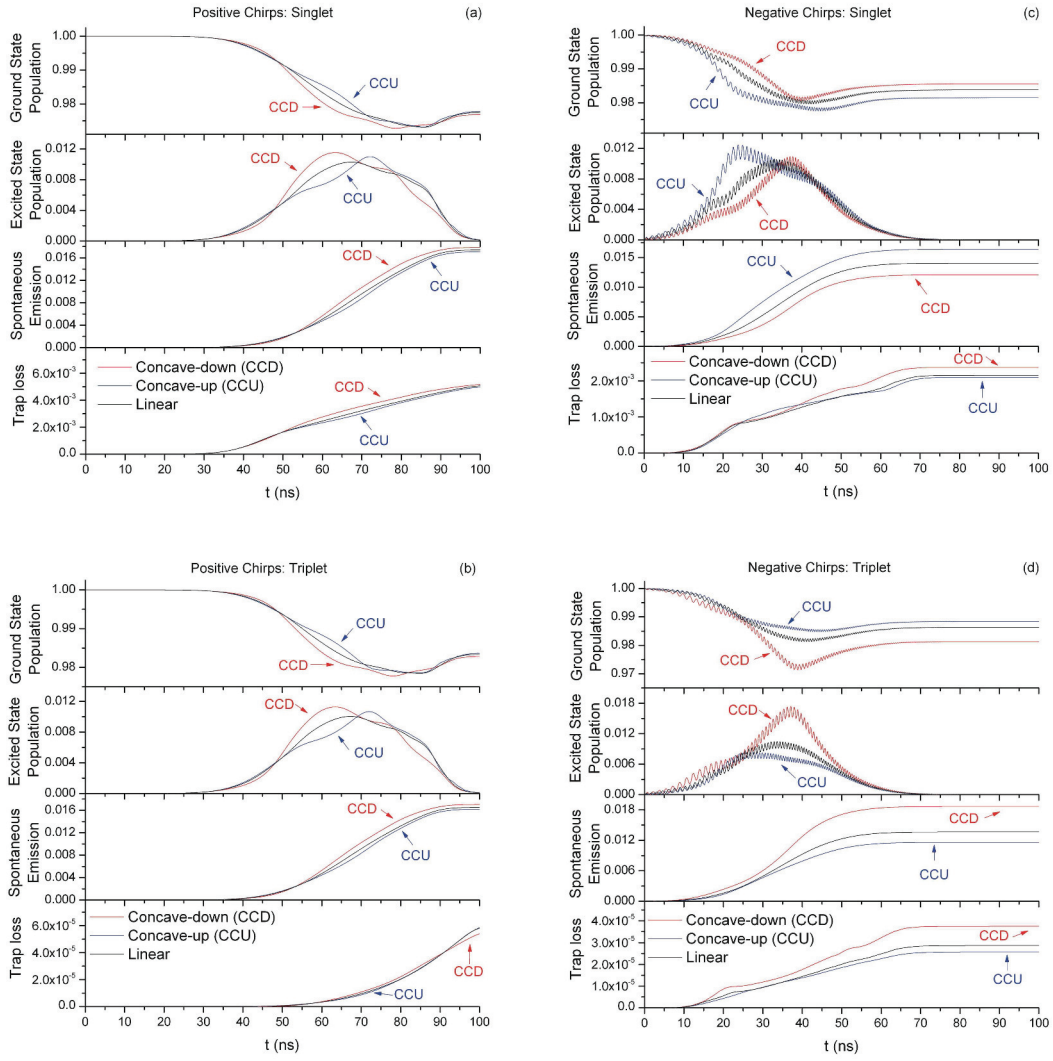

Figure 4.7. Population Evolutions

Ground- and excited-state population, spontaneous emission sink population, and trap loss for positive chirps (singlet (a) and triplet (b) potentials) and negative chirps (singlet (c) and triplet (d) potentials) with $\Delta_p/2\pi$ = -750 MHz.

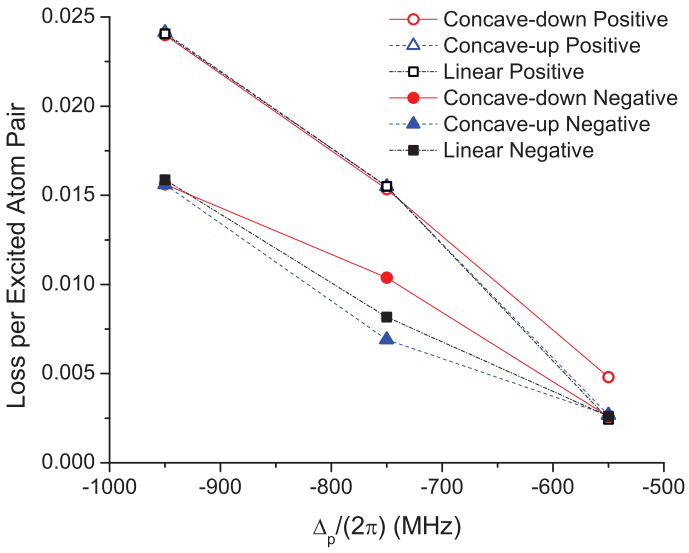

Figure 4.8. Weighted Average Loss Per Excited Atom Pair

Weighted average of singlet and triplet loss per excited atom pair, defined in the text. This quantity is shown for the positive and negative concave-down, concave-up, and linear chirps. The lines connecting the points are to guide the eye.

To gain further insight, we examine the loss per excited atom pair for each case. This is defined as the trap loss divided by the average excited-state fraction during the 100 ns observation window and is a measure of the likelihood for an excited atom pair to undergo trap loss as opposed to spontaneous emission. The weighted average of the singlet and triplet loss per excited atom pair for the positive and negative concave-down, concave-up, and linear chirps is shown in Fig. 4.8. The amount of loss per excited atom pair decreases for both the positive and negative chirps as the pulse detuning, Δ_p, gets closer to resonance. This is due to the fact that excitation at larger R results in less acceleration and therefore a greater chance for spontaneous emission before encountering the absorbing boundary. The largest separation occurs for the negative chirps with $\Delta_p/2\pi$ = -750 MHz. Here the concave-down chirp has the most loss per excited atom pair, followed by the linear chirp and then the concave-up chirp. This trend is consistent with that of the trap loss (Fig. 4.7(c,d)), indicating that the efficiency of loss for a given amount of excitation, and not simply the amount of excitation, is important. We find that for the positive chirps there is no significant difference among the shapes for each detuning. The variation that occurs at $\Delta_p/2\pi$ = -550 MHz for the positive chirps is due to these shapes going through the atomic resonance ($R = \infty$) at slightly different times and with slightly different slopes, as expected for the frequency chirps shown in Fig. 4.6 (a).

Examples of the excited-state wave packet evolution can be seen in Fig. 4.9. We show snapshots of $|\Psi_e|^2 R^2$ for $R < 1000\ a_0$ for positive chirps (Fig. 4.9 (a-c)) and negative chirps (Fig. 4.9 (e-g)), starting on the singlet potential. The results for the triplet potential are similar and therefore not shown. We focus first on the overall difference between the positive and negative chirps. For the positive chirp with $\Delta_p/2\pi$ = -750 MHz (Fig. 4.9 (a-c)), the excitation of the wave packet moves outward as time progresses. For the corresponding negative chirp, however, the excitation of the wave

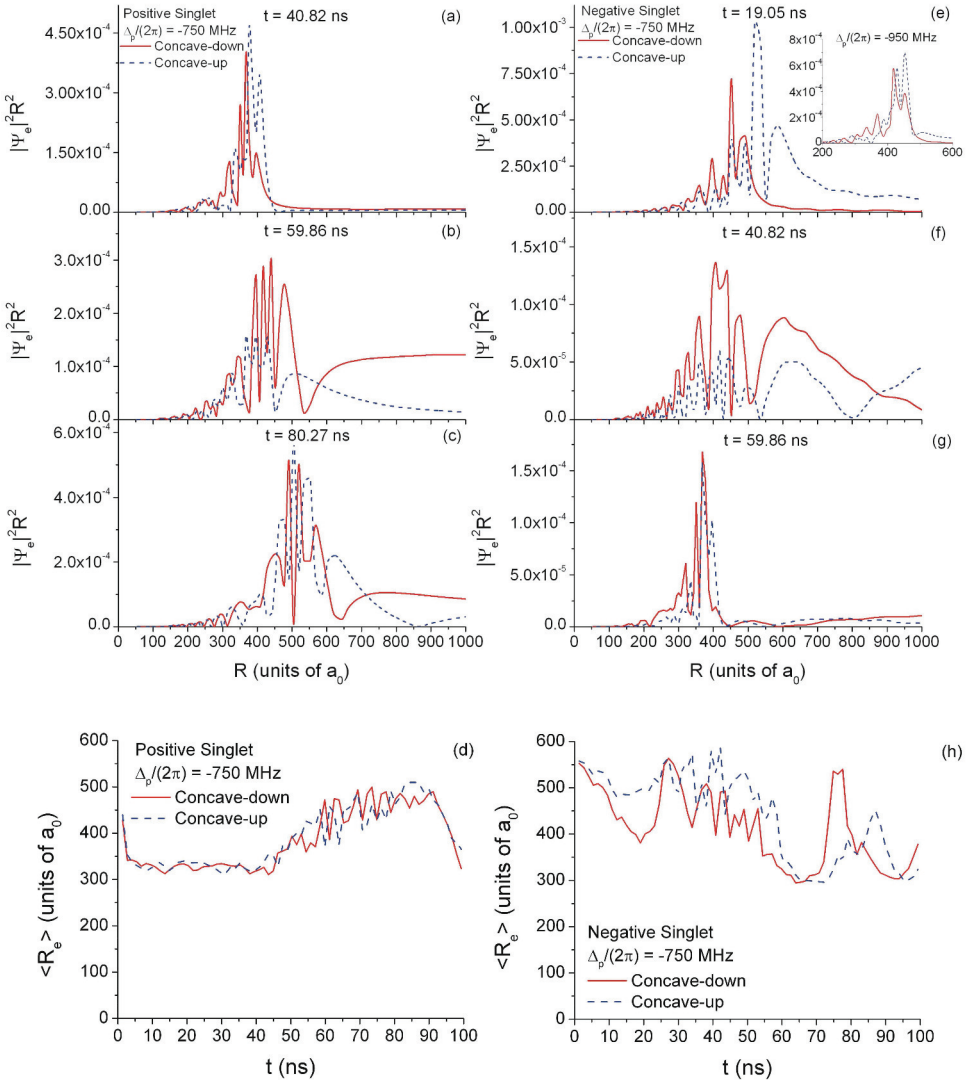

Figure 4.9. Evolution of $|\Psi_e|^2 R^2$ and <R>

Evolution of $|\Psi_e|^2 R^2$ for concave-down and concave-up positive (a-c) and negative (e-g) chirps. For all frames, the singlet potential is assumed and the chirp has $\Delta_p/2\pi$ = -750 MHz. Successive frames show various times during the chirp, as indicated. The insert in (e) shows $\Delta_p/2\pi$ = -950 MHz at the same time as the main frame (19.05 ns). The center of the 40 ns FWHM intensity pulse occurs at 60 ns (b) for the positive chirps and at 40 ns (f) for the negative chirps (see Fig. 4.6). Also shown, in (d) and (h), are the temporal evolutions of the excited-state expectation value of R.

packet moves inward as the chirp proceeds, which is the same direction as the motion caused by the attractive nature of the excited-state potential. This difference between the two chirp directions is clearly seen by comparing Figs. 4.9 (d) and 4.9 (h), which show $<R_e>$, the excited-state expectation value of R, as a function of time for the positive and negative chirps, respectively. These trends are similar for linear chirps and for the other detunings, neither of which, for reasons of clarity, are shown in Fig. 4.9. Note that towards the end of the positive chirp (Fig. 4.9 (d)), the intensity is low and excitation is no longer occurring, so the already existing excited-state wave function begins to move inward on the attractive potential. Note also the significant difference between Figs. 4.9 (c) and (g). Both are at times approximately 20 ns after the peak of the pulse, but Fig. 4.9 (g) has a much smaller amplitude. This is due to coherent collision blocking where the negative chirp drives population back down to the ground state as the excitation radius follows the wave packet motion inward, and is consistent with the generally smaller trap loss seen for negative versus positive chirps.

We now examine the dependence on chirp shape in Fig. 4.9. For the positive chirp, there is not much difference in the evolution of $<R_e>$ between concave-down and concave-up shapes (Fig. 4.9 (d)). The results are also similar for the linear chirp (not shown). However, for the negative chirp (Fig. 4.9 (h)), the differences in $<R_e>$ for the two chirp shapes are more pronounced. Comparing the wave packets at the beginning of the shaping, we see that for the negative chirp with $\Delta_p/2\pi$ = -750 MHz (Fig. 4.9 (e)) the concave-up chirp provides more overall excitation. This is likely due to the wave packet motion being less synchronized with the higher instantaneous chirp rate, resulting in less de-excitation (see also Fig. 4.7 (c)). Despite this, a larger portion of the wave packet created by the concave-down chirp is able to more quickly accelerate inward on the excited-state potential than for the other shapes. At the

same time, for $\Delta_p/2\pi$ = -950 MHz (shown in the insert of Fig. 4.9 (e)), there is less of a difference between concave-down and concave-up wave packets.

In order to estimate the trap-loss rate constant β from a single energy eigenstate calculation, we start by finding the number of molecules per chirped pulse leading to loss N_{mol}. Since the gas is dilute and the Hamiltonian is represented on a finite grid in coordinate space, we divide the trap volume V into many small boxes of volume ν_{box} where the number of small boxes is larger than the total number of atoms in the trap, N. Then the number of excited-state molecules leading to loss at a given temperature T (taken to be 50 μK) is given by:

$$N_{mol} = \frac{1}{2} N^2 \frac{\nu_{box}}{V} \langle \hat{P}_e \rangle_{T,box} \tag{4.15}$$

[79]. Following the procedure in Sect. 5 of [79], the thermally averaged probability to make such a molecule, $\langle \hat{P}_e \rangle_{T,box}$, is given by:

$$\langle \hat{P}_e \rangle_{T,box} = \frac{2\pi^2 \hbar^3}{\mu^{3/2} \nu_{box}} \frac{P_{E_0}}{\Delta E_0 \sqrt{kT}}, \tag{4.16}$$

where E_0 is the single energy eigenstate, ΔE_0 is the energy width of this level (the inverse of the density of states in the box), μ is the reduced mass, and P_{E_0} is the probability to induce an excited-atom loss event, examples of which are shown as losses in Fig. 4.7. We note that Eq. 4.16 applies when the Wigner-Kramers-Brillouin (WKB) approximation is valid, which is the case in our energy range [79]. This corresponds to the trap loss coming primarily from atom pairs whose energy E_0 is close to kT. The number of atoms lost per pulse, N_{atoms}, is twice the number of corresponding molecules N_{mol}:

$$N_{atoms} = \frac{2\pi^2 \hbar^3 N^2}{\mu^{3/2} V} \frac{P_{E_0}}{\Delta E_0 \sqrt{kT}}. \tag{4.17}$$

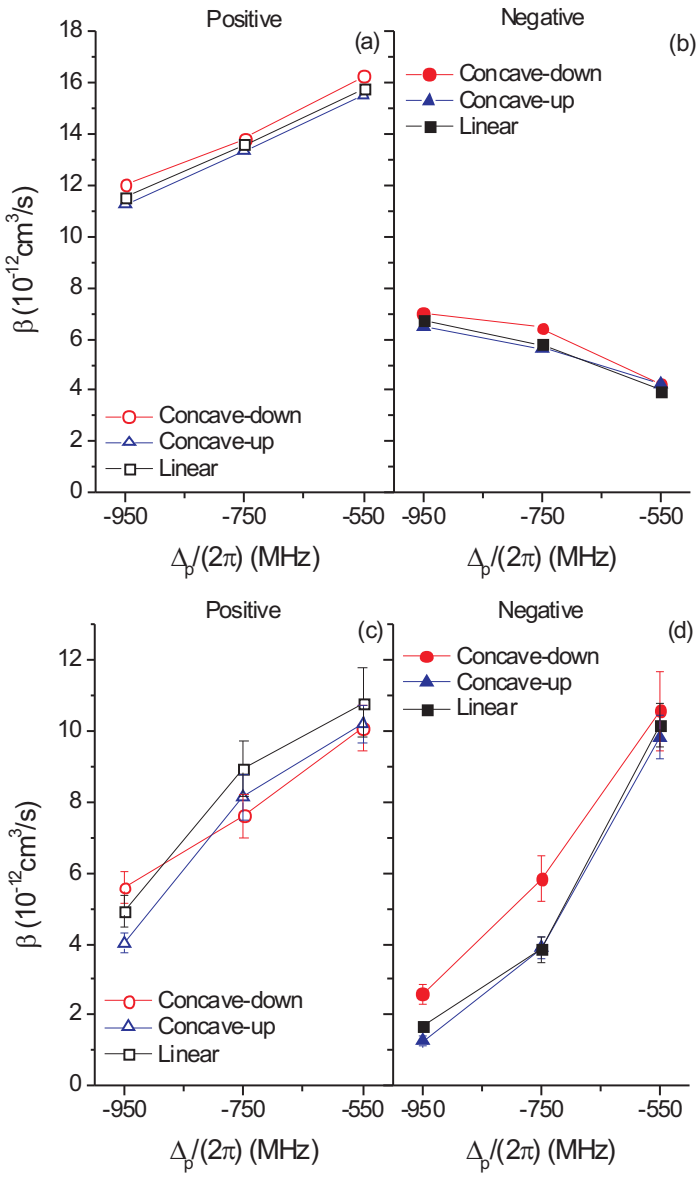

Figure 4.10. Quantum Dynamical Calculations of β

Quantum dynamical calculations of $\beta(\Delta_p)$ for concave-down, concave-up, and linear positive (a) and negative (b) chirps. Experimental $\beta(\Delta_p)$ for concave-down, concave-up, and linear positive (c) and negative (d) chirps. The lines connecting points are to guide the eye.

The collisonal trap-loss rate constant β, where $\beta * N/V$ is the time-averaged loss rate per atom, can then be defined as:

$$\beta = \frac{N_{atoms} P_{cycle}}{t} \frac{V}{N^2}, \tag{4.18}$$

where P_{cycle} is the number of pulses per cycle of the experiments (typically 60) and t is the repetition time, 722 μs. Plugging in the relevant numbers for this experiment [80] leads to:

$$\beta = P_{E_0} * 1.04 * 10^{-8} \frac{cm^3}{s}. \tag{4.19}$$

Using this conversion (Eq. 4.19), and preforming the weighted average of the singlet and triplet ground states, we find the absolute values for β as shown in Fig. 4.10 (a,b). We note that the efficiency of the absorbing boundary, which we assume to be 100 %, will affect the absolute values of β. However, the results are rather insensitive to the boundary's location. For example, shifting the absorbing boundary from 100 a_0 to 150 a_0 increased the singlet-state trap loss for the $\Delta_p/2\pi$ = -750 MHz positive linear chirp (Fig. 4.7a) by only 0.66%. This is because the attractive potential is sufficiently steep that any excited-state collisional flux reaching these small values of R is accelerated very quickly to even smaller values of R.

Focusing first on the results for the nonlinear positive chirps (Fig. 4.10 (a)), we see that the values of β for the various chirp shapes are similar at a given Δ_p, showing that there is little dependence of β on the details of the nonlinearity of the positive chirp. These results are consistent with the excitation radius of the positive chirp sweeping outward, away from the excited-state wave packet trajectory, as seen in Fig. 4.9 (a-c). These results are also consistent with the smooth nature of the population plots in Fig. 4.7 (a,b). There is also a general trend of β decreasing as the

detuning gets farther from resonance. This is due to less atom pairs being available for excitation at the corresponding smaller values of R.

Now focusing on the results for the nonlinear negative chirps (Fig. 4.10 (b)), we see that the values for the negative chirps are smaller than those of the positive chirps. As mentioned earlier, this is attributed to the positive chirps having efficient excitations with no further interactions, whereas the negative chirp may have further interactions which drive the population back down to the ground-state. The general trend in this detuning range is a reduction in β as we approach resonance, which is opposite to the behavior for the positive chirps. Although there are more atom pairs available at large R (i.e., closer to resonance), this enhancement in initial atom-pair excitation is more than compensated for by the increased likelihood of coherent collision blocking for these slow-moving pairs, resulting in less overall loss. We note again that flux enhancement, due to long-range excitation followed by spontaneous emission and then re-excitation at shorter range [106], is not included in the quantum dynamical calculations. As mentioned in section 4.2.2, the simulations do take into account spontaneous emission, but do not allow for the decayed wavefunction to be re-excited. The evolution of the population in the spontaneous emission sink is shown in Fig. 4.7 (c,d) for the negative chirp with $\Delta_p/2\pi$ = -750 MHz. At the various negative chirp detunings examined, the sink populations at t = 100 ns, averaged over chirp shape and singlet and triplet ground states, are: $\sim$ 0.008 for -950 MHz; $\sim$ 0.014 for -750 MHz; and $\sim$ 0.031 for -550 MHz. This trend indicates that flux enhancement effects will be most important at the smallest negative detuning (-550 MHz). In our previous measurements with linear chirps, and in the corresponding classical Monte-Carlo simulations [106], we found that this flux enhancement mechanism dominates the loss for negative chirps centered closer to resonance than $\Delta_p/2\pi$ = -600 MHz,

consistent with the sink population trend discussed above. Excluding the contribution of flux enhancement will thus have the largest effect at -550 MHz.

We now examine the effect of chirp shape for the negative chirps. At $\Delta_p/2\pi$ = -550 MHz, the various shapes yield similar values of β. However, $\Delta_p/2\pi$ = -750 MHz and -950 MHz are in the collision blocking regime [106]. Specifically, at $\Delta_p/2\pi$ = -750 MHz, the concave-down chirp yields a higher β than that of the concave-up or linear chirps. There is a similar but smaller separation at $\Delta_p/2\pi$ = -950 MHz, indicating that the values of β are starting to converge. This is consistent with measurements at larger detunings [80] where β becomes independent of chirp shape. Since the excitation occurs at short range where the attractive potential is steep, the changing excitation radius cannot keep up with the wave packet motion and multiple interactions are less likely to occur. From the wave packet dynamics for $\Delta_p/2\pi$ = -750 MHz (Fig. 4.9 (e-g)), we see that a larger portion of the wave packet created by the concave-down chirp is able to more quickly accelerate inwards on the excited-state potential, giving rise to the larger β. These dynamics also lead to a larger loss per excited atom pair as seen in Fig. 4.8. In fact, by comparing Fig. 4.10 (b) and Fig. 4.8, we conclude that the chirp shape dependence for $\Delta_p/2\pi$ = -750 MHz is due mainly to the efficiency of loss for a given excitation, as opposed to the amount of initial excitation. The further interactions possible in this regime are further exemplified through the oscillations seen in Fig. 4.7 (c,d).

The measured values of β induced by these nonlinear chirps [80] are shown in Fig. 4.10 (c,d). As can be seen from the data for the positive chirps in Fig. 4.10 (c), there is no significant difference in β due to the shaping of the positive chirps, except possibly at $\Delta_p/2\pi$ = -950 MHz. This is expected since the positive chirp sweeps outward, away from the evolving excited-state wave packet. These results are similar to those of the simulations shown in Fig. 4.10 (a).

The data shown in Fig. 4.10 (d) for the negative chirps shows a dependence on the nonlinearity of the chirp. Specifically, the concave-down chirp is found to have a value of β that is 50(20)% larger than those of the concave-up and linear chirps at $\Delta_p/2\pi$ = -750 MHz [80]. There is a similar trend at $\Delta_p/2\pi$ = -950 MHz. These variations are also seen in the simulations (Fig. 4.10 (b)), although to a lesser extent. At $\Delta_p/2\pi$ = -550 MHz, comparing the simulations with the measurements is problematic because of the important role of flux enhancement. Nevertheless, it is interesting that both show little dependence on the chirp shape. However, the detuning dependence of the simulations and the measurements is quite different because the former does not include flux enhancement.

4.2.4 Conclusion

In summary, we have presented quantum dynamical calculations of excited-state trap-loss collisions caused by frequency-chirped light. The dependencies on chirp direction, chirp shape, and center detuning have been examined and compared to the results of a recent experiment. The basic trends are in agreement. In particular, the loss rate for positive chirps shows little dependence on chirp shape, while for negative chirps, a dependence is seen for certain center detunings. This is attributed to the coherent return of collisional flux to the ground state as the resonant radius for excitation follows the accelerating excited-state flux inward. Although the simulations do account for spontaneous emission, only a single attractive excited-state potential is considered and the hyperfine structure is ignored. Despite these simplifications, qualitative agreement with the experiment is found and evidence for coherent control is seen in the dependence on the shape for the negative chirp. An interesting future direction is to extend the simulations from trap-loss collisions to photoassociation and to utilize coherent control to optimize the formation of bound molecules.

4.3 Production of Ultracold Molecules with Chirped Nanosecond Pulses: Evidence for Coherent Effects*

4.3.1 Introduction

Applying the concepts of coherent control to the manipulation of ultracold systems is a topic of considerable current interest. Coherent control [14, 85] usually involves internal degrees of freedom, such as molecular vibration and rotation, while cooling and trapping techniques [47] deal with external degrees of freedom. The time scales are also quite different: coherent control is typically done with ultrafast lasers while motion at ultralow temperatures is very slow. A particularly noteworthy convergence of these two fields is the formation of ultracold molecules from ultracold atoms by the process of photoassociation [88] (PA). This free-bound transition is a simple binary reaction starting with a narrow range of continuum energies, so coherence can be expected to play an important role [35].

In recent years, there have been many proposals for PA with shaped ultrafast pulses [35] to efficiently form ultracold molecules for their many potential applications [8]. So far, experimental progress towards coherently controlled PA has been limited to photodestruction of already existing ultracold molecules [36, 109] and coherent transients in PA with femtosecond pulses [39, 40]. In recent work, we have used frequency-chirped light on the nanosecond time scale to coherently control laser-induced inelastic collisions. Because our nanosecond pulses are well matched to the long-range motion of the colliding atoms, the collision rate depends on the chirp direction [106] and shape [80]. In the present work, we apply our chirped pulses to the more easily modeled process of PA and directly detect the resulting ground-state molecules. We find that the formation rate depends on chirp direction, in agreement

*Text and figures in sections 4.3.1-4.3.4 reprinted with permission from [45]. Copyright 2013 The American Institute of Physics.

with quantum simulations. These simulations reveal that despite the presence of spontaneous emission, a significant portion of this dependence arises from a coherent effect: stimulated emission into a specific high vibrational level.

4.3.2 Experiment

In the experiment [106], we illuminate ultracold ^{87}Rb atoms with nanosecond-scale pulses of frequency-chirped light, forming $^{87}Rb_2$ via PA. These excited molecules subsequently radiatively decay into high vibrational levels (v") of the $a\ ^3\Sigma_u^+$ metastable state which are detected by resonantly-enhanced multiphoton ionization (REMPI). The ultracold atoms are provided by a phase-stable magneto-optical trap (MOT) loaded by a slow atomic beam from a separate source MOT. The atomic temperature and peak density are $\sim$150 μK and $\sim$5x10^{10} cm^{-3}, respectively.

The frequency-chirped light is produced by modulating the injection current of an external-cavity diode laser with a 5 MHz triangle wave, but with programmed adjustments to produce approximately linear positive and negative chirps with equal slopes during the pulse. Each chirp covers $\sim$1 GHz in 100 ns and is centered on the PA transition, a strong line located 7.79 GHz below the $5S_{1/2}(F = 2) \rightarrow 5P_{3/2}(F' = 3)$ asymptote and determined to have 0_g^- character [110]. To minimize amplitude modulation, the chirped light injection locks a separate 150 mW slave diode laser [111]. A sequence of 40 ns FWHM Gaussian pulses is generated by switching with an acousto-optical modulator. The timing selects the central regions of either the positive or negative chirps.

REMPI detection of the resulting Rb_2 molecules is performed with 5 ns, 4 mJ pulses from a pulsed dye laser tuned to λ=601.9 nm and focused to $\sim$3 mm diameter at the MOT. Based on previous work [31, 110], this light ionizes high-v" levels of the $a\ ^3\Sigma_u^+$ state expected to be populated by PA to long-range excited states. The

REMPI spectrum is similar to that from molecules produced by MOT light, and is dominated by a broad feature at 601.9 nm. Individual high-lying v" levels are not resolved due to the 0.2 cm^{-1} laser bandwidth. The resulting Rb_2^+ ions are accelerated to a Channeltron detector and distinguished from Rb^+ by time of flight. The timing of the experiment is as follows. A sequence of up to 5x10^4 chirped (or unchirped) pulses, at a repetition rate f = 5 MHz, is applied to the trapped atoms and 25 μs later, the REMPI pulse fires and the ions are detected. The entire cycle is repeated at 10 Hz. The MOT beams are extinguished for 50 μs centered on the REMPI pulse to avoid ionization of excited atoms. We use a sequence of chirped PA pulses, so to obtain the molecular formation rate R, we must account for the loss of molecules during this PA window. There is photodestruction of $a\ ^3\Sigma_u^+$ molecules by subsequent chirped pulses at a time-averaged rate Γ_{PD} as well as their escape from the detection region at a rate Γ_{esc}. The number N of detectable molecules evolves according to:

$$N(t) = \frac{R}{\Gamma_{PD} + \Gamma_{esc}}(1 - e^{-(\Gamma_{PD}+\Gamma_{esc})t}). \tag{4.20}$$

We measure $\Gamma_{esc} = 108(7)\ s^{-1}$ using decay of the REMPI signal from MOT-produced molecules (i.e., without chirped light) as the REMPI pulse is delayed within a fixed 7 ms window following extinction of the MOT. We determine Γ_{PD} and R by varying the length of the PA window (i.e., the number of chirped pulses) and fitting to Eq. 4.20 as shown in Fig. 4.11(a). Here, $\Gamma_{PD} \sim 200\ s^{-1}$ for the positive chirp, implying a photodestruction probability of ~4x10^{-5} per pulse. Γ_{PD} is linear in intensity and depends somewhat on chirp direction.

The quantity of interest is the formation rate R shown in Fig. 4.11(b). For each chirp direction, R increases with intensity, but exhibits some degree of saturation. The important point is the pronounced dependence on chirp: the positive chirp has a rate higher than the negative chirp, but lower than the unchirped case.

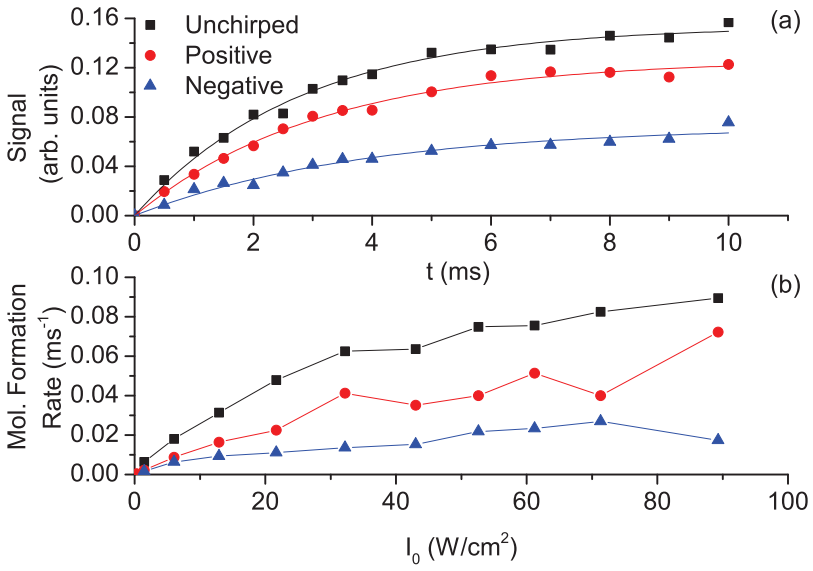

Figure 4.11. Experimental Data

(a) Rb_2^+ REMPI signals vs. photoassociation time for unchirped, positively, and negatively chirped pulses, along with fits to Eq. 4.20. The peak intensity of the pulses is $I_0 = 32.2$ W/cm^2. (b) Rb_2 formation rate vs. peak intensity for the various chirps.

4.3.3 Theory

To model the ultracold collisional dynamics, we solve the time-dependent Schrödinger equation. The dressed-state Hamiltonian reads:

$$\hat{H} = \begin{pmatrix} \hat{T} + \hat{V}_{gJ} & \hbar\Omega_0(t) & \hbar\Omega_1(t) \\ \hbar\Omega_0^*(t) & \hat{T} + \hat{V}_0 + \hbar\Delta & 0 \\ \hbar\Omega_1^*(t) & 0 & \hat{T} + \hat{V}_1 + \hbar\Delta \end{pmatrix}, \tag{4.21}$$

where $\hat{T}$ is the kinetic energy operator and $\hat{V}_j$ (j = g, 0 or 1 for the $a\ ^3\Sigma_u^+$, 0_g^- ($P_{3/2}$) and 1_g ($P_{3/2}$) electronic states) are the internuclear potentials [112] with coefficients [113] adjusted for the proper scattering length [75, 76]. The two excited states correspond to the assignment of [110]. $\Delta/2\pi$ = -7.79 GHz is the central detuning of the light from the asymptote $[5S_{1/2}(F = 2) + 5P_{3/2}(F' = 3)]$. The 0_g^- detuning is shifted [110] to yield the correct experimental spacing of ∼0.6 GHz and to be centered on v'=78. For partial waves beyond s, we add a rotational barrier $V_J = J(J + 1)/2\mu R^2$ to the $a\ ^3\Sigma_u^+$ potential. Here μ is the reduced mass.

The time-dependent couplings between the $a\ ^3\Sigma_u^+$ (g) and excited (j=0,1) states due to the chirped pulse are given by: $\hbar\Omega_j = \mu_{gj}\epsilon_0 e^{[-\frac{(t-t_{center})^2}{2\sigma^2} + i\widetilde{\omega}(t)(t-t_{center})]}$, where μ_{gj} are the R-independent transition dipole moments, ϵ_0 is the peak electric field, σ = 17 ns, t_{center} is the center of the pulse, and $\widetilde{\omega}(t)$ are instantaneous frequency offsets from Δ derived from smoothed interpolations of the heterodyne signals [44].

To enable efficient computation for nanosecond timescales, we use a basis of vibrational levels calculated on a time-independent mapped Fourier grid [72, 97, 114]. In this new basis, the Hamiltonian reads:

$$\hat{H} = \begin{pmatrix} \hat{H}_g & \hbar\hat{\Omega}_0(t) & \hbar\hat{\Omega}_1(t) \\ \hbar\hat{\Omega}_0^*(t) & \hat{H}_{e0} & 0 \\ \hbar\hat{\Omega}_1^*(t) & 0 & \hat{H}_{e1} \end{pmatrix}, \tag{4.22}$$

where $\hat{H}_j$ are the vibrational energies from the field-free diagonalization and the $\hat{\Omega}_j$ now include the Franck-Condon factors (FCFs). Since our experimental bandwidths are small ($<$ 1 GHz) and our intensities are low ($<$ 90 W/cm^2), a limited bandwidth above or below the relevant asymptote is taken to represent each of the vibrational Hamiltonians: $\sim$15 GHz for 0_g^- and 1_g; and 278 GHz (16 MHz) for the $a\ ^3\Sigma_u^+$ bound (scattering) manifold. We have verified that this representation is sufficient by extending the basis sets and checking convergence. The initial single state is a box-normalized scattering state at $\mathrm{E}_0 = k_B\mathrm{T}$, where T = 150 μK is the sample temperature.

Spontaneous decay is accounted for by adding multiple sink channels, weighted by their FCFs, corresponding to decay from each of the excited-state (0_g^- and 1_g) vibrational levels [78] into various vibrational levels or the continuum of $a\ ^3\Sigma_u^+$. Although this model precludes the possibility of multiple incoherent excitations, almost all of the population that decays into detectable levels is far from resonance and would therefore not participate in subsequent dynamics.

The computation gives the production probability per pulse, $P_{E_0,J}$, for a given initial box-normalized state and partial wave J. Following [79], we find the number of molecules per pulse:

$$N_{mol,J} = \frac{\pi^2\hbar^3 N n P_{E_0,J}}{\mu^{3/2}\sqrt{E_0}\,\frac{dE}{dn}\big|_{E_0}}, \tag{4.23}$$

where n is the atomic density, N is the atom number, and $\frac{dE}{dn}\big|_{E_0}$ is the density of energy states evaluated at E_0. To find the formation rate for each intensity, R_J(I),

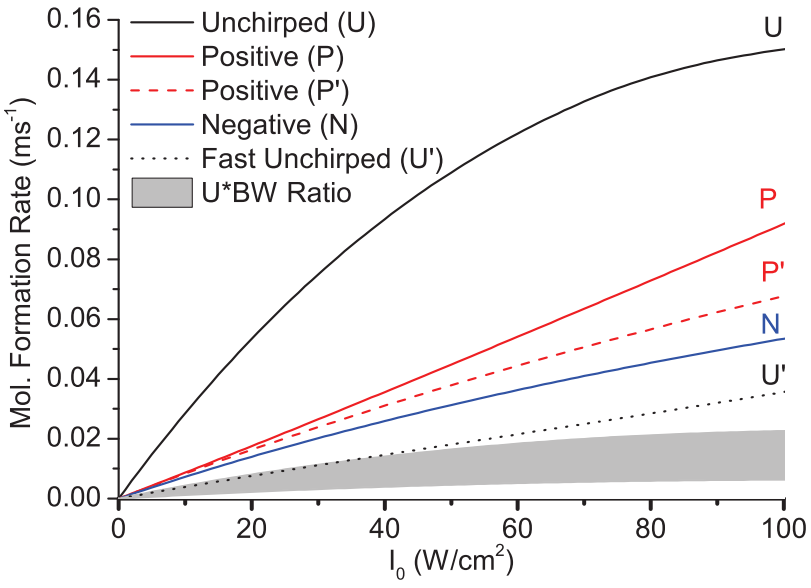

Figure 4.12. Quantum Mechanical Simulations: Molecular Formation Rates

Simulated molecular formation rates vs. peak intensity for unchirped (U), positively (P), and negatively (N) chirped pulses. The dashed curve (P') is for the positive chirp, but excluding the coherent contribution to v"=39. The shaded region is the range of results for the unchirped pulses scaled by the ratio of the unchirped bandwidth to the chirped bandwidth (see text). The dotted curve U' is for a pulse shorter by a factor of 48.

we multiply by the chirp repetition rate f: $R_J(I) = N_{mol,J} * f$. Next, we spatially average over the Gaussian density distribution in the trap (average $1/e^2$ radius = 156 μm) and the Gaussian intensity profile of the photoassociation laser (average $1/e^2$ radius = 119 μm). Following [79], we find the overall formation rate at peak intensity I_0 by summing over all partial waves necessary for convergence: $R(I_0) = \sum_{J=0}^{5}(2J+1)R_J(I_0)$.

In Fig. 4.12 we plot these simulated Rb_2 formation rates vs. peak intensity for various chirped pulses. The values shown are derived from the total number of molecules in $a\ ^3\Sigma_u^+$ (v"= 0-39) at t=200 ns after the beginning of the chirp. More than 93% of those molecules reside in v"=37-39 and are thus within the REMPI

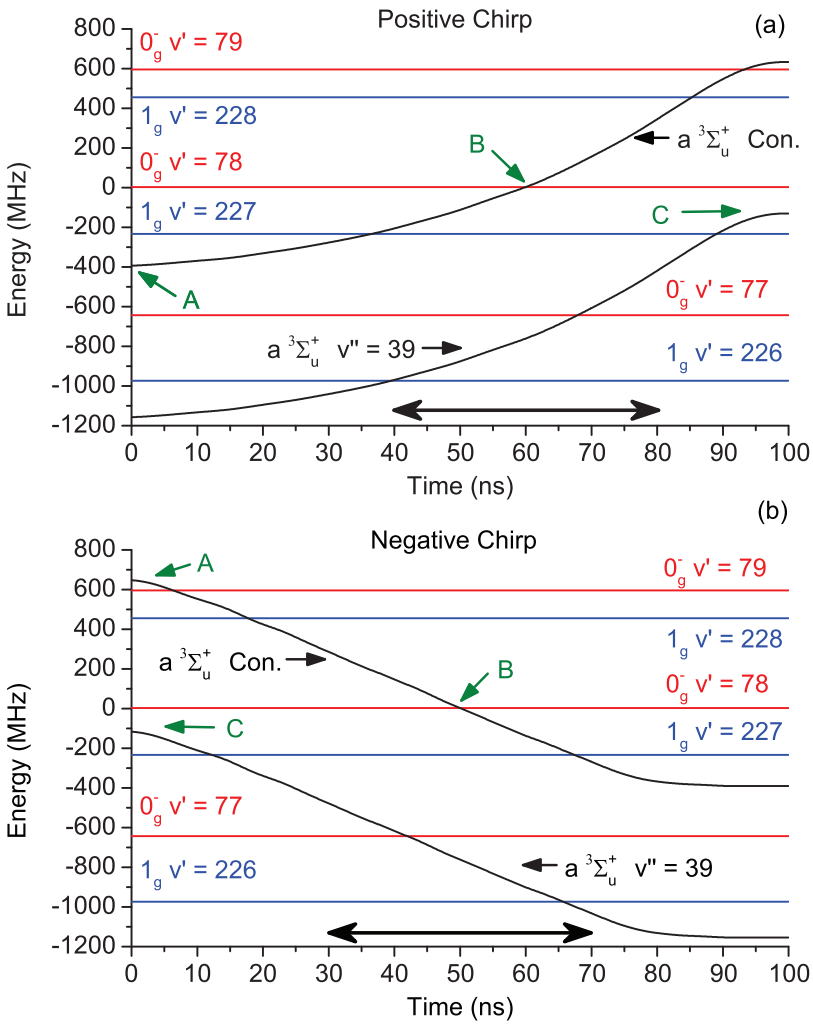

Figure 4.13. Quantum Mechanical Simulations: Dressed-state Picture

Evolution of the molecular levels during the positive (a) and negative (b) chirps. Horizontal lines are the relative energies of the vibrational levels of the excited 0_g^- and 1_g molecular states, while the energies of the $a\ ^3\Sigma_u^+$ zero-energy continuum and the v"= 39 level, with the energy of the chirped photon added, are represented by the upper and lower black curves, respectively. In this picture, a curve crossing indicates resonance with the corresponding transition. Ground-excited couplings are not included in these plots. Double-ended arrows indicate the pulse widths (FWHM). The point labeled A is the initial continuum state, B indicates resonance with the 0_g^- (v'=78) level, and C indicates the approach to resonance with the transition 0_g^- (v'=78) $\rightarrow$ $a\ ^3\Sigma_u^+$ (v"=39).

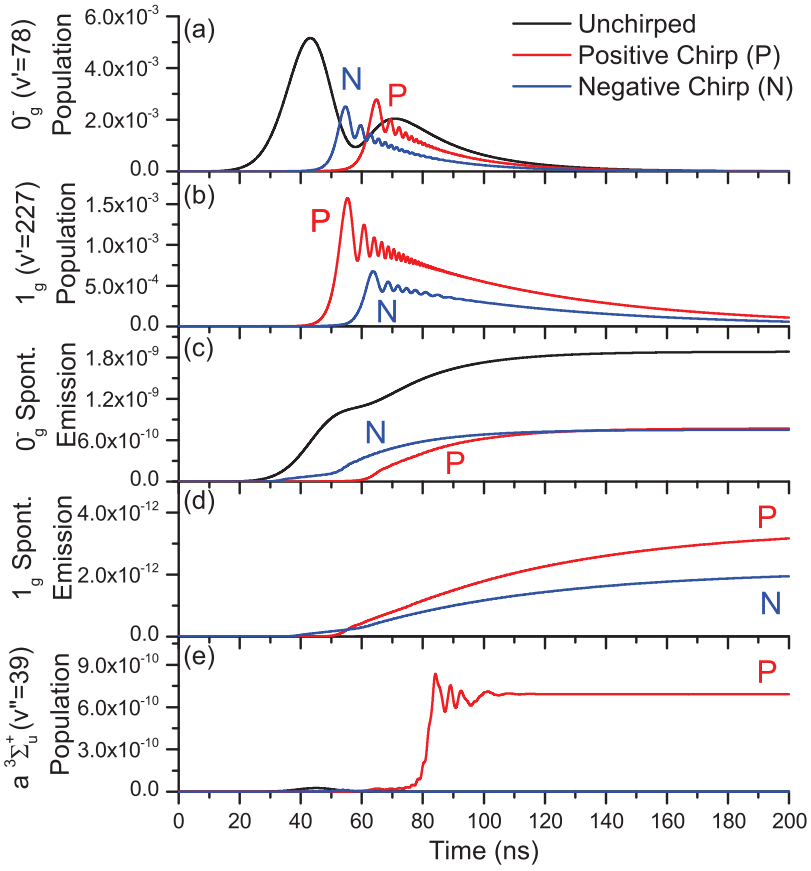

Figure 4.14. Quantum Mechanical Simulations: Time Evolution

Populations of various molecular states during the unchirped, positively, and negatively chirped pulses for $I_0 = 89.3$ W/cm^2: (a) 0_g^- (v'=78); (b) 1_g (v'=227); (c) $a\ ^3\Sigma_u^+$ bound levels populated by spontaneous emission (SE) from 0_g^-; (d) $a\ ^3\Sigma_u^+$ bound levels populated by SE from 1_g; (e) $a\ ^3\Sigma_u^+$ (v"=39) resulting from stimulated emission from 0_g^- (v'=78). Note that in (e), only the positive chirp has a significant contribution.

bandwidth. The highest level, v"=40, is excluded because it is bound by only 39 MHz and therefore easily photodissociated by the chirped light. Also, its large outer turning point inhibits detection at our REMPI wavelength. The duration of the chirp is only 100 ns, but we allow spontaneous emission to run its course. Comparing to the experimental results in Fig. 4.11(b), we see good overall agreement, especially for the dependence on chirp: the rate for positive chirps exceeds that for negative chirps, but is less than that for unchirped pulses.

Comparing chirped and unchirped results is problematic because the pulses have different bandwidths. Ultrafast pulse shaping in the frequency domain [115] leaves the frequency bandwidth fixed while stretching the pulse in time. In contrast, our addition of chirp in the time domain maintains the 40 ns FWHM pulse, but increases the bandwidth (FWHM) from the transform limit of 11 MHz to 524 MHz. In the simulations, we vary the center detuning of the unchirped pulse, with the peak intensity fixed at 89.3 W/cm^2, and find a 22 MHz FWHM when plotting formation rate vs. detuning. Doing the same in the experiment, we find a bandwidth of 79 MHz. The limits of the shaded region of Fig. 4.12 indicate scalings of the unchirped results (curve U) by the ratio of each of these bandwidths to the chirped bandwidth of 524 MHz. This scaling allows a comparison at the same intensity per unit bandwidth. From this point of view, both the negative and positive chirps are more efficient than unchirped pulses. For completeness, we have also used a much shorter 0.84 ns FWHM unchirped pulse, increasing the peak intensity to keep the pulse energy fixed. This transform limit is 524 MHz, the same as for the 40 ns chirped pulses, but its simulated molecular formation rate (curve U' in Fig. 4.12) is lower. This is again consistent with higher efficiency for chirped PA at a fixed intensity per unit bandwidth.

The main conclusion from Figs. 4.11(b) and 4.12 is that the positive chirp gives a higher production rate than the negative chirp. By examining the evolutions of the

various populations, we have identified the mechanism responsible for this difference. In Fig. 4.13, we show the relative energies of the excited levels involved in the chirp. We also show the $a\ ^3\Sigma_u^+$ zero-energy continuum and v"=39 level, with the photon energy added. For clarity, the v"=40 level, bound by only 39 MHz, is not shown. These time dependent energies reflect the frequency variations of the chirps: positive in (a) and negative in (b). Curve crossings represent resonances with transitions between the corresponding states. For example, at point B in Fig. 4.13(a), the chirp is resonant with the PA transition from the zero-energy continuum to 0_g^- (v'=78).

In Fig. 4.14, we plot the time-dependent populations of various excited and $a\ ^3\Sigma_u^+$ states. Figs. 4.14(a) and 4.14(b) show the populations of the two dominant excited states, 0_g^- (v'=78) and 1_g (v'=227), respectively. As expected, the time ordering of population transfer to these states reverses with chirp direction. The unchirped pulse excites only to 0_g^- (v'=78) since it is never resonant with 1_g (v'=227). The excited-state populations eventually decay due to spontaneous emission. As shown in Figs. 4.14(c) and 44.14(d), a small fraction of these decays populates $a\ ^3\Sigma_u^+$ high-v" levels, with 0_g^- dominating due to better FCFs. Interestingly, as shown in Fig. 4.14(e), there is another contribution to v"=39, but only for the positive chirp. Referring back to Fig. 4.13(a), we see that at point C, resonance between 0_g^- (v'=78) and $a\ ^3\Sigma_u^+$ (v"=39) is approached and 0_g^- (v'=78) population is stimulated *down* to $a\ ^3\Sigma_u^+$ (v"=39). In contrast, for the negative chirp (Fig. 4.13(b)), C occurs near the beginning of the chirp, when there is no excited population to be stimulated down. The time ordering of these resonances is crucial to the population transfer and breaks the symmetry between positive and negative chirps. If we omit this coherent contribution to the formation rate for the positive chirp, we obtain curve P' in Fig. 4.12, demonstrating that this contribution is responsible for the majority of the difference between positive and negative chirps. The remaining difference is due to

the shape variation between positive and negative chirps (Fig. 4.13). We have verified in the simulations that symmetric linear positive and negative chirps give identical results when this coherent contribution is omitted. This coherent contribution would be even larger if spontaneous emission did not deplete the excited-state population before the stimulated emission occurs.

4.3.4 Conclusions

In summary, we have investigated the formation of ultracold molecules using frequency-chirped light on the nanosecond timescale. We see a significant enhancement for the positive chirp relative to the negative chirp in both the experimental data and the quantum simulations. The evolutions of the various state populations reveal the mechanism responsible: photoassociation followed by stimulated emission into a high-vibrational level of $a\ ^3\Sigma_u^+$. Although we observed a similar trend ($\beta_{pos} > \beta_{neg}$) in the rate constant β for trap-loss collisions induced by chirped light [44, 80, 106], the mechanism here is quite different. The collisional work utilized smaller detunings and thus longer-range excitation, so the time scale of the chirp and the atomic motion were better matched. In the present work, the excited-state vibrational period is $\sim$1.7 ns, much shorter than the chirped pulses. Going to faster timescales and higher intensities, together with controlling the details of the chirped pulses [67], should allow further optimization of the molecular formation.

4.3.5 Unchirped Pulse Bandwidth Measurement

Since comparing the chirped and unchirped results directly is problematical due to their different bandwidths, scaling the molecular formation simulation results for the unchirped pulse by the ratio of the unchirped bandwidth to the chirped bandwidth, as shown in figure 4.12, allows a comparison at the same intensity per unit bandwidth. We conduct a probe scan (section 3.4.2) under similar experimental conditions as

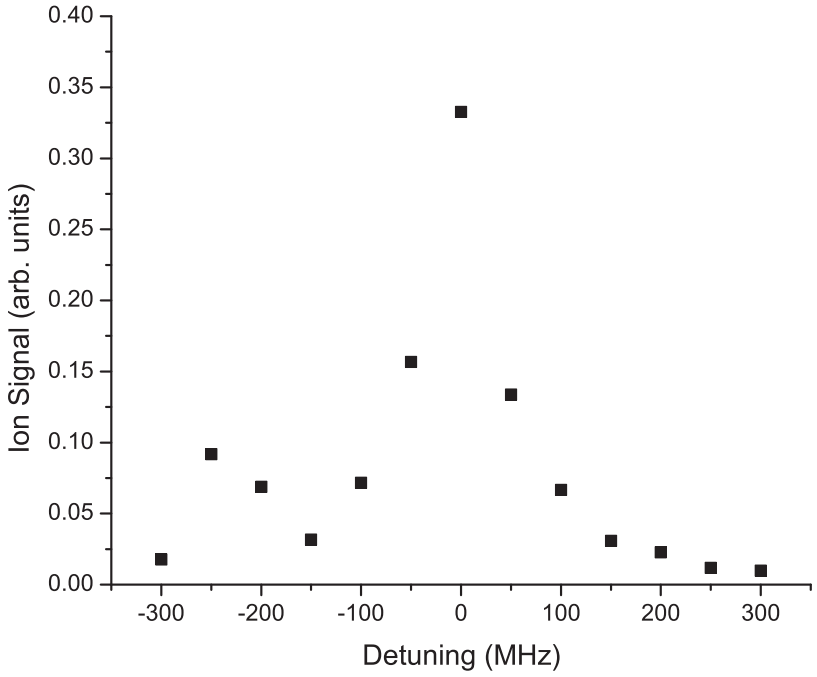

Figure 4.15. Unchirped Pulse Bandwidth Measurement

Probe scan to determine the unchirped pulse bandwidth. A Lorentzian fit of the data yields a bandwidth of 79 MHz. The small peak at $\sim$ -250 MHz is likely 1_g (v'=227).

described in section 4.3.2 and reference [62]. During the scan, we vary the center detuning of the PA laser with a detuning of 0 MHz corresponding to 0_g^- (v'=78), located 7.79 GHz below the $5S_{1/2}(F = 2) + 5P_{3/2}(F' = 3)$ asymptote. The resulting molecular signal, after subtracting the MOT background signal, is shown as a function of the center detuning in figure 4.15. A Lorentzian fit of the data yields a FWHM bandwidth of 79 MHz, significantly less than the 525 MHz bandwidth of the chirped pulses, and somewhat more than the transform limit of 11 MHz.

4.3.6 Photodestruction

In the experiments, we typically use a sequence of chirped pulses. Therefore, it is important to also consider the photodestruction of molecules by a subsequent pulse.

Starting $a\ ^3\Sigma_u^+$ Vibrational Level	Photodestruction from 1 Pulse		
	Unchirped	1 GHz Positive Linear	1 GHz Negative Linear
38	9.59E-08	4.20E-06	4.23E-06
39	4.08E-07	8.11E-06	8.11E-06
40	8.44E-04	1.50E-03	1.50E-03

Table 4.8. Photodestruction probability from various 100 ns chirps with an intensity FWHM of 40 ns and a peak intensity of 100 W/cm^2.

Photodestruction resulting from a single unchirped pulse, 1 GHz positive linear chirp, or 1 GHz negative linear chirp are included.

Experimentally being able to simultaneously optimize the formation and minimize this destruction would produce the most molecules.

We model the photodestruction by starting the simulations with all of the population in one of the bound vibrational levels of the $a\ ^3\Sigma_u^+$. We propagate through time applying the same chirps as before. Since most of our stimulated population ends up in the $a\ ^3\Sigma_u^+$ v"=39 state, we focus our investigation on $a\ ^3\Sigma_u^+$ v"=38 to 40. The results for a single chirp with an intensity FWHM of 40 ns and a peak intensity of 100 W/cm^2 are shown in table 4.8. Although these results are the photodestruction probability due to one chirp, by running the simulations for several chirps, we found that the photodestruction is cumulative. Extending this to the 5 MHz experimental repetition rate (section 4.3.2, references [45, 62]), we find comparable loss rates to those seen in that experiment. As we expected, all population from v"=40 is completely photodestroyed, while the losses from $a\ ^3\Sigma_u^+$ v"=38 and 39 are somewhat lower then the experimental loss rates (section 4.3.2, references [45, 62]). The linear chirps have significantly more photodestruction than the unchirped pulses. The range of frequencies (and thus vibrational levels) covered by the chirps allows for more avenues of photodestruction. Although we haven't examined the populations in detail, this photodestruction is presumably due to re-excitation of the ground-state molecules, followed by spontaneous emission back into the continuum. Doubling the

Starting $a\ ^3\Sigma_u^+$ Vibrational Level	Photodestruction from 1 Pulse		
	Unchirped	1 GHz Positive Linear	1 GHz Negative Linear
38	1.91E-07	8.40E-06	8.46E-06
39	8.20E-07	1.62E-05	1.62E-05
40	2.89E-03	2.67E-03	2.67E-03

Table 4.9. Photodestruction probabilities from various 100 ns chirps with an intensity FWHM of 40 ns and a peak intensity of 200 W/cm^2.

Photodestruction resulting from a single unchirped, 1 GHz positive linear chirp, or 1 GHz negative linear chirp are included.

peak intensity to 200 W/cm^2, the photodestruction roughly doubles, as shown in table 4.9. Again, the photodestruction from state $a\ ^3\Sigma_u^+$ v" = 40 is large enough that with the chirps repeating every 200 ns, all of the population ending up in this state is completely photodestroyed by subsequent pulses.

Based on the work in this section (section 4.3, reference [45]), we became interested in how the photodestruction would scale for faster chirps and chirps with ranges long enough to pass through the 0_g^- v'=78 $\rightarrow$ $a\ ^3\Sigma_u^+$(v"=39) resonance. The molecular formation rates for such chirps are shown in section 4.5, later in this chapter. As a first attempt, we look at 50 ns chirps with 20 ns FWHM intensity pulses. The chirp time and FWHM are reduced by a factor of two from those used in the experiment. The photodestruction for 100 and 200 W/cm^2 peak intensities for unchirped, 1 and 2 GHz positive linear chirps, and 1 and 2 GHz negative linear chirps are shown in table 4.10. Although this table shows the same trend of the photodestruction roughly doubling by increasing the peak intensity from 100 W/cm^2 to 200 W/cm^2, the overall photodestruction rate is reduced for the faster chirps by about a factor of two. This is not surprising since there is also a decrease in the formation rate for the same intensity. Increasing the chirp range from 1 GHz to 2 GHz does not dramatically affect the photodestruction rate, although as shown in section 4.5 this does significantly enhance the formation rate thereby increasing overall molecular

Photodestruction from 1 Pulse					
100 W/cm^2 Peak Intensity					
Starting $a\ ^3\Sigma_u^+$ Vibrational Level	Unchirped	Positive Linear		Negative Linear	
		1 GHz	2 GHz	1 GHz	2 GHz
38	4.81E-08	2.11E-06	3.54E-06	2.09E-06	3.53E-06
39	2.09E-07	4.05E-06	3.90E-06	4.06E-06	3.90E-06
40	9.52E-04	7.30E-04	6.78E-04	7.30E-04	6.77E-04
200 W/cm^2 Peak Intensity					
Starting $a\ ^3\Sigma_u^+$ Vibrational Level	Unchirped	Positive Linear		Negative Linear	
		1 GHz	2 GHz	1 GHz	2 GHz
38	9.59E-08	4.22E-06	7.08E-06	4.18E-06	7.07E-06
39	4.19E-07	8.11E-06	7.79E-06	8.14E-06	7.80E-06
40	2.81E-03	1.27E-03	1.22E-03	1.27E-03	1.22E-03

Table 4.10. Photodestruction probabilities from various 50 ns chirps with an intensity FWHM of 20 ns and peak intensities of 100 and 200 W/cm^2.

Photodestruction resulting from a single unchirped pulse, 1 or 2 GHz positive linear chirp, or 1 or 2 GHz negative linear chirp are included.

yield. Going even faster, to 28.75 ns chirps with 15 ns FWHM intensity pulses, shows a further reduction in the photodestruction rate, as shown in table 4.11. Again, increasing the peak intensity yields a proportional increase in the photodestruction and there is not a significant difference between the 1 GHz and 2 GHz chirps. Lastly, we investigate photodestruction from 37.5 ns chirps with 15 ns FWHM intensity pulses. The parameters used for the experimental results are described in Chapter 5. The photodestruction for 100 and 200 W/cm^2 peak intensities for unchirped, positive linear, positive concave-down, positive shaped, and negative linear chirps are shown in table 4.12. These chirps show similar trends as before. The photodestruction roughly doubles by doubling the peak intensity. For both peak intensities, the chirps have more photodestruction than the unchirped pulse. Both of the positive shaped chirps have the most photodestruction overall. Minimizing these photodestruction rates while maximizing the formation rates would yield the most molecules.

Photodestruction from 1 Pulse					
100 W/cm^2 Peak Intensity					
Starting $a\ ^3\Sigma_u^+$ Vibrational Level	Unchirped	Positive Linear		Negative Linear	
		1 GHz	2 GHz	1 GHz	2 GHz
38	3.65E-08	2.31E-06	2.68E-06	2.17E-06	2.67E-06
39	1.62E-07	2.94E-06	2.92E-06	3.02E-06	2.91E-06
40	1.03E-03	5.21E-04	5.01E-04	5.32E-04	4.97E-04
200 W/cm^2 Peak Intensity					
Starting $a\ ^3\Sigma_u^+$ Vibrational Level	Unchirped	Positive Linear		Negative Linear	
		1 GHz	2 GHz	1 GHz	2 GHz
38	7.28E-08	4.63E-06	5.37E-06	4.35E-06	5.33E-06
39	3.25E-07	5.89E-06	5.83E-06	6.05E-06	5.81E-06
40	2.57E-03	9.35E-04	9.05E-04	9.54E-04	8.97E-04

Table 4.11. Photodestruction probabilities from various 28.75 ns chirps with an intensity FWHM of 15 ns and peak intensities of 100 and 200 W/cm^2.

Photodestruction resulting from a single unchirped pulse, 1 or 2 GHz positive linear chirp, or 1 or 2 GHz negative linear chirp are included.

Photodestruction from 1 Pulse					
100 W/cm^2					
Starting $a\ ^3\Sigma_u^+$ Vibrational Level	Unchirped	Positive			Negative
		Linear	Concave-down	Shaped	Linear
37	1.57E-08	1.38E-06	1.74E-06	9.17E-07	1.38E-06
38	3.64E-08	2.65E-06	2.07E-06	8.13E-07	2.63E-06
39	1.61E-07	2.91E-06	5.60E-06	5.95E-06	2.93E-06
40	9.99E-04	5.09E-04	4.33E-04	1.87E-04	5.10E-04
200 W/cm^2					
Starting $a\ ^3\Sigma_u^+$ Vibrational Level	Unchirped	Positive			Negative
		Linear	Concave-down	Shaped	Linear
37	3.10E-08	2.76E-06	3.47E-06	1.83E-06	2.75E-06
38	7.24E-08	5.30E-06	4.14E-06	1.63E-06	5.27E-06
39	3.23E-07	5.82E-06	1.12E-05	1.19E-05	5.86E-06
40	2.51E-03	9.18E-04	7.71E-04	3.46E-04	9.18E-04

Table 4.12. Photodestruction probabilities from various 37.5 ns chirps with an intensity FWHM of 15 ns and peak intensities of 100 and 200 W/cm^2.

Photodestruction resulting from a single unchirped pulse, positive linear chirp, positive concave-down, positive shaped, or negative linear chirp are included.

4.4 Enhancement of Ultracold Molecule Formation by Local Control in the Nanosecond Regime*

4.4.1 Introduction

Following in the footsteps of ultracold atoms, molecules at ultralow energies have generated significant excitement in recent years [8]. Applications in precision spectroscopy, quantum information processing, many-body dipolar systems, as well as investigations of chemistry at ultracold temperatures, all stand to benefit from enhanced production efficiency and improved manipulation of ultracold molecules. There are two general methods for their production: reducing the temperature of already-existing molecules; or assembling the molecules from their precooled constituent atoms. In the latter case, ultracold photoassociation (PA) [86–89] is an important example. Here, two ultracold atoms collide in the presence of laser light tuned to excite from the low-energy continuum to a bound excited state of the diatomic molecule. The atom pair undergoes a free-to-bound transition and the resulting excited molecule can subsequently decay, via incoherent spontaneous emission, into a bound level of the ground state. Since this decay is not controlled, and typically populates the states of interest with low probability, there is interest in employing the techniques of quantum control in order to increase the efficiency of photoassociative molecule formation [35].

Quantum control [116, 117] is based on employing interfering pathways to enhance an objective such as molecular formation. This type of control has been suggested as a means of manipulating ultracold collisions to enhance PA yield [18, 79, 90–97, 99, 100, 118], stabilizing the final bound-state populations [119], and enhancing the amplitude at short internuclear distances prior to the PA step [98]. Another

*Text and figures reprinted with permission from [46]. Copyright 2015 Institute of Physics.

control objective has been to cool or concentrate molecular vibrations into a single state [120]. Experimental attempts to apply ultrafast control to the formation of ultracold molecules have so far been unsuccessful, although destruction of already existing molecules with shaped pulses has been realized [36, 37]. This lack of success is likely due to the mismatch between the timescales of the molecular system and the applied field.

The global objective of control is achieved theoretically by an iterative process, which is implemented by solving optimal control theory (OCT) equations. Local control [121–125] (LC) is a simpler unidirectional and non-iterative time propagation scheme which adjusts the field at each instant of time in order to optimize the target at the next time step. The success of LC depends crucially on the choice of the local objective. Therefore, in some cases, adjustment of the target throughout the evolution, based on knowledge of the system dynamics, can be advantageous. Normally, LC is realized via control of the amplitude. However, in order to emulate experimental capabilities, in the present work, we fix the pulse amplitude and utilize control of the phase.

To date, most of the calculational efforts involving the application of quantum control to ultracold molecule formation have involved ultrafast time scales and deeply-bound vibrational levels [35]. In contrast, we recently explored, both experimentally and theoretically, the production of ultracold molecules on slower time scales and in high vibrational levels [45]. Using 40 ns pulses of frequency-chirped light, we found evidence for coherent effects, specifically a significant dependence on the direction of the linear chirp. In the present paper, we extend our previous quantum calculations to somewhat faster time scales, and more importantly, incorporate local control of the phase in order to optimize the formation of ground-state molecules. We find that this type of quantum control, either with one frequency or two simultaneous frequencies,

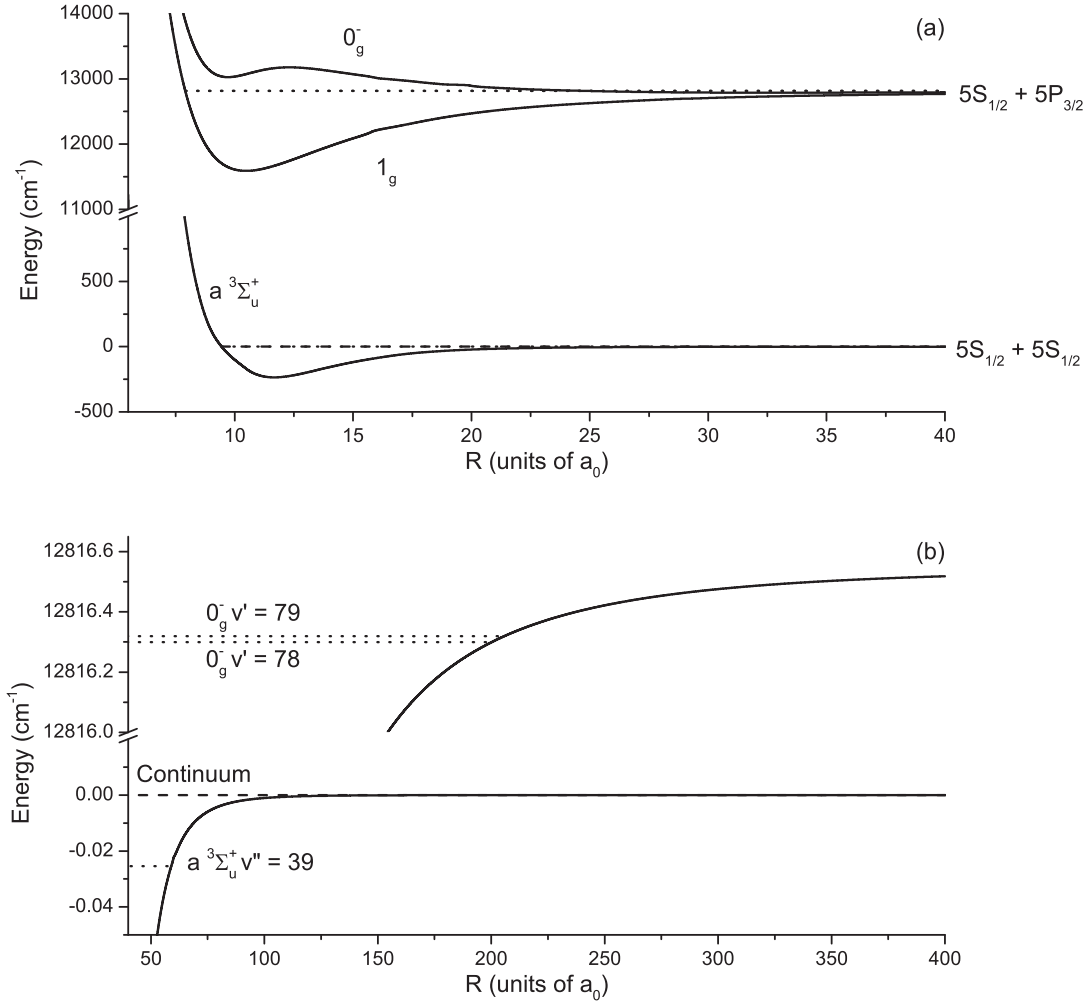

Figure 4.16. Energy Levels

Energy levels considered in the present work. Note differences in scales for ground and excited states. (a) Relevant molecular potentials included in the simulations. Note that that pure-long-range well of the 0_g^- state at R = 33 a_0 is barely visible. (b) Expanded view of the four most important levels: the initial free-atom ground-state continuum (dashed line); the $a\ ^3\Sigma_u^+$ (v"=39) final target state, bound by 764 MHz; and the 0_g^- (v'=78 and 79) intermediate excited states, located 7.79 GHz and 7.20 GHz, respectively, below the $5s_{1/2}$(F=2)+$5p_{3/2}$(F'=3) asymptote.

can indeed enhance the molecular production. The experimental realization of these controlled pulses should be possible.

The system we examine here is that utilized in our recent experiments [45] and shown in Fig. 4.16: photoassociative production of $^{87}Rb_2$ in the v'=78 and v'=79 vibrational levels of the 0_g^- state just below the $5s_{1/2}$+$5p_{3/2}$ asymptote. These states give efficient PA [110] since their outer turning points are at long range. The target state, which is ultimately detected, is the barely-bound v"=39 level of the $a\ ^3\Sigma_u^+$ lowest-lying triplet potential. In the recent experiments, we found evidence for coherent effects. The calculations showed that stimulated emission from the excited state to the target state, occurring later in the positive chirp, was responsible for the majority of the difference in molecular formation rates when using positive vs. negative chirps. In the present paper, we use 15 ns pulses and numerically explore a variety of time-dependent frequencies (or phases) of the laser field.

The paper is organized as follows. In Section 4.4.2, we provide more details on the system and its parameters, discuss the calculational techniques, and briefly describe local control theory and its use in controlling the phase. In Section 4.4.3, we present results of the simulations, including a comparison of one frequency and two simultaneous frequencies, as well as a discussion of interference effects. Section 4.4.4 comprises concluding remarks.

4.4.2 Theoretical Model with Local Control of the Phase

The model of the PA process is taken to be similar to ref. [45]. The ground $a^3\Sigma_u^+$ triplet state and the two 0_g^- and 1_g excited electronic states are considered according to [110] and denoted by $j = g, e_0$, and e_1, respectively. The dressed state Hamiltonian that includes the nuclear and electronic degrees of freedom is given by:

$$\hat{H} = \hat{H}_0 + \hat{H}_\epsilon = \begin{pmatrix} \hat{H}_g & 0 & 0 \\ 0 & \hat{H}_{e_0} & 0 \\ 0 & 0 & \hat{H}_{e_1} \end{pmatrix} + \begin{pmatrix} 0 & \hbar\hat{\Omega}_0(t) & \hbar\hat{\Omega}_1(t) \\ \hbar\hat{\Omega}_0^*(t) & 0 & 0 \\ \hbar\hat{\Omega}_1^*(t) & 0 & 0 \end{pmatrix}. \tag{4.24}$$

Here $\hat{H}_j$ is the field-free Hamiltonian for the electronic state j, the coupling between the states is given by the Rabi frequency $\hat{\Omega}_j = \mu_{gj}\epsilon(t)$, μ_{gj} are the transition dipole matrix elements between vibrational states including the Franck-Condon overlap, and $\epsilon(t)$ is the time dependent electric field:

$$\epsilon(t) = \epsilon_0 e^{[-\frac{(t-t_{center})^2}{2\sigma^2} + i\widetilde{\omega}(t)(t-t_{center})]} \tag{4.25}$$

where ϵ_0 is the peak electric field, t_{center} is the center time of the pulse, σ is the pulse temporal width, and $\widetilde{\omega}$ is the instantaneous frequency offset. As described in ref. [45], the basis sets used in the time-dependent calculations are obtained by diagonalizing the Hamiltonian on a mapped Fourier grid [72]. They span bandwidths of $\sim$ 15 GHz for the 0_g^- state (v' = 67 to 87), $\sim$ 15 GHz for the 1_g state (v' = 217 to 239), 278 GHz for the $a\ ^3\Sigma_u^+$ bound-state manifold (v" = 30 to 40), and 16 MHz (0.77 mK) for the $a\ ^3\Sigma_u^+$ continuum. As in [45], we ignore the contributions from the $a\ ^3\Sigma_u^+$ (v"=40) level since it is bound by only 39 MHz and thus easily photodissociated by the chirped light. The sum over partial waves and accounting for the thermal ensemble at an assumed temperature of 150 μK are discussed in ref. [45]. Spontaneous decay is modeled [44, 45] by adding a sink channel for each decay path from the various excited-state (0_g^- and 1_g) vibrational levels into bound states or the continuum of $a\ ^3\Sigma_u^+$. These individual channel decay rates are determined by the excited-state lifetimes [77, 78], 26.2 ns for 0_g^- and 22.8 ns for 1_g, and the Franck-Condon factors. Although this sink-channel model precludes the possibility of multiple incoherent excitations during

the pulse, its use is justified because only a small fraction (10^{-4} for 0_g^-(v'=78)) of spontaneous decays populates the target state, and this occurs mainly after the pulse.

The goal of this work is to use the ability to modulate the instantaneous field frequency $\widetilde{\omega}(t)$ to optimize the formation of bound molecules in the ground state, without changing the amplitude. This usually corresponds to a projection operator into some desired bound state within the ground (target) electronic state.

Due to the narrow feasible bandwidth and limited response time of the experimental $\widetilde{\omega}$, the computed control field should have a relatively simple structure with a clear mechanism in order to make it experimentally acceptable. Moreover, the relatively heavy computational load for the simulation of the dynamics demands a noniterative method, and to this point the unidirectional local control (LC) method is used. Due to its simple structure, LC results in control fields that are more directly meaningful mechanistically and, as a result, also transferable into experimentally feasible pulses.

Within the LC approach, the goal is a maximization of a target operator $\hat{P}$, which usually corresponds to a projection operator into some desired state. The time dependence of the expectation value $\left\langle \hat{P} \right\rangle$ is given by:

$$\frac{d\langle \hat{P} \rangle}{dt} = \frac{1}{i\hbar}\langle [\hat{P}, \hat{H}] \rangle + \langle \frac{\partial \hat{P}}{\partial t} \rangle = \frac{i}{\hbar}\langle [\hat{H}_\epsilon, \hat{P}] \rangle_\Psi \tag{4.26}$$

where the fact that the target state is an eigenstate of $\hat{H}_0$ is used in the last relation. Note that targeting a time-dependent goal [112] could also be easily incorporated into LC by utilizing the third term in eq. 4.26. Inserting eq. 4.26 into eq. 4.24 gives:

$$\frac{d\langle \hat{P} \rangle}{dt} = -\frac{1}{2}\sum_k \Im \left\{ \hat{\Omega}_{kt} \left\langle \hat{P} \right\rangle_{gk} \right\} = -2\epsilon_0 e^{-\frac{(t-t_{center})^2}{2\sigma^2}} \sum_k \tilde{\mu}_{gk} B_k \sin(\varphi_k + \tilde{\omega}(t)(t - t_{center})) \tag{4.27}$$

where the index k denotes the intermediate level, $\hat{\Omega}_{kt}$ is its coupling to the target state, and $\left\langle \hat{P} \right\rangle_{gk} \equiv B_k \exp(i\varphi_k)$ is the matrix element of $\hat{P}$ over the initial ground state wave function and the state k. The goal of the control is therefore to adjust the temporal phase of the field $\tilde{\omega}(t)$ to maintain a monotonic increase of the projection into the target state. We note that a similar application of optimal control theory for the same goal with a given target time will give a similar condition to eq. 4.27. The difference would be that the matrix element $\left\langle \hat{P} \right\rangle_{gk}$ will be obtained between the initial ground state and the intermediate state which was obtained by backward propagation from the target state [124].

Note that the coupling structure (eq. 4.26), does not allow a direct dipole transition between the initial scattering state and the target state. Commonly in local control applications, this situation leads to erratic and less efficient fields, which could be remedied by significant seeding of the intermediate state in the early stages of the control. To achieve this, we add a seeding step into the control formalism. This is done by defining a switch for the target, which will coincide with the intermediate level(s) initially and will move gradually to the final target later in the pulse, as detailed in the next section.

4.4.3 Results

The interpretation, based on quantum calculations, of our recent experiments [45] on frequency-chirped molecular formation was that stimulated emission from the 0_g^-(v'=78) excited state to the $a\ ^3\Sigma_u^+$(v"=39) target state, occurring later in the positive chirp, enhanced the formation for this chirp direction. Several possibilities come to mind for further enhancement. Employing shorter pulses and faster chirps will reduce the effects of incoherent spontaneous emission of the 0_g^- state, whose radiative lifetime is 26.2 ns [77, 78]. We have incorporated this in the present calculations,

using 15 ns full-width-half-maximum (FWHM) Gaussian intensity pulses (vs. 40 ns in the recent experiments) and 28.75 ns linear chirps (vs. 100 ns). Also, for the linear chirp of 1 GHz in 100 ns utilized in the experiments, the frequency difference of 764 MHz between the absorption to the excited state and the stimulated emission to the target state meant that if the first step were resonant at the peak of the pulse, then the second step would occur at relatively low intensity. We have therefore expanded the nominal chirp range to 2 GHz to allow both steps to occur near the peak of the pulse. These parameters, 15 ns FWHM pulse and linear chirp of 2 GHz in 28.75 ns, are the benchmark we will use for comparison. Finally, and most importantly, we have removed the restriction of a single linear chirp and allowed for two frequencies as well as an arbitrary temporal variation of the phase (or frequency), with the formation ultimately optimized by local control.

As a first step in attempting to further improve the molecular formation rate, we simply add a second frequency which is chirped synchronously with the first, the idea being that beam 1 would provide the excitation and beam 2 the stimulated emission. Both frequencies are of equal intensity and are linearly chirped with a frequency offset between them of $\Delta/(2\pi)$. The chirp of beam 1 is timed so that it is resonant with the v'=78 level at the peak of the pulse. The results are shown in Fig. 4.17. Note that in calculating molecular formation rates, both here and in subsequent figures, we average over a two-dimensional Gaussian intensity distribution, since this would typically be the case in experiments. As in [45], we assume a Gaussian intensity distribution of the photoassociation laser (average $1/e^2$ radius = 119 μm) and a Gaussian atomic density distribution (average $1/e^2$ radius = 156 μm) with a peak value of $5\text{x}10^{10}$ cm^{-3}. The chirps repeat at a rate of 5 MHz. Although this situation exhibits interesting structure as a function of $\Delta/(2\pi)$, including peaks when $\Delta/(2\pi)$ approximately matches both the excited-state splitting (593 MHz) and the final-state binding energy (764 MHz),

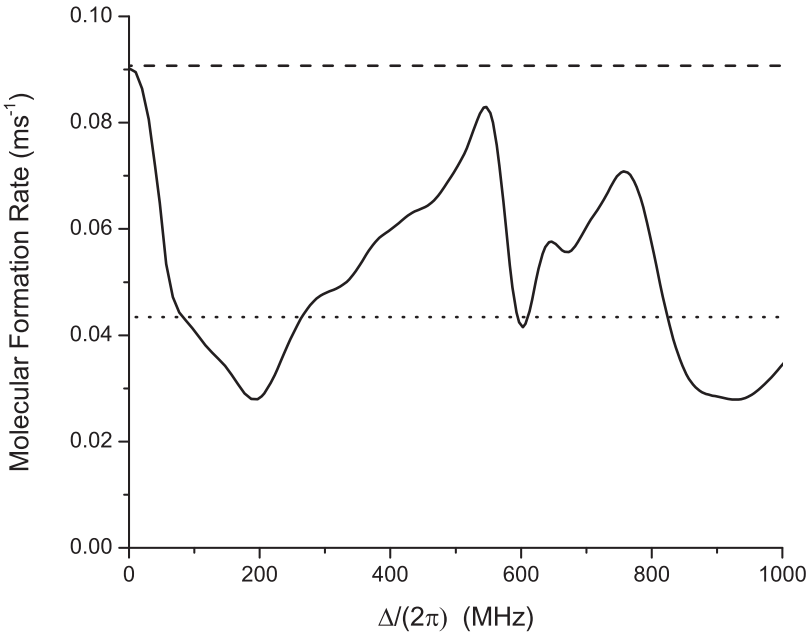

Figure 4.17. Molecular Formation Rate for Two Linearly-Chirped Beams

Molecular formation rate for two linearly-chirped beams (solid curve) vs. their frequency offset $\Delta/(2\pi)$. Each beam has a peak intensity I = 100 W/cm^2, yielding a total intensity of 200 W/cm^2. For comparison, the results for a single linearly-chirped beam with I = 100 W/cm^2 (dotted horizontal line) and 200 W/cm^2 (dashed horizontal line) are also shown.

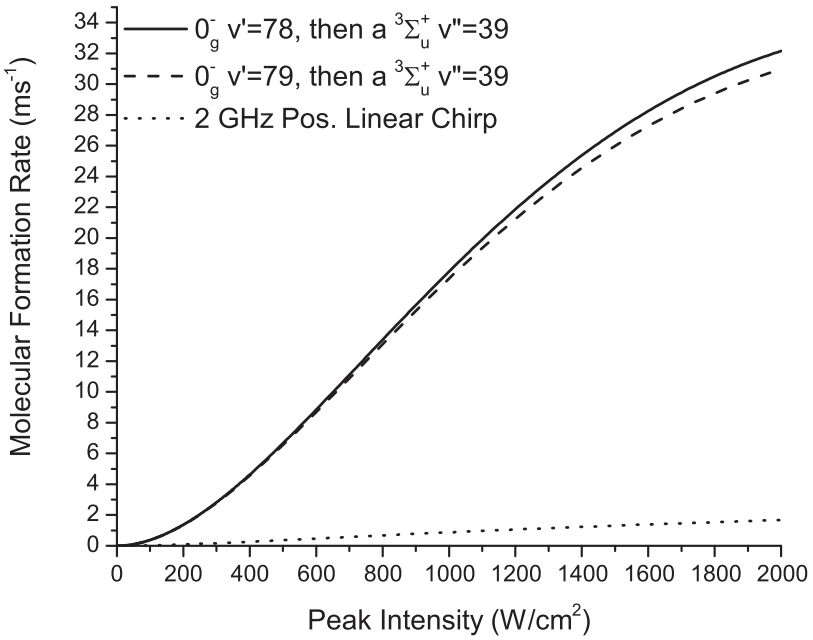

Figure 4.18. Molecular Formation Rate for a Single Beam Optimized by Local Control

Molecular formation rate for a single beam, optimized by local control, as a function of peak intensity. The solid curve is using v'=78 as the intermediate state, while the dashed curve is for v'=79. For comparison, the results for the linear chirp, 2 GHz in 28.75 ns, are shown as the dotted curve.

there is no enhancement relative to the single-beam case, when compared at the same total intensity (solid curve vs. dashed curve). On the other hand, if we start with beam 1 (dotted curve) and then add beam 2 (solid curve), thereby doubling the total intensity, we do see a significant enhancement for most values of $\Delta/(2\pi)$.

As a next step, we use a single beam, but incorporate local control of the phase vs. time in order to optimize the formation rate. This rate vs. intensity is shown in Fig. 4.18. Compared to the original linear chirp with a single frequency, local control results in a dramatic enhancement. The temporal variation of the frequency which yields the optimum formation is shown in Fig. 4.19. We note that in order to

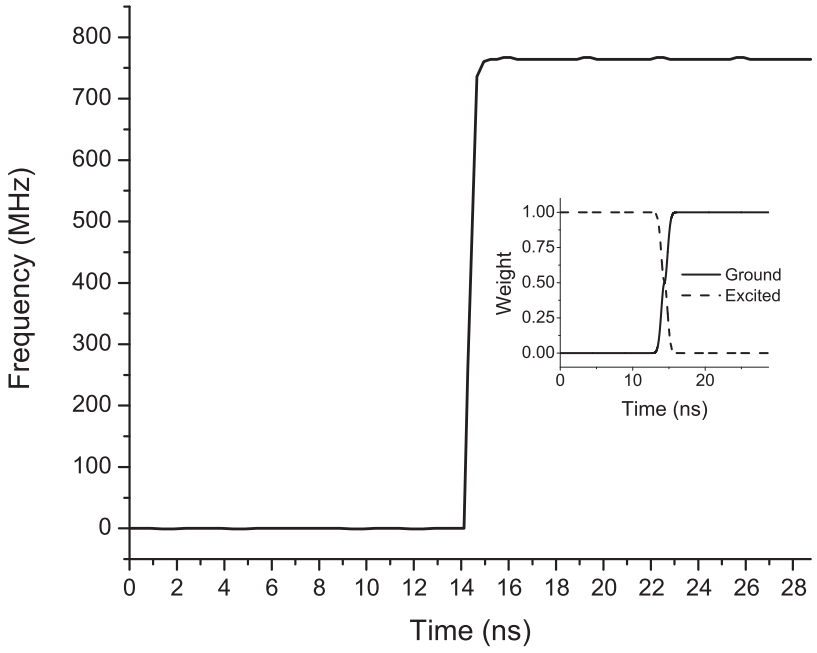

Figure 4.19. Local-Control-Optimized Frequency vs. Time

Solid curve: frequency vs. time, as optimized by local control, for the v'=78 results of Fig. 4.18. The intensity pulse, not shown, is a Gaussian with 15 ns FWHM, centered at 14.4 ns, with a peak intensity of 100 W/cm^2. Frequencies are relative to the transition from the zero-energy continuum to v'=78. The weighting function used for the local control (see text for details) is shown in the inset.

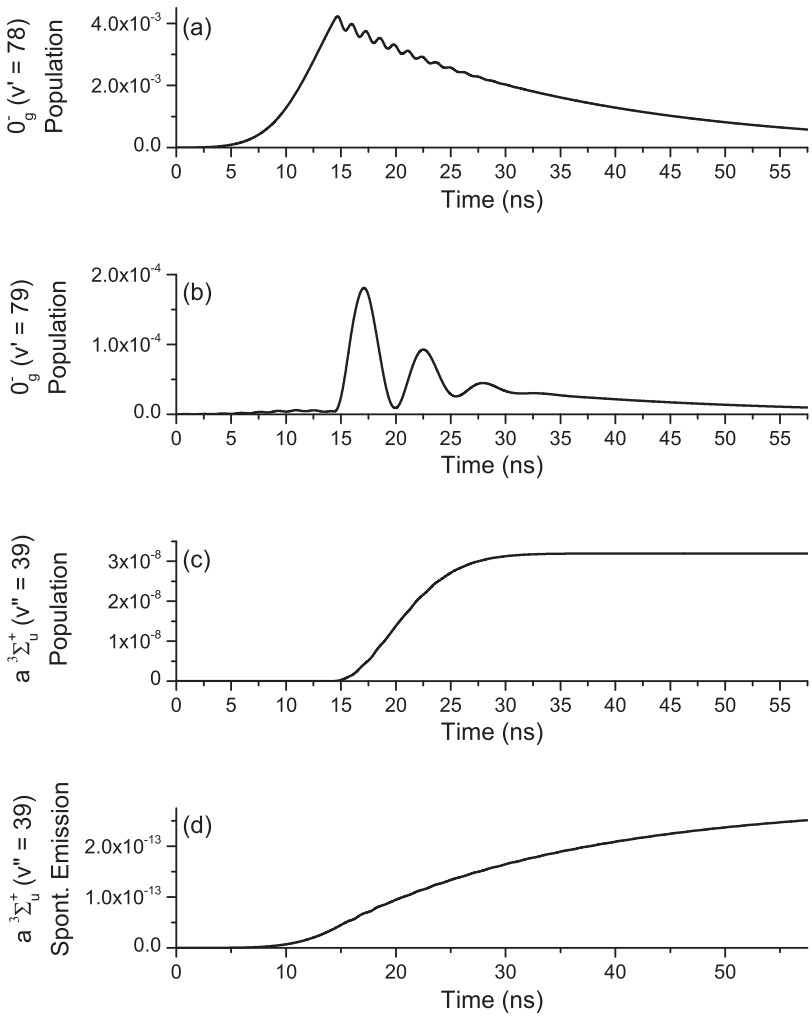

Figure 4.20. Population Evolution

State populations vs. time when the formation is optimized by local control using v'=78 as the intermediate state: (a) v'=78; (b) v'=79; (c) v"=39; (d) v"=39 due to spontaneous emission. The peak intensity is I = 100 W/cm^2 and the 15 ns FWHM pulse is centered at 14.4 ns. Not shown are populations of the 1_g excited states, which have a much smaller maximum of 2.74x10^{-5} in v'=228, and the population of the other bound ground-state levels from spontaneous emission, which approach a total of only 1.13x10^{-9} at long times.

converge, the control must be provided with some guidance. This is done by setting the initial frequency to resonantly excite either 0_g^-(v'=78) or 0_g^-(v'=79), and then optimizing production of the selected excited state during the first half of the pulse and optimizing production of the target state ($a\ ^3\Sigma_u^+$(v"=39)) during the second half. In the optimization algorithm, the weights of the intermediate (excited) state and the final (target) state in the optimization evolve smoothly during the pulse, as shown in the inset. The optimum step-function behavior for the frequency has a relatively simple interpretation: the frequency stays resonant with the excitation step until the peak of the pulse, optimizing the excited-state population, and then as the weighting shifts, the frequency jumps to the stimulated emission transition, optimizing the transfer. This expected behavior is confirmed in Fig. 4.20, where we plot the temporal evolution of the various populations when v'=78 is chosen as the intermediate state. Note that these population plots assume a well-defined (peak) intensity and the results are not averaged over intensity. During the first half of the pulse, the v'=78 population builds up, while during the second half, a small fraction of this population is stimulated down to v"=39. Most of the v'=78 population eventually spontaneously decays back into the continuum or into other v" levels. As seen in Fig. 4.20(d), the spontaneous emission contribution to v"=39 is very small. We note that v'=79 does acquire some population ($< 5\%$ of that in v'=78) when the frequency quickly passes through this resonance during its upward jump.

It is evident from Fig. 4.19 that local control optimizes the formation rate by an almost instantaneous jump in frequency. An interesting question, especially regarding experimental realization, is how instantaneous this jump needs to be. To address this, we replaced the local control with an analytic variation of the frequency to simulate a rounded step function:

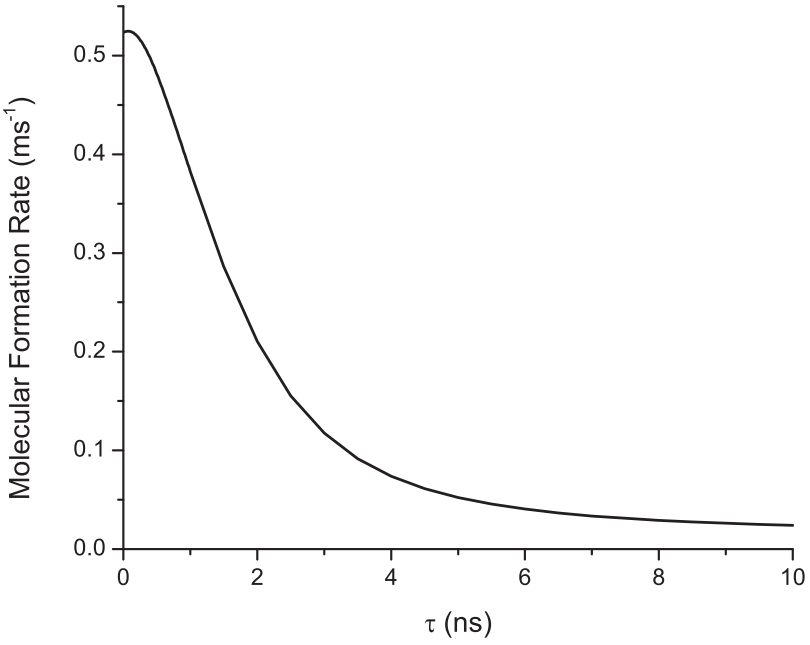

Figure 4.21. Molecular Formation Rate vs. Rounding Time

Molecular formation rate vs. rounding time τ of the frequency jump. Here the nearly instantaneous jump in frequency resulting from local control optimization is replaced by Eq. 4.28. The peak intensity is 100 W/cm^2 For comparison, the molecular formation rate optimized by local control (Fig. 4.18) is 0.573 (ms^{-1}) at this intensity.

$$f(t) = A * (1/2 + (1/\pi) * arctan[(t - t_{center})/\tau]) \tag{4.28}$$

The parameter A was chosen to match the jumps in phase and frequency emerging from the local control optimization. The formation rate vs. the rounding time τ of the frequency jump is shown in Fig. 4.21. The rate falls to 50% of its peak value for a rounding time of 1.64 ns, which should be experimentally achievable.

The sudden jump in frequency at the peak of the pulse corresponds to a sudden jump in the temporal derivative of the phase. In order to test for coherent effects, we modified the situation described above by simply adding a phase shift during the second half of the pulse. The results, shown in Fig. 4.22, confirm that there is indeed

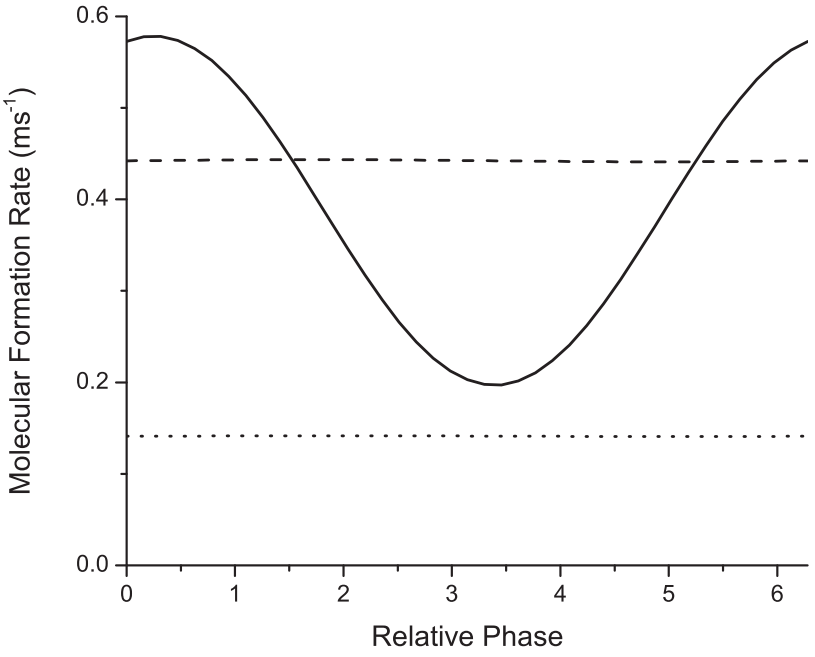

Figure 4.22. Molecular Formation Rate vs. Phase Shift

Molecular formation rate vs. phase shift added at the peak of the pulse. The formation rate was optimized by local control prior to shifting the phase. Results are shown for a peak intensity I = 100 W/cm^2. The dotted and dashed horizontal lines correspond to two unchirped frequencies at total peak intensities of 100 W/cm^2 and 200 W/cm^2, respectively. See text for details.

a strong dependence on this phase. The maximum at approximately zero phase shift is simply a consequence of the fact that the phase has already been optimized by the local control. Since the LC-optimized frequency variation (Fig. 4.19) is a jump between the upward transition and the downward transition, it is useful to compare these results with those obtained by simply having both resonant frequencies present throughout the pulse, as shown by the horizontal lines in Fig. 4.22. The lower (dotted) line is for the same total peak intensity (100 W/cm^2) as for the solid curve, split evenly between the two frequencies. The upper (dashed) line is for a peak intensity of 100 W/cm^2 for each frequency. Interestingly, in both cases, the pulse for which the frequency jumps optimally between the two values outperforms the pulse where both frequencies are continuously present. We have also calculated the formation rate when the two frequencies are applied as separate Gaussian pulses delayed by one pulse width (15 ns). For the intuitive pulse order, where the excitation from the continuum to v'=78 is applied before the stimulated emission from v'=78 to v"=39, we find a slight improvement relative to overlapping pulses (dashed and dotted lines in Fig. 4.22): 0.16 vs 0.14 for a total peak intensity of 100 W/cm^2; and 0.48 vs 0.44 for a total peak intensity of 200 W/cm^2. Using instead the counterintuitive pulse order, which corresponds to the case of STIRAP [126], the formation rate is reduced by approximately one order of magnitude. This is not surprising because STIRAP is an adiabatic process and here we are far from the adiabatic regime due to the combination of short pulse, low intensity, and relatively weak free-to-bound and bound-to-bound transitions.

Encouraged by both the enhancement provided by guided local control (see Fig. 4.19 inset), and the evidence for coherence seen in the dependence on phase shift, we investigated the possibility of further enhancement by taking advantage of two intermediate states. To do this, we set the initial frequency to be midway between

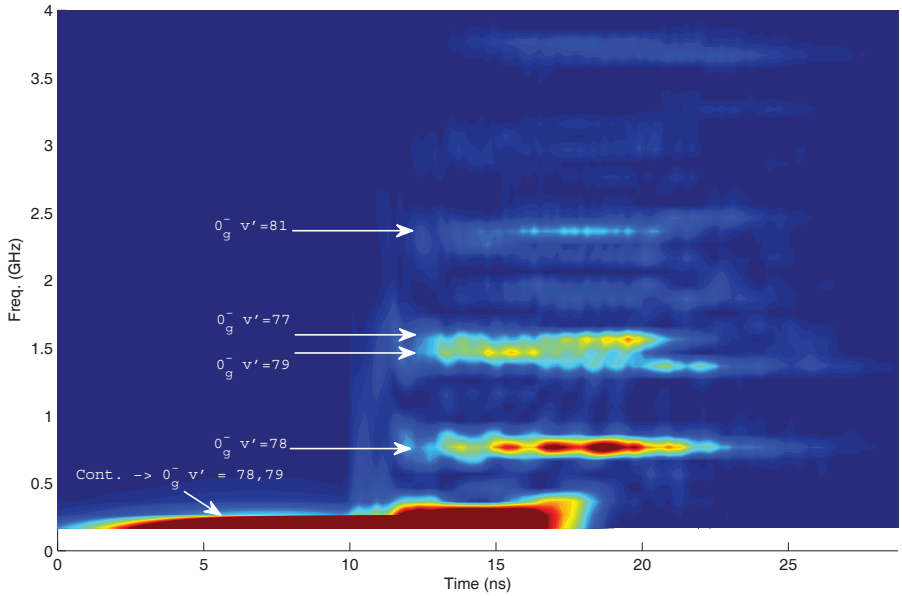

Figure 4.23. Sliding Window FFT

Sliding-window FFT of the Gaussian pulse with the optimizing phase pattern resulting from local control with two intermediate states. The width of the sliding window is 15 ns and the 15 ns FWHM intensity pulse is centered at 14.4 ns. Only absolute values of relative frequency are shown, with zero frequency corresponding to the initial frequency. This is located midway between the transitions from the continuum to 0_g^- (v'=78 and 79), which are separated by 593 MHz. Various 0_g^- (v') $\rightarrow$ *a* $^3\Sigma_u^+$(v"=39) downward transition frequencies are indicated with horizontal arrows, while the upward transitions from the continuum to v'=78 and 79 are located within the bright band below 300 MHz.

the v'=78 and v'=79 intermediate states and use local control to optimize the v'=78 population. Note that because a one-photon transition is not sensitive to phase, the detuning remains at its initial value during this initial time interval. Near the peak of the pulse, we then switch to optimizing the v"=39 target state. The weighting is the same as that in the insert to Fig. 4.19. The result is an improved target state population, $5.60\text{x}10^{-8}$, compared to the value of $3.20\text{x}10^{-8}$ obtained with a single intermediate state (Fig. 4.20(c)) at the same intensity of 100 W/cm^2. Interestingly, this enhancement is accomplished while significantly suppressing the intermediate state populations by being off-resonant, $1.98\text{x}10^{-4}$ in v'=78 and $1.99\text{x}10^{-4}$ in v'=79, compared to the value of $4.23\text{x}10^{-3}$ in the resonant single-intermediate-state case (Fig. 4.20(a)). However, the optimizing phase pattern is very complicated, exhibiting instantaneous rates of change of frequency up to ∼100 GHz/ns. We show in Fig. 4.23 a false-color plot of a sliding-window fast Fourier transform (FFT) of the resulting pulse. The various frequencies present in the FFT correspond to transitions in the system, as indicated by the arrows. It is seen that multiple intermediate states are populated as a consequence of the rapid phase variations. This less obvious optimization shows the power of local control. However, such a complicated phase variation does not allow a simple interpretation, and more importantly, is not experimentally feasible due to the rapid phase variations and the dependence of the details on intensity.

As a final step, we combine the two-frequency scheme and guided local control, aiming to take advantage of quantum interference between paths. As described above and displayed in Figs. 4.18, 4.19, and 4.20, we use local control to optimize the molecular formation, going through the v'=78 excited state. We then do the same but going through the v'=79 excited state. The optimizing frequency vs. time for these two cases are essentially the same except for a constant offset corresponding to the frequency difference between v'=79 and v'=78. We then combine these two

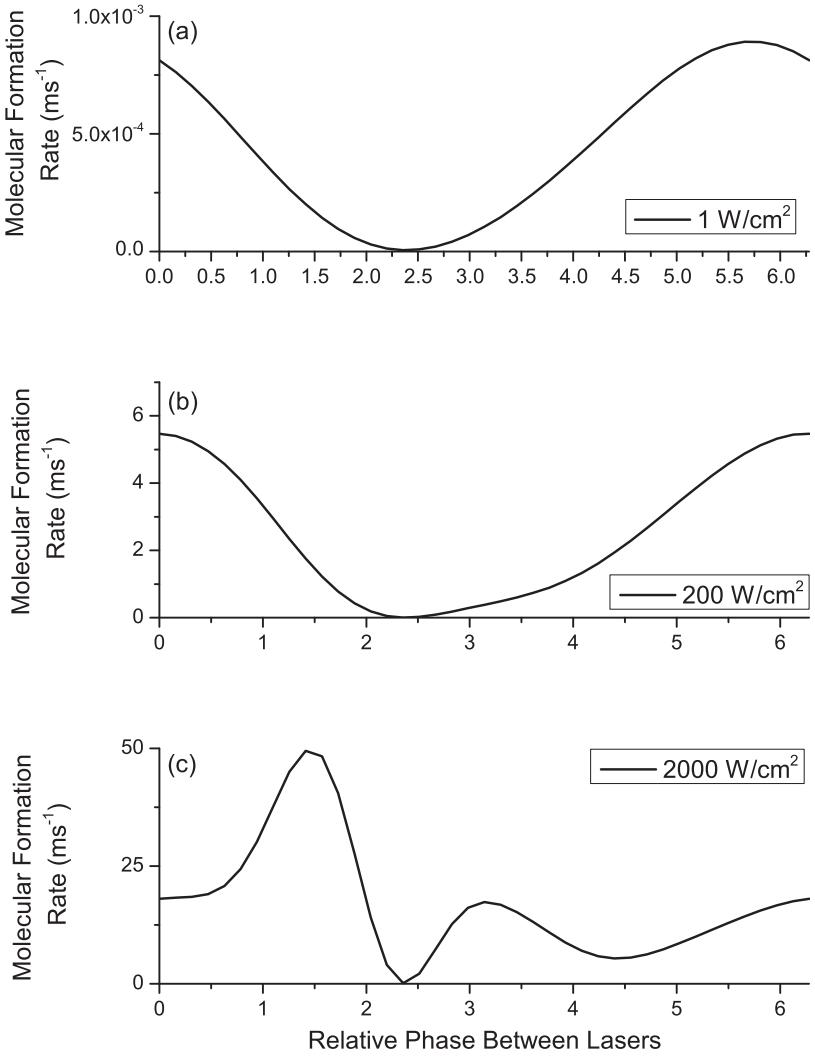

Figure 4.24. Two-Frequency Molecular Formation Rates

Molecular formation rate for the case of two frequencies, initially tuned to the v'=78 and v'=79 excited states, where the temporal evolutions have been separately optimized by local control. Plotted is the formation rate when these two fields, with an added relative phase, are simultaneously applied. Results are shown for several total peak intensities: (a) I = 1 W/cm^2; (b) I = 200 W/cm^2; (c) I = 2000 W/cm^2.

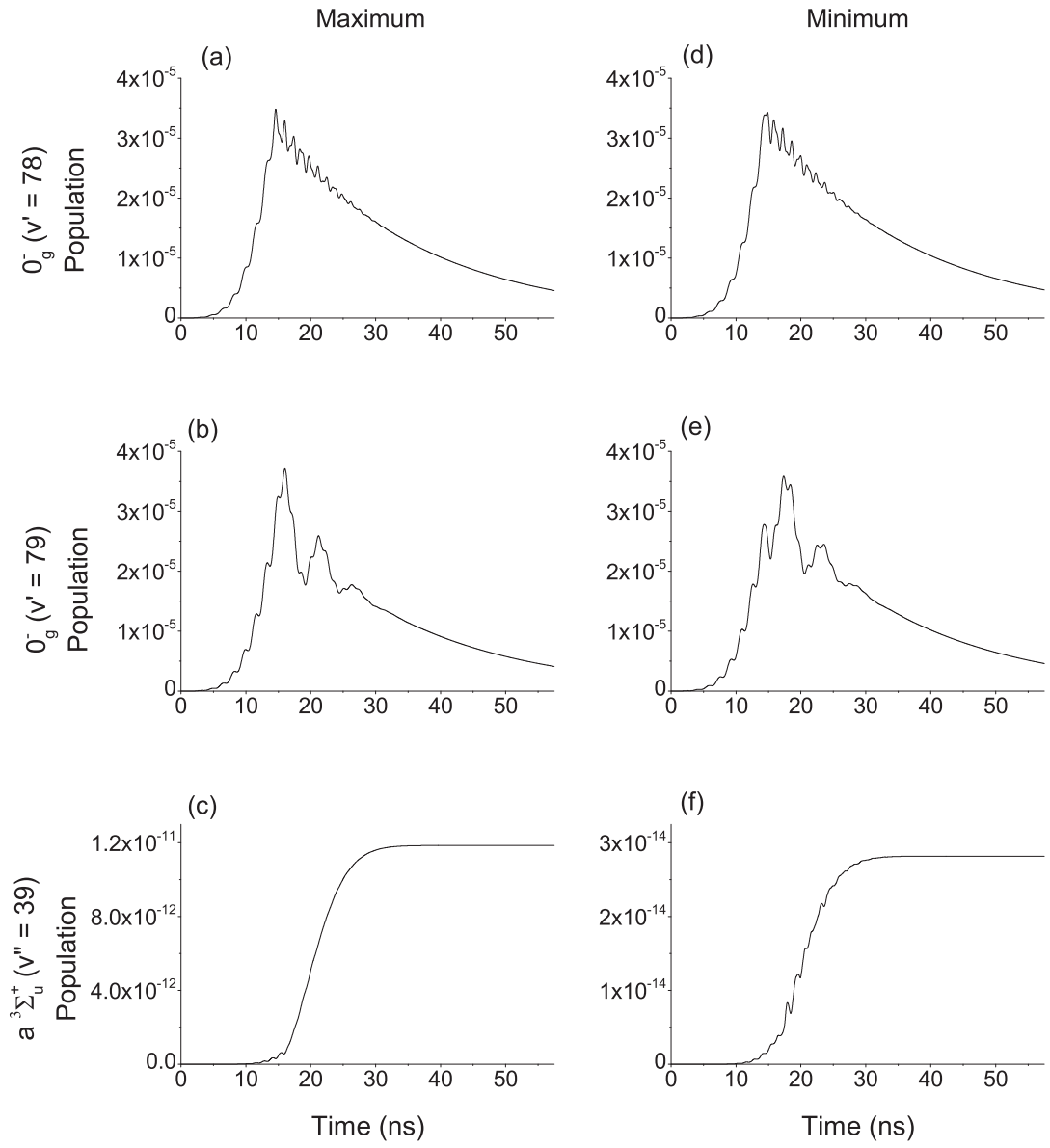

Figure 4.25. Two-Frequency Population Evolution for I = 1 W/cm^2

State populations vs. time for the two-frequency case with I = 1 W/cm^2, as in Fig. 4.24(a). For (a)-(c), the relative phase = 5.655 rad, yielding the maximum molecular formation rate, while for (d)-(f), the relative phase = 2.513 rad, yielding the minimum rate. The v'=78 populations are shown in (a) and (d); v'=79 in (b) and (e); and v"=39 in (c) and (f).

equal-intensity beams, having separately optimized their individual formation rates, and adjust their relative phase. The results, shown in Fig. 4.24 for several different intensities, exhibit what appears to be almost complete constructive and destructive interference. At first glance, this is not unexpected. We are going from the initial state to the final state via two paths of almost equal amplitude. However, when we consider that the initial state is a continuum and that the total rate of spontaneous emission is not negligible, the degree of contrast is somewhat surprising. To understand the details of the interference, we examine the various state populations for the two relative phases which give maximum and minimum molecular formation rates. We first explore the case of low intensity, 1 W/cm^2 (total intensity, shared between the two beams), which should be in the perturbative limit. We see in Fig. 4.25 that the populations in the intermediate states, v'=78 and v'=79, are quite similar. For the optimum relative phase (5.655 rad), the two paths through these two intermediate states interfere constructively, yielding a maximum target state (v"=39) population. For a relative phase of 2.513 rad, the intermediate state populations are still similar, but the time dependence is slightly shifted in time, causing destructive interference in the target state and reducing the yield by more than two orders of magnitude.

Switching now to a higher total intensity of 200 W/cm^2, on the order of what has been realized experimentally [45], we see a similar contrast in the final yield. However, examining the state populations, as shown in Fig. 4.26, we find that the manifestations of the interference are quite different. Comparing the cases of corresponding to the maximum (relative phase = 0) and and the minimum (relative phase = 2.513 rad) in Fig. 4.24(b), we see a significant change in not only the final state (v"=39) population, but also in the intermediate state (v'=78 and v'=79) populations. It appears that the key ingredient for destructive interference is having approximately equal intermediate state populations, while for maximum target state

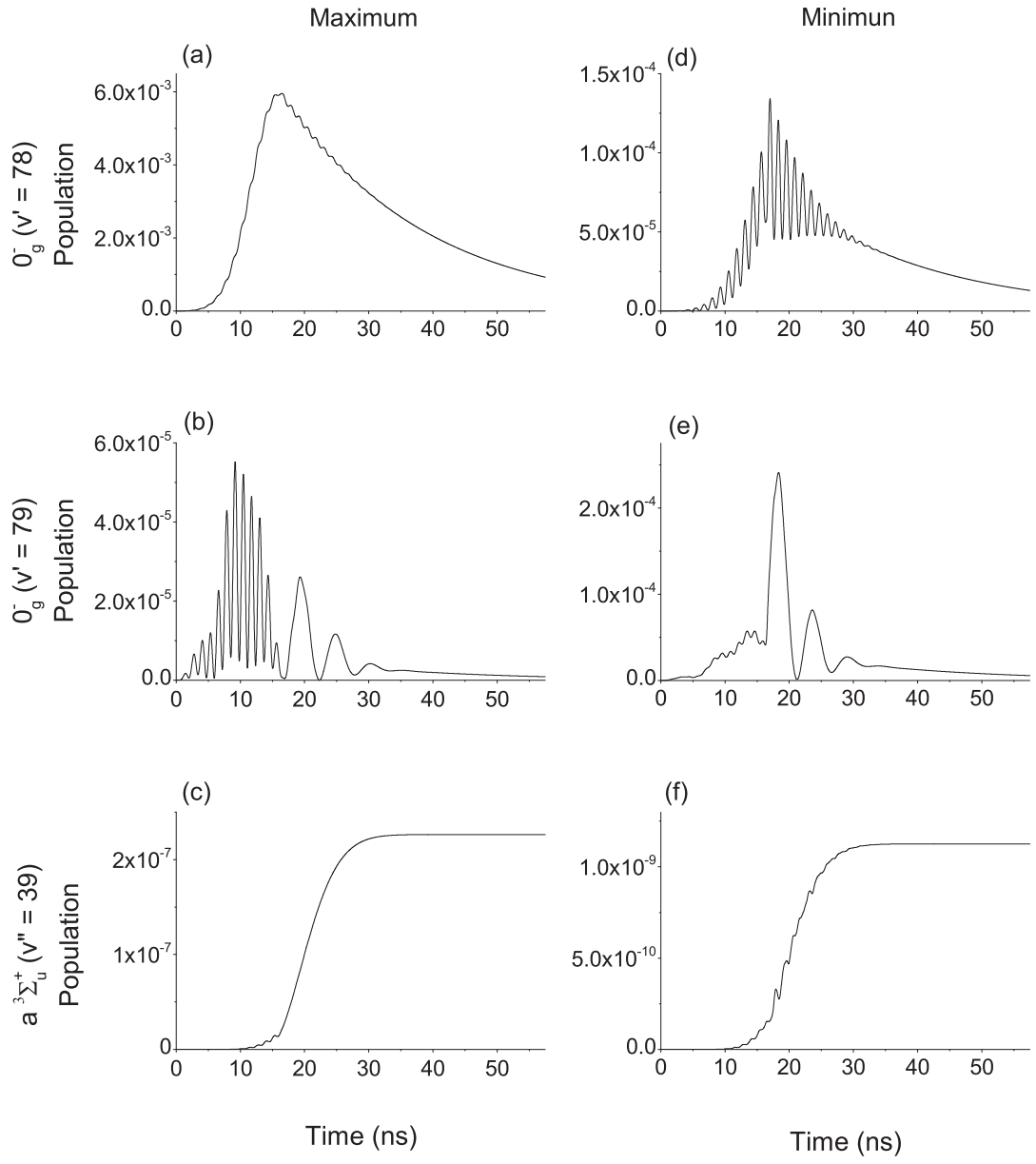

Figure 4.26. Two-Frequency Population Evolution for I = 200 W/cm^2

State populations vs. time for the two-frequency case with I = 200 W/cm^2, as in Fig. 4.24(b). For (a)-(c), the relative phase = 0, resulting in maximum v"=39 population, while for (d)-(f), the relative phase = 2.513 rad, yielding the minimum population in v"=39. The v'=78 populations are shown in (a) and (d); v'=79 in (b) and (e); and v"=39 in (c) and (f).

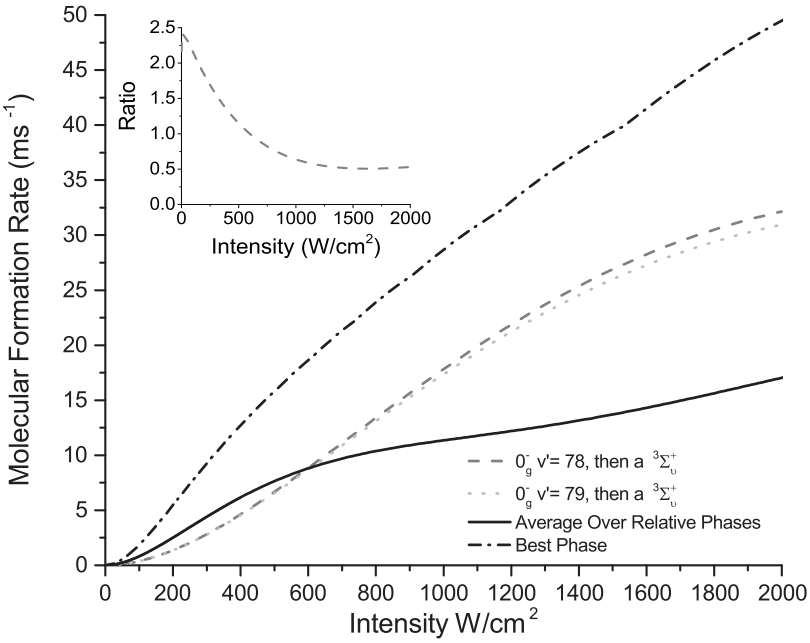

Figure 4.27. Two-Frequency Molecular Formation Rate

Molecular formation rate vs. total peak intensity for the case of two frequencies (solid curve). These results are averaged over the relative phase. When this phase is at its optimum value for each intensity, we obtain the dashed-dotted curve. For comparison, we also show the results when each frequency is applied separately (dashed curve for v'=78, dotted curve for v'=79). The inset shows the ratio of the two-frequency phase-averaged formation rate to the one-frequency (v'=78) rate. Note that in all cases, the horizontal axis refers to the total intensity: the sum of the two intensities in the two-frequency case; and the individual intensities in the one-frequency case.

population, these intermediate state populations are very different. Comparing Figs. 4.26(a) and 4.26(d), we see that the v'=78 population is reduced by a factor of ∼40 simply by changing the relative phase of the light driving the transition to and from v'=79. Clearly there is a strong interaction between the two arms of this "interferometer". The nontrivial nature of the interference is reinforced by the complicated phase dependence of the formation rate at higher intensities, as shown in Fig. 4.24(c).

If we average the formation rate over the relative phase, as shown in Fig. 4.27, we find that at low intensities, there is still significant enhancement over the case of the single beam with local control, when comparing at the same total intensity. This is encouraging because it implies that the relative phase does not need to be stabilized in order to gain some enhancement. Of course, if the relative phase is stabilized at its optimum value, even more enhancement, by roughly a factor of two, is realized.

4.4.4 Conclusion

We have examined the possibility of enhancing photoassociative ultracold molecule formation using local control of the phase. We find that local control does indeed outperform a simple linear chirp, and that the optimum frequency variation corresponds to a nearly instantaneous jump from the continuum-to-excited-state transition to the excited-state-to-bound-state transition. The dependence on phase verifies that the process has a significant coherent aspect. We can improve the formation rate even further by combining two local-control-optimized beams which drive transitions to and from different excited states. Surprisingly, even after averaging over relative phase, we find, at the same total intensity, an enhancement relative to the single-beam case under some conditions. We can take advantage of the strong dependence on this relative phase and obtain an additional enhancement at a fixed optimal phase. The explored values for intensity, pulse width, and frequency variation should be experimentally realizable with nanosecond-time-scale pulse shaping techniques.

Interesting avenues for future investigations include incorporation of local control of not only the phase, as we have done here, but also the amplitude, in the optimization algorithm. Also, in experiments, an important practical aspect is that a sequence of chirped pulses is typically used. Therefore, the photodestruction of molecules by a subsequent pulse must be considered [45]. Simultaneous optimization of formation

and minimization of this destruction would therefore be a useful endeavor. Finally, it would be useful to compare the results of local control to more global types of control such as genetic algorithms.

4.5 Faster Chirps

To take advantage of the molecular formation mechanism described in section 4.3 (reference [45]), we investigate the effects of increasing the chirp rate, employing chirp shaping, and increasing the intensity. We increase the chirp rate by extending the chirp range to ensure that we cross the 0_g^- v'=78 $\rightarrow$ $a\ ^3\Sigma_u^+$(v"=39) transition, and decreasing the chirp time which will also reduce the effects of spontaneous emission. However, in general, a faster chirp rate will require a higher intensity. The molecular formation rates for 50 ns chirps with 20 ns FWHM Gaussian intensity pulses are presented in section 4.5.1, 28.75 ns chirps with 15 ns FWHM Gaussian intensity pulses are presented in section 4.5.2, and 37.5 ns chirps with 15 ns FWHM Gaussian intensity pulses are presented in section 4.5.3.

4.5.1 50 ns Chirps with 20 ns FWHM Intensity Pulses

We ran the simulations, as described in section 4.3 (reference [45]), but with 50 ns chirps and 20 ns FWHM Gaussian intensity pulses. This chirp time and intensity FWHM are exactly half the values used previously. Instead of just restricting the chirp range to 1 GHz, we also ran 2 GHz chirps. The chirp shapes are shown in figure 4.28(a) and the molecular formation rates are shown in figure 4.28(b). In all cases, the intensity pulse is centered on the chirp and the chirp is centered on the upward ($a\ ^3\Sigma_u^+$ continuum $\rightarrow$ 0_g^-(v'=78)) transition. For the chirp to cross the downward resonance (0_g^-(v'=78) $\rightarrow$ $a\ ^3\Sigma_u^+$(v"=39)) after there is population in the excited state, the chirp has to evolve an additional 764 MHz (dotted line in figure 4.28(a)). Although the 1

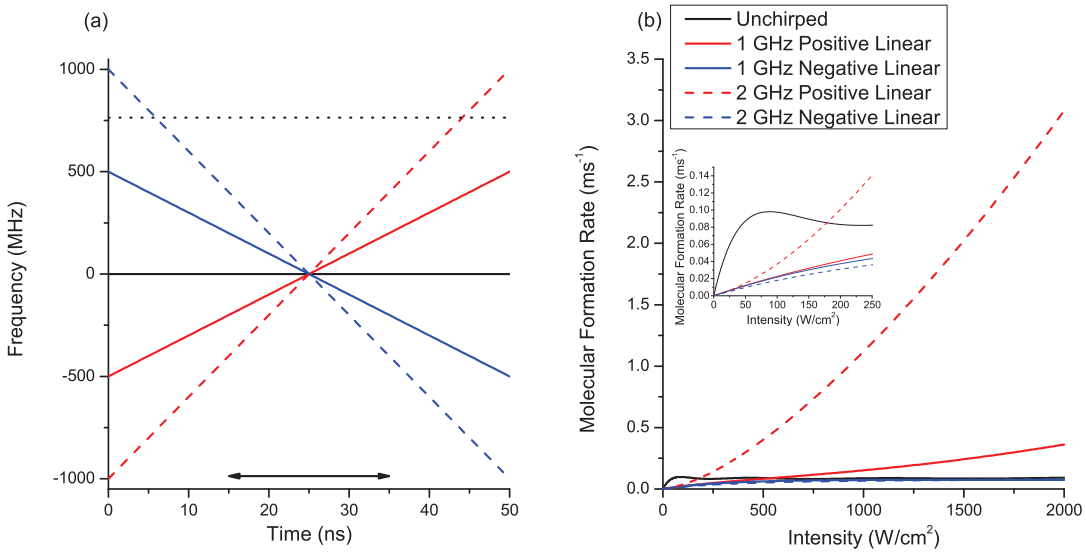

Figure 4.28. 50 ns Chirps with 20 ns FWHM Gaussian Intensity Pulses

Simulations of 50 ns chirps with 20 ns FWHM Gaussian intensity pulses for unchirped, as well as 1 and 2 GHz positive and negative linear chirps. (a) Chirp frequency vs. time and (b) molecular formation rate vs. intensity. The insert in (b) shows lower intensities. The double-ended arrow in (a) indicates the pulse width (FWHM). Frequencies are relative to the PA transition to 0_g^-(v'=78). The horizontal dotted line in (a) indicates the 0_g^-(v'=78) $\rightarrow$ $a\ ^3\Sigma_u^+$(v"=39) transition.

GHz positive chirp approaches this resonance, only the 2 GHz positive chirp crosses it, as shown in the dressed-state picture in figure 4.29. By doubling the chirp range (2 GHz instead of 1 GHz), reducing the chirp time (50 ns instead of 100 ns), and doubling the intensity (200 W/cm^2 instead of 100 W/cm^2), the positive chirp formation rate becomes greater than that for the unchirped pulse. This enhancement is due to an increase in the stimulated emission from 0_g^-(v'=78) $\rightarrow$ $a\ ^3\Sigma_u^+$(v"=39). For higher intensities, both the 1 and 2 GHz positive linear chirp molecular formations rates can both exceed those from the unchirped pulse. Even for up to 2000 W/cm^2, the negative chirps' molecular formation rates only start to converge with the unchirped pulse, never exceeding it. The insert of figure 4.28(b) shows lower intensities that are currently feasible with the current probe setup (section 3.3). The photodestruction rates for a single unchirped pulse and linear chirps at peak intensities of 100 and 200 W/cm^2 are shown in table 4.10. Taking these rates into account, these faster positive chirps are producing significantly more molecules than were formed in section 4.3, reference [45].

4.5.2 28.75 ns Chirps with 15 ns FWHM Intensity Pulses

To see if we could further enhance the molecular formation rate, we tried some simple shaping with some even faster chirps. These chirps are 28.75 ns with 15 ns FWHM Gaussian intensity pulses. For these time scales, we again ran the unchirped as well as 1 and 2 GHz positive and negative linear chirps. We also tried a positive concave-down chirp which is a 2 GHz positive linear chirp with a Gaussian added to it. The idea here is that with the Gaussian, the chirp slowly, and thus more adiabatically, goes through the resonance 0_g^-(v'=78) $\rightarrow$ $a\ ^3\Sigma_u^+$(v"=39). Taking the extreme version of this idea, we take a slow linear chirp, offset it, and add a hyperbolic tangent function. With this chirp, we have a slow linear ramp through both of the

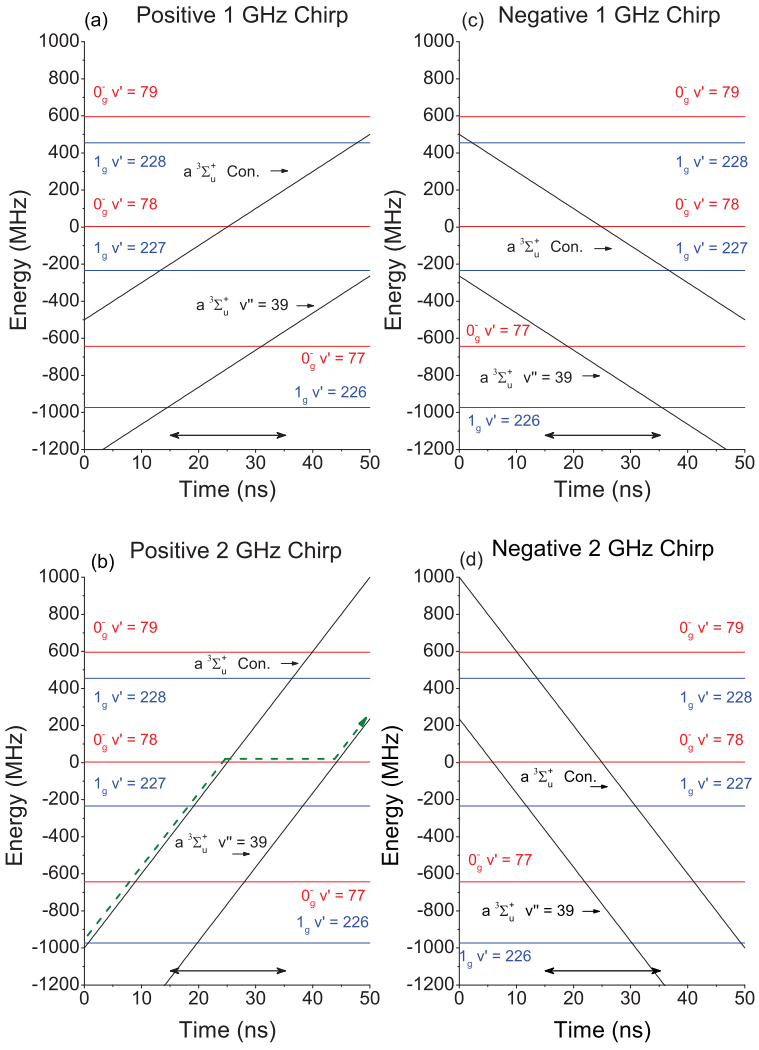

Figure 4.29. Quantum Mechanical Simulations: 50 ns Chirps with 20 ns FWHM Gaussian Intensity Pulses; Dressed-state Picture

Evolution of the molecular levels during the positive (a+b) and negative (b+d) chirps. 1 GHz linear chirps are shown in (a+c) and 2 GHz linear chirps are shown in (b+d). Horizontal lines are the relative energies of the vibrational levels of the excited 0_g^- and 1_g molecular states, while the energies of the $a\ ^3\Sigma_u^+$ zero-energy continuum and the v"= 39 level, with the energy of the chirped photon added, are represented by the upper and lower black curves, respectively. In this picture, a curve crossing indicates resonance with the corresponding transition. Double-ended arrows indicate the pulse widths (FWHM). In (b), the adiabatic path from the continuum to v"=39 is shown as a dashed curve.

resonances ($a\ ^3\Sigma_u^+$ continuum $\rightarrow 0_g^-$(v'=78) and 0_g^-(v'=78) $\rightarrow\ a\ ^3\Sigma_u^+$(v"=39)) and quickly change between these two frequencies using a hyperbolic tangent function. This rapid change helps to minimize spontaneous emission, while maintaining more adiabatic behavior when passing through the two resonances. The chirp shapes are shown in figure 4.30(a) and the corresponding molecular formation rates are shown in figure 4.30(b). By employing some simple shaping, we can better match the chirp to the dynamics and further enhance the molecular formation rate. The dressed-state pictures for the linear cases are similar to figure 4.29, but with a chirp time of 28.75 ns instead of 50 ns and are therefore not shown. The dressed-state pictures for the two shaped positive chirps are shown in figure 4.31. A positive hyperbolic tangent chirp enhances the molecular formation by a factor of >5 over the unchirped pulses at low intensities (figure 4.30(b) insert) and by a factor of ∼100 at higher intensities (figure 4.30). For higher intensities, all of the positive chirp molecular formations rates can exceed those from the unchirped pulse. Again, even for up to 2000 W/cm^2, the negative chirps' molecular formation rates only start to converge with the unchirped pulse, never exceeding it. The intensity range of the insert of figure 4.28(b) shows lower intensities that are currently feasible with the current probe setup (section 3.3).

Although these positive chirps do enhance the molecular formation rate by quite a bit, these molecular formation rates are not even a third of those produced with the local control determined step-like function (section 4.4 (also reference [46]) for which the chirp is shown in figure 4.19 and the molecular formation rate results are shown in figure 4.18). Although the timescales of the local control pulse are experimentally feasible, with the current probe setup (section 3.3), this fast change would be difficult. The slower hyperbolic tangent chirp (figure 4.30 (a)) can be produced with the current probe setup (section 3.3). Also, with the linear chirps at the beginning and end, the center detuning of the probe laser is less critical, making such an experiment easier.

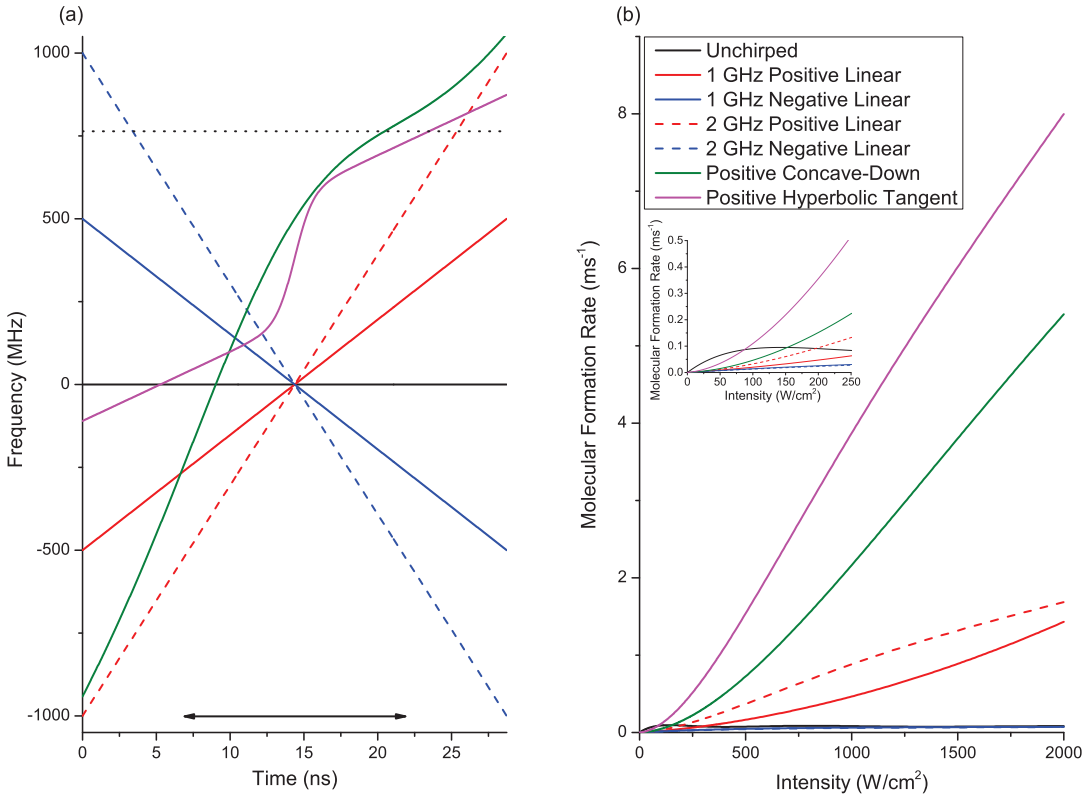

Figure 4.30. 28.75 ns Chirps with 15 ns FWHM Gaussian Intensity Pulses

Simulations of 28.75 ns chirps with 15 ns FWHM Gaussian intensity pulses for unchirped as well as 1 and 2 GHz positive and negative linear chirps, positive concave-down chirp, and positive hyperbolic tangent chirp. (a) Chirp frequency vs. time and (b) molecular formation rate vs. intensity. The insert in (b) shows lower intensities. The double-ended arrow in (a) indicates the pulse width. Frequencies are relative to the PA transition to 0_g^-(v'=78). The horizontal dotted line indicates the 0_g^-(v'=78) $\rightarrow$ $a\ ^3\Sigma_u^+$(v"=39) transition.

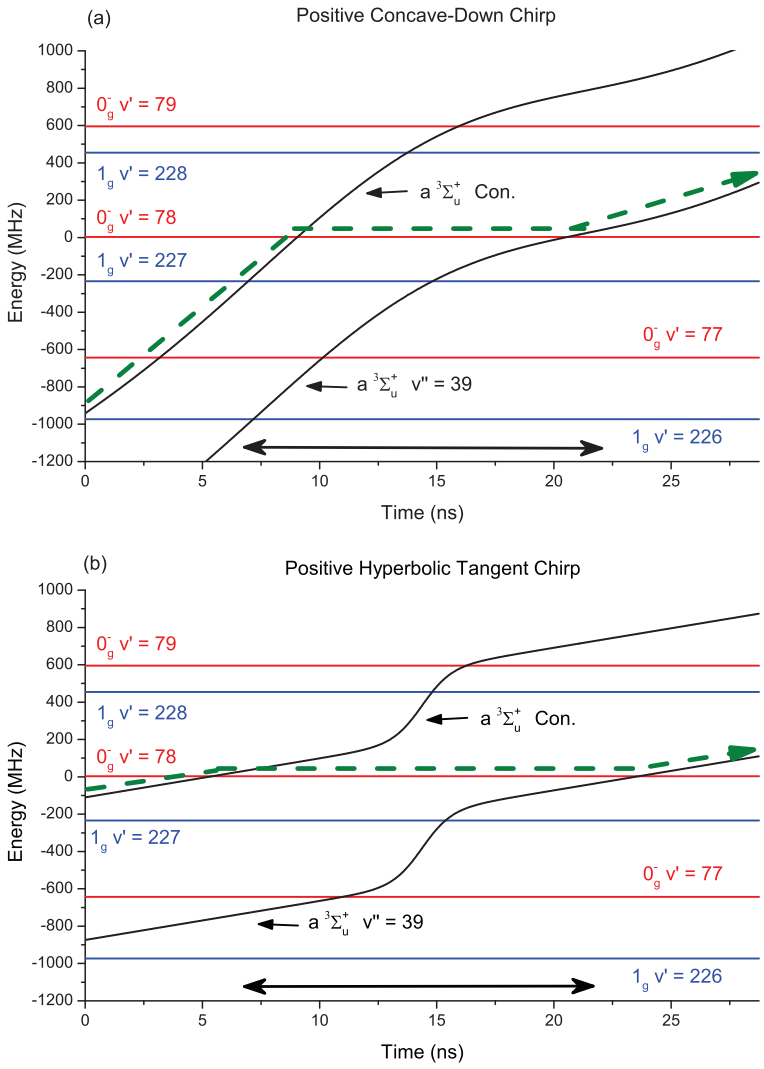

Figure 4.31. Quantum Mechanical Simulations: 28.75 ns Chirps with 15 ns FWHM Gaussian Intensity Pulses; Dressed-state Picture

Evolution of the molecular levels during the positive concave-down (a) and hyperbolic tangent (b) chirps. Horizontal lines are the relative energies of the vibrational levels of the excited 0_g^- and 1_g molecular states, while the energies of the $a\ ^3\Sigma_u^+$ zero-energy continuum and the v"= 39 level, with the energy of the chirped photon added, are represented by the upper and lower black curves, respectively. In this picture, a curve crossing indicates resonance with the corresponding transition. Double-ended arrows indicate the pulse widths (FWHM). The adiabatic paths from the continuum to v"=39 are shown as dashed curves. Note that in (b), both crossings (at 5.3 ns and 23.4 ns) have small slopes, leading to increased adiabaticity.

The photodestruction probabilities for a single unchirped pulse and linear chirps at peak intensities of 100 and 200 W/cm^2 are shown in table 4.11. Taking these rates into account, these faster positive chirps are producing substantially more molecules than were formed in section 4.3 (also reference [45]), although still significantly less than predicted by the local control (section 4.4, reference [46]).

4.5.3 37.5 ns Chirps with 15 ns FWHM Intensity Pulses

We investigate chirps that are almost three times as fast as those described in section 4.3 (reference [45]). These chirps are 37.5 ns long with 15 ns FWHM intensity pulses (the same FWHM/chirp time ratio as in section 4.3 (reference [45])). The corresponding photodestruction probabilities are presented in table 4.12 and the corresponding experiments are described in the next chapter (Chapter 5).

The chirp shapes, resulting from smoothed (using a 2 ns FWHM Gaussian function) interpolated instantaneous frequencies (shown in figure 5.4) derived from heterodyne signals, are shown in figure 4.32(a) and the corresponding molecular formation rates are shown in figure 4.32(b). The dressed-state pictures for the linear cases are similar to figure 4.29, but with a chirp time of 37.5 ns instead of 50 ns and are therefore not shown. The dressed-state pictures for the two shaped positive chirps are shown in figure 4.33. As with some of the earlier shapes at other timescales, by extending the chirp range to go through the 0_g^-(v'=78) $\rightarrow$ $a\ ^3\Sigma_u^+$(v"=39) transition, the positive chirps are able to have a higher formation rate than the unchirped pulse at higher intensities. By employing some shaping, the positive concave-down and positive shaped chirps are able to have an even higher molecular formation rate than the positive linear chirp. The corresponding populations for a peak intensity of 200 W/cm^2 are shown in figure 4.34. The excited-state populations, 0_g^- (v'=78), are shown in figure 4.34(a). The unchirped pulse is able to excite by far the most popu-

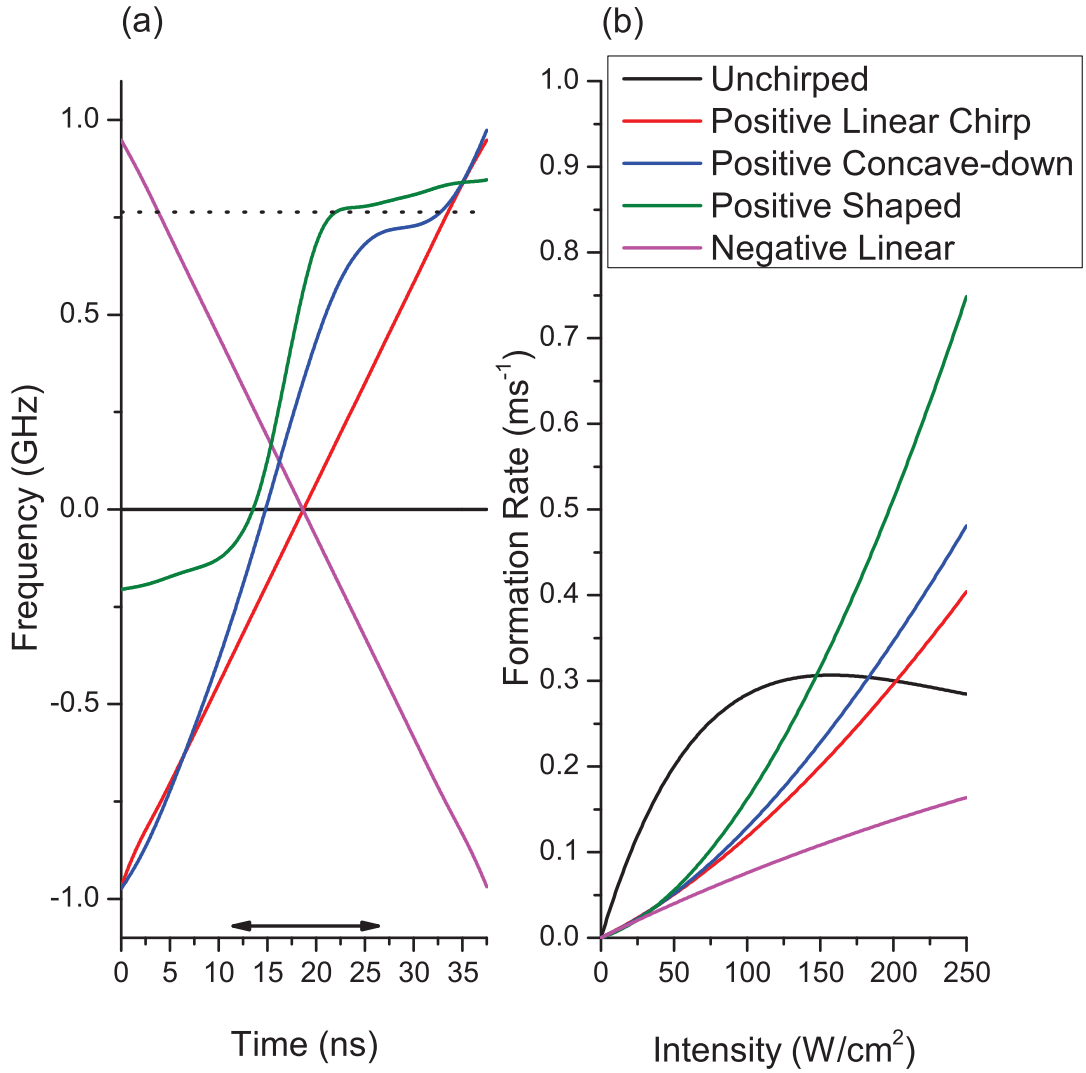

Figure 4.32. 37.5 ns Chirps with 15 ns FWHM Gaussian Intensity Pulses

Simulations of 37.5 ns chirps with 15 ns FWHM Gaussian intensity pulses for unchirped as well as 1 and 2 GHz positive and negative linear chirps, positive concave-down chirp, and positive hyperbolic tangent chirp. (a) Chirp frequency vs. time and (b) molecular formation rate vs. intensity. The insert in (b) shows lower intensities. The double-ended arrow in (a) indicates the pulse width. Frequencies are relative to the PA transition to 0_g^-(v'=78). The horizontal dotted line indicates the 0_g^-(v'=78) $\rightarrow$ $a\ ^3\Sigma_u^+$(v"=39) transition.

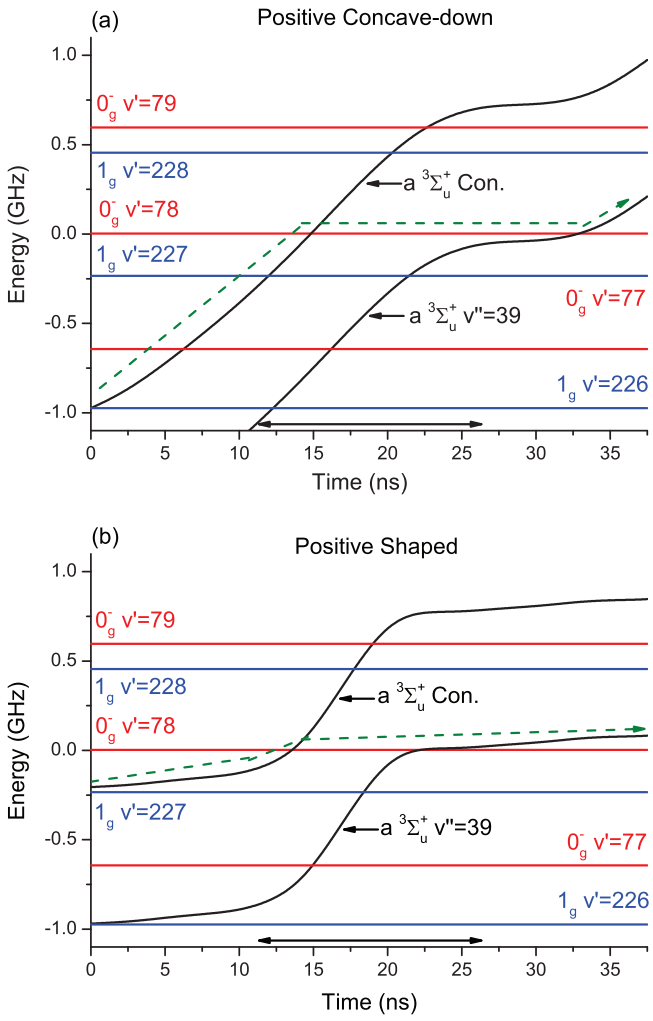

Figure 4.33. Quantum Mechanical Simulations: 37.5 ns Chirps with 15 ns FWHM Gaussian Intensity Pulses; Dressed-state Picture

Evolution of the molecular levels during the positive concave-down (a) and shaped (b) chirps. Horizontal lines are the relative energies of the vibrational levels of the excited 0_g^- and 1_g molecular states, while the energies of the $a\ ^3\Sigma_u^+$ zero-energy continuum and the v"= 39 level, with the energy of the chirped photon added, are represented by the upper and lower black curves, respectively. In this picture, a curve crossing indicates resonance with the corresponding transition. Double-ended arrows indicate the pulse widths (FWHM). The adiabatic paths from the continuum to v"=39 are shown as dashed curves.

lation by being resonant with this transition throughout the chirp time. The positive and negative linear chirps excite the next most population. The subtle differences in the two linear traces are due to the chirps not being quite symmetric since they were experimentally produced. The positive concave-down and positive shaped chirps have even less population in the excited state. Their peak populations also occur earlier in time. Looking back at the chirp shapes (figures 4.32(a) and 4.33), both the positive concave-down and positive shaped chirps hit the PA resonance before the peak of the intensity pulse. This difference in time accounts for not only the time shift, but also the reduction in overall population of the excited state. The spontaneous emission, SE, from 0_g^- is shown in figure 4.34(b). Unsurprisingly, the unchirped pulse has the most SE due to the larger amount of population in the excited state. The positive and negative linear as well as the positive concave-down chirps produce about half as much SE from the 0_g^-. The positive shaped chirp has about half again as much SE from the 0_g^-. The stimulated emission, STE, contribution to $a\ ^3\Sigma_u^+$ (v"=39) is shown in figure 4.34(c). Only the positive chirps have a significant STE contribution. For the positive linear chirp, the STE is slightly more than the SE, showing that compared to figure 4.14 from the 100 ns chirps, going through the transition 0_g^-(v'=78) $\rightarrow$ $a\ ^3\Sigma_u^+$(v"=39) does indeed increase the STE contribution. By adding the simple shaping of the positive concave-down chirp, we were able to increase this STE contribution to $\sim$5 times the SE contribution. The positive shaped chirp has by far the most STE contribution at almost 16 times the SE. For the positive shaped in particular, the STE sufficiently dominates to enhance the molecular formation rate to be about twice that of the unchirped pulse even though the unchirped pulse does much better at excitation (figure 4.34(a)).

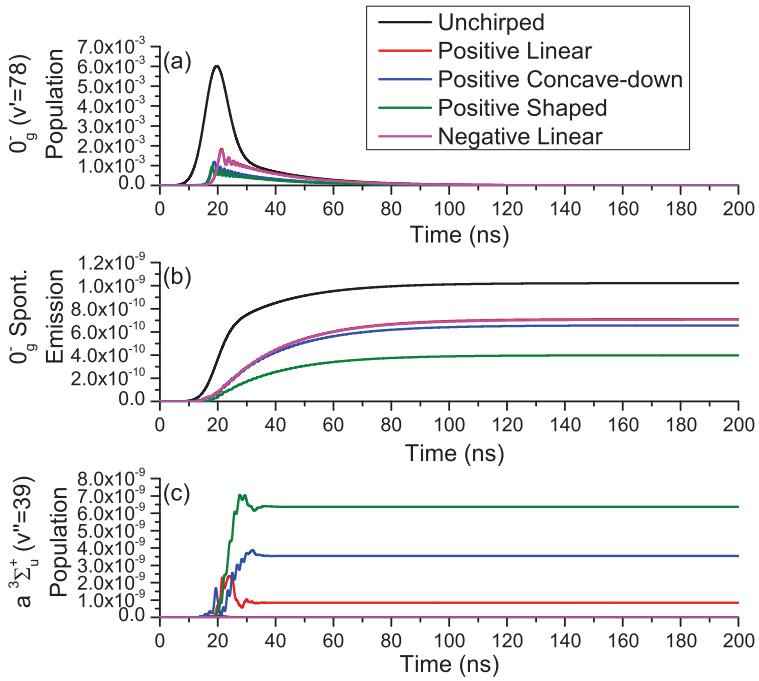

Figure 4.34. Quantum Mechanical Simulations: Time Evolution

Populations of various molecular states during the unchirped, positive linear, positive concave-down, positive shaped, and negative linear pulses for a peak intensity of 200 W/cm^2: (a) 0_g^- (v'=78); (b) $a\ ^3\Sigma_u^+$ bound levels populated by spontaneous emission from 0_g^-; (c) $a\ ^3\Sigma_u^+$ (v"=39) resulting from stimulated emission from 0_g^- (v'=78); Note that in (c) only the positive chirps have a significant contribution. Not shown are populations of the 1_g excited states which for the unchirped pulse (largest of the shapes) have a much smaller maximum value of 2.3E-5 in v'=228, and the population of other bound ground-state levels from spontaneous emission, which approach a maximum total of only 1.6E-14 at long times.

Chapter 5
Experimental Results

This chapter focuses on photoassociation (PA) experiments resulting in ultracold molecule formation in the triplet ground state, $a\ ^3\Sigma_u^+$. We start with ultracold ^{87}Rb atoms in our MOT in the continuum and apply a frequency-chirped probe laser. This PA laser forms the molecules in the 0_g^-(v'=78) state. For some chirp parameters, the PA laser is then able to stimulate the excited molecule population down to $a\ ^3\Sigma_u^+$(v"=39). For all chirps, some excited molecules spontaneously decay into $a\ ^3\Sigma_u^+$(v"=39), as well as other vibrational levels and the continuum. Once molecules are formed in $a\ ^3\Sigma_u^+$(v"=39), we are able to use REMPI detection to directly detect the molecules, as shown in figure 5.1.

In this chapter, we present the typical experimental parameters utilized in our studies of the formation of ultracold molecules. Results on MOT-formed molecules under various MOT conditions are also described, and, most importantly, we explore the effects of applying the frequency-chirped photoassociation laser.

5.1 Typical Parameters

Typical experimental parameters are given in table 5.1. The trap beam detuning was chosen to be slightly farther from resonance than in previous experiments (section 4.3, references [45, 62]) in order to increase MOT stability and reduce MOT-formed molecules (see next section, section 5.2). The MOT density and atom number were

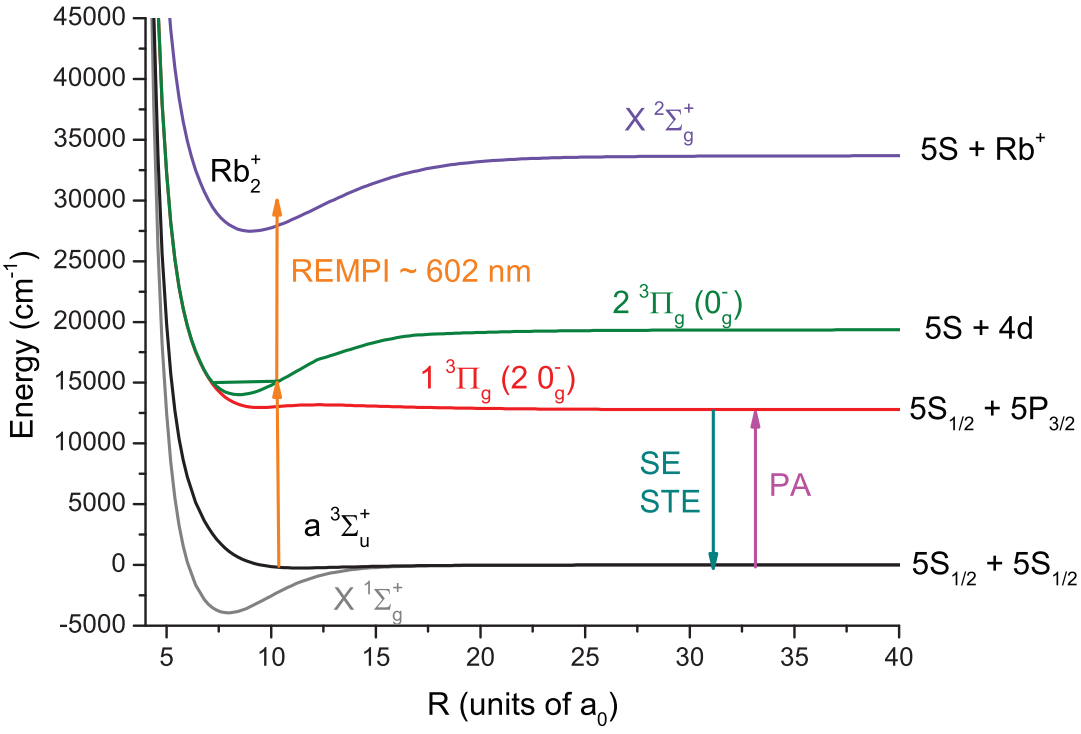

Figure 5.1. Potential Energy Curves

Potential energy curves with molecule formation and detection pathways. Arrows indicate photoassociation (PA) from the continuum to 0_g^-, stimulated (STE) and spontaneous (SE) emission to the triplet ground state, $a\ ^3\Sigma_u^+$, and REMPI to Rb_2^+.

MOT detuning	-14 MHz
MOT peak density	8 x 10^{10} cm^{-3}
MOT atom number	2 x 10^6
MOT $1/e^2$ radius x,y direction	178 μm
MOT $1/e^2$ radius z direction	159 μm
PA $1/e^2$ beam waist x direction	144 μm
PA $1/e^2$ beam waist y direction	116 μm
Maximum PA peak intensity	201 W/cm^2
REMPI pulse energy	4.8 mJ
REMPI beam diameter	3 mm
REMPI wavelength, λ_{det}	16608.5 cm^{-1}

Table 5.1. Typical experimental parameters for photoassociation experiments

chosen to enhance the overall photoassociation rate. The PA $1/e^2$ beam waist is just slightly smaller than the MOT $1/e^2$ radii. The REMPI detection beam is only slightly focused and has a diameter much larger than the MOT to ensure a large detection volume since the produced molecules are not trapped.

5.2 MOT-formed Molecules

First, we investigate the background MOT-formed molecules. Although the exact mechanism is unknown, presumably these molecules are formed by the MOT laser at large internuclear separations, since the MOT lasers are detuned by only -14 MHz from the atomic $5S_{1/2}$ (F=2) $\rightarrow$ $5P_{3/2}$ (F'=3) asymptote. It is important to understand how this background signal scales with the number of MOT atoms, N, as well as their REMPI spectra.

To measure the MOT-formed molecules as a function of the number of MOT atoms, N, we fixed the REMPI detection laser on a molecular resonance at 16607.67 cm^{-1}. While maintaining a constant MOT density of $\sim$1x10^{11} cm^{-1}, we attenuated the LVIS loading beam to reduce the number of UHV MOT atoms. The resulting MOT-formed molecules vs. N is shown in figure 5.2. Unsurprisingly, the background MOT-formed molecule signal increases with N. Note that since the density is held approximately constant, the $1/e^2$ MOT radii are also increasing with N. The larger MOT-formed molecule signal may be tolerable with a sufficiently large PA formation rate, but for our parameter space we found that going to a smaller MOT (the parameters are given in table 5.1) was preferable.

The MOT-formed molecule REMPI spectrum is shown in figure 5.3. With this scan, we cover a larger range than usual (at least from the 5s $\rightarrow$ 14d to the 5s $\rightarrow$ 17d two-photon atomic lines, as assigned by a simple calculation based on [69]).

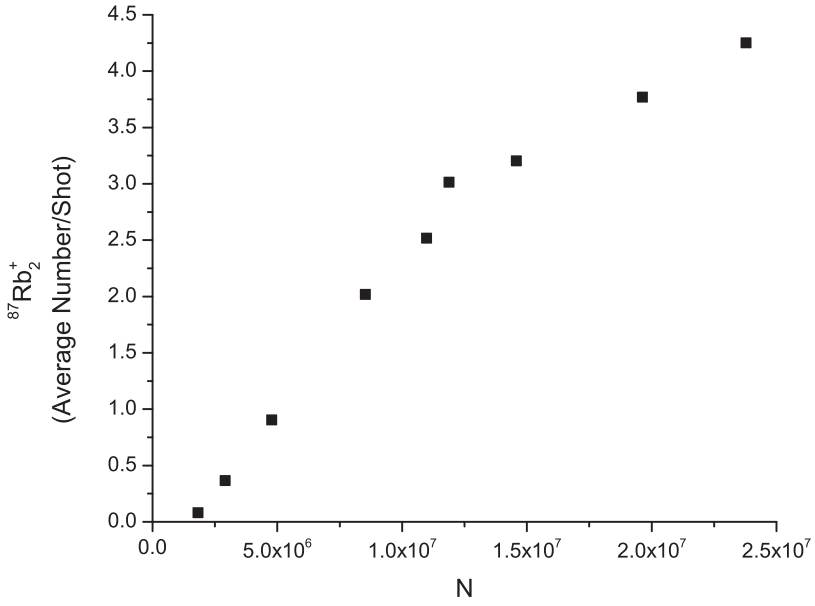

Figure 5.2. MOT-Formed $^{87}Rb_2^+$ vs. Number of MOT Atoms

MOT-formed $^{87}Rb_2^+$ as a function of the number of MOT atoms, N. The density is kept constant at $\sim$1x10^{11} cm^{-3}. The REMPI detection laser is fixed at 16607.7 cm^{-1}. The ion counts are averaged over 1000 shots.

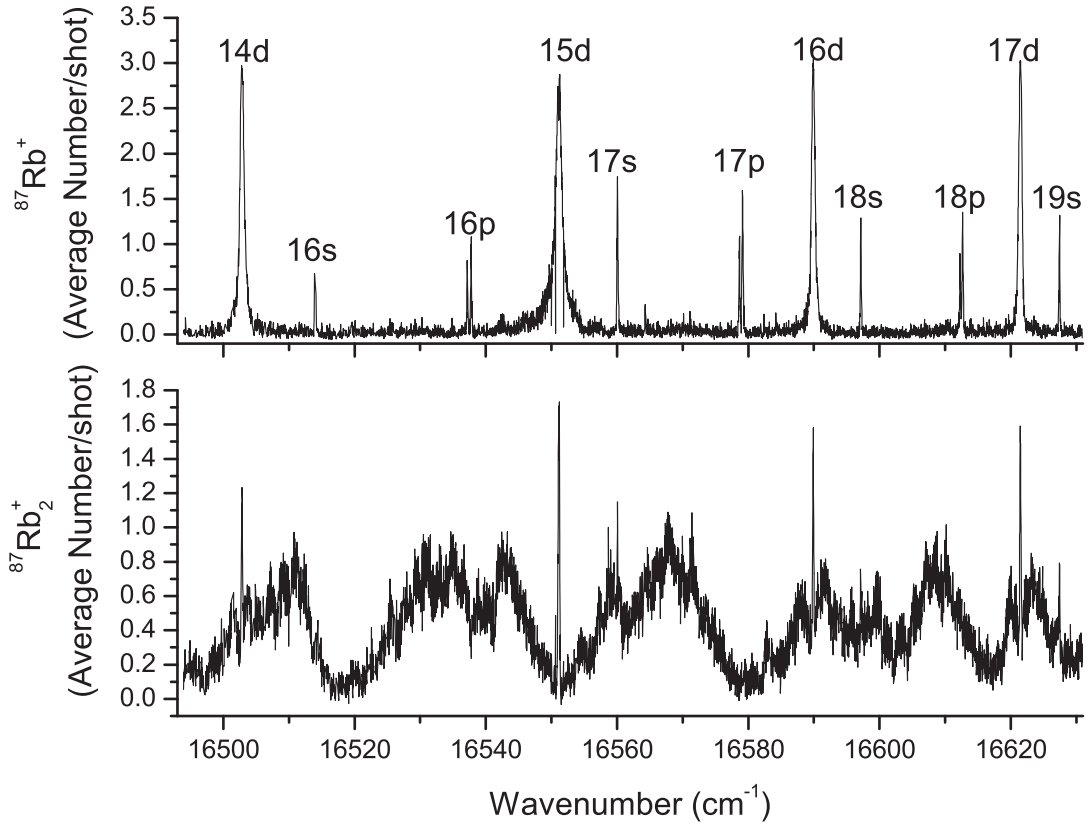

Figure 5.3. MOT-Formed $^{87}Rb_2^+$ REMPI Scan

MOT-formed $^{87}Rb^+$ and $^{87}Rb_2^+$ as functions of REMPI frequency. The ion counts are averaged over 10 shots and the REMPI laser is stepped by 0.001 nm. N $\sim$ 4.5x10^6 for this data.

There is some small leakage of the atomic signal into the molecular channel due to a combination of atomic signal strength as well as detector and electronics bandwidth.

5.3 Chirp Shapes

For the chirps in this section, we employ the phase modulation loop setup described in section 3.3 with a loop time of 62.35 ns. Following section 3.3.3, we analyze heterodyne signals for each chirp. The AWG outputs and corresponding derived instantaneous frequencies are shown in figure 5.4. The chirp ranges were chosen to ensure that we went through the 0_g^-(v'=78) $\rightarrow$ $a\ ^3\Sigma_u^+$(v"=39) transition. Compared to the unchirped, positive linear, and negative linear chirps previously investigated on longer timescales (section 4.3; reference [45]), these chirps are 37.5 ns long versus 100 ns; have close to twice the range: almost 2 GHz versus $\sim$ 1 GHz; have a shorter intensity pulse: 15 ns versus 40 ns; and have twice the intensity: 200 W/cm^2 versus 100 W/cm^2. Additionally we incorporate some shaping. First, we add a Gaussian to the positive linear chirp to get the positive concave-down chirp. This chirp has about the same range as the positive linear chirp, but goes through the 0_g^-(v'=78) $\rightarrow$ $a\ ^3\Sigma_u^+$(v"=39) transition slower and more adiabatically. Unfortunately, with this chirp shape, the PA transition occurs earlier (at a lower intensity) and with a slightly steeper slope than for the positive linear chirp. Based on our knowledge from the quantum mechanical simulations (Chapter 4), we wanted to create a shape that was more adiabatic on both transitions and more symmetric for the intensities on both transitions. We attempted to make a hyperbolic tangent chirp similar to the one described in section 4.5.2 as an experimentally easier version of the local-control-optimized step-like function (section 4.4; reference [46]) for which the chirp is shown in figure 4.19. By increasing the injection lock intensities for the phase modulation

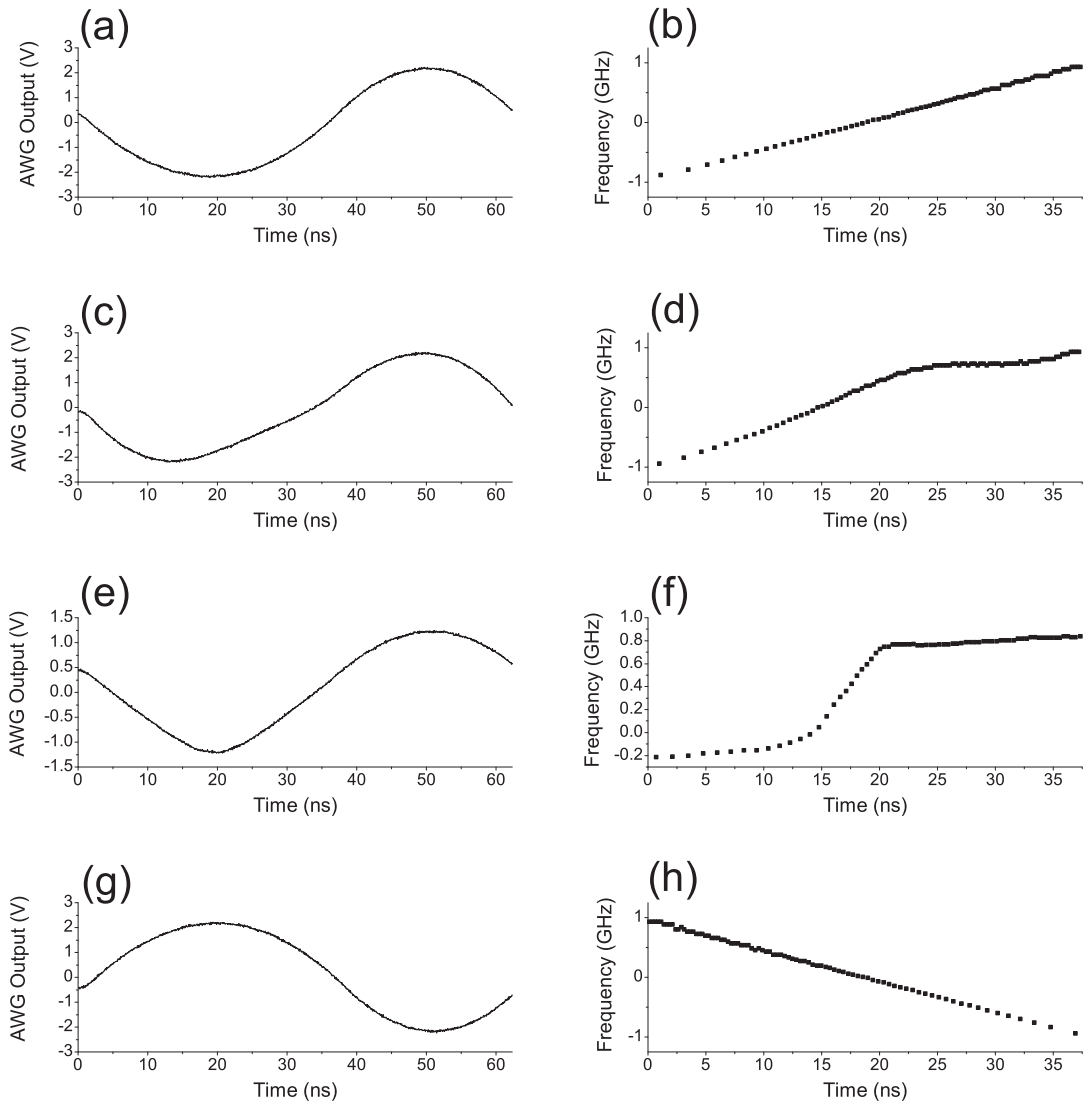

Figure 5.4. Frequency Chirps

Frequency chirp characterization for (a+b) positive linear, (c+d) positive concave-down, (e+f) positive shaped, and (g+h) negative linear chirps. The AWG outputs are shown in a,c,e, and g. The derived instantaneous frequencies versus time of the desired portions are shown in b,d,f, and h. These derived frequencies have the reference frequency subtracted out so that 0 corresponds to the PA resonance.

loop, we were able to produce a chirp similar to these shapes, the positive shaped chirp, as shown in figure 5.4(f).

5.4 Results

In this section we describe the results of applying unchirped, positive linear, positive concave-down, positive shaped, and negative linear chirps. REMPI and probe scans determine λ_{det} and the center probe frequency respectively. We determine the escape rate, Γ_{esc}, the photodestruction rate, Γ_{PD}, the steady-state number of molecules, N(∞), and the formation rate, R, for unchirped, positive linear, positive concave-down, positive shaped, and negative linear chirps.

5.4.1 REMPI Scans

In order to determine the optimum detection laser wavelength, λ_{det}, we perform REMPI scans (section 3.4.1). A long REMPI scan, taken with a large MOT and an unchirped 40 ns FWHM Gaussian pulse is shown in figure 5.5. Here the peak intensity is 30 W/cm^2 and the photoassociation laser is centered 7.79 GHz below the $5S_{1/2}$ (F=2) $\rightarrow$ $5P_{3/2}$ (F'=3) asymptote. Although not shown, it is important to remember that the MOT-formed molecule background signal is not subtracted here. Some of the overall signal change is due to the energy decreasing with wavelength, as shown in figure 3.4. This spectrum was taken to see if there is a better REMPI wavelength to use. Since there is nothing significantly better, to be consistent with our previous measurements [45], we keep $\lambda_{det} \sim 16608$ cm^{-1}.

We switch to a smaller MOT, whose parameters are shown in table 5.1, and perform REMPI scans with and without the unchirped 15 ns FWHM PA light, as shown in figure 5.6. The unchirped pulse, with a peak intensity of 105.9 W/cm^2 and an on-time of 10 ms, is centered 7.79 GHz below the $5S_{1/2}$ (F=2) $\rightarrow$ $5P_{3/2}$

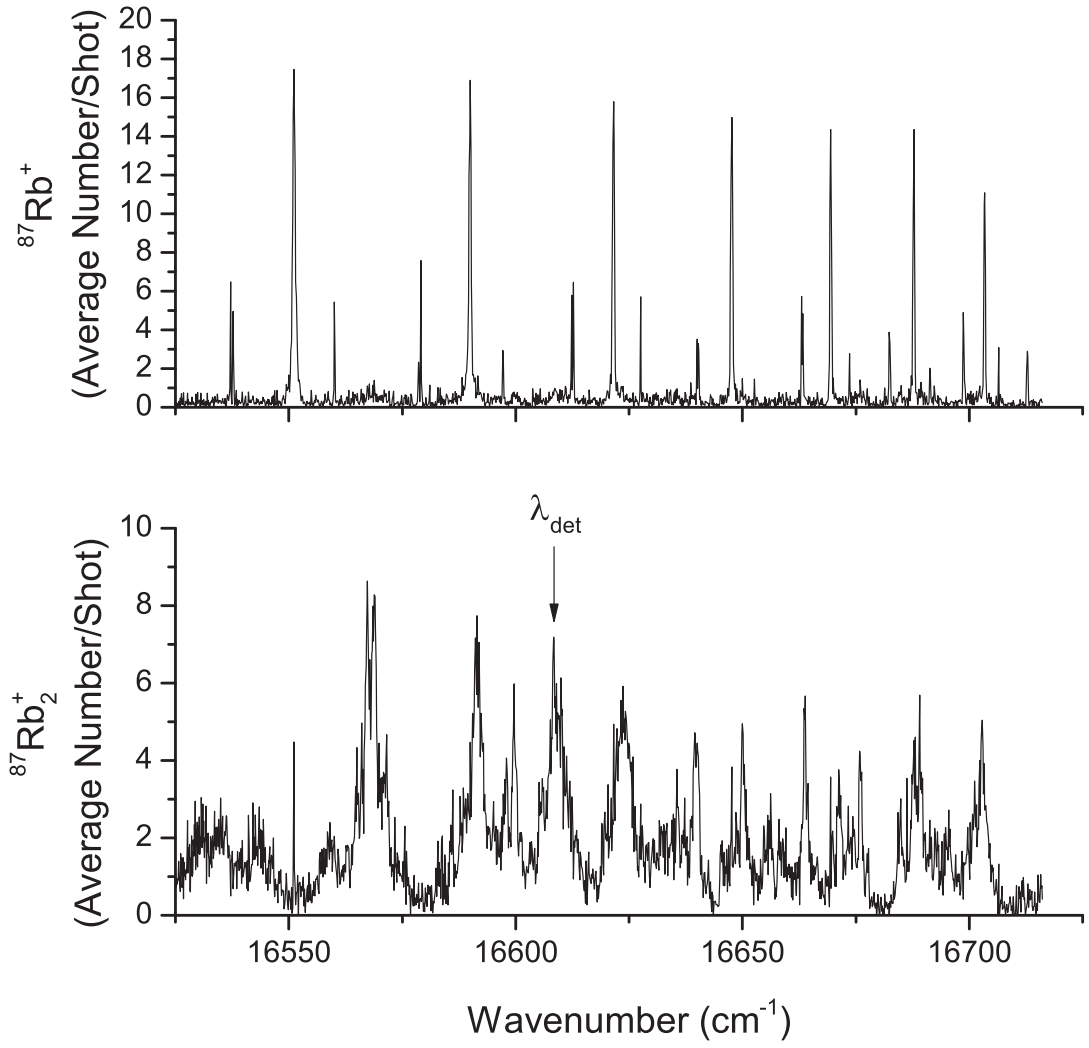

Figure 5.5. Extended REMPI Scans with Probe Laser

$^{87}Rb^+$ and $^{87}Rb_2^+$ REMPI scans. The ion counts are averaged over 10 shots and the REMPI laser is stepped by 0.001 nm. The unchirped 40 ns FWHM probe laser has a peak intensity of ∼30 W/cm^2. N $\sim$ 2.5x10^7 for this data.

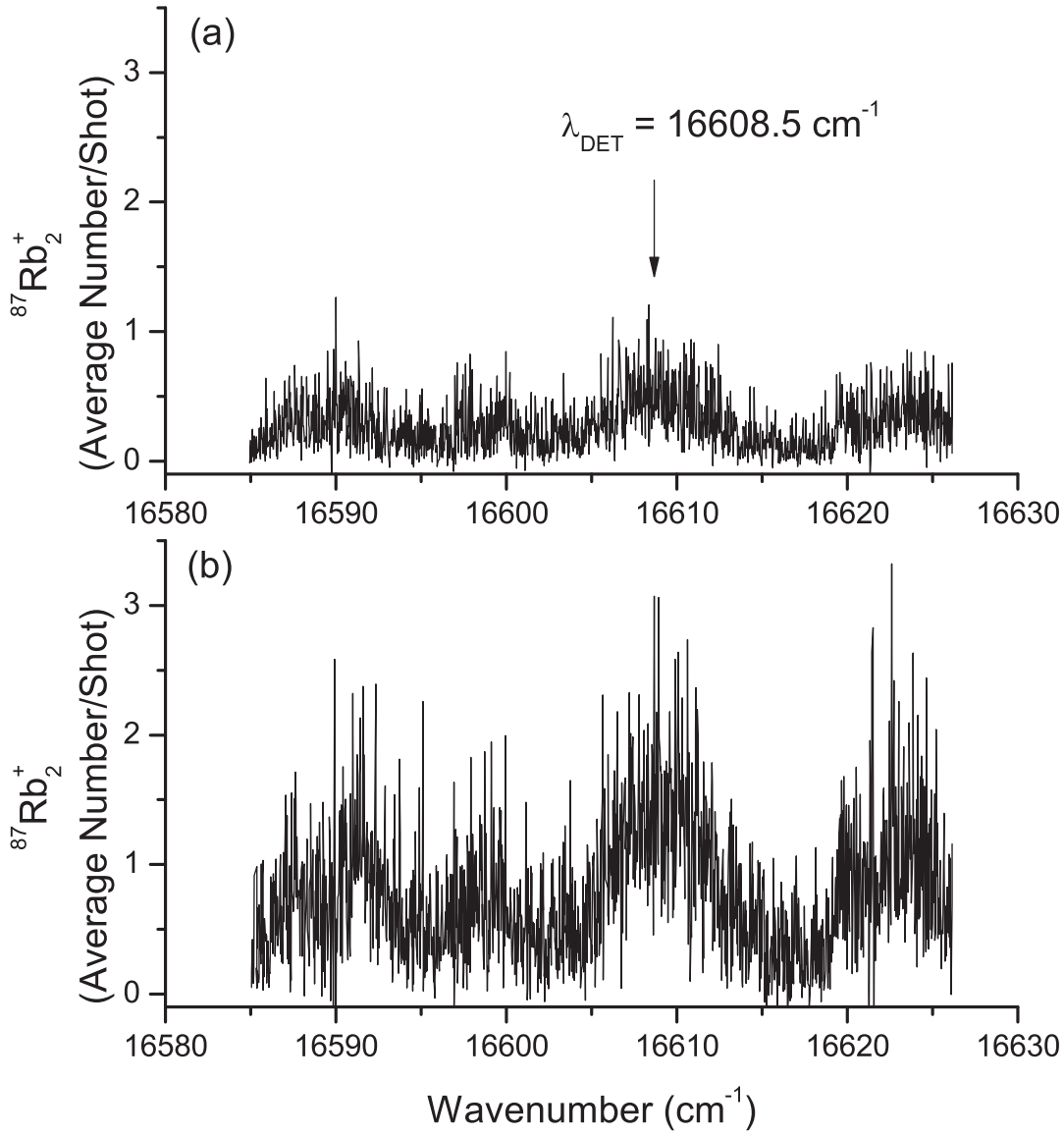

Figure 5.6. REMPI Scans

(a) MOT-formed $^{87}Rb_2^+$ and (b) unchirped PA $^{87}Rb_2^+$ REMPI scans. The ion counts are averaged over 10 shots and the REMPI laser is stepped by 0.001 nm. The unchirped probe laser has a peak intensity of 105.9 W/cm^2 and is tuned to a PA resonance at -7.79 GHz in (b).

(F'=3) asymptote. The unchirped pulse shows a significant enhancement in the molecular signal relative to MOT-formed molecules only. From these REMPI spectra, we determine the optimum $\lambda_{det} = 16608.5$ cm^{-1}.

5.4.2 Probe Scan

To determine the optimal probe detuning and the unchirped pulse bandwidth, we perform a probe scan with the 15 ns FWHM unchirped pulse at a peak intensity of 105.9 W/cm^2. The resulting molecular signal, after subtracting the MOT background signal, is shown as a function of the center detuning referenced to the PA line 7.79 GHz below the $5S_{1/2}$ (F=2) $\rightarrow$ $5P_{3/2}$ (F'=3) asymptote in figure 5.7. A Lorentzian fit of the data yields a bandwidth of 120 MHz FWHM, significantly more than the transform limit of 29 MHz.

5.4.3 Molecular Formation Rate

Now in addition to the unchirped pulse, we apply the chirps shown in section 5.3 and determine their molecular formation rates. All of the data taken in this section is averaged over 1000 shots. In order to determine the formation rate for these various chirps, we must determine the escape rate, Γ_{esc}, the steady-state number, N(∞), and the photodestruction rate, Γ_{PD}.

First, we turn the MOT off for 7 ms and vary the amount of off-time before the detection pulse to find the escape rate, Γ_{esc}. The resulting normalized decay curve is shown in figure 5.8. We fit the data using equation 3.6 which yields $\Gamma_{esc} = 0.100 \pm 0.004$ ms^{-1}. This rate is determined mainly by the detection beam geometry and is consistent with our previous results [45].

Then we measure the $^{87}Rb_2^+$ signal for various intensities and probe beam on-times. The background MOT-formed $^{87}Rb_2^+$ signal is measured separately and subtracted out. The resulting $^{87}Rb_2^+$ signals are shown in figures 5.9-5.13. All of the curves

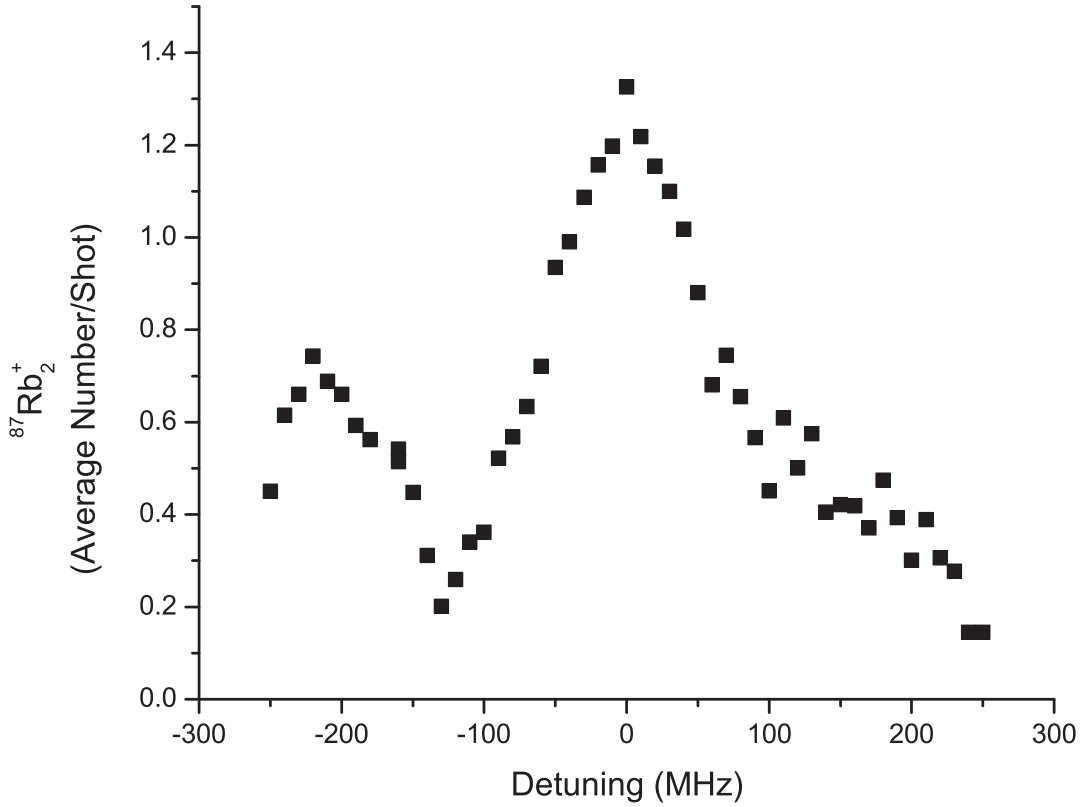

Figure 5.7. Probe Scan

Probe scan to determine the optimal probe detuning and unchirped pulse bandwidth. A Lorentzian fit of the data yields a bandwidth of 120 MHz FWHM. The smaller peak at $\sim$ -220 MHz is likely 1_g (v'=227). The detunings are relative to the PA resonance at -7.79 GHz.

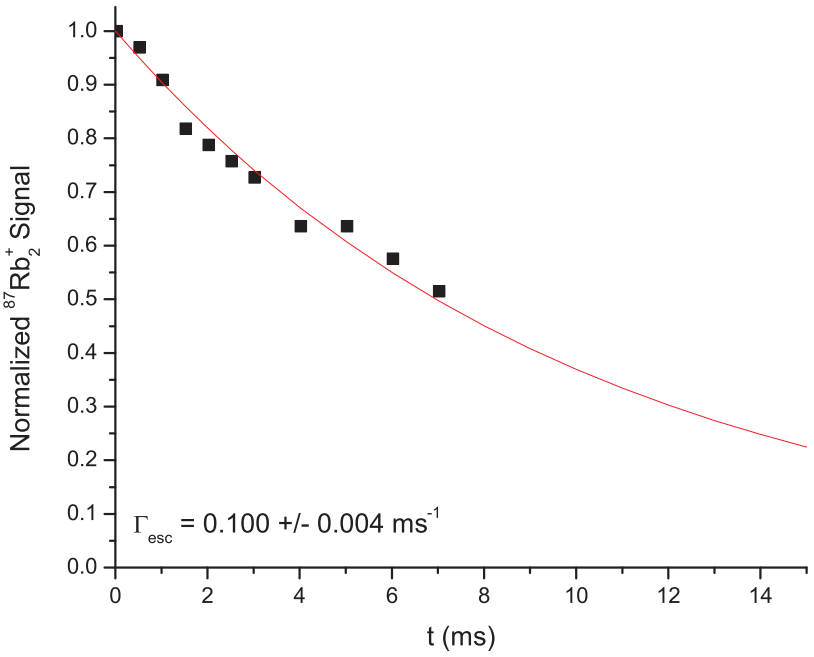

Figure 5.8. Escape Rate

With the MOT off for 7 ms, we measure the $^{87}Rb_2^+$ signal for various amounts of off-time before the detection pulse. A fit of the normalized data yields the escape rate $\Gamma_{esc} = 0.100 \pm 0.004$ ms^{-1}.

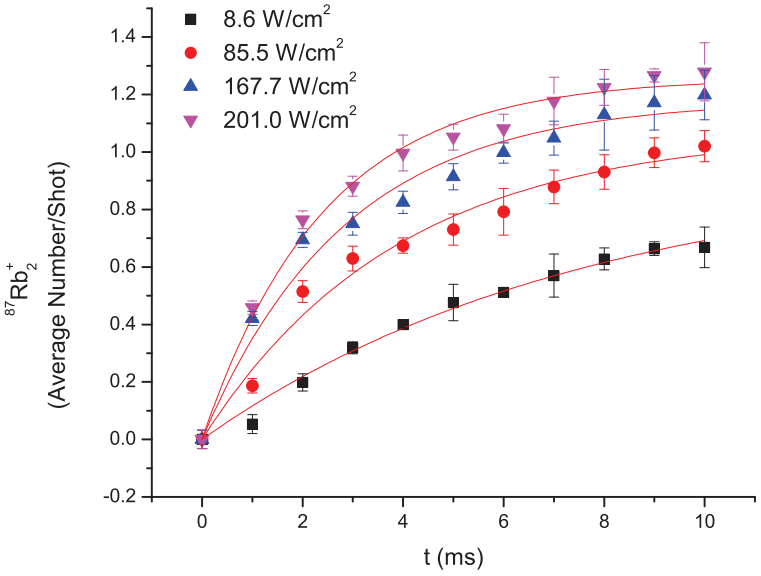

Figure 5.9. $^{87}Rb_2^+$ Signal as a Function of Unchirped Pulse Probe On-time

We measure the $^{87}Rb_2^+$ signal as a function of the probe on-time, t, for unchirped pulses for various peak intensities. Exponential fits yield the steady-state numbers and Γ, from which Γ_{PD} and R can be extracted.

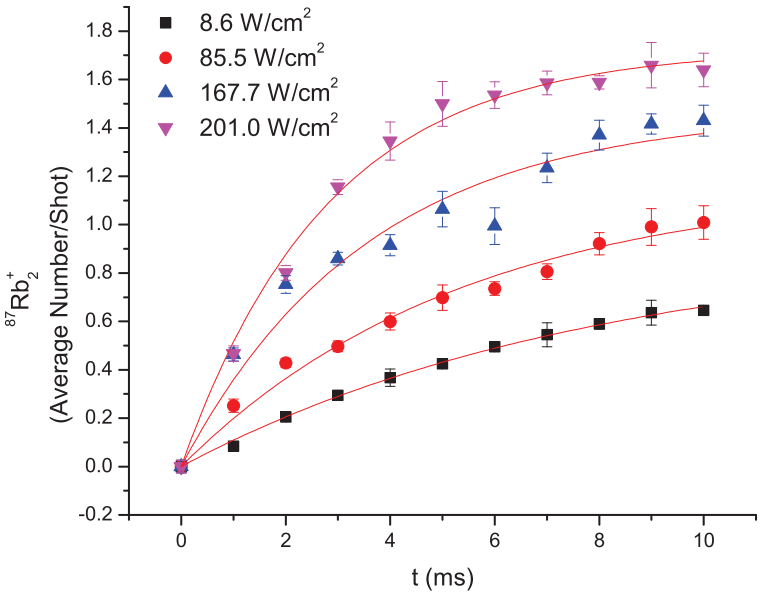

Figure 5.10. $^{87}Rb_2^+$ Signal as a Function of Positive Linear Probe On-time

We measure the $^{87}Rb_2^+$ signal as a function of the probe on-time, t, for positive linear chirps for various peak intensities. Exponential fits yield the steady-state numbers and Γ, from which Γ_{PD} and R can be extracted.

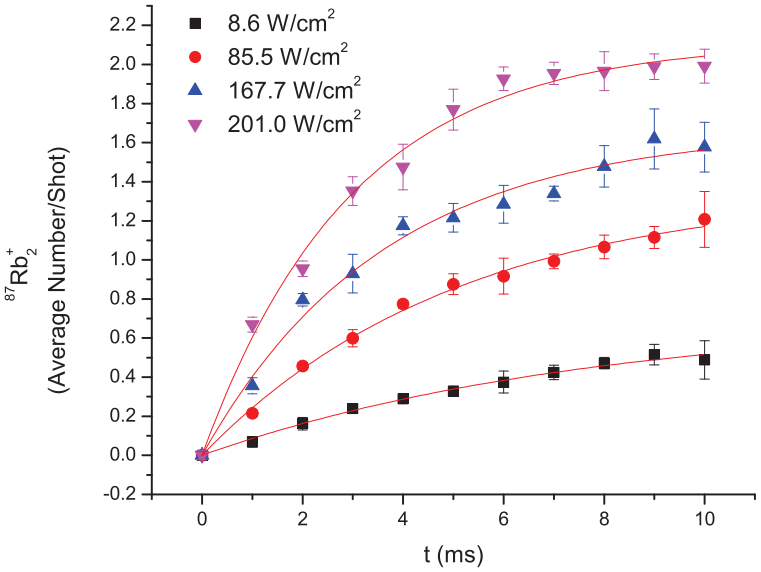

Figure 5.11. $^{87}Rb_2^+$ Signal as a Function of Positive Concave-down Probe On-time

We measure the $^{87}Rb_2^+$ signal as a function of the probe on-time, t, for positive concave-down chirps for various peak intensities. Exponential fits yield the steady-state numbers and Γ, from which Γ_{PD} and R can be extracted.

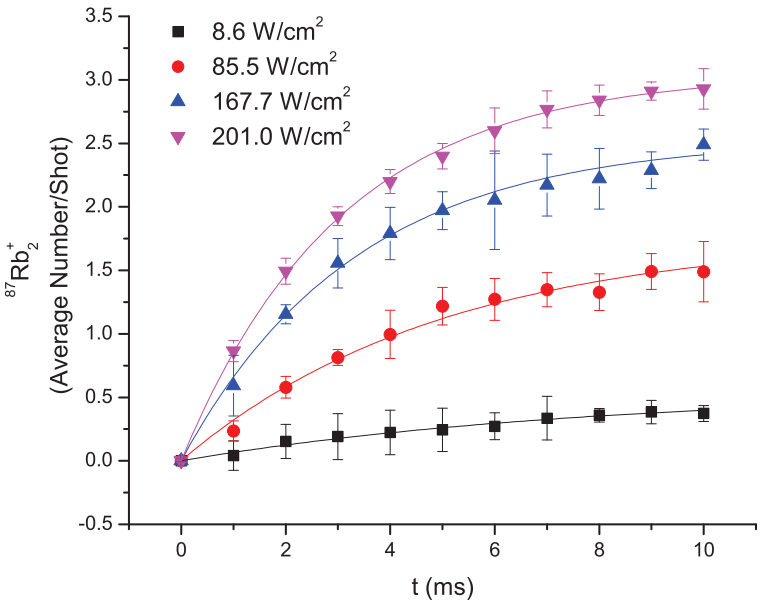

Figure 5.12. $^{87}Rb_2^+$ Signal as a Function of Positive Shaped Probe On-time

We measure the $^{87}Rb_2^+$ signal as a function of the probe on-time, t, for positive shaped chirps for various peak intensities. Exponential fits yield the steady-state numbers and Γ, from which Γ_{PD} and R can be extracted.

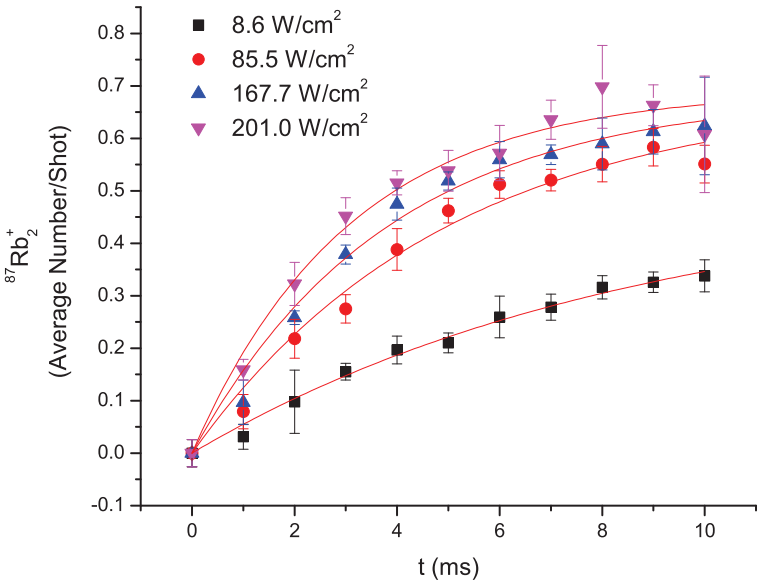

Figure 5.13. $^{87}Rb_2^+$ Signal as a Function of Negative Linear Probe On-time

We measure the $^{87}Rb_2^+$ signal as a function of the probe on-time, t, for negative linear chirps for various peak intensities. Exponential fits yield the steady-state numbers and Γ, from which Γ_{PD} and R can be extracted.

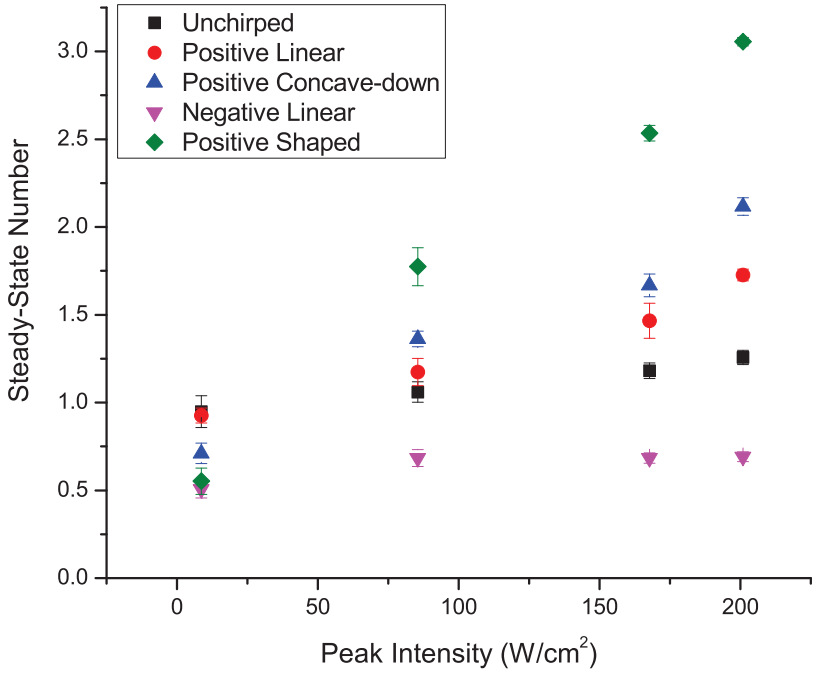

Figure 5.14. Steady-State $^{87}Rb_2^+$

Steady-state numbers for unchirped, positive linear, positive concave-down, and negative linear chirps are shown as function of peak intensity. These values are obtained from fits to the data in figures 5.9-5.13.

increase with increasing PA on-time as well as with increasing intensity. Exponential fits to equation 3.4 yield the steady-state numbers and Γ, from which Γ_{PD} and R can be extracted.

The steady-state numbers, N(∞), as functions of PA peak intensity for the various chirps are shown in figure 5.14. Although there is not very much variation in the steady-state values for unchirped and negative linear chirps, the positive linear and positive concave-down chirps do increase with intensity. This is likely due to the stimulated emission to $a\ ^3\Sigma_u^+$(v"=39) caused by these chirps.

The loss rates as functions of peak intensity are shown in figure 5.15. For the I = 0 point, we use Γ_{esc}. Γ_{PD} is linear with intensity, as expected. The slopes are slightly

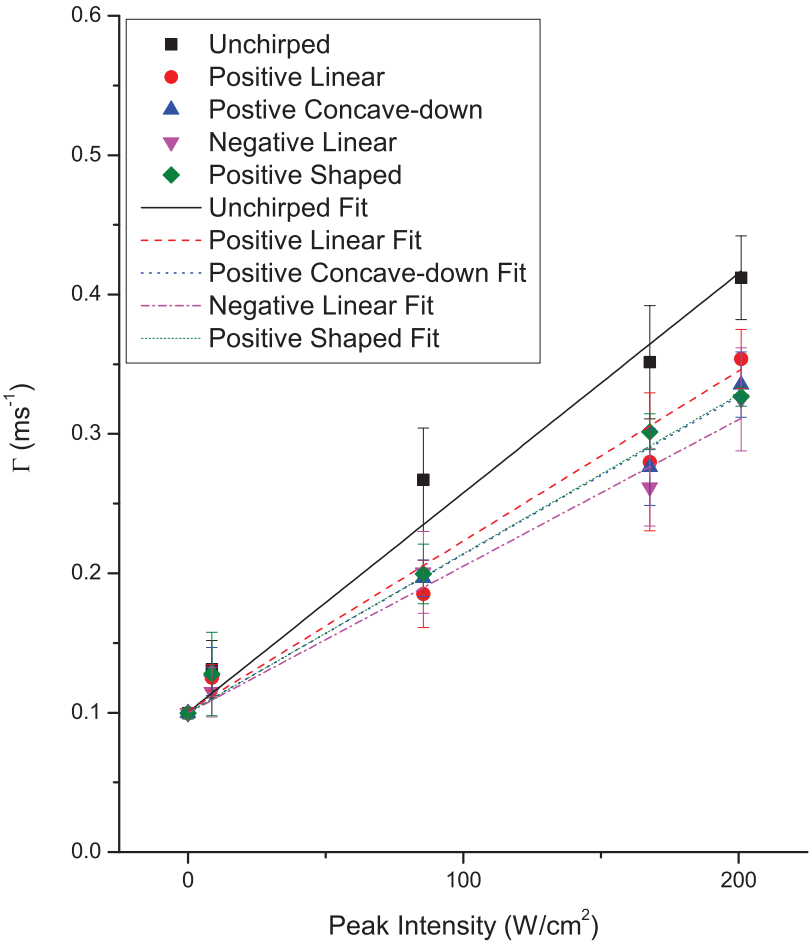

Figure 5.15. Loss Rates

Loss rates for unchirped, positive linear, positive concave-down, and negative linear chirps are shown as a function of intensity. These values are obtained from fits to the data in figures 5.9-5.13 while $\Gamma(0) = \Gamma_{esc}$ is obtained from a fit to the data in figure 5.8. The loss rates are fit well by linear functions.

Simulated Photodestruction Rates (ms^{-1})					
100 W/cm^2					
Starting $a\ ^3\Sigma_u^+$ Vibrational Level	Unchirped	Positive			Negative
		Linear	Concave-down	Shaped	Linear
39	5.07E-03	9.18E-02	1.77E-01	1.88E-01	9.25E-02
200 W/cm^2					
Starting $a\ ^3\Sigma_u^+$ Vibrational Level	Unchirped	Positive			Negative
		Linear	Concave-down	Shaped	Linear
39	1.02E-02	1.84E-01	3.54E-01	3.75E-01	1.85E-01

Table 5.2. Simulated photodestruction rates from various 37.5 ns chirps with an intensity FWHM of 15 ns and peak intensities of 100 and 200 W/cm^2.

Photodestruction rates resulting from unchirped pulses, positive linear chirps, positive concave-down chirps, positive shaped chirps, or negative linear chirps are included. These simulation results are based on the probabilities from table 4.12.

different for the various chirps. Extracting the quantum mechanical simulation results from the photodestruction probabilities for $a\ ^3\Sigma_u^+$ (v"=39) (table 4.12), we find the values presented in table 5.2. Although these results are on the same basic scale as the experimental values, the details are quite different. The positive shaped pulses result in the most photodestruction followed by the linear pulses, and then the unchirped pulses. In the experiment, the unchirped pulses resulted in the most photodestruction.

In order to determine the behavior at various intensities, not just the four intensities included in the above figures, we measure $^{87}Rb_2^+$ for various intensities with the PA light on for 10 ms, as shown in figure 5.16.

Now, having determined N(∞), Γ_{esc}, and Γ_{PD}, the formation rate, R, can be determined from equation 3.4. Finally, we plot R as a function of peak intensity in figure 5.17 (a). The corresponding molecular formation rates from the quantum mechanical simulations are shown in figure 5.17 (b). Although the details and overall scales are slightly different, the quantum mechanical simulations show a similar trend to that seen in the experiments. Although both experimentally and with the simulations at low intensities the unchirped pulse is dominant, whereas the positive chirps have

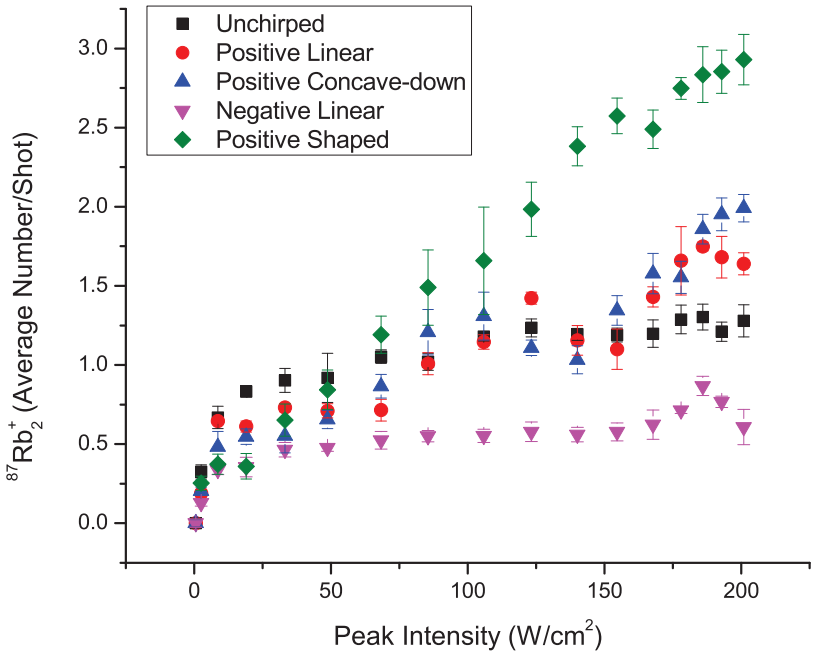

Figure 5.16. $^{87}Rb_2^+$ as a Function of Peak Intensity

Average $^{87}Rb_2^+$ per shot as a function of peak intensity. The probe laser is on for 10 ms.

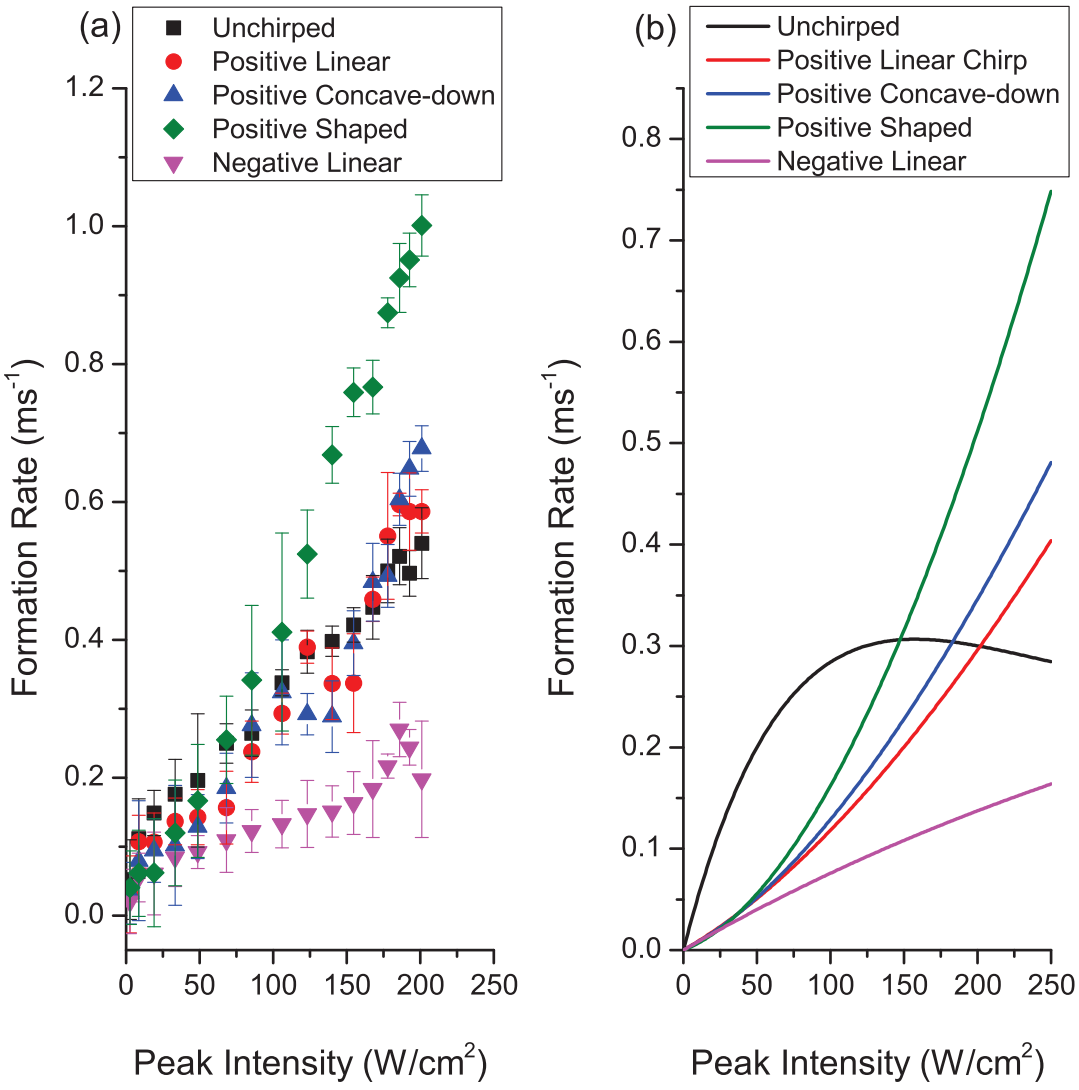

Figure 5.17. Formation Rates

$^{87}Rb_2^+$ formation rates, R, as a function of peak intensity experimentally (a) and from the quantum mechanical simulations (b) (repeat of figure 4.32(b)). Experimentally, R is determined from the data in figures 5.8-5.16.

Chirp	$\mathbf{R/R}_{unc}$
Unchirped	1
Positive Linear	1.09
Positive Concave-Down	1.25
Positive Shaped	1.85
Negative Linear	0.37

Table 5.3. Normalized Formation Rates

Formation rates at 201 W/cm^2 relative to that for the unchirped pulse.

a higher formation rate at the higher intensities. A summary of these normalized experimental formation rates are shown in table 5.4.3. As expected, the negative linear chirp has the lowest formation rate. As shown in the quantum mechanical simulations (section 4.5.3), the enhancement of the positive chirps is due to stimulated emission from 0_g^- (v'=78) to $a\ ^3\Sigma_u^+$ (v"=39). In our previous work [45], the positive chirp yielded a lower formation rate than the unchirped pulse and according to the simulations, the stimulated emission was similar to the spontaneous emission contribution. In the work presented in this chapter, the positive shaped chirp yields 1.85 times the formation rate of the unchirped pulse at higher intensities and according to the simulations, the stimulated emission is almost 16 times the spontaneous emission contribution, as shown in figure 4.34. This enhancement occurs for the positive shaped chirp even though it is much less efficient at excitation compared to other chirp shapes, especially the unchirped pulse.

We have demonstrated the formation of $^{87}Rb_2^+$ with nanosecond-timescale frequency-chirped pulses. For three of the chirps, the positive linear, positive concave-down, and positive shaped, at high intensities these formation rates are higher than for an unchirped pulse. Compared to our previous work [45], these chirps are larger ($\sim$1.8 GHz vs. $\sim$1 GHz) and faster (37.5 ns vs. 100 ns), and the pulses have shorter duration (15 ns vs. 40 ns) and higher peak intensity ($\sim$200 W/cm^2 vs. $\sim$100 W/cm^2). We

were also able to incorporate some shaping in the positive concave-down and shaped chirps. These factors combine to increase the contribution of stimulated emission and minimize the role of spontaneous emission, causing the positive chirps to be the most efficient for molecule formation.

Chapter 6
Conclusions/Outlook

6.1 Conclusions

In summary, we have presented results on the effects of nanosecond-timescale frequency-chirped laser light on the formation of ultracold ground-state molecules. We studied these effects through quantum mechanical simulations and through photoassociation experiments.

Using quantum mechanical simulations, we investigated:

1. ultracold atomic trap-loss collisions, examining the dependencies on chirp direction, chirp shape, and the center detuning. The loss rate for the negative chirp has a chirp shape dependence for certain center detunings while the positive chirp shows very little dependence on chirp shape. This dependency is attributed to the coherent return of collisional flux to the ground state as the resonant radius for excitation follows the accelerating excited-state flux inward. The basic trends are in agreement with the results of a corresponding experiment.

2. the formation of ultracold molecules, revealing the mechanism responsible for a significant enhancement of ultracold molecule formation by the positive chirp relative to the negative chirp. Photoassociation to the 0_g^-(v'=78) followed by stimulated emission to $a\ ^3\Sigma_u^+$(v"=39) is responsible for this enhancement. The

relative enhancement is similar to what is seen in the experimental data. Although at these timescales ($\sim$ 1 GHz in 100 ns; 40 ns FWHM), the unchirped pulse has the highest molecular formation rate, extending the chirp range as well as going to faster timescales with higher intensities should further optimize the positive chirp formation rate enhancement.

3. utilizing local control of the phase, gaining further enhancements over a simple linear chirp. We found that the local-control-optimized frequency chirp corresponds to a near instantaneous jump from the continuum-to-excited-state transition to the excited-state-to-bound-state transition. By combining two local-control-optimized beams to drive transitions to and from different excited states, we can gain further improvement.

Experimentally, we investigated:

1. MOT-formed molecules. We examined the dependency of the number of MOT-formed molecules detected on the number of MOT atoms as well as MOT-formed molecule REMPI scans.

2. $^{87}Rb_2^+$ formation rates with unchirped, positive linear, positive concave-down, positive shaped, and negative linear chirps. Although at low intensities the unchirped pulse still dominates, at 201 W/cm^2, all of the positive chirps were found to have a higher formation rate than the unchirped pulse or negative linear chirp. In particular, the positive shaped chirp formation rate is 1.85 times the unchirped pulse formation rate.

6.2 Future/Outlook

There are a number of interesting avenues to investigate on the horizon. Experimentally, adding an intensity modulator and corresponding amplifier as well as

upgrading the electronics will provide faster chirps with the time resolution for a variety of atomic and molecular experiments. Incorporating 795 nm lasers to address the Rb D_1 line will give rise to further opportunities. For the photoassociation experiments, optimizing the detuning (below the D_2 or D_1 lines), chirp range, chirp rate, and intensity could significantly enhance the molecular formation rate.

6.2.1 Future Simulations

With the current simulations code (both for the collision simulations and for the molecular formation rate simulations), we have just started investigating the vast parameter space. Exploring different chirp shapes, rates, ranges, and detunings should provide useful insight into interesting parameters to explore experimentally. Incorporating and optimizing intensity modulation throughout the chirp should also enhance various parameters of interest for atomic and molecular experiments. For extensions of molecular formation simulations, in particular, it would be useful to include minimization of photodestruction as part of the optimization. It would also be interesting to compare the local control optimization to other optimization techniques.

6.2.1.1 Photodestruction

In the photoassociation experiments, we typically use a sequence of pulses. Therefore, it is important to investigate and minimize the photodestruction (PD) of molecules by subsequent pulses. We have already started investigating this effect in the simulations, as shown in section 4.3.6.

As a further step in this direction, we took the local control code, from section 4.4, and added a second channel. This second channel starts with all of the population in the target state, $a\ ^3\Sigma_u^+$(v"=39), and is subject to the same electric field, allowing us to simultaneously monitor the PD rate. We take a weighted sum of the local control optimization for the formation channel and minimization of the PD channel

to find the overall optimal phase. For this weighting scheme, a PD channel weight of zero corresponds to complete weight of the formation rate, R, which leads to the formation rates shown in figure 4.18 and the local-control-optimized phase shown in figure 4.19. Conversely, a PD channel weight of one corresponds to complete weight of the PD channel, leading to almost no formation. Using the equations in section 3.4.3.2, especially for the steady state number of molecules, equation 3.5, we can put together the following table of formation rates, R, photodestruction rates, Γ_{PD}, and steady-state values with and without the escape rate, Γ_{esc}, for various PD channel weights, as shown in table 6.2.1.1. As we give increasing weight to the PD channel, the steady-state number increases. We calculated the steady-state values with and without an escape rate. Currently we do not trap the produced molecules and thus they are able to escape. If one trapped them, one could neglect the escape rate. It is important to note that in the original local control formulation, there is a weighting scheme between the ground state, $a\ ^3\Sigma_u^+$(v"=39), and excited state, 0_g^-(v'=78), as shown in the insert of figure 4.19. In this original formulation, the ground state already had complete weight by the end of the pulse. Adding weight of this second channel adds further weight to the ground state throughout the chirp. Although we only show the values for a peak intensity of 2000 W/cm^2, lower intensities show a similar trend. Clearly, placing higher priority on minimizing the photodestruction of $a\ ^3\Sigma_u^+$(v"=39) leads to a higher steady-state value.

Unfortunately, the phase, and thus frequency, necessary to produce such high steady-state values are quite complicated. Using a PD channel weight of 0.9, and taking a sliding-window FFT, we derive the frequency vs. time shown in figure 6.1. Although the overall structure is quite complicated, perhaps further theoretical investigation will illuminate a more experimentally feasible way to simultaneously

PD Channel Weight	R (ms^{-1})	Γ_{PD} (ms^{-1})	Steady State Number with $\Gamma_{esc} = 0.1$ ms^{-1}	Steady State Number with $\Gamma_{esc} = 0$ ms^{-1}
0	3.22E+01	4.26E-01	6.11E+01	7.55E+01
0.1	2.84E+01	3.81E-01	5.92E+01	7.47E+01
0.2	2.86E+01	3.77E-01	5.99E+01	7.58E+01
0.3	2.86E+01	3.73E-01	6.04E+01	7.66E+01
0.4	2.85E+01	3.70E-01	6.08E+01	7.72E+01
0.5	2.85E+01	3.65E-01	6.12E+01	7.79E+01
0.6	2.83E+01	3.59E-01	6.17E+01	7.89E+01
0.7	2.81E+01	3.50E-01	6.25E+01	8.04E+01
0.8	2.79E+01	3.34E-01	6.42E+01	8.34E+01
0.9	2.75E+01	2.95E-01	6.97E+01	9.33E+01
0.91	2.75E+01	2.87E-01	7.09E+01	9.55E+01
0.92	2.74E+01	2.79E-01	7.24E+01	9.84E+01
0.93	2.74E+01	2.68E-01	7.44E+01	1.02E+02
0.94	2.73E+01	2.55E-01	7.71E+01	1.07E+02
0.95	2.70E+01	2.37E-01	8.02E+01	1.14E+02
0.96	2.66E+01	2.14E-01	8.48E+01	1.24E+02
0.97	2.62E+01	1.83E-01	9.27E+01	1.43E+02
0.98	2.54E+01	1.37E-01	1.07E+02	1.85E+02
0.99	2.19E+01	6.59E-02	1.32E+02	3.32E+02
0.991	2.10E+01	5.69E-02	1.34E+02	3.70E+02
0.992	2.04E+01	4.78E-02	1.38E+02	4.27E+02
0.993	1.99E+01	3.89E-02	1.43E+02	5.11E+02
0.994	1.95E+01	3.03E-02	1.50E+02	6.45E+02
0.995	1.94E+01	2.20E-02	1.59E+02	8.82E+02
0.996	2.00E+01	1.46E-02	1.75E+02	1.37E+03
0.997	2.19E+01	7.71E-03	2.03E+02	2.84E+03
0.998	1.95E+01	7.06E-04	1.94E+02	2.76E+04
0.999	1.19E+00	1.46E-05	1.19E+01	8.16E+04
1	1.65E-06	6.20E-06	1.65E-05	2.66E-01

Table 6.1. Simulation Formation Rate, Photodestruction Rate, and Steady-State Numbers

Results of local control simulations with a second photodestruction channel with various weights. The resulting formation rates, photodestruction rates, and steady-state numbers are given for a peak intensity of 2000 W/cm^2.

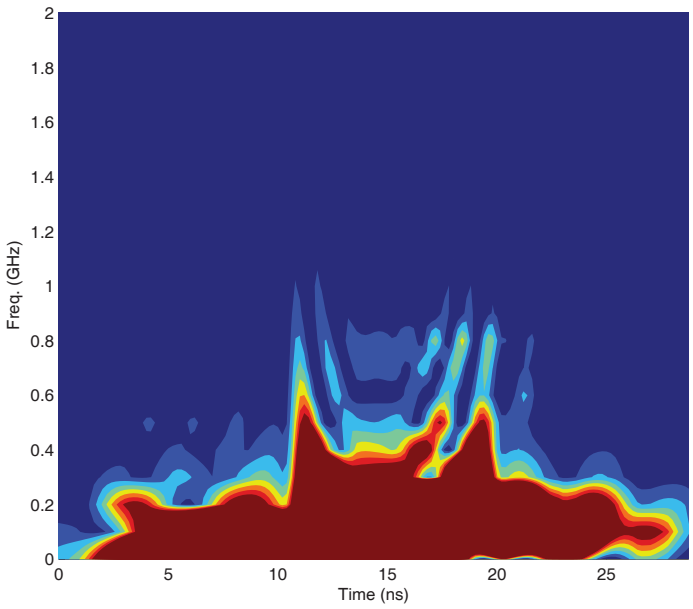

Figure 6.1. Sliding-window FFT of Local-Control-Optimized Phase

Sliding-window FFT of the Gaussian pulse with the optimizing phase pattern resulting from the local-control-optimized phase to minimize photodestruction of molecules in the $a\ ^3\Sigma_u^+$(v"=39) state. The width of the sliding window is 15 ns and the 15 ns FWHM intensity pulse is centered at 14.375 ns. Only absolute values of relative frequency are shown, with zero frequency corresponding to the initial frequency located at the transition from the continuum to 0_g^-(v'=78). The weight of the separate photodestruction channel is 0.9 and the peak intensity is 2000 W/cm^2.

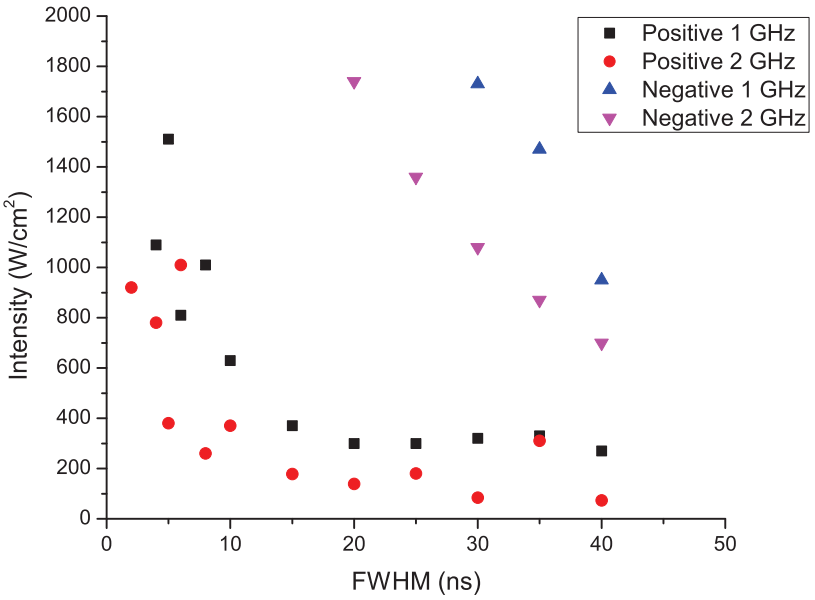

Figure 6.2. Fixed Formation Rate Intensity Scaling

We fix the formation rate at 0.1 ms^{-1} and determine the necessary intensity for various FWHMs as well as 1 and 2 GHz positive and negative chirps.

maximize the molecular formation rate while minimizing the photodestruction. Continuing these investigations would be invaluable to future experimental endeavors.

6.2.2 Intensity Scaling

As we incorporate faster pulses, we will need to increase the peak intensity to maintain the same pulse energy. To this end, we investigated in the simulations the necessary intensity to keep a fixed molecular formation rate, 0.1 ms^{-1}, for various chirps. We fixed the chirp range to be either 1 or 2 GHz for positive or negative linear chirps. We fixed the Gaussian intensity pulse FWHM to be 0.4 times the chirp time and to be always centered on the center of the chirp which is tuned to the transition from the continuum to 0_g^-(v'=78). Preliminary results on the necessary intensities as a function of pulse FWHM are shown in figure 6.2. As expected, as

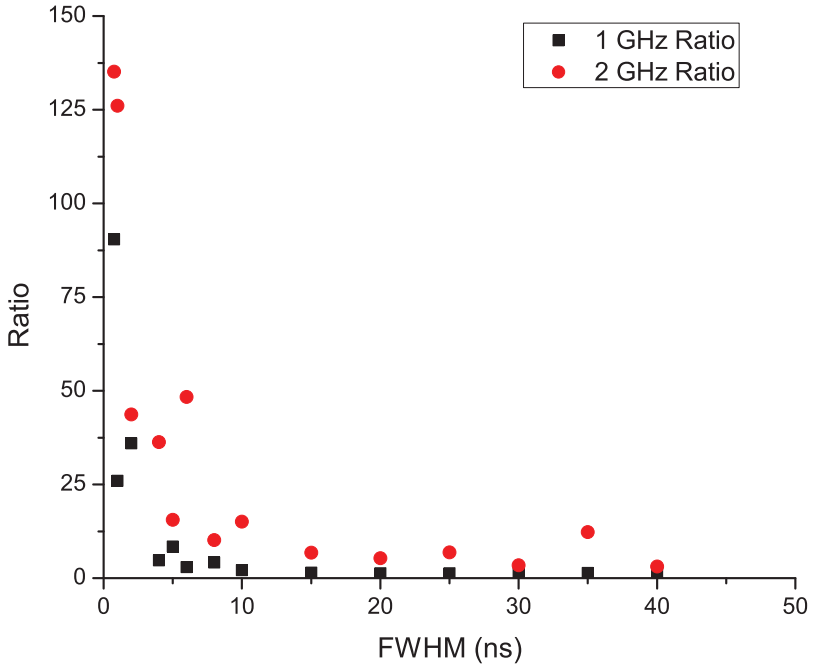

Figure 6.3. Ratio of Molecular Formation Rates for Positive and Negative Chirps

The ratio of molecular formation rates for positive and negative chirps at the intensity necessary for the positive chirp to achieve a formation rate of 0.1 ms^{-1} for various intensity pulse widths.

we go to shorter pulses, we need to increase the peak intensity. Also, as expected, the 2 GHz positive chirp requires the least intensity to obtain the same formation rate. The scatter in the points for the positive chirps appears to be from destructive interference occurring in the stimulated emission channel, but further investigation would be necessary to find the root cause.

Now, keeping the intensities and formation rates for the positive chirps fixed, we find the corresponding formation rates for the same intensities for the negative chirps. Then we find the ratios between the positive and negative chirp formation rates shown in figure 6.3. As we go to shorter intensity pulses, although we do need higher intensities to achieve the same formation rate, the coherent stimulated emission contribution increases, thereby increasing the ratio between the positive and

negative chirps. Using longer chirps, such as a 2 GHz linear chirp that goes through the 0_g^-(v'=78) $\rightarrow$ $a\ ^3\Sigma_u^+$(v"=39) transition, further enhances this effect.

6.2.2.1 Intensity Modulation

Incorporating intensity modulation will give us greater control over the intensity for each local frequency, which could potentially lead to significant enhancements for many atomic and molecular experiments. For the molecular formation rate simulations, it could be quite advantageous to have more intensity on both the excitation step ($a\ ^3\Sigma_u^+$ continuum $\rightarrow$ 0_g^-(v'=78)) and the stimulated emission step (0_g^-(v'=78) $\rightarrow$ $a\ ^3\Sigma_u^+$(v"=39)). Having independent intensity control would allow us to cover both of these transitions independently without needing a particular chirp rate.

This enhanced control also lets us explore counterintuitive pulse orders corresponding to stimulated Raman adiabatic passage (STIRAP) [126]. As a preliminary investigation, we study the molecular formation rate for two fixed frequencies (corresponding to the resonances $a\ ^3\Sigma_u^+$ continuum $\rightarrow$ 0_g^-(v'=78) and 0_g^-(v'=78) $\rightarrow$ $a\ ^3\Sigma_u^+$(v"=39)) delayed by one pulse width (15 ns). We perform the simulations in the intuitive and counterintuitive order and extend the simulations to large intensities. At currently feasible peak intensities ($\leq$ 200 W/cm^2), the counterintuitive order yields an order of magnitude less molecules than the intuitive order. Extending to much larger peak intensities, the counterintuitive order does better than the intuitive order, starting at about 6.74*10^5 W/cm^2, as shown in preliminary results in figure 6.4. Further investigation into the validity of the simulations at such high intensities, the effect of varying the pulse delay, and the addition of frequency chirps instead of fixed frequencies is needed. Although at first glance, this seems like a tremendous amount of intensity, and is certainly well beyond our current experimental capabilities, implementing a pulsed amplifier in a Ti-sapphire crystal [127] pumped by the second

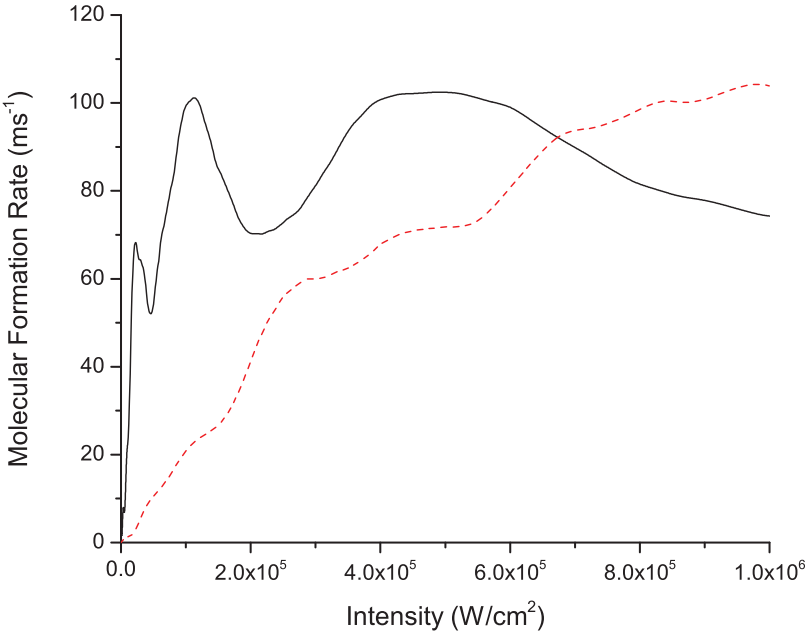

Figure 6.4. Preliminary STIRAP Results

Molecular formation rate for two frequencies delayed by one pulse width (15 ns) for the intuitive pulse order (solid black line) and counterintuitive pulse order (dashed red line).

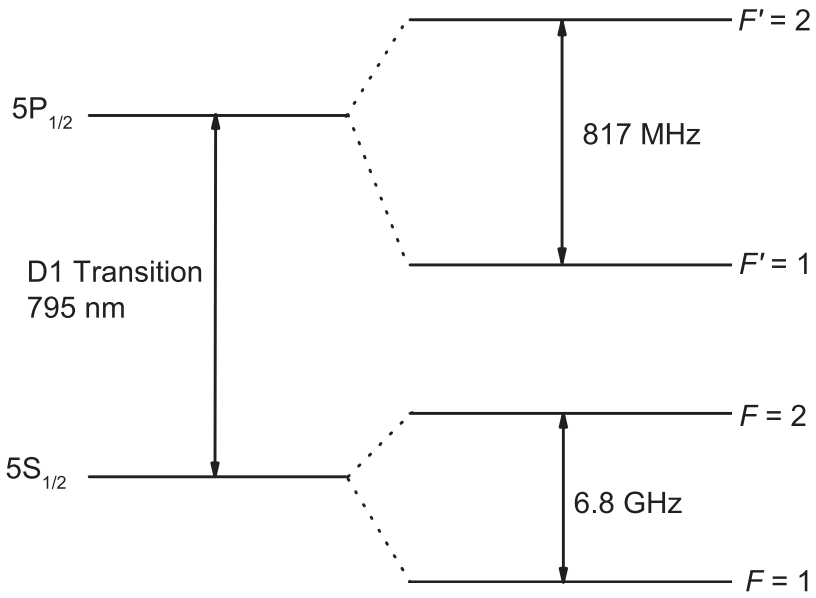

Figure 6.5. ^{87}Rb D1 Transitions

Energy level diagram for ^{87}Rb atoms showing hyperfine levels F of the ground electronic state ($5S_{1/2}$) and hyperfine levels F' of the electronic excited state ($5P_{1/2}$).

harmonic of our Nd:YAG could provide peak intensities $> 10^6$ W/cm^2. Employing STIRAP by itself or in conjunction with other chirped pulses could significantly increase the molecular formation rate.

6.2.3 The D_1 Line

Performing experiments near the D_1 line is appealing primarily due to having fewer hyperfine levels present. The potentials are primarily attractive, so conducting experiments (or simulations) in this regime would more closely correspond to a system with a single excited state. Reducing the expansive parameter space currently under investigation below the D_2 line would make coherent control experiments easier to perform and interpret. The hyperfine energy levels for ^{87}Rb D_1 line are shown in figure 6.5. There are fewer hyperfine levels than for the D2 line (figure 2.2). The

hyperfine structure for ^{85}Rb is also less complicated for the D_1 than for the D_2 line.

6.2.3.1 795 nm Lasers

In order to address the D_1 line, as shown in figure 6.5, the lasers have to be tuned to 795 nm. We found the most cost-effective and highest power solution to be 808 nm diodes that could be cooled to 795 nm. Unfortunately, diodes typically tune $\sim$ 1 nm per 4° C, so going from 808 nm to 795 nm requires quite a bit of cooling. We designed ECDL and FRDL enclosures that could be flushed and cooled to sub-zero temperatures to reach the desired wavelength. The mechanical drawings are shown in section A.1. For both laser designs, the aluminum housing incorporates water cooling for the dual stage thermo-electric cooler (TEC) and valves for flushing. The master laser window had to be carefully positioned to account for the angle change due to the wavelength. During assembly, one has to be careful to use water-free components in order to avoid condensation. Once the lasers are set up, they are lightly baked ($<$ 40° C) and flushed with nitrogen to remove any water. The length of time to bake and flush varies with lab humidity levels, but is typically 3 hours. Once the laser is water free and sealed, the cooling begins. For the particular diode we ended up using, Sanyo DL-8031-031A, rated at 160 mW, we found going to a temperature of $\sim$ -23° C ($\sim$ -31° C for the slave) was sufficient to be near the resonance at 795 nm. During the setup for the master laser, the grating has to be adjusted at sub-zero temperatures. There are two small holes with screws that can be briefly removed to adjust the horizontal and vertical grating positions. If these holes are opened for too long, one needs to go back to room temperature, re-flush and bake, and then cool down again.

Currently we have built two of these master lasers and one slave laser. For a master laser, a saturated absorption setup was put together as a precursor to locking.

While scanning the PZT, we were able to see saturated absorption features for the D1 line. These three 795 nm lasers are incorporated into the probe setup (section 3.3) through a network of flip mirrors.

6.2.3.2 Frequency-chirped photoassociation below the $5S_{1/2} + 5P_{1/2}$ asymptote

Using the 795 nm lasers to perform photoassociation below the $5S_{1/2} + 5P_{1/2}$ asymptote has many advantages. The current experiments and simulations below the D_2 line show relatively low molecular yields due to unfavorable Franck-Condon factors. The long range 0_g^- potential for the D_1 line has R^{-6} character leading to more favorable Franck-Condon factors to the ground state. Excited Rb_2^* that has been photoassociated below the D_1 line will not undergo the fine-structure predissociation that can happen below the D_2 line. Thus photoassociating below the D_1 line is likely to enhance ground-state molecule yields. Furthermore, implementing the techniques described below in section 6.2.4, will give more intensity and further control over the frequency-chirped pulses. The combination of these techniques and photoassociating below the D1 line could significantly enhance our ground-state molecule yield.

6.2.4 Faster Chirps, Intensity Modulation, Amplification, and Optimization

Quite a bit of effort has been spent on expanding the current capabilities. Increasing the resolution and speed capabilities of the phase modulation, adding intensity modulation, and adding more overall intensity through amplification are important steps towards future experiments. In this section, phase modulation extensions, intensity modulation, and amplification by tapered amplifiers will be discussed.

Approx. Linear Chirp Time (ns)	7 Cycles		4 Cycles	
	$\sim \Delta$f (GHz)	V_{pp} (V)	$\sim \Delta$f (GHz)	V_{pp} (V)
60	1.1	6.5	1	9.8
30	1.5	5	1.1	6
15	1.4	2.5	1	3
10	1.2	1.25	1.2	2.25

Table 6.2. Δf and AWG Output Voltages for Various Chirp Times

Peak-to-peak voltage, V_{pp}, necessary to create $\geq$ 1 GHz linear chirps on various time scales with 4 or 7 loop cycles with the PM unterminated. The approximate frequency chirp range, Δf, is derived from the heterodyne signal.

6.2.4.1 Phase Modulation Extensions

For the experiments presented in this thesis a 7 m fiber delay line with four self-injection loops in the probe setup (section 3.3, figure 3.11) is used in order to have a short repetition time of 450 ns. Adjusting the fiber delay line, the number of self-injection loops, and the voltage, allows quite a bit of flexibility in the chirp parameters. For example, we also investigated chirps using a longer 40 m delay line, which allows an $\sim$180 ns window for chirps. A summary of the number of self-injection cycles and peak-to-peak voltage necessary to create $\geq$ 1 GHz linear chirps on various time scales using the 40 m delay line is given in table 6.2.4.1. The derived instantaneous frequency from heterodyne signal analysis (section 3.3.3) is shown in figure 6.6. With the current technology, chirps going 1 GHz in $\leq$ 10 ns is quite feasible. The current loop setup is good for chirps on the 10 to 60 ns timescale. Upgrading to a faster AWG (with corresponding faster diagnostics) and being able to apply more voltage to the modulator would allow even faster chirps and further control. If one desires chirps only a few ns in duration, one could switch to a single-pass configuration since enough voltage could be applied without the need for multiple injection loops. The phase modulator can also be used to produce multi-line spectra with peak spacings in the 100 MHz range as described in reference [128].

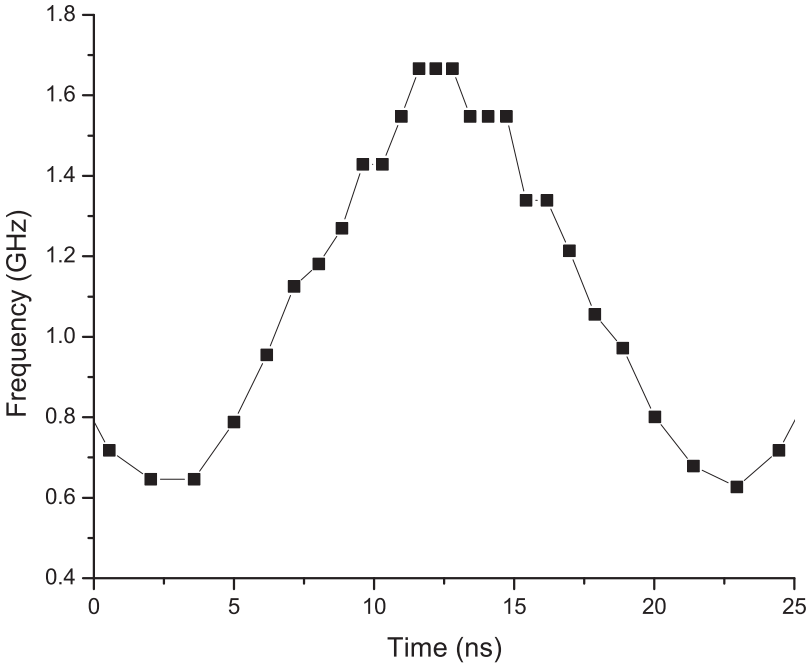

Figure 6.6. $\leq$ 10 ns Chirp

Instantaneous frequency vs. time as derived from the heterodyne signal.

6.2.4.2 Intensity Modulation

Experiments incorporating faster chirps will need to generate correspondingly faster intensity pulses too. The current probe setup (figure 3.11) incorporates a 200 MHz AOM which can produce Gaussian pulses with FWHM $\geq$ 11 ns. In order to produce faster pulses or to incorporate any pulse shaping, we will need to use an intensity modulator. Our intensity modulator (EO Space AZ-0K5-05-PFA-PFA-790) is a "Z-cut" fiber-coupled lithium niobate waveguide device. The main disadvantage to the "Z-cut" style is a residual phase modulation with the intensity modulation. This residual phase modulation is characterized in reference [129]. "X-cut" modulators are also available without the residual phase modulation, but these typically have higher insertion loss and require higher drive voltages. When used in conjunction with a phase modulator, the residual phase modulation can be compensated, as described in reference [129]. Using the current 240 MHz AWG, pulses can be a couple of ns FWHM, such as the $\sim$2.5 ns FWHM pulse shown in figure 6.7. Modulating the intensity in an arbitrary way allows one to control the intensity at various frequencies during a chirp. Not being restricted to a single Gaussian intensity pulse allows the flexibility and control necessary for many experiments.

6.2.4.3 Tapered Amplifier

One of the disadvantages of the phase and intensity modulators is their low input damage threshold of 5 mW CW. The probe setup described in section 3.3 gets around this limitation by injecting the phase modulated light into a slave, gaining full intensity while maintaining the frequency modulation. For single-pass setups, without injecting the light into a slave, the resulting phase- and amplitude-modulated pulse needs to be amplified. One such method is using a tapered amplifier (TA).

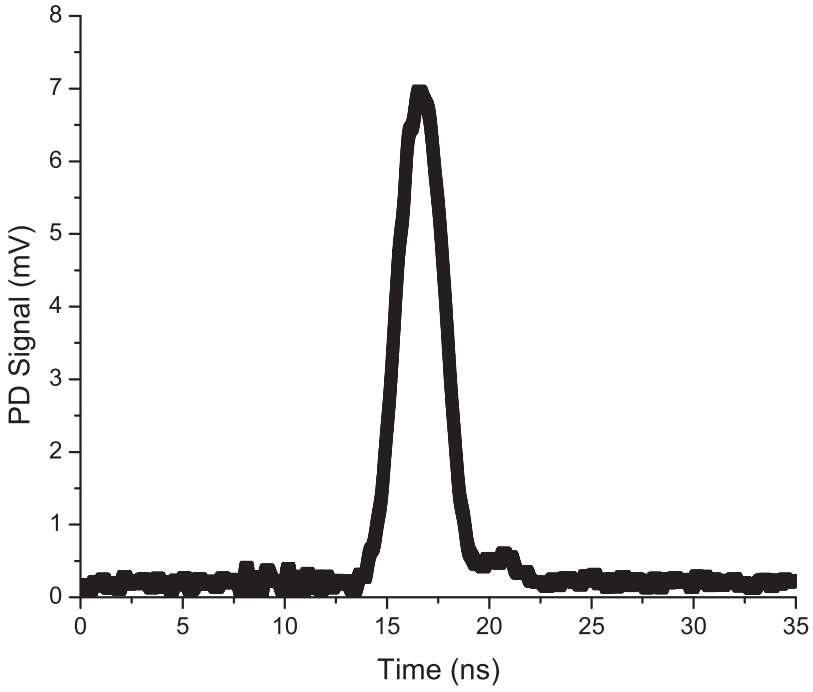

Figure 6.7. ∼2.5 ns FWHM Intensity Pulse

A fast intensity pulse using the intensity modulator. A Gaussian fit of the pulse yields a ∼2.5 ns FWHM.

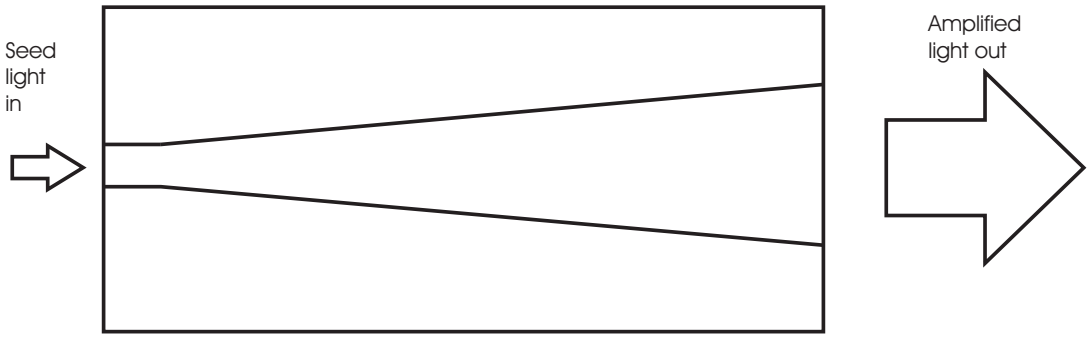

Figure 6.8. Tapered Amplifier (TA) Schematic

Simplified top-view schematic of a TA chip. Seed light is injected through a narrow aperture (typically ≤ 3 μm wide) into the rear facet, entering a short, straight index-guided waveguide section (typically ~ 0.5 mm long). This straight section ensure that only the fundamental transverse mode is excited. Then the light is coupled into a longer gain-guided tapered section (typically ≤ 3 mm long). Expanding into this taper section enables high power while maintaining single-mode operation. The amplified output is emitted through an aperture (typically ~ 200 μm wide) in the front facet. The angle (typically $\sim 6°$) of the taper is chosen so that the beam from the straight section diffracts and expands to fill the entire tapered region.

A TA chip is a semiconductor device that can achieve high power while retaining the narrow linewidth and stability of the seed laser. When unseeded, the amplified spontaneous emission (ASE) covers a broad range (30 nm). Typically the TA has a gain of at least 13 dB at the peak of the gain curve ($\sim$ 8 nm FWHM). The chips themselves are very small (the emission planes are typically a couple of mm), so they are often mounted on C-Mounts. A schematic of the TA chip is shown in figure 6.8. ASE is emitted in both directions, with significantly more on the output end due to the taper.

We designed and constructed a homemade TA setup based on reference [130]. A more recent, updated, and detailed description is given in reference [131]. A diagram of our setup is shown in figure 6.9. The mechanical drawings for the TA mounts are shown in section A.2.1. Two aspheric lenses (one to focus the input seed light and one to collimate the TA output) are housed in the oxygen-free high-conductivity (OFHC)

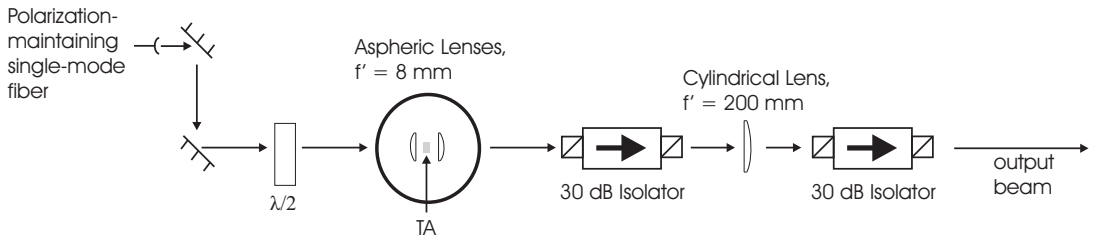

Figure 6.9. TA Setup

The seed light for the TA comes from a single-mode polarization-maintaining fiber. The polarization of this seed light is matched to the TA using a half-waveplate. The light is focused onto the TA chip using an f' = 8 mm aspheric lens. The output of the TA is roughly collimated using another f' = 8 mm aspheric lens. Due to the rapid asymmetric divergence of the TA, an f' = 200 cylindrical lens is used to correct the astigmatism. The output of the TA also goes through a total of 60 dB of isolation to protect against backwards coupling and damage to the TA chip.

copper assemblies. The choice of OFHC copper is important since it is in direct thermal and electrical contact with the TA C-mount. The copper blocks are mounted on top of two stages of TECs inside a water-cooled aluminum housing. We found that two stages of TECs were necessary to prevent alignment drifts due to thermal expansion of the metal. It is crucial to apply a thin layer of thermally conductive paste along both the TEC-copper and TEC-aluminum interfaces. The output of the TA chip is highly divergent, asymmetric, and astigmatic. Typically the beam divergence is very different for the two transverse directions with the beam diverging more in the vertical direction than in the horizontal direction. The aspheric lens collimates the output beam in the vertical direction while an AR-coated cylindrical lens collimates the horizontal component. TA chips are very sensitive to optical feedback, so great care is taken to minimize retroreflections by aligning 60 dB of optical isolation to prevent light from entering the front facet of the TA. It is important to use isolators that can accommodate large beam diameters (typically ~ 5 mm) due to the divergence and larger beam size of the TA light. The aluminum housing with Brewster angle windows helps keep the TA in a dust free environment. TAs are also very sensitive

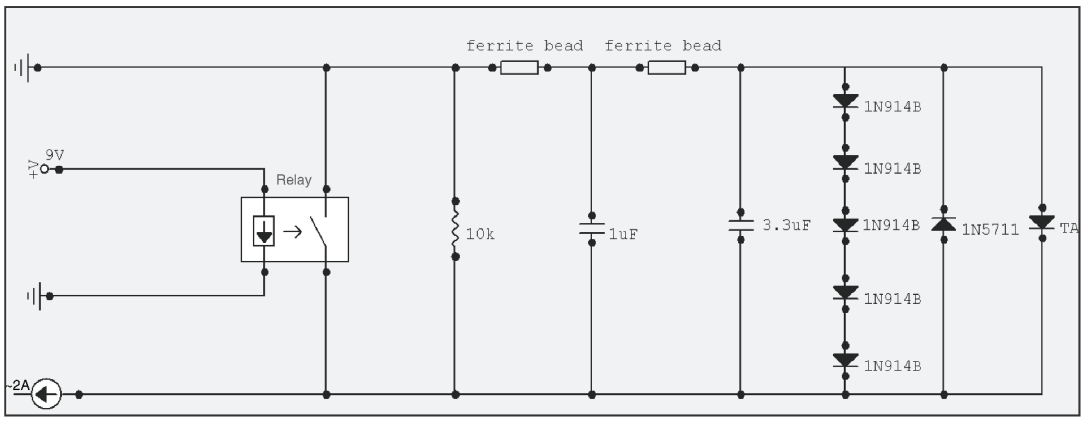

Figure 6.10. TA Electrical Protection Circuit

The TA electrical protection circuit employs various diodes to prevent any reverse voltage. A relay switch grounds the TA when not in use, diodes protect the TA from forward and backward transients, and the ferrite beads and capacitors form a low-pass filter.

to reverse voltage. Typically they tolerate no reverse voltage. Therefore, we employ an electrical protection circuit, as shown in figure 6.10.

The design was first tested with a 500 mW 795 nm TA (Sacher Lasertechnik TPA-0795-500 with an operating current of 2.3 A). This diode is specified to have at least 37 dB side-mode suppression at 794.9 nm. The electronics for the TA consist of a combined current driver (up to 3 A) and temperature controller (up to +/- 4 A, 32W) (Sacher Lasertechnik PilotPC-3000). The anode of the C-mount is connected to ground through the copper block with a screw holding the C-mount in place. However, for the cathode, a wire needs to be very carefully soldered to the metal wing protruding from the diode. This wire needs to be carefully strain-relieved in order to prevent damage to the chip. There are very delicate and very small electrical wires bonding this metal wing to the chip that can be easily damaged. The first alignment of a TA is not trivial. The author has found it helpful to first use the ASE emanating from the input facet (at very low diode current) to backwards align through the polarization-maintaining single-mode fiber. Then it is helpful to use the

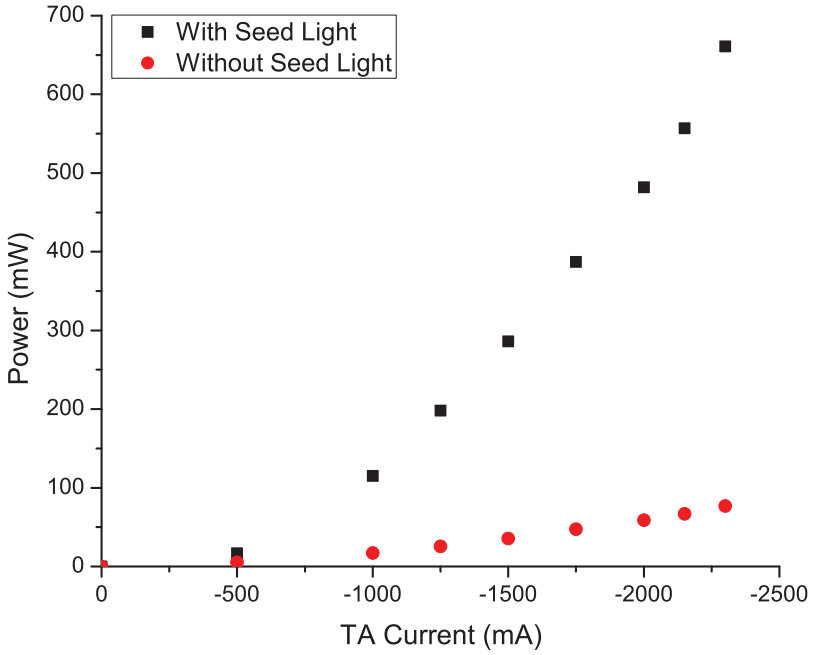

Figure 6.11. TA Output Power vs. Current

The TA output power with and without seed light.

TA as a photodetector to get some initial coupling of the seed light. A photocurrent of 5 or 6 mA indicates sufficient optical coupling. It is important to remember that not only are the focus and alignment important, but also the polarization of the seed light. Once this initial coupling is completed, we slowly increase the diode current initially by 500 mA and then in steps of ∼200 mA while optimizing the output power. Once optimized, with 10.6 mW of CW seed light out of the fiber, we were able to get 661 mW out of the TA (78 mW ASE with seed light blocked) with the TA current at the nominal operating current of -2.3 A. This is a gain of almost 18 dB. The TA output power vs. TA current is shown in figure 6.11. Also shown is the output power without seed light. This ASE has to be carefully measured by quickly blocking and unblocking the seed light since extended periods without seed light can damage the TA chip. A steeper ASE curve would indicate damage to the chip. We reduced the

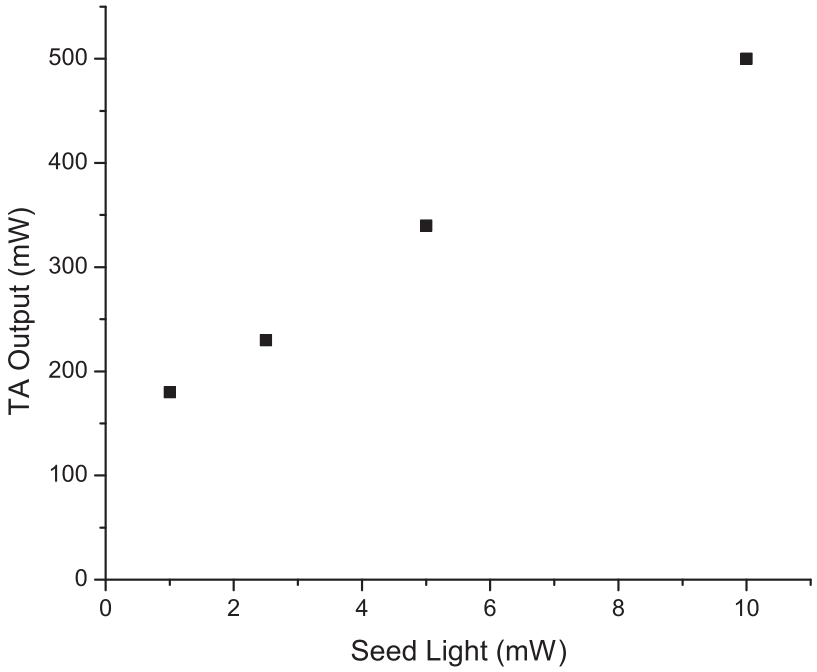

Figure 6.12. TA Output Power vs. TA Seed Light

The TA output power with various amounts of seed light taken at a constant TA current of -2.15 A.

operating current to ensure a maximum of 500 mW out of the TA and measured the output as a function of seed light, as shown in figure 6.12. With this coupling, we can get close to half the maximum output with only 2.5 mW of seed light. With a slightly better optical alignment, we were able to get the full 500 mW out of the TA with 10 mW of seed light at a slightly lower TA current of -2.05 A.

To characterize the TA output, we coupled a small fraction of the output into a polarization-maintaining single-mode fiber using a beam splitter and telescope arrangement. The efficiency of the fiber coupling was found to be only ∼47%. This efficiency is not surprising due to the non-single-mode nature of the TA light. It could be perhaps slightly improved through a more careful matching of the telescope optics, however, most commercial systems only claim ∼50% efficiency. To test the

frequency and amplitude response of the TA, we set up the probe loops (section 3.3) with the 795 nm lasers as described in section 6.2.3.1. Instead of going through the loops, we used the output AOM as a chop AOM and placed the fibers in a single-pass configuration connected to this output fiber. We coupled the output light into the optical heterodyne setup with a 1 GHz photodiode (Thorlabs D400FC) and took measurements of the output of the loop setup with the PM only, with the intensity modulation only, and with both. Then we coupled the output into the TA and took the same set of measurements. A small fraction of the TA output light was coupled into a fiber, as described above, and then that light was coupled into another fiber for the optical heterodyne setup. We had to be careful with the electronic timing to make sure that the time-averaged power for the modulators was ≤ 5 mW and that some light was coupled into the TA most of the time. The TA frequency chirp is shown in figure 6.13(b). The TA reproduced the roughly 1 GHz in 7 ns frequency chirp reasonably well. The TA amplitude pulses are shown in figure 6.14. The TA reproduced the Gaussian fitted FWHM pulses from the probe setup to within 5%. This error is primarily due to the low coupling efficiency into the heterodyne fiber and relatively slow heterodyne detection electronics. The reduction in intensity for the 2.2 ns FWHM pulse is due to the AWG not faithfully following the programmed Gaussian pulse, as well as the resolution of the detection electronics. This would not be a problem if we used faster electronics. Since we are measuring the pulse after a beam splitter coupled into a fiber and then coupled into the heterodyne fiber, the absolute peak power is hard to determine. Rough estimates based on average output power put the peak power for the slowest 22 ns FWHM pulse to be ~ 480 mW and, based on the relative heights from Gaussian fits, that for the 2.2 ns FWHM pulse to be ~ 425 mW. We also took a heterodyne signal applying voltages to both the phase modulator and intensity modulator. Although not trivial to analyze directly,

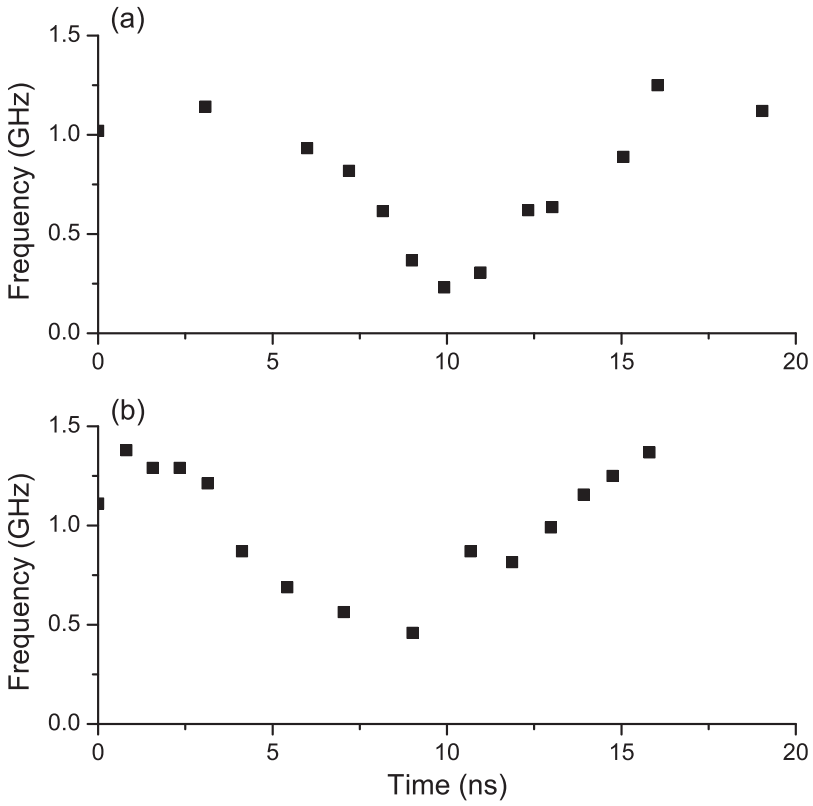

Figure 6.13. TA Frequency Chirp

The instantaneous frequency of the input (a) and of the TA output (b). The time shift is due to electronic delays and the difference in overall frequency is due to a difference in reference laser frequency. The chirps are roughly 1 GHz in 7 ns.

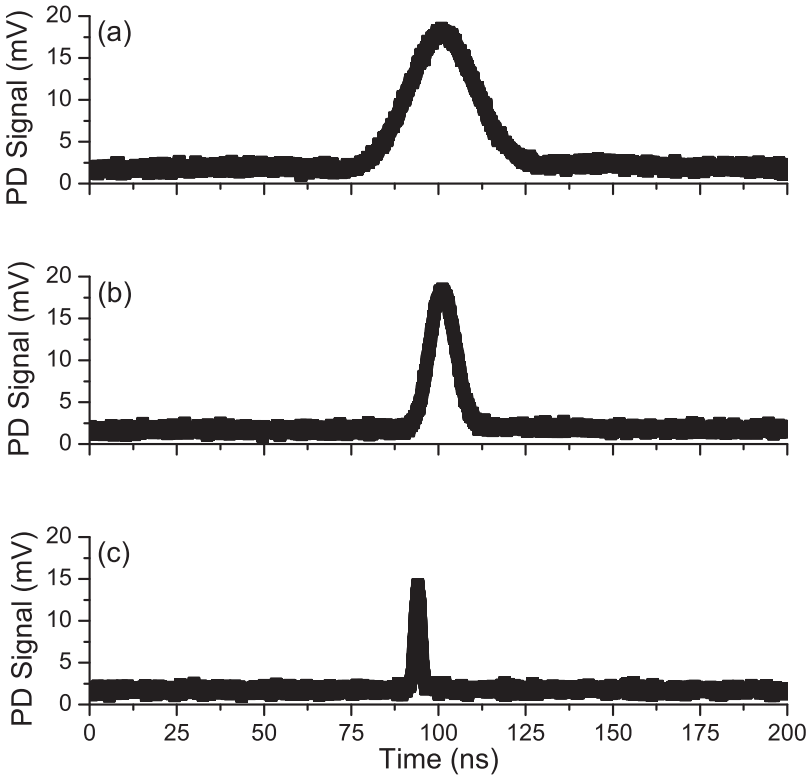

Figure 6.14. TA Pulses

TA output pulses with Gaussian fitted FWHMs of 22 ns (a), 8.69 ns (b), and 2.16 ns (c).

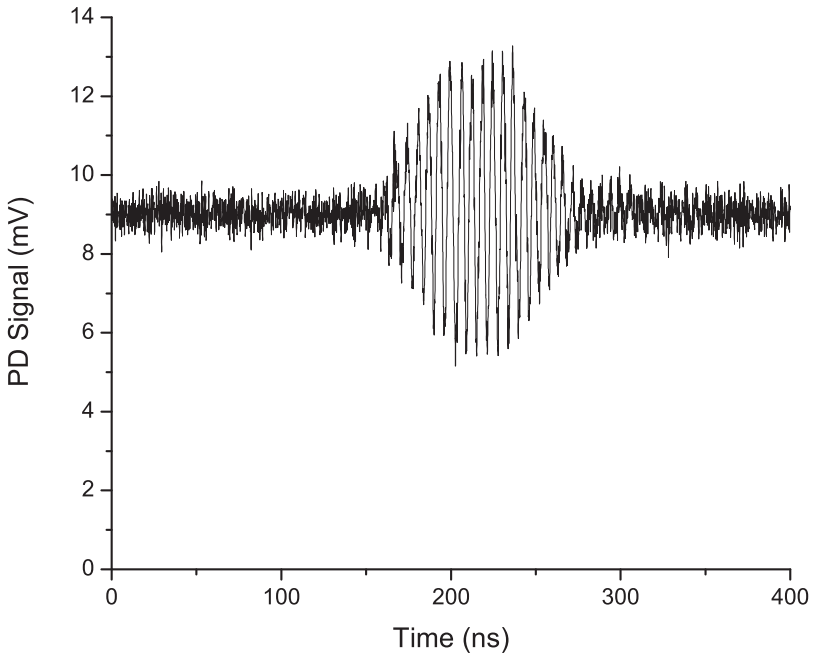

Figure 6.15. TA Heterodyne Signal of 780 nm Pulse

780 nm intensity pulse using the 795 nm TA. The 160 MHz heterodyne frequency is a result of the cumulative AOM shifts from the loop setup.

it appeared to still be following the $\sim$ 1 GHz in 7 ns chirp as shown in figure 6.13(b) and have a $\sim$2 ns FWHM pulse as shown in figure 6.14(c). Improving the coupling efficiency to the heterodyne fiber, employing a farther detuned reference laser for the heterodyne, and incorporating faster electronics for the pulse generation and for the heterodyne signal detection would greatly improve the analysis.

In an attempt to use the 795 nm 500 mW TA to amplify 780 nm frequency-chirped pulses, we lowered the TA temperature close to the lab dew point ($\sim$10 $^\circ$ C) to shift the gain curve of the TA. With $\sim$9 mW of seed power in conjunction with the intensity modulator, we were able to get the $\sim$ 80 ns FWHM pulse shown in figure 6.15. Although we did get some gain, the output power was greatly reduced by being on the edge of the TA gain curve. We estimate that the output power is $\sim$ 100 mW

from $\sim$ 9 mW of seed power. Using a TA with a gain curve centered at 780 nm would provide a higher gain.

The copper sections of the TA mount were modified to accommodate a larger tapered amplifier chip, such as the 2 W 785 nm M2K laser tapered amplifier chip m2k-TA-0785-2000CM. These larger chips typically have higher outputs (2W in this case), but have a correspondingly longer cavity length (4300 μm in this case), necessitating minor changes to the mechanical housing for the tapered amplifier, as shown in section A.2.2. These higher output chips also require a higher operating current, 4 A in this case, which exceeds the Sacher Lasertechnik PilotPC-3000, requiring a higher output driver to reach full power. This chip's gain curve is centered closer to 780 nm and would provide significantly more gain at that wavelength then we saw using the 795 nm TA as in figure 6.15.

Since the TA faithfully follows frequency-chirps and intensity pulses, the TA is a very useful amplifier. For even more gain, it is even possible to use a TA in a double-pass configuration, allowing high output powers with much smaller seed light intensities (often $\sim$ 200 μW) [132]. A double-pass arrangement with this 2W 780 nm tapered amplifier as part of a faster single-pass pulse-shaping system incorporating a $\sim$ 4 GHz AWG (Euvis AWG801) is currently under development [133]. Having higher intensities available will be useful for a variety of atomic and molecular experiments.

6.2.4.4 Optimization

Optimization of the chirp shapes and intensity pulses will become necessary to enhance the experiment yield. Many coherent control experiments already employ genetic or evolutionary algorithms. For the current photoassociation experiments, being able to optimize the detuning, chirp shape, chirp range, chirp rate, and intensity could significantly enhance the molecular formation rate. With our current

setup, such an algorithm with a feedback loop would take a very long time to run. Steps would have to be taken to improve MOT stability and ion count signal-to-noise ratios to make implementing such an algorithm feasible. Genetic and evolutionary algorithms could be used to optimize any number of parameters in a variety of atomic and molecular experiments.

6.2.5 Local-Control-Optimized Frequency Experiments

Performing experiments to test the results presented in section 4.4, which was published as reference [46], should show significant enhancement in the molecular formation rate. Implementing faster electronics would allow us to faithfully reproduce the local-control-optimized frequency shape shown in figure 4.19. Investigating the coherent aspect of the phase dependence and expanding to two lasers, potentially with interference effects, would be very interesting avenues to explore.

6.2.6 Stimulated Molecule Formation with Irreversibility

A common problem with stimulated emission molecule formation is reversibility, preventing accumulation of molecules in the desired state. We could use an extended-range frequency-chirped PA pulse to take atoms from the continuum, form molecules in 0_g^-(v'=78), and stimulate them down to $a\ ^3\Sigma_u^+$(v"=39). Incorporating some shaping of the frequency chirp and perhaps some intensity modulation could enhance the formation rate in $a\ ^3\Sigma_u^+$(v"=39). Then we would use a separate laser with around 100 W/cm^2 at about 757 nm to pump the molecular population from $a\ ^3\Sigma_u^+$(v"=39) to 1_g(v'=8). This population would spontaneously decay in ∼20 ns to $a\ ^3\Sigma_u^+$(v"=0) with a probability of 37% [134]. This accumulation scheme is shown in figure 6.16. This entire scheme can be repeated many times ($\sim 10^5$) to irreversibly accumulate a large molecular population in $a\ ^3\Sigma_u^+$(v"=0). The main advantage is that the molecules

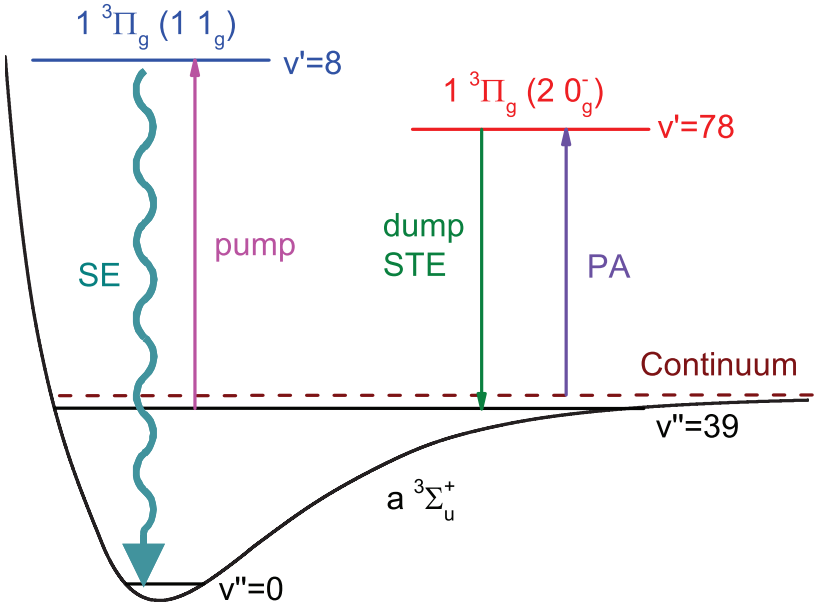

Figure 6.16. Stimulated Molecule Formation with Irreversability

We start with atoms in the continuum and use a frequency-chirped PA pulse to form molecules in the 0_g^-(v'=78) and stimulate them down to the $a\ ^3\Sigma_u^+$(v"=39). Then we use a separate pump laser to drive the population to 1_g(v'=8) and allow the population to spontaneously decay into $a\ ^3\Sigma_u^+$(v"=0).

formed by a chirped pulse are transfered irreversibly before the next chirped pule can destroy them.

6.2.7 "Amplified" Coherent Control

By applying a chirp covering the various atomic hyperfine energy levels, we can investigate the difference between fluorescence for the positive and negative chirps. For the positive chirp, we expect optical pumping to result in very few photons since the chirp passes through the non-cycling F=3 $\rightarrow$ 2 transition first. For the negative chirp, we expect cycling, resulting in many photons. The F=3 $\rightarrow$ 4 transition yields lots of photons because the exclusive decay back into F=3 allows us to repeat the cycle many times, providing "amplification". The hyperfine energy levels are shown in figure 6.17. We performed preliminary experiments using the output of the loop setup (section 3.3). We used the output AOM of the loop setup as a chop AOM before the modulators in a single-pass configuration. To keep well below the 5 mW time-averaged damage threshold for the modulators, we had a peak intensity of 28 mW and the chop AOM was on for 1 μs every 100 μs.

The output light was sent through a Rb cell with a CCD camera to image the atomic fluorescence. Based on the focus into the Rb cell, we had only $\sim$ 300 mW/cm^2 going into the Rb cell. The cell and camera were covered with a box with a small hole to reduce the background. The chirped beam timing and frequency ramps are shown in figure 6.18. We employed 400 MHz in 10 ns frequency chirps with 5 ns FWHM Gaussian pulses centered on either the positive or negative slopes. Analyzing the camera images showed preliminary results that the negative chirp signal was $\sim$1.3 times the positive chirp signal. This signal could be improved with more intensity and a higher chirp repetition rate. Performing the same experiment on the MOT, where Doppler broadening is not present and the atoms experience a uniform intensity,

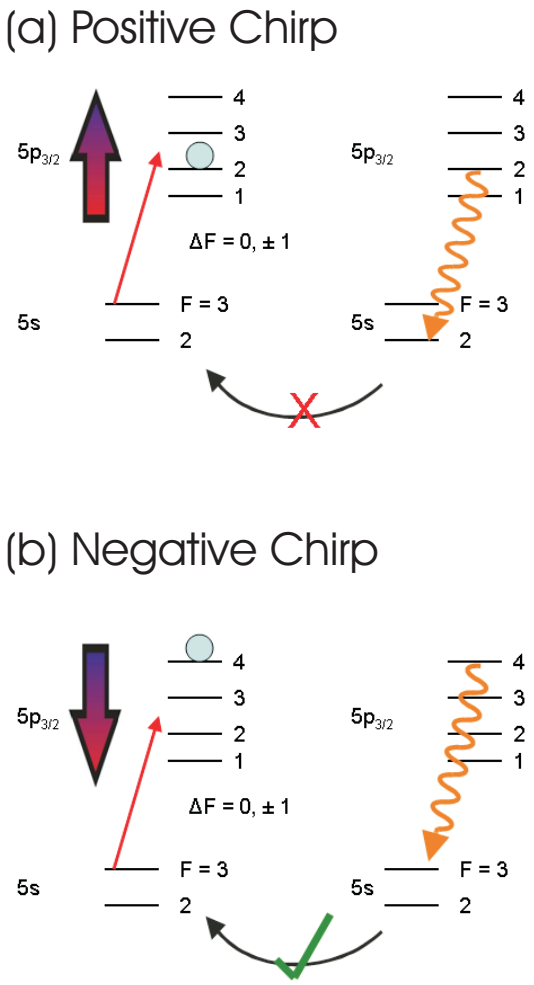

Figure 6.17. "Amplified" Coherent Control

Optical pumping for the positive chirp (a) results in few photons compared to the cycling for the negative chirp (b) which results in many photons.

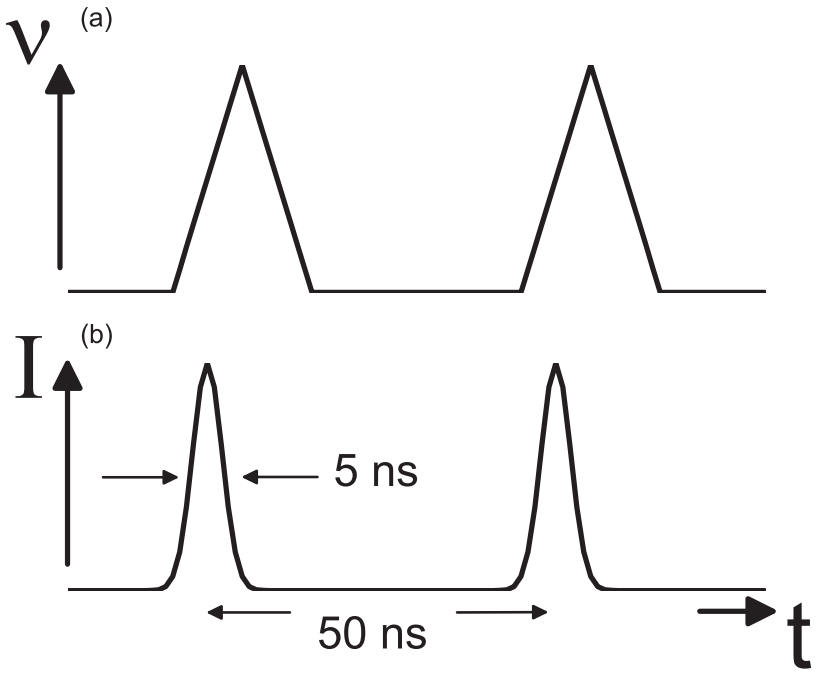

Figure 6.18. "Amplified" Coherent Control Chirped Pulse Timing

The ramp wave frequency chirp is shown in (a) and the Gaussian intensity pulse timing is shown in (b). Here the positive chirp is being selected.

as well as employing the techniques described in section 6.2.4, should significantly enhance the signal.

6.3 Final Remarks

We have presented results on the effects of nanosecond-timescale frequency-chirped laser light on the formation of ultracold ground-state molecules both experimentally and through quantum mechanical simulations. Through the simulations we were able to understand the mechanism responsible for the enhancement of the molecular formation rate for the positive chirp over the negative chirp, and then we were able to use this knowledge experimentally to enhance the molecular formation rate of the positive shaped chirp to 1.85 times the unchirped pulse. These results are an important advancement towards the efficient production of ultracold molecules in their electronic, rovibrational ground states. Interesting avenues for future investigations include incorporation of faster electronics, an intensity modulator, and a tapered amplifier, which will aid in future advancements.

Appendix A
Mechanical Drawings

This appendix contains mechanical drawings. The 795 nm master and slave laser mechanical drawings are in section A.1. The tapered amplifier mechanical drawings for the 795 nm 500 mW chip are in section A.2.1. Updated tapered amplifier mechanical drawings to accommodate a 2W 780 nm chip are shown in section A.2.2. All dimensions are in inches.

A.1 795 nm Lasers

These lasers are designed to address the Rb D_1 line, as described in section 6.2.3.1.

A.1.1 795 nm Master Laser

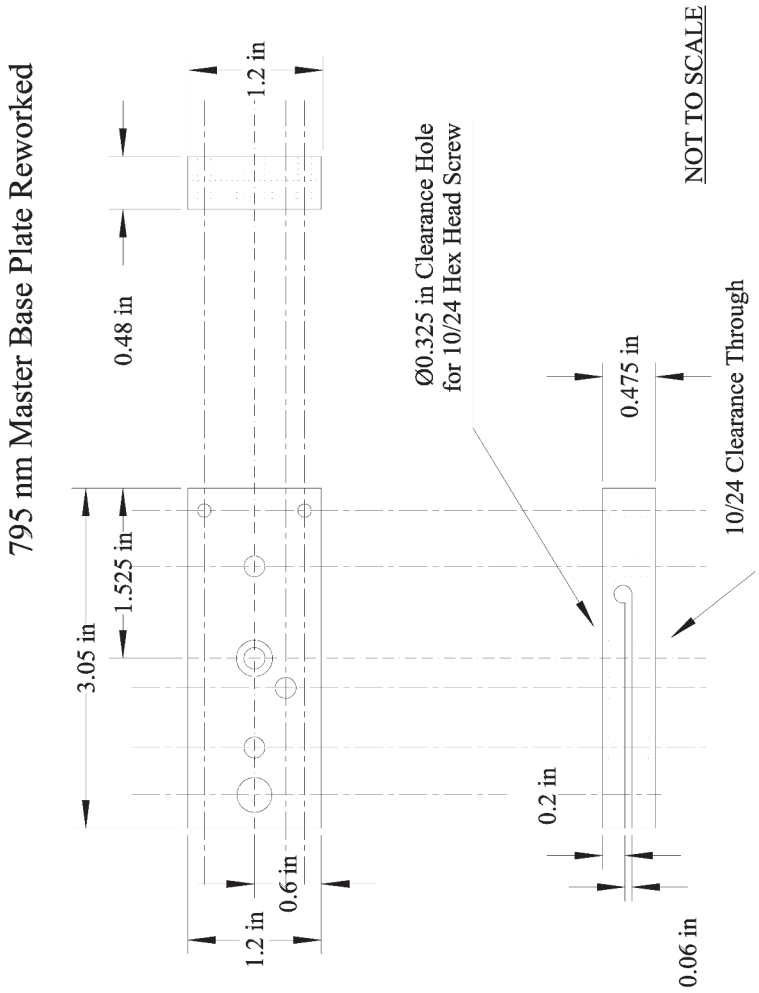

Figure A.1. 795 nm ECDL Base Plate Drawing

Overview of aluminum 795 nm ECDL base plate. Modified from base plate drawing by Aleksandr Estrin.

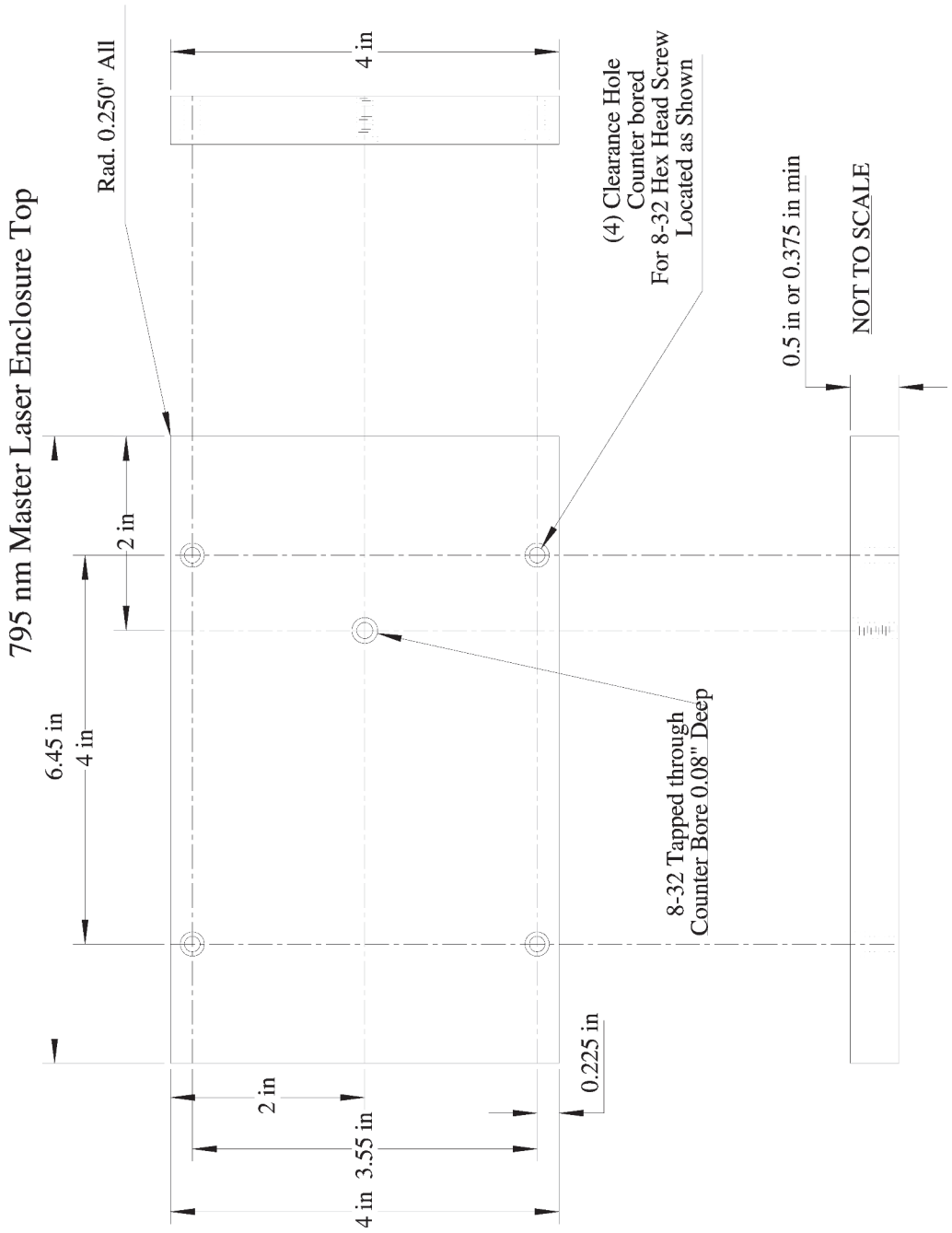

Figure A.2. 795 nm ECDL Top Drawing

Overview of plexiglass 795 nm ECDL box top.

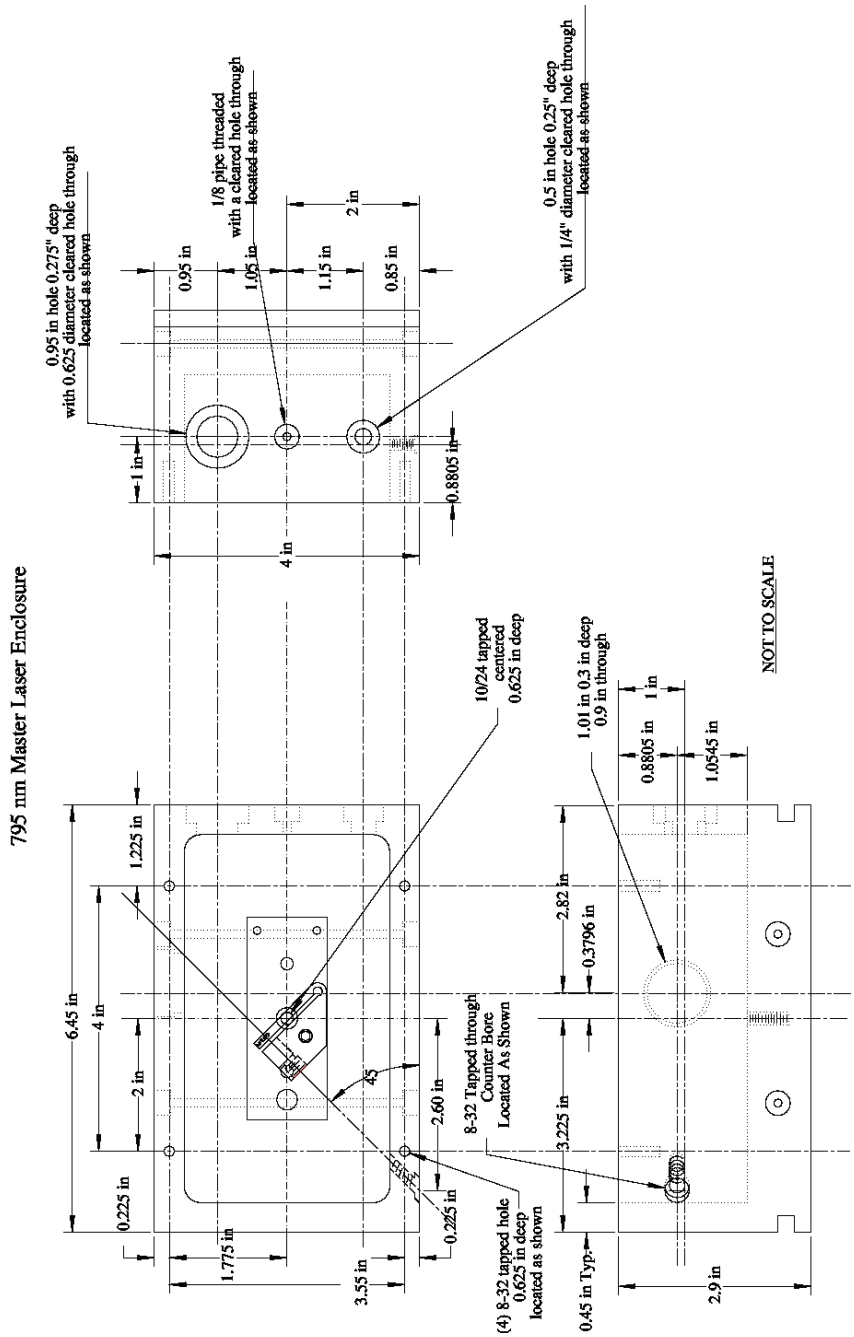

Figure A.3. 795 nm ECDL Drawing

Overview of aluminum 795 nm ECDL. Modified from ECDL drawing by Andrew Scott.

A.1.2 795 nm Slave Laser

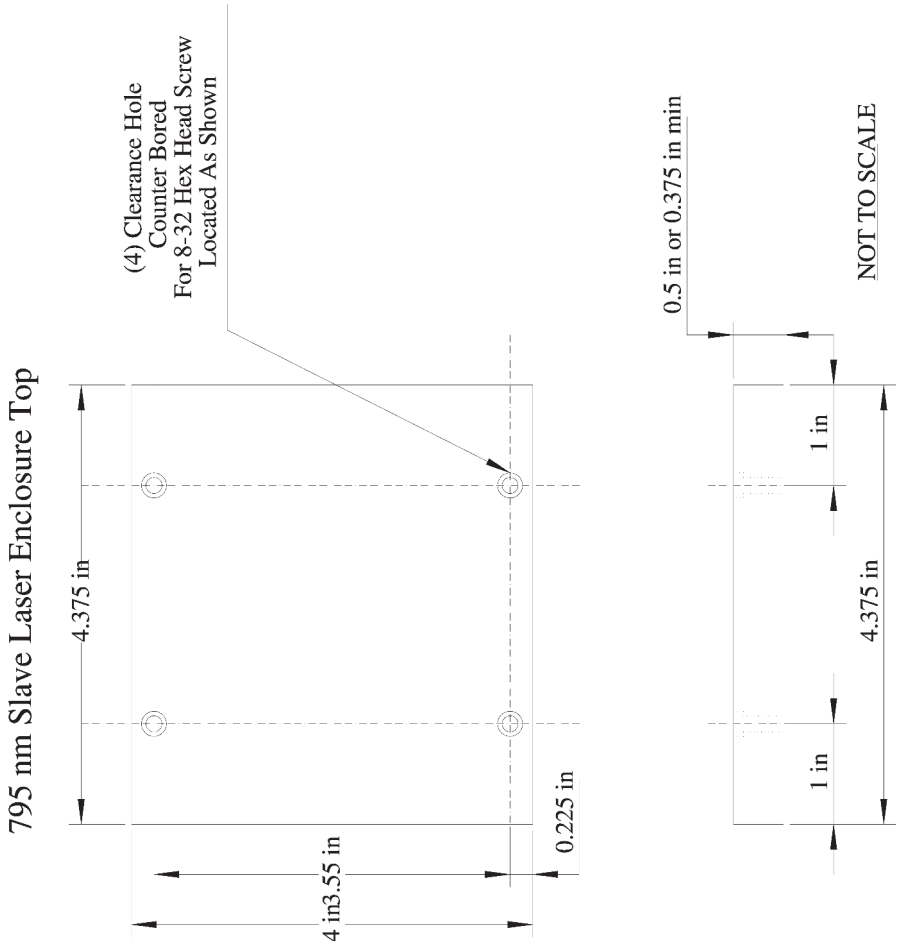

Figure A.4. 795 nm FRDL Top Drawing

Overview of plexiglass 795 nm FRDL box top.

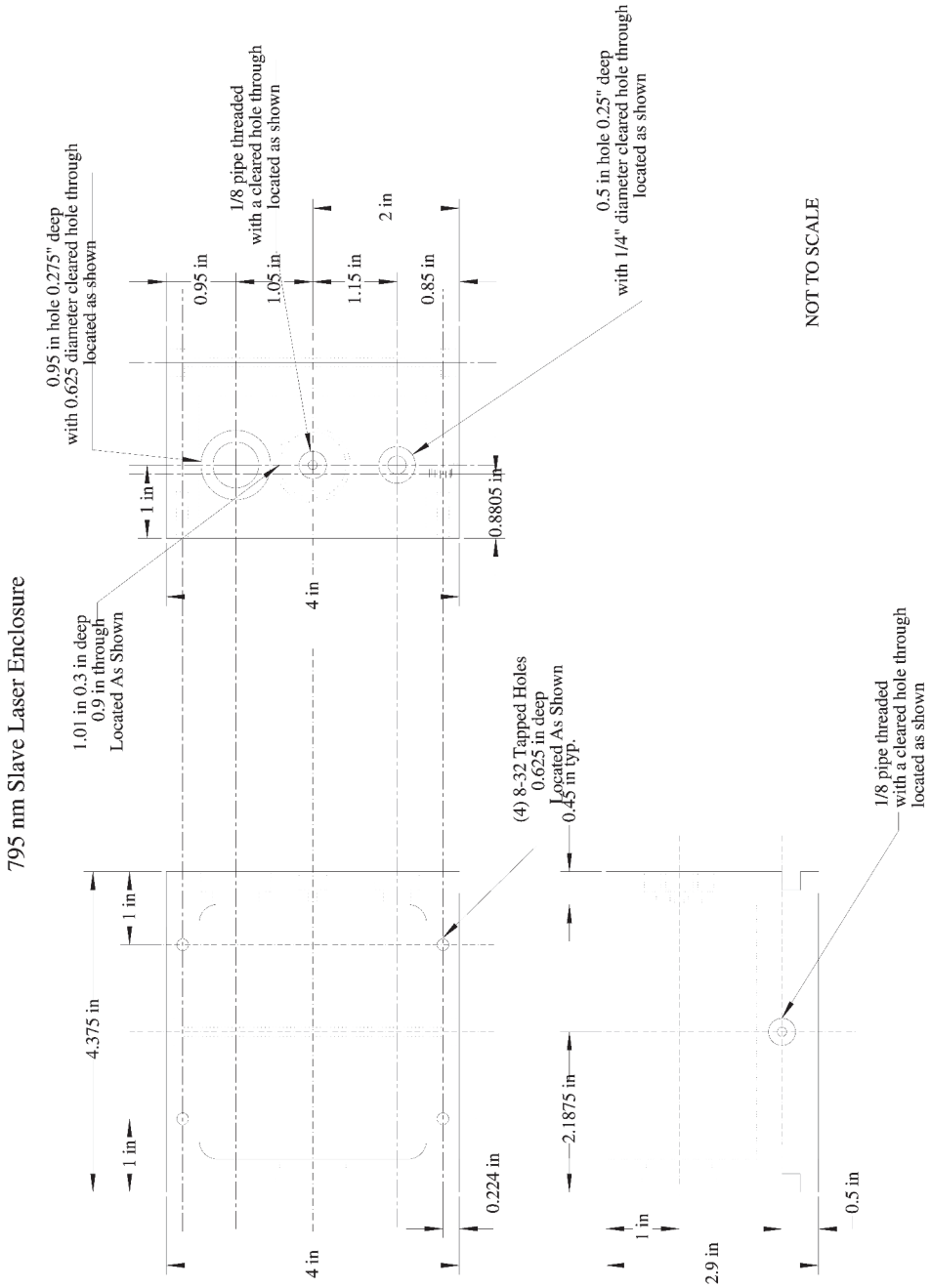

Figure A.5. 795 nm FRDL Drawing

Overview of aluminum 795 nm FRDL.

A.2 Tapered Amplifiers

Tapered amplifiers are one method of amplifying a phase- and amplitude-modulated pulse, as described in section 6.2.4.3.

A.2.1 500 mW 795 nm Tapered Amplifier

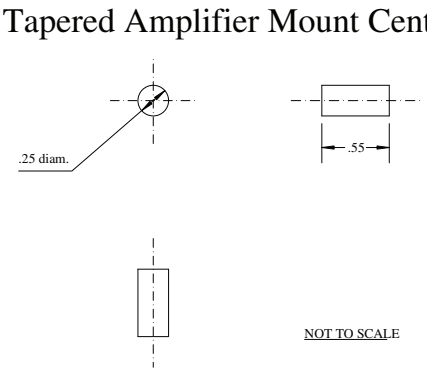

Figure A.6. Tapered Amplifier Centering Rods Drawing

The tapered amplifier aluminum centering rods help secure and line up the two copper blocks.

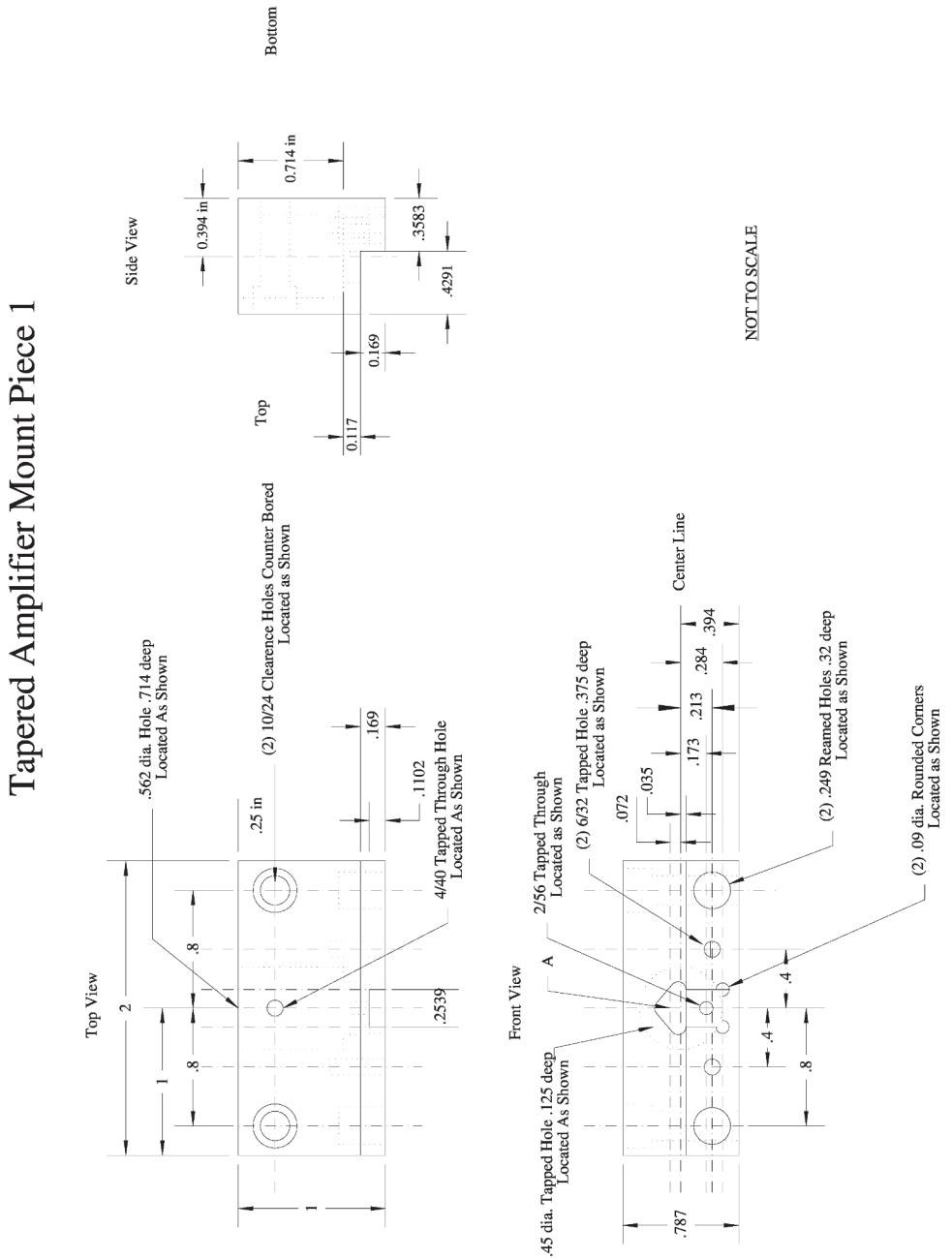

Figure A.7. Tapered Amplifier Mount Piece 1 Drawing

Overview of tapered amplifier copper mount piece 1.

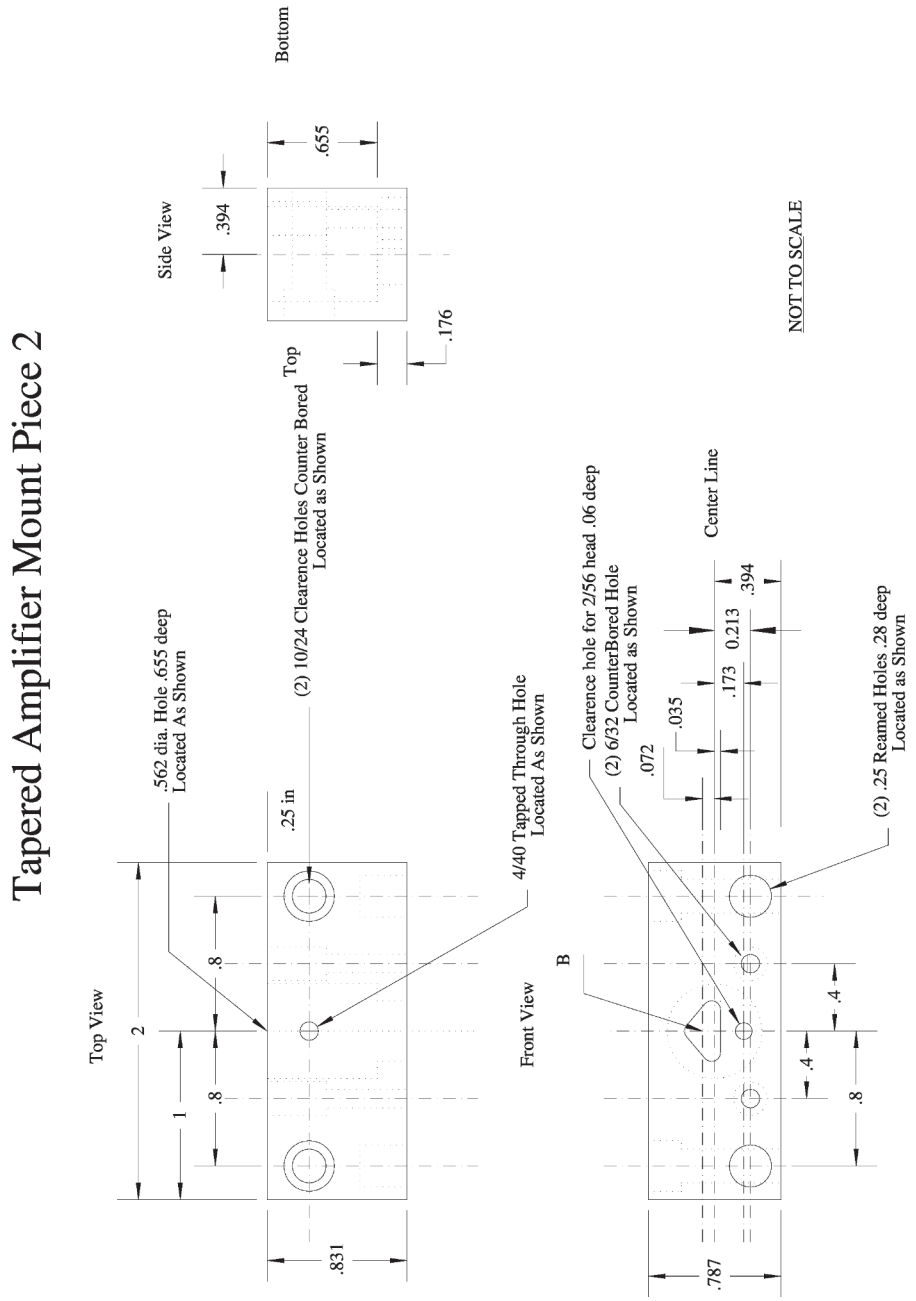

Figure A.8. Tapered Amplifier Mount Piece 2 Drawing

Overview of tapered amplifier copper mount piece 2.

A:

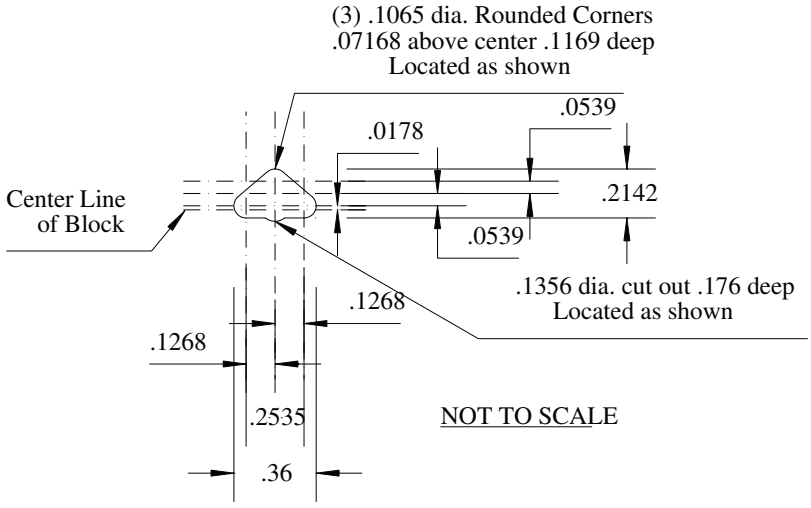

Figure A.9. Tapered Amplifier Mount Piece 1 View A Drawing

Close-up of tapered amplifier mount piece 1 view A.

B: NOT TO SCALE

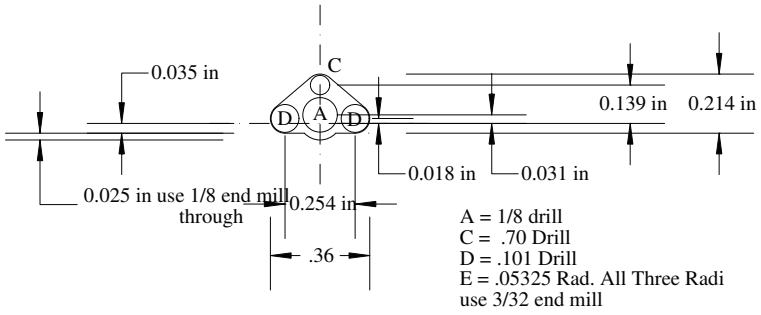

Figure A.10. Tapered Amplifier Mount Piece 2 View B Drawing

Close-up of tapered amplifier mount piece 2 view B.

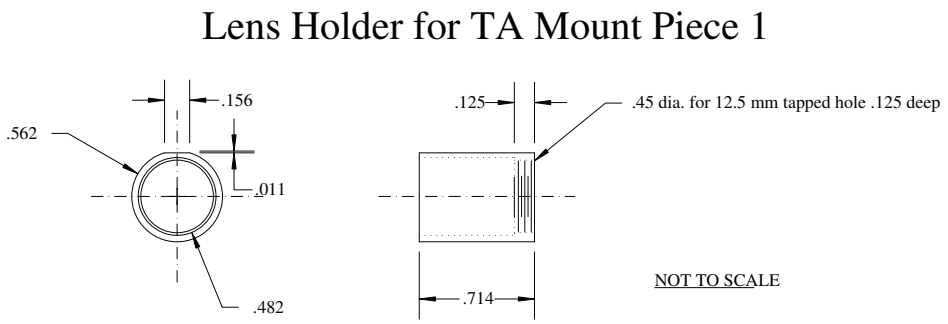

Figure A.11. Tapered Amplifier Mount Piece 1 Lens Holder Drawing

This is a threaded aluminum lens holder that is inserted into tapered amplifier mount piece 1.

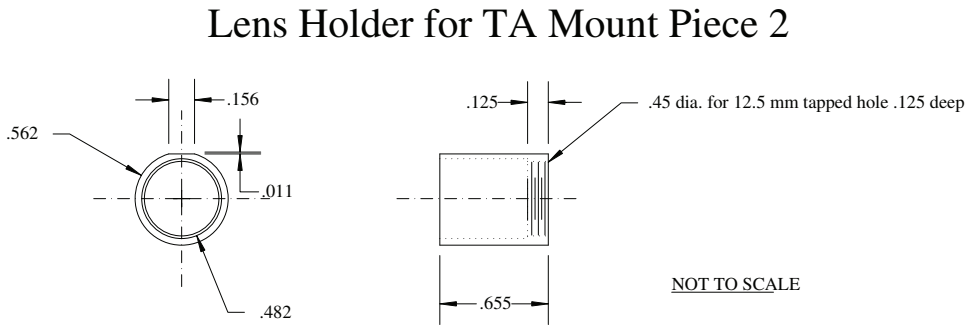

Figure A.12. Tapered Amplifier Mount Piece 2 Lens Holder Drawing

This is a threaded aluminum lens holder that is inserted into tapered amplifier mount piece 2.

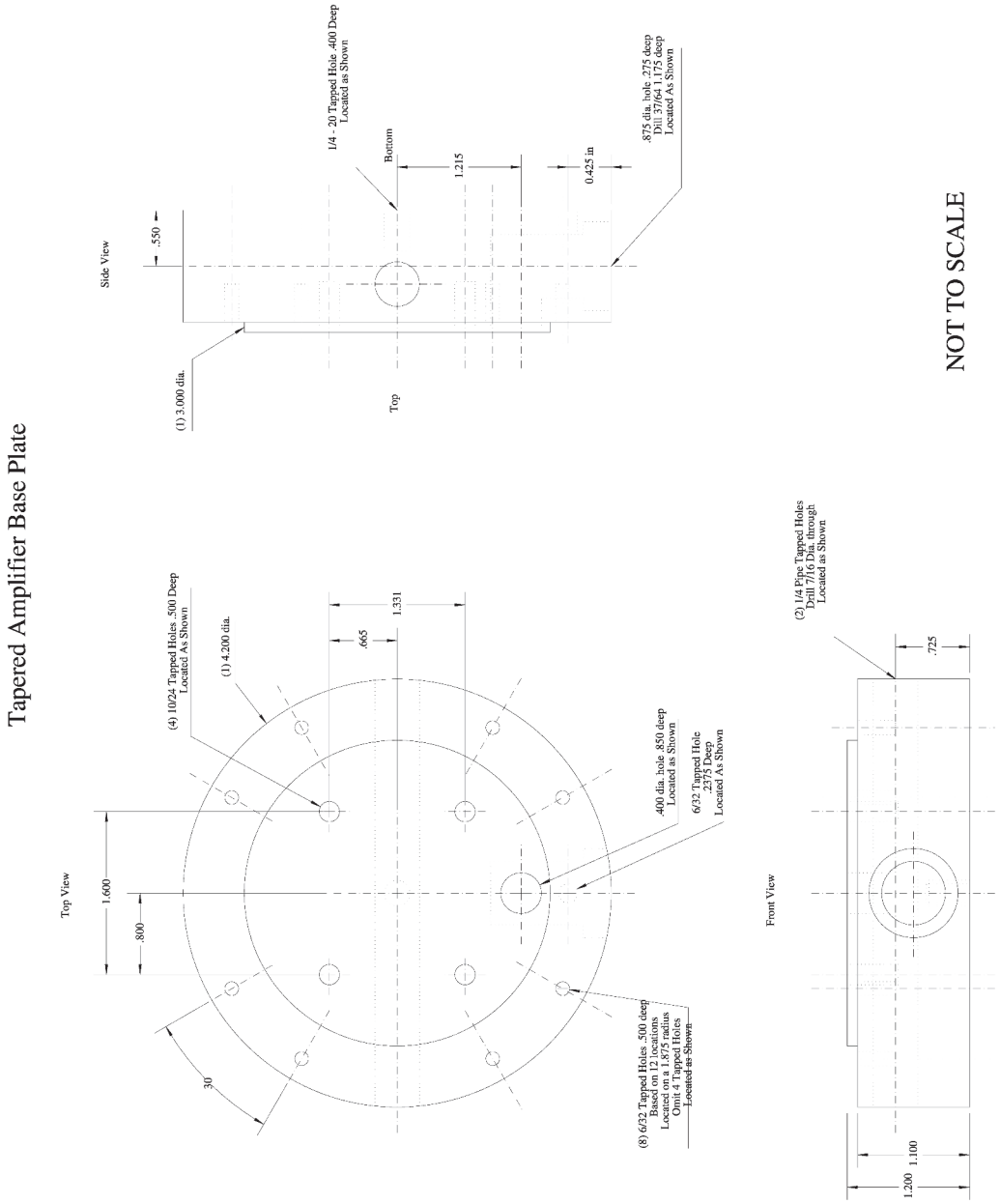

Figure A.13. Tapered Amplifier Base Plate Drawing

Tapered amplifier water cooled aluminum base plate. This base plate design secures the copper tapered amplifier blocks in place, provides water cooling for the TECs, and has a hole intended for a weather-tight fitting to be used for electrical access.

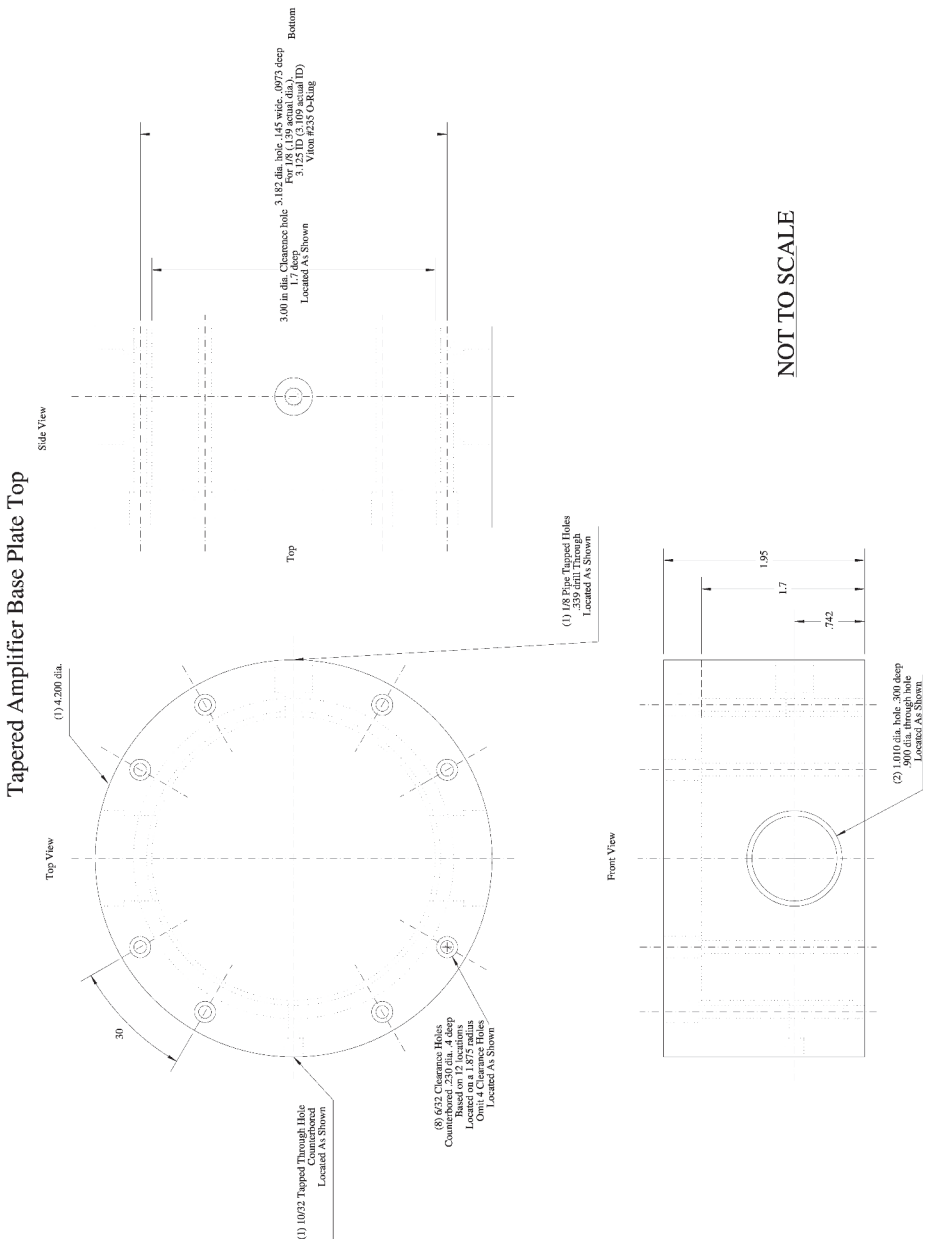

Figure A.14. Tapered Amplifier Base Plate Top Drawing

Tapered amplifier aluminum base plate top. Holes along the optical axis are for Brewster angle windows. Holes perpendicular to that axis are for gas flushing the TA mount, if cooling to below the dew point. There is a ring for an o-ring along the bottom to seal the tapered amplifier.

A.2.2 2 W 780 nm Tapered Amplifier

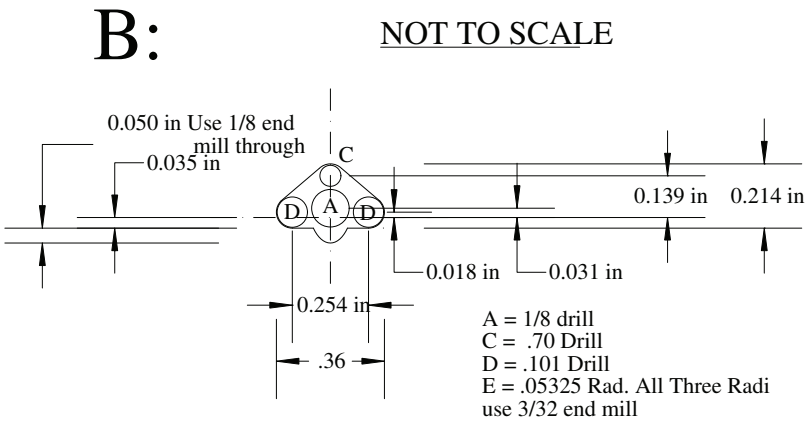

Figure A.15. Tapered Amplifier Mount Piece 2 View B Modified for 2 W TA Drawing

Close-up of tapered amplifier mount 2 view B. The dip under A may need to be further extended depending on divergence of chip.

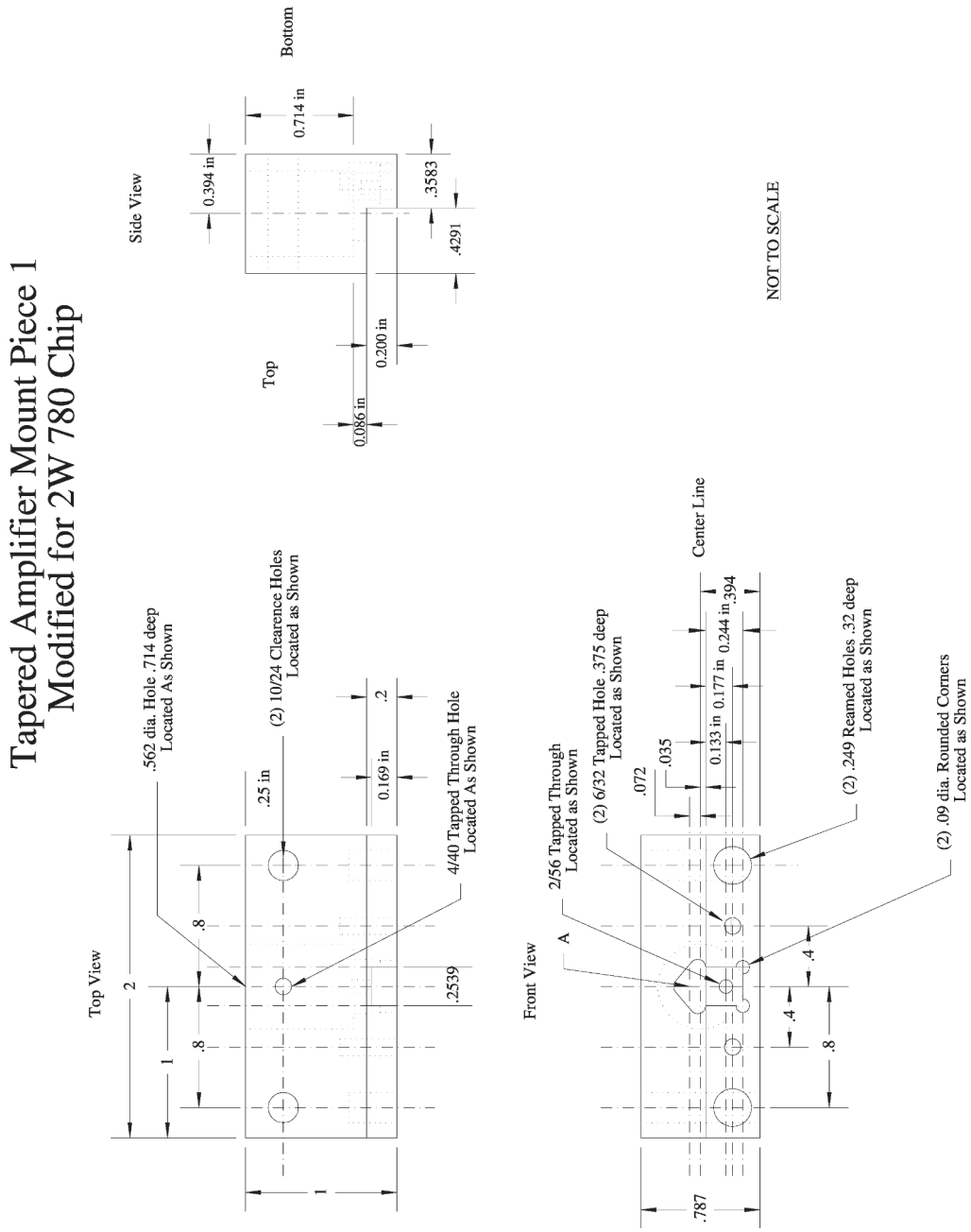

Figure A.16. Tapered Amplifier Mount Piece 1 Modified for 2 W TA Drawing

Overview of tapered amplifier copper mount piece 1.

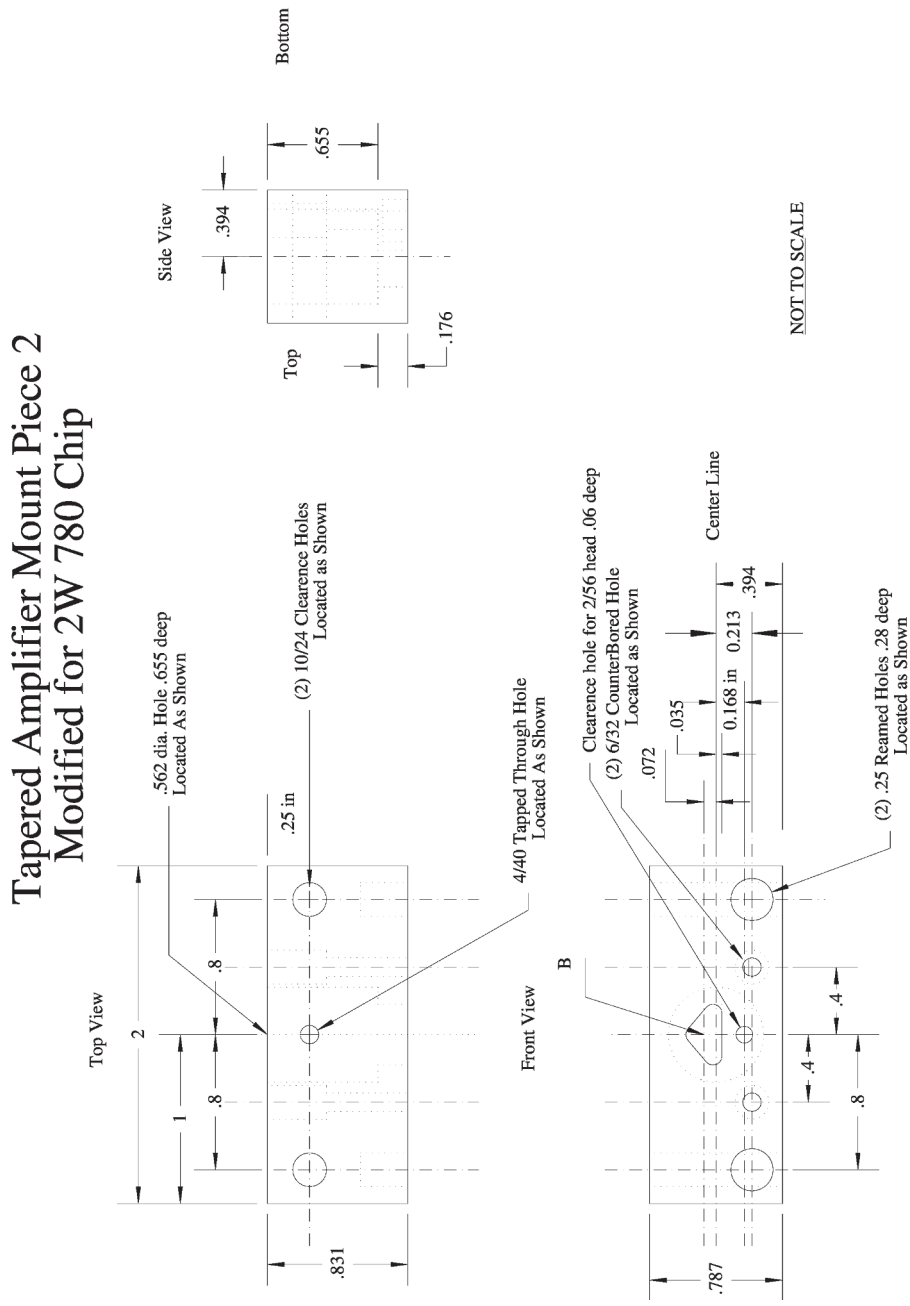

Figure A.17. Tapered Amplifier Mount Piece 2 Modified for 2 W TA Drawing

Overview of tapered amplifier copper mount piece 2.

Bibliography

[1] W. D. Phillips, Rev. Mod. Phys. **70**, 721 (1998).

[2] S. Chu, Rev. Mod. Phys. **70**, 685 (1998).

[3] C. N. Cohen-Tannoudji, Rev. Mod. Phys. **70**, 707 (1998).

[4] W. Ketterle, Rev. Mod. Phys. **74**, 1131 (2002).

[5] E. A. Cornell and C. E. Wieman, Rev. Mod. Phys. **74**, 875 (2002).

[6] D. J. Wineland, Rev. Mod. Phys. **85**, 1103 (2013).

[7] S. Haroche, Rev. Mod. Phys. **85**, 1083 (2013).

[8] *Cold molecules: theory, experiment, applications*, edited by R. V. Krems, W. C. Stwalley, and B. Friedrich (CRC press, Boca Raton, FL, 2009).

[9] L. D. Carr and J. Ye, eds., *Focus on Cold and Ultracold Molecules*, New J. Phys., Vol. 11 (2009).

[10] D. S. Jin and J. Ye, eds., *Ultracold Molecules*, Chem. Rev., Vol. 112 (ACS Publications, 2012).

[11] L. Carr, D. DeMille, R. Krems, and J. Ye, eds., *Focus on New Frontiers of Cold Molecules Research*, New J. Phys., Vol. 17 (2015).

[12] *Cold Atoms and Molecules*, edited by M. Weidemüller and C. Zimmermann (Wiley-VCH, Weinheim, Germany, 2009).

[13] A. Assion, T. Baumert, M. Bergt, T. Brixner, B. Kiefer, V. Seyfried, M. Strehle, and G. Gerber, Science **282**, 919 (1998).

[14] M. Shapiro and P. Brumer, *Principles of the quantum control of molecular processes* (Wiley, New York, New York, 2003).

[15] M. Shapiro and P. Brumer, Rep. Prog. Phys. **66**, 859 (2003).

[16] P. Brumer and M. Shapiro, Chem. Phys. Lett. **126**, 541 (1986).

[17] H. Tang, R. Kosloff, and S. A. Rice, J. Chem. Phys **104**, 5457 (1996).

[18] J. Vala, O. Dulieu, F. Masnou-Seeuws, P. Pillet, and R. Kosloff, Phys. Rev. A **63**, 013412 (2000).

[19] V. S. Batista and P. Brumer, Phys. Rev. Lett. **89**, 143201 (2002).

[20] J. M. Doyle, B. Friedrich, J. Kim, and D. Patterson, Phys. Rev. A **52**, R2515 (1995).

[21] H. L. Bethlem, G. Berden, and G. Meijer, Phys. Rev. Lett. **83**, 1558 (1999).

[22] E. Shuman, J. Barry, and D. DeMille, Nature **467**, 820 (2010).

[23] M. T. Hummon, M. Yeo, B. K. Stuhl, A. L. Collopy, Y. Xia, and J. Ye, Phys. Rev. Lett. **110**, 143001 (2013).

[24] V. Zhelyazkova, A. Cournol, T. Wall, A. Matsushima, J. Hudson, E. Hinds, M. Tarbutt, and B. Sauer, Phys. Rev. A **89**, 053416 (2014).

[25] W. C. Stwalley, Phys. Rev. Lett. **37**, 1628 (1976).

[26] M. W. Zwierlein, J. R. Abo-Shaeer, A. Schirotzek, C. H. Schunck, and W. Ketterle, Nature **435**, 1047 (2005).

[27] K.-K. Ni, S. Ospelkaus, M. De Miranda, A. Pe'er, B. Neyenhuis, J. Zirbel, S. Kotochigova, P. Julienne, D. Jin, and J. Ye, Science **322**, 231 (2008).

[28] F. Lang, K. Winkler, C. Strauss, R. Grimm, and J. H. Denschlag, Phys. Rev. Lett. **101**, 133005 (2008).

[29] A. Fioretti, D. Comparat, A. Crubellier, O. Dulieu, F. Masnou-Seeuws, and P. Pillet, Phys. Rev. Lett. **80**, 4402 (1998).

[30] A. N. Nikolov, E. E. Eyler, X. T. Wang, J. Li, H. Wang, W. C. Stwalley, and P. L. Gould, Phys. Rev. Lett. **82**, 703 (1999).

[31] C. Gabbanini, A. Fioretti, A. Lucchesini, S. Gozzini, and M. Mazzoni, Phys. Rev. Lett. **84**, 2814 (2000).

[32] D. Wang, J. Qi, M. Stone, O. Nikolayeva, H. Wang, B. Hattaway, S. Gensemer, P. Gould, E. Eyler, and W. Stwalley, Phys. Rev. Lett. **93**, 243005 (2004).

[33] U. Schlöder, C. Silber, T. Deuschle, and C. Zimmermann, Phys. Rev. A **66**, 061403 (2002).

[34] J. Deiglmayr, A. Grochola, M. Repp, K. Mörtlbauer, C. Glück, J. Lange, O. Dulieu, R. Wester, and M. Weidemüller, Phys. Rev. Lett. **101**, 133004 (2008).

[35] C. P. Koch and M. Shapiro, in Jin and Ye [10], pp. 4928–4948.

[36] W. Salzmann, U. Poschinger, R. Wester, M. Weidemüller, A. Merli, S. M. Weber, F. Sauer, M. Plewicki, F. Weise, A. M. Esparza, L. Wöste, and A. Lindinger, Phys. Rev. A **73**, 023414 (2006).

[37] B. L. Brown, A. J. Dicks, and I. A. Walmsley, Phys. Rev. Lett. **96**, 173002 (2006).

[38] J. Ulmanis, J. Deiglmayr, M. Repp, R. Wester, and M. Weidemüller, in Jin and Ye [10], pp. 4890–4927.

[39] W. Salzmann, T. Mullins, J. Eng, M. Albert, R. Wester, M. Weidemüller, A. Merli, S. Weber, F. Sauer, M. Plewicki, *et al.*, Phys. Rev. Lett. **100**, 233003 (2008).

[40] D. J. McCabe, D. G. England, H. E. Martay, M. E. Friedman, J. Petrovic, E. Dimova, B. Chatel, and I. A. Walmsley, Phys. Rev. A **80**, 033404 (2009).

[41] H. E. Martay, D. J. McCabe, D. G. England, M. E. Friedman, J. Petrovic, and I. A. Walmsley, Phys. Rev. A **80**, 033403 (2009).

[42] T. Mullins, W. Salzmann, S. Götz, M. Albert, J. Eng, R. Wester, M. Weidemüller, F. Weise, A. Merli, S. M. Weber, F. Sauer, L. Wöste, and A. Lindinger, Phys. Rev. A **80**, 063416 (2009).

[43] A. Merli, F. Eimer, F. Weise, A. Lindinger, W. Salzmann, T. Mullins, S. Götz, R. Wester, M. Weidemüller, R. Ağanoğlu, and C. P. Koch, Phys. Rev. A **80**, 063417 (2009).

[44] J. L. Carini, J. A. Pechkis, C. E. Rogers III, P. L. Gould, S. Kallush, and R. Kosloff, Phys. Rev. A **85**, 013424 (2012).

[45] J. L. Carini, J. A. Pechkis, C. E. Rogers, P. L. Gould, S. Kallush, and R. Kosloff, Phys. Rev. A **87**, 011401(R) (2013).

[46] J. L. Carini, S. Kallush, R. Kosloff, and P. L. Gould, New J. Phys. **17**, 025008 (2015).

[47] H. J. Metcalf and P. Van der Straten, *Laser cooling and trapping* (Springer, 1999).

[48] D. Wineland and H. Dehmelt, Bulletin APS **20**, 637 (1975).

[49] T. W. Hänsch and A. L. Schawlow, Opt Commun **13**, 68 (1975).

[50] A. Rauschenbeutel, H. Schadwinkel, V. Gomer, and D. Meschede, Opt. Commun. **148**, 45 (1998).

[51] M. J. Wright, *Coherent Control of Ultracold Collisions with Frequency-Chirped Light*, Ph.D. thesis, University of Connecticut (2006).

[52] S. D. Gensemer, *Characterization and Control of Ultracold Collisions*, Ph.D. thesis, University of Connecticut (1999).

[53] P. Pillet, A. Crubellier, A. Bleton, O. Dulieu, P. Nosbaum, I. Mourachko, and F. Masnou-Seeuws, J. Phys. B **30**, 2801 (1997).

[54] E. Raab, M. Prentiss, A. Cable, S. Chu, and D. E. Pritchard, Phys. Rev. Lett. **59**, 2631 (1987).

[55] Z. Lu, K. Corwin, M. Renn, M. Anderson, E. Cornell, and C. Wieman, Phys. Rev. Lett. **77**, 3331 (1996).

[56] L. Ricci, M. Weidemüller, T. Esslinger, A. Hemmerich, C. Zimmermann, V. Vuletic, W. König, and T. W. Hänsch, Opt. Commun. **117**, 541 (1995).

[57] M. F. Stone, *Stabilized External-cavity Diode Lasers*, Master's thesis, State University of New York at Stony Brook (2001).

[58] R. Kowalski, S. Root, S. Gensemer, and P. Gould, Rev. Sci. Instrum. **72**, 2532 (2001).

[59] Y. Huang, *Production, Detection and Trapping of Ultracold Molecular Rubidium*, Ph.D. thesis, University of Connecticut (2006).

[60] J. Lozeille, A. Fioretti, C. Gabbanini, Y. Huang, H. Pechkis, D. Wang, P. Gould, E. Eyler, W. Stwalley, M. Aymar, *et al.*, Eur. Phys. J. D **39**, 261 (2006).

[61] M. Ascoli, *Spectroscopy of States with Ion-Pair Character Near Rb(5s)+Rb(4d)*, Ph.D. thesis, University of Connecticut (2015).

[62] J. A. Pechkis, *Coherent Control of Trap-Loss Collisions and Molecule Formation with Frequency-Chirped Light*, Ph.D. thesis, University of Connecticut (2010).

[63] T. Bergmann, T. Martin, and H. Schaber, Rev. Sci. Instrum. **60**, 792 (1989).

[64] T. Bergmann, T. Martin, and H. Schaber, Rev. Sci. Instrum. **60**, 347 (1989).

[65] T. Bergmann, H. Goehlich, T. Martin, H. Schaber, and G. Malegiannakis, Rev. Sci. Instrum. **61**, 2585 (1990).

[66] T. Bergmann, T. Martin, and H. Schaber, Rev. Sci. Instrum. **61**, 2592 (1990).

[67] C. E. Rogers III, M. J. Wright, J. L. Carini, J. A. Pechkis, and P. L. Gould, J. Opt. Soc. Am. B **24**, 1249 (2007).

[68] J. Banerjee, *Ultracold Heteronuclear KRb Molecules: Production of the Lowest Vibrational Levels of the Ground State and Spectroscopy of the Excited States*, Ph.D. thesis, University of Connecticut (2013).

[69] C. Lorenzen and K. Niemax, Phys. Scripta **27**, 300 (1983).

[70] R. Kosloff, Annu. Rev. Phys. Chem. **45**, 145 (1994).

[71] E. Fattal, R. Baer, and R. Kosloff, Phys. Rev. E **53**, 1217 (1996).

[72] S. Kallush and R. Kosloff, Chem. Phys. Lett. **433**, 221 (2006).

[73] V. Kokoouline, O. Dulieu, R. Kosloff, and F. Masnou-Seeuws, Phys. Rev. A **62**, 032716 (2000).

[74] R. Kosloff, J. Phys. Chem. **92**, 2087 (1988).

[75] J. Roberts, N. Claussen, J. P. Burke Jr, C. H. Greene, E. Cornell, and C. Wieman, Phys. Rev. Lett. **81**, 5109 (1998).

[76] S. Geltman and A. Bambini, Phys. Rev. Lett. **86**, 3276 (2001).

[77] R. Gutterres, C. Amiot, A. Fioretti, C. Gabbanini, M. Mazzoni, and O. Dulieu, Phys. Rev. A **66**, 024502 (2002).

[78] P. Julienne and J. Vigué, Phys. Rev. A **44**, 4464 (1991).

[79] C. P. Koch, R. Kosloff, E. Luc-Koenig, F. Masnou-Seeuws, and A. Crubellier, J. Phys. B **39**, S1017 (2006).

[80] J. A. Pechkis, J. L. Carini, C. E. Rogers III, P. L. Gould, S. Kallush, and R. Kosloff, Phys. Rev. A **83**, 063403 (2011).

[81] E. Luc-Koenig and F. Masnou-Seeuws, in Krems *et al.* [8], Chap. 7, p. 245.

[82] O. Dulieu, M. Raoult, and E. Tiemann, J. Phys. B **39** (2006).

[83] *Cold and Ultracold Molecules*, Faraday Discussions, Vol. 142 (Royal Society of Chemistry, 2009).

[84] J. Bahns, W. Stwalley, and P. Gould, J. Chem. Phys **104**, 9689 (1996).

[85] S. A. Rice and M. Zhao, *Optical control of molecular dynamics* (Wiley, New York, New York, 2000).

[86] H. Thorsheim, J. Weiner, and P. Julienne, Phys. Rev. Lett. **58**, 2420 (1987).

[87] W. C. Stwalley and H. Wang, J. Mol. Spectrosc. **195**, 194 (1999).

[88] K. M. Jones, E. Tiesinga, P. D. Lett, and P. S. Julienne, Rev. Mod. Phys. **78**, 483 (2006).

[89] W. C. Stwalley, P. L. Gould, and E. E. Eyler, in Krems *et al.* [8], Chap. 5, p. 169.

[90] E. Luc-Koenig, R. Kosloff, F. Masnou-Seeuws, and M. Vatasescu, Phys. Rev. A **70**, 033414 (2004).

[91] E. Luc-Koenig, M. Vatasescu, and F. Masnou-Seeuws, Eur. Phys. J. D **31**, 239 (2004).

[92] C. P. Koch, R. Kosloff, and F. Masnou-Seeuws, Phys. Rev. A **73**, 043409 (2006).

[93] U. Poschinger, W. Salzmann, R. Wester, M. Weidemüller, C. P. Koch, and R. Kosloff, J. Phys. B **39**, S1001 (2006).

[94] B. L. Brown and I. A. Walmsley, J. Phys. B **39**, S1055 (2006).

[95] C. P. Koch, E. Luc-Koenig, and F. Masnou-Seeuws, Phys. Rev. A **73**, 033408 (2006).

[96] J. Mur-Petit, E. Luc-Koenig, and F. Masnou-Seeuws, Phys. Rev. A **75**, 061404 (2007).

[97] S. Kallush, R. Kosloff, and F. Masnou-Seeuws, Phys. Rev. A **75**, 043404 (2007).

[98] S. Kallush and R. Kosloff, Phys. Rev. A **76**, 053408 (2007).

[99] S. Kallush and R. Kosloff, Phys. Rev. A **77**, 023421 (2008).

[100] C. P. Koch, M. Ndong, and R. Kosloff, in *Two-photon coherent control of femtosecond photoassociation* [83], pp. 389–402.

[101] S. Ghosal, R. J. Doyle, C. P. Koch, and J. M. Hutson, New J. Phys. **11**, 055011 (2009).

[102] E. Luc-Koenig, F. Masnou-Seeuws, and R. Kosloff, Phys. Rev. A **76**, 053415 (2007).

[103] F. Fatemi, K. M. Jones, H. Wang, I. Walmsley, and P. D. Lett, Phys. Rev. A **64**, 033421 (2001).

[104] G. Veshapidze, M. Trachy, H. Jang, C. Fehrenbach, and B. DePaola, Phys. Rev. A **76**, 051401 (2007).

[105] M. J. Wright, S. Gensemer, J. Vala, R. Kosloff, and P. Gould, Phys. Rev. Lett. **95**, 063001 (2005).

[106] M. Wright, J. Pechkis, J. Carini, S. Kallush, R. Kosloff, and P. Gould, Phys. Rev. A **75**, 051401 (2007).

[107] J. Weiner, V. S. Bagnato, S. Zilio, and P. S. Julienne, Rev. Mod. Phys. **71**, 1 (1999).

[108] M. Aymar and O. Dulieu, J. Chem. Phys **122**, 204302 (2005).

[109] B. L. Brown, A. J. Dicks, and I. A. Walmsley, Phys. Rev. Lett. **96**, 173002 (2006).

[110] M. Kemmann, I. Mistrik, S. Nussmann, H. Helm, C. J. Williams, and P. S. Julienne, Phys. Rev. A **69**, 022715 (Feb 2004).

[111] M. Wright, P. Gould, and S. Gensemer, Rev. Sci. Instrum. **75**, 4718 (2004).

[112] C. P. Koch and R. Kosloff, Phys. Rev. A **81**, 063426 (2010).

[113] R. Gutterres, C. Amiot, A. Fioretti, C. Gabbanini, M. Mazzoni, and O. Dulieu, Phys. Rev. A **66**, 024502 (2002).

[114] B. Londono, A. Derevianko, J. Mahecha, A. Crubellier, and E. Luc-Koenig, Phys. Rev. A **85**, 033419 (2012).

[115] A. M. Weiner, Rev. Sci. Instrum. **71**, 1929 (2000).

[116] S. A. Rice, Science **258**, 412 (1992).

[117] P. Brumer and M. Shapiro, Annu. Rev. Phys. Chem. **43**, 257 (1992).

[118] C. P. Koch and R. Moszyński, Phys. Rev. A **78**, 043417 (2008).

[119] C. P. Koch, J. P. Palao, R. Kosloff, and F. Masnou-Seeuws, Phys. Rev. A **70**, 013402 (2004).

[120] M. Viteau, A. Chotia, M. Allegrini, N. Bouloufa, O. Dulieu, D. Comparat, and P. Pillet, Science **321**, 232 (2008).

[121] V. Engel, C. Meier, and D. J. Tannor, Adv. Chem. Phys. **141**, 29 (2009).

[122] R. Kosloff, S. A. Rice, P. Gaspard, S. Tersigni, and D. Tannor, Chem. Phys. **139**, 201 (1989).

[123] J. P. Palao and R. Kosloff, Phys. Rev. A **68**, 062308 (2003).

[124] D. J. Tannor, *Introduction to quantum mechanics:A Time-Dependent Perspective* (University Science Books, 2007).

[125] R. S. Judson and H. Rabitz, Phys. Rev. Lett. **68**, 1500 (1992).

[126] N. V. Vitanov, T. Halfmann, B. W. Shore, and K. Bergmann, Annu. Rev. Phys. Chem. **52**, 763 (2001).

[127] R. Seiler, T. Paul, M. Andrist, and F. Merkt, Rev. Sci. Instrum. **76**, 103103 (2005).

[128] C. E. Rogers III, J. L. Carini, J. A. Pechkis, and P. L. Gould, Rev. Sci. Instrum. **82**, 073107 (2011).

[129] C. E. Rogers III, J. L. Carini, J. A. Pechkis, and P. L. Gould, Opt. Express **18**, 1166 (2010).

[130] R. A. Nyman, G. Varoquaux, B. Villier, D. Sacchet, F. Moron, Y. Le Coq, A. Aspect, and P. Bouyer, Rev. Sci. Instrum. **77**, 033105 (2006).

[131] J. C. Kangara, A. J. Hachtel, M. C. Gillette, J. T. Barkeloo, E. R. Clements, S. Bali, B. E. Unks, N. A. Proite, D. D. Yavuz, P. J. Martin, *et al.*, Am. J Phys **82**, 805 (2014).

[132] V. Bolpasi and W. von Klitzing, Rev. Sci. Instrum. **81**, 113108 (2010).

[133] C. E. Rogers III, Personal Communication (2015).

[134] M. A. Bellos, D. Rahmlow, R. Carollo, J. Banerjee, O. Dulieu, A. Gerdes, E. E. Eyler, P. L. Gould, and W. C. Stwalley, Phys. Chem. Chem. Phys. **13**, 18880 (2011).